

**Metallo-Supramolecular Assemblies as Functional
Architectures**

Victoria Emily Pritchard

Submitted in accordance with the requirements for the degree of
Doctor of Philosophy

The University of Leeds
School of Chemistry

May 2016

The candidate confirms that the work submitted is his/her own, except where work which has formed part of jointly-authored publications has been included. The contribution of the candidate and the other authors to this work has been explicitly indicated below. The candidate confirms that appropriate credit has been given within the thesis where reference has been made to the work of others

References for the jointly authored papers:

F. Thorp-Greenwood, V. E. Pritchard, M. P. Coogan, M. J. Hardie, ‘Tris-rhenium fac-tricarbonyl polypyridine-functionalised cyclotriguaiacylene ligands with rich and varied emission.’, *Organometallics*, **2016**, 35, 1632–1642

[F. Thorp-Greenwood synthesised one of the compounds, M. Coogan assisted with the photophysical measurements at Lancaster University and M. Hardie supervised the work. The paper was written through the joint efforts of all involved.]

This copy has been supplied on the understanding that it is copyright material and that no quotation from the thesis may be published without proper acknowledgement.

The right of Victoria Emily Pritchard to be identified as Author of this work has been asserted by her in accordance with the Copyright, Designs and Patents Act 1988.

© 2016 The University of Leeds and Victoria Emily Pritchard

Acknowledgements

Firstly, and most importantly, I would like to thank Professor Michael Hardie for giving me this opportunity and taking a chance on me despite my rather late application. I've learnt more than I ever thought I could.

To Diego and Eli, this thesis wouldn't have been possible without your continued support, thank you; and to Mike, thank you for instilling in me the confidence to even apply for a PhD.

Special thanks must also go to Dr Stuart Warriner, for not only your Mass Spec wisdom, but also your somewhat dubious 'inspirational' pep talks.

To members of the Willans, Halcrow and McGowan groups, past and present; thank you for making the Inorganic Section such an enjoyable place to work, and for making sure that the Inorganic Christmas meals are always an event to remember, despite the extensive time we spend in the German Market beforehand.

To the veterans of the Section, long since gone, Ben, Jonny, Rianne, Carlo and Tom; thank you for imparting your knowledge of not only chemistry but also the best bars in Leeds. Honorable mentions must go to Amedeo and Carlo for teaching all of us the intricacies of Italian hand gestures. To Tom for being the only person capable of smuggling a pork pie into Singapore and Rafal for truly convincing people you were the King of Poland.

And thank you to current Hardie group members, Jonny, Hayder and Sam. Watching you all grow and improve since you started has made me realise just how much I've grown-up in my time at Leeds, I know you'll all be successful

To Jordan and Mike, the annoying brothers that I never wanted, thank you. You two may drive me insane and mercilessly tease me, but the last 2 years would have been pretty dull without you, although they would have involved a lot less milk and 100% fewer ambulances.

And to James, I owe you a lot. I know I wouldn't be the chemist, or person, I am today without you holding me to your exacting standards, thank you. You remain, to this day, the only person who could pull off salmon chinos and an orange polo.

But perhaps most importantly, I want to thank my family. My parents, who never once doubted me, I owe you more than I could ever articulate. I hope that I've made you proud and I'll carry the Dr. Pritchard Jr. title with pride.

Abstract

This thesis concerns the rational design of supramolecular metal-complexes and assemblies through combination of tripodal ligands and geometrically directing metallotectons. The aim of this work is to impart functionality into the resultant complexes, with a view towards applications exploiting the inherent luminescent emission of the systems.

The metallotectons discussed in this thesis all derive from low-spin d^6 metal centres, with incorporation of ancillary ligands designed to retain and modulate the resultant luminescent emission leading to high-fidelity control over the emissive outcome.

Three families of complexes were synthesised; incorporating Re(I), Ru(II) and Ir(III) in combination with supporting ancillary ligands and a pair of bi-dentate bipyridine-appended cavitand ligands. The photophysical properties of these systems were investigated and rationalised with respect to both the structural motif of the cavitand ligands and the structure of the metallotecton.

The Ir(III) family of complexes was expanded upon to give rise to both tri-metallic and mono-metallic systems, retaining vacant coordination sites. These vacant sites were subsequently exploited in the formation of heterometallic and heteronuclear assemblies employing secondary Ir(III) metallotectons and Ru(II) metallotectons respectively. This novel, modular approach allows for high-fidelity control over the emission properties and gives rise to a ‘function-driven’ route towards metallo-supramolecular design.

The self-assembly of the aforementioned d^6 -metallotectons in combination with mono-dentate cavitand ligands was also investigated, leading to the formation of the first example of an ambi-dentate heteroleptic Re(I) metallocryptophane and a Ru(II)-cornered metallo-cube. A family of novel luminescent Ir(III) metallocryptophanes were also formed, one of which was crystallographically elucidated. The emission colour was modulated between blue-green and intense yellow luminescence depending on the nature of the ligand, and with large internal cavities these cages possess potential in host-guest chemistry.

Table of Contents:

Acknowledgements	III
Abstract	IV
Table of Contents:	V
List of Figures:	VIII
List of Tables:	XIII
List of Schemes:	XIV
List of Equations:	XV
List of Abbreviations:	XVI
1: Chapter 1	
<i>Introduction</i>	1
1.1 Overview	1
1.2 Luminescence	1
1.2.1 Phosphorescence	4
1.2.2 Applications	6
1.2.2.1 Biomedical Imaging	6
1.2.2.2 OLEDs and LEECs.....	8
1.3 Supramolecular Chemistry	11
1.3.1 Metallo-supramolecular Chemistry	11
1.4 Cyclotrimeratrylene	24
1.5 Project Outline	31
1.6 Bibliography	32
2: Chapter 2	
<i>Synthesis of cyclotriguaiacylene derived ligands and the resultant rhenium(I) complexes</i>	47
2.1 Introduction	47
2.2 Ligand synthesis	48
2.3 Rhenium(I) complexes of L1 and L2	53
2.4 Photophysical properties of C1.1 and C2.1	58
2.4.1 Photophysical properties of C1.1	59
2.4.2 Photophysical properties of C2.1	61
2.4.3 Comparison of C1.1 and C2.1	62
2.5 Crystallographic analysis of L1 and C1.1	62
2.5.1 Solid state structure of L1	62

2.5.2	Solid state structure of C1.1	64
2.6	Towards heteroleptic ambidentate metallocryptophanes	67
2.7	Conclusions and future direction.....	73
2.8	Experimental	74
2.8.1	General Considerations	74
2.8.2	X-ray crystallography.....	82
2.8.3	Photophysical studies	83
2.9	Bibliography.....	84

3: Chapter 3

	<i>Tri- and mono- homometallic iridium complexes of CTG-type ligands</i>	89
3.1	Introduction	89
3.2	Preparation of homo tri-metallic iridium species	90
3.3	Preparation of mono-metallic iridium species	97
3.4	Spectroscopic analysis of tri- and mono-metallic iridium complexes	102
3.5	Photophysical properties of tri- and mono-metallic Ir species.....	107
3.6	Conclusions and further direction	114
3.7	Experimental	116
3.7.1	Synthesis.....	116
3.7.2	Photophysical studies	122
3.8	Bibliography.....	123

4: Chapter 4

	<i>Hetero tri-metallic iridium complexes of CTG-type ligands</i>	124
4.1	Introduction	124
4.2	Preparation of hetero tri-metallic iridium complexes	126
4.3	Spectroscopic analysis of heterometallic systems.....	129
4.3.1	High-resolution mass spectrometric analysis of heterometallic iridium complexes	129
4.3.2	¹ H NMR analysis of heterometallic iridium species	133
4.4	Photophysical analysis of heterometallic fluorinated systems	136
4.5	Conclusions and further direction	142
4.6	Experimental	145
4.6.1	Synthesis.....	145
4.6.2	Photophysical studies	150
4.7	Bibliography.....	151

5: Chapter 5

<i>Heteronuclear ruthenium-iridium complexes and ruthenium containing supramolecular assemblies</i>	155
5.1 Introduction	155
5.2 Preparation of tri-metallic ruthenium complexes	155
5.2.1 Spectroscopic analysis of ruthenium complexes	158
5.2.2 Photophysical analysis of ruthenium complexes	162
5.3 Preparation of heteronuclear ruthenium-iridium complexes	164
5.3.1 Spectroscopic analysis of heteronuclear complexes	167
5.4 Towards the preparation of ruthenium containing supramolecular assemblies	171
5.5 Conclusions and further directions	178
5.6 Experimental	180
5.6.1 Synthesis	180
5.6.2 Photophysical studies	184
5.7 Bibliography	184

6: Chapter 6

<i>Luminescent metallocryptophanes</i>	187
6.1 Introduction	187
6.2 Preparation of homocage metallocryptophanes	190
6.2.1 Spectroscopic analysis of metallocryptophanes	192
6.2.2 Crystallographic analysis of metallocryptophane CC4.3	197
6.3 Speciation studies of homo- and heterocage metallocryptophanes	206
6.4 Photophysical properties of metallocryptophanes	213
6.4.1 Photophysical properties of CC3.1	214
6.4.2 Photophysical properties of CC4.3	215
6.4.3 Comparison of the photophysics of CC3.1 and CC4.3	215
6.5 Expanding the complexity	217
6.6 Conclusions and future direction	221
6.7 Experimental	223
6.7.1 Synthesis	223
6.7.2 X-ray crystallography	225
6.7.3 Photophysical Studies	226
6.8 Bibliography	227

List of Figures:

Figure 1.1: Simplified schematic to show the basic premise of photoluminescence.....	2
Figure 1.2: Simplified schematic to show the basic premise of electroluminescence.....	3
Figure 1.3: (a) Simplified schematic depicting the HOMO-LUMO energy gap, (b) colour-coded chemical structure of a model iridium complex.....	3
Figure 1.4: Simplified Jablonski diagram, showing both fluorescence and phosphorescence processes.....	5
Figure 1.5: Chemical structure and confocal microscopy images of a fructose appended imaging agent.....	7
Figure 1.6: Chemical structure of Iridium(III) imaging agent.....	8
Figure 1.7: General schematic depicting the multitude of layers required for OLED fabrication.....	9
Figure 1.8: General schematic depicting the set-up of LEEC formation.....	10
Figure 1.9: Stoddart's Molecular Borromean rings.....	12
Figure 1.10: Examples of topologically complex interlocked molecules.....	13
Figure 1.11: A series of Fe(II) tetrahedra from the Nitschke group.....	14
Figure 1.12: SCXRD structures of a porphyrin-panelled trigonal prism and Pd ₆ L ₄ octahedron from the Fujita group.....	16
Figure 1.13: Cp*-capped metalla-assemblies.....	17
Figure 1.14: Ruthenium cage assemblies.....	18
Figure 1.15: Chemical structure of the emissive polypyridyl motif.....	19
Figure 1.16: Emissive MOFs.....	20
Figure 1.17: (a) Ruthenium cryptate (b) Ir ₄ (CN) ₄ tetramer, (c) Ru ₃ L tri-nuclear assembly (d) Ir ₃ L.....	21
Figure 1.18: (a) Chemical structure of emissive Re ₂ Pd ₂ metalla-square (b) Ru ₂ M ₂ metallomacrocycle.....	23
Figure 1.19: Chemical structure of the tri-benzo cyclononatriene family of ligands.....	24
Figure 1.20: (a) Cu ₄ L ₄ CTC tetrahedron (b) Pt ₃ L redox-active tri-nuclear CTC complex.....	25
Figure 1.21: Enantiomeric description of metallocryptophane cages.....	27
Figure 1.22: SCXRD structures of (a) the stella octangular Pd ₆ L ₈ assembly and (b) an NHC-directed Pd ₃ L ₂ metallocryptophane.....	28

Figure 1.23: SCXRD structure of (a) $[\text{Pd}(\text{Cl})_2]_3\text{L}$ and the chemical structure of Wytko's copper-binding hexakis(bipyridyl)-CTV	29
Figure 1.24: Tris-substituted CTV-type ligands from Verboom, Atwood and Bohle.	30
Figure 1.25: SCXRD structure of $[\text{Cu}(\text{Cl})_2]_3\text{L}$ and the self-inclusion 'hand-shake' motif exhibited.....	30
Figure 2.1: Interpreted ^1H NMR spectrum of L1 in CDCl_3 solvent.	50
Figure 2.2: Interpreted ^1H NMR spectrum of L2 in d_6 -DMSO.	51
Figure 2.3: Interpreted ^1H - ^1H COSY NMR spectrum of L2	52
Figure 2.4: Assigned HR ESI-MS of L2	53
Figure 2.5: ^1H NMR spectra of C1.1 in d_3 -MeCN (top) and C2.1 in d_6 -DMSO/ d_3 -MeCN (bottom).	55
Figure 2.6: Assigned ^1H - ^1H COSY NMR spectrum of C1.1	56
Figure 2.7: HR ESI-MS of C1.1 (top) and C2.1 (bottom).....	57
Figure 2.8: Overlaid UV-Visible spectra of C1.1 and C2.1 in DMSO solution.....	59
Figure 2.9: Overlaid excitation and emission profiles of C1.1 in DMSO.	59
Figure 2.10: Overlaid excitation and emission profiles of C2.1 in DMSO.	61
Figure 2.11: a) Labelled ASU of $\text{L1}\cdot[(\text{Et})_2\text{O}]$	63
Figure 2.12: ASU of C1.1 ,.....	64
Figure 2.13: a) viewing the enantiomeric pair-stack looking down the crystallographic c axis b) the difference in the triangular pyramid described by each enantiomer.	66
Figure 2.14: Packing structure of C1.1	67
Figure 2.15: Side-view of C1.1	68
Figure 2.16: HR ESI-MS of C1.1B	69
Figure 2.17: HR ESI-MS of CC1.1	71
Figure 2.18: Stacked ^1H NMR spectra following the formation of CC1.1	72
Figure 3.1: Nomenclature relating to iridium complexes in the literature and in this work.....	89
Figure 3.2: Expanded HR-ESI-MS of C1.2 (top) and C2.2 (bottom).....	93
Figure 3.3: Possible stereoisomers of C1.2/C2.2	95
Figure 3.4: In situ emission of mono-metallic C1.3 (left) and C2.3 (right) with excitation at 405 nm.....	99
Figure 3.5: Expanded HR-ESI-MS of mono-metallic C1.3 (top) and C2.3 (bottom).....	100
Figure 3.6: Expanded HR ESI-MS of mono-metallic C1.3	101

Figure 3.7: Expanded HR-ESI MS of mono-metallic C2.3	101
Figure 3.8: Stacked spectra exemplifying the complex ¹ H NMR spectra recorded for a) L1 in d-CHCl ₃ b) tri-metallic C1.2 in d ₂ -DCM c) mono-metallic C1.3 in d ₂ -DCM.	102
Figure 3.9: Structure of L1	103
Figure 3.10: Expanded ¹ H NMR spectrum of C1.2 in CD ₃ CN	104
Figure 3.11: Expanded structure of mono-metallic C1.3	105
Figure 3.12: Expanded ¹ H NMR spectrum of C2.2 in CD ₃ CN.	106
Figure 3.13: Stacked spectra exemplifying the complex ¹ H NMR spectra recorded for a) L2 in d ₆ -DMSO b) tri-metallic C2.2 in d ₂ -DCM c) mono-metallic C2.3 in d ₂ -DCM.	107
Figure 3.14: Overlaid emission spectra for C1.2 and C1.3 recorded in deaerated acetonitrile.	108
Figure 3.15: Overlaid emission spectra of C2.2 and C2.3 recorded in deaerated acetonitrile.	109
Figure 3.16: Dark-room image revealing the contrast in emission properties between L1 and L2 containing complexes.	111
Figure 3.17: Overlaid emission spectra of C1.2 , 2.2 , 1.3 and 2.3 when incorporated into a doped PMMA thin-film.	112
Figure 3.18: Dark-room images of C1.2 , 1.3 , 2.2 and 2.3	114
Figure 4.1: CIE chart highlighting the white-light containing central area	125
Figure 4.2: Generic HOMO-LUMO energy gap scheme related to the colour coded general [Ir(C [^] N) ₂ (N [^] N)] structure.	126
Figure 4.3: HR ESI-MS of C1.4	130
Figure 4.4: HR ESI-MS of C2.4	130
Figure 4.5: HR-MS of C1.5a (top) and C2.5a (bottom).	131
Figure 4.6: HR ESI-MS of C1.5	132
Figure 4.7: HR ESI-MS of C2.5	133
Figure 4.8: Chemical structure and nomenclature of both iridium metallotectons employed in the formation of C1.4 , C2.4 , C1.5 and C2.5	134
Figure 4.9: Stacked ¹ H NMR spectra of C1.4 and C1.5 in CD ₃ CN.	134
Figure 4.10: Stacked ¹ H NMR spectra of C2.4 and C2.5 in CD ₃ CN	135
Figure 4.11: Overlaid emission spectra of C1.4 and C1.5 recorded in deaerated acetonitrile solution.	136
Figure 4.12: Overlaid emission spectra of C2.4 and C2.5 recorded in deaerated acetonitrile solution.	138

Figure 4.13: Dark-room images of fluorinated C1.4-5 and C2.4-5 in acetonitrile solution, with the homometallic C1.2-3 and C2.2-3 shown for comparison.	140
Figure 4.14: Overlaid emission spectra of C1.4, 1.5, 2.4 and 2.5 incorporated into a PMMA doped thin-film.	141
Figure 4.15: Dark-room images of C1.4, 1.5, 2.4 and 2.5 incorporated in PMMA doped thin-films.	142
Figure 4.16: Generic scheme for the synthesis of ABB type emissive systems. ...	143
Figure 5.1: HR ESI-MS of C1.6	159
Figure 5.2: HR ESI-MS of C2.6	160
Figure 5.3: Assigned ¹ H NMR spectrum of C1.6 in CD ₃ CN.....	161
Figure 5.4: ¹ H NMR spectrum of C2.6 in CD ₃ CN	162
Figure 5.5: Overlaid emission spectra for C1.6 and C2.6 recorded in acetonitrile solution.....	163
Figure 5.6: HR ESI-MS of C1.7	167
Figure 5.7: HR ESI-MS of C2.7	168
Figure 5.8: Chemical structure of heteronuclear C1.7 and C2.7	169
Figure 5.9: Overlay of ¹ H NMR spectra in CD ₃ CN of (a) tris-ruthenium C1.6 , (b) tris-iridium C1.2 and (c) heteronuclear C1.7	170
Figure 5.10: Overlay of ¹ H NMR spectra in CD ₃ CN of (a) tris-ruthenium C2.6 , (b) tris-iridium C2.2 and (c) heteronuclear C2.7	171
Figure 5.11: Targeted cubic supramolecular structure CC4.1	172
Figure 5.12: Timecourse ¹ H NMR study of the formation of CC4.1	173
Figure 5.13: Interpreted partial 2D NOESY NMR spectrum of CC4.1 in d ₃ -MeNO ₂ solvent.....	174
Figure 5.14: Timecourse ¹ H NMR study of the formation of CC4.2	176
Figure 5.15: Interpreted 2D ¹ H- ¹ H NOESY spectrum of CC4.2 in d ₃ -MeNO ₂ solvent.	177
Figure 6.1: SCXRD structure of Ag ₃ L ₂ [2]-catenane and Pd ₃ L ₂ NHC-containing metallocryptophane.	188
Figure 6.2: SCXRD structures of Baranoff's tetramer and Lusby's M ₆ L ₄ capsule and Chandrasekhar's M ₂ L ₂ dimer, all containing the Ir(ppy) ₂ metallotecton.	189
Figure 6.3: General scheme for the formation of M ₃ L ₂ cryptophanes, where M=[Ir(ppy) ₂] ⁺	191
Figure 6.4: HR ESI-MS of M ₃ L ₂ assembly CC3.1	192
Figure 6.5: HR ESI-MS of M ₃ L ₂ assembly CC4.3	193
Figure 6.6: Structure of the iridium metallotecton (M) employed in formation of M ₃ L ₂ metallocryptophanes.	194

Figure 6.7: ^1H NMR timecourse experiment following the formation of [CC3.1•3(PF ₆)].	194
Figure 6.8: ^1H NMR timecourse experiment following the formation of [CC4.3•3(PF ₆)].	195
Figure 6.9: DOSY NMR spectrum of [CC4.3•3(PF ₆)] in d ₃ -MeNO ₂ , showing a D _c of $3.56 \times 10^{-10} \text{ m}^2 \text{ s}^{-1}$.	196
Figure 6.10: DOSY NMR spectrum of L4 in d ₃ -MeNO ₂ , showing a D _L of $5.2 \times 10^{-10} \text{ m}^2 \text{ s}^{-1}$.	197
Figure 6.11: Visible appearance of crystals of CC4.3•3(BF ₄ ⁻).	198
Figure 6.12: Racemic route to chiral metallocryptophanes MM- $\Lambda\Lambda\Lambda$ and PP- $\Delta\Delta\Delta$.	199
Figure 6.13: The view down the centre of the cavitand for the two Cage Types in the unit cell.	200
Figure 6.14: Torsion angle of the pyridyl ligands in a [Ir(ppy) ₂ (py) ₂] complex,...	201
Figure 6.15: Packing diagram looking down the crystallographic a axis .	203
Figure 6.16: Complementary nature of the phenylpyridine and ligand cavity angles of CC4.3	205
Figure 6.17: HR ESI-MS of heteroleptic cage	207
Figure 6.18: HR ESI-MS of CC3.1 and CC4.3	208
Figure 6.19: Chemical structures of the structurally analogous ligands employed in palladium containing supramolecular assemblies	209
Figure 6.20: Stacked ^1H NMR spectra of CC4.3	211
Figure 6.21: Overlaid ^1H NMR spectra of CC4.3 after 6 months self-sorting, shown	212
Figure 6.22: Absorption and Emission profiles of CC3.1 in DCM solution, doped thin-film and powder form.	214
Figure 6.23: Absorption and Emission profiles of CC4.3 in DCM solution, doped thin-film and powder form.	215
Figure 6.24: Dark-room images of CC3.1 and CC4.3 in DCM solution after irradiation with 360 nm light.	216
Figure 6.25: Solid-state emission of CC3.1 and CC4.3 in doped thin-film (top) and powder form (bottom).	216
Figure 6.26: Structure of the ligand employed in unsuccessful M ₃ L ₂ attempts, L6 and the resultant M ₃ L ₂ assembly CC6.1.	218
Figure 6.27: HR ESI-MS of M ₃ L ₂ assembly CC6.1.	219
Figure 6.28: ^1H NMR spectra depicting a) metallocatena b) L6 and c) 10 minutes after combining the two components.	220

List of Tables:

Table 2.1: Selected bond lengths (Å) and angles (°) from the crystal structure of C1.1	66
Table 2.2: selected inter-atomic and topological distances of C1.1	66
Table 3.1: Emission maxima, quantum yield and lifetime analysis of C1.2-3 and C2.2-3	110
Table 3.2: Emission maxima, quantum yield and lifetime analysis of C1.2-3 and C2.2-3 in PMMA doped thin-films.	113
Table 4.1: Emission maxima, quantum yield and lifetime analysis of C1.4-5 and C2.4-5	139
Table 4.2: Emission maxima, quantum yield and lifetime analysis of C1.4-5 and C2.4-5 in PMMA doped thin-films.	142
Table 6.1: Schematic of triangular based pyramid and the distances used to calculate the cage volume, along with relevant inter-atomic bond distances from the SCXRD data of [CC4.3•3 (BF ₄)].	202

List of Schemes:

Scheme 1.1: Formation of both ether- and ester-linked CTG ligand families.	26
Scheme 1.2: Formation of palladium Pd ₃ L ₂ metallocryptophane assemblies from Shinkai and Schaly.	27
Scheme 2.1: Full synthetic route towards racemic <i>M</i> and <i>P</i> cyclotriguaiacylene.	48
Scheme 2.2: General synthetic route towards L1-L4	49
Scheme 2.3: General synthetic route towards C1.1 and C2.1	54
Scheme 2.4: Symmetric and un-symmetric stretches of C≡O ligands, with respect to their IR stretching bands.	58
Scheme 2.5: Formation of heteroleptic metallocryptophane CC1.1	70
Scheme 3.1: The general route to formation of [Ir(C [^] N) ₂ (N [^] N)] species.	90
Scheme 3.2: Formation of C1.2 and C2.2 , tri-metallic iridium species.	92
Scheme 3.3: Potential inter-conversion cycle for all cyclotriguaiacylene ligands.	96
Scheme 3.4: Formation routes to tri-metallic C1.2 and C2.2 and their mono-metallic congeners C1.3 and C2.3	98
Scheme 4.1: Two-step route of heterometallic iridium complexes C1.4 and C2.4	127
Scheme 4.2: Two-step, in situ formation of heterometallic iridium complexes C1.5 and C2.5	128
Scheme 5.1: General synthetic route towards tri-metallic C1.6 and C2.6	157
Scheme 5.2: Modular synthesis of heteronuclear C1.7 and C2.7 from mono-iridium precursors C1.3 and C2.3	166
Scheme 5.3: Synthesis of 'piano stool' acetonitrile ruthenium precursor.	172
Scheme 5.4: Formation of the second ruthenium 'piano-stool' complex.	175
Scheme 6.1: Formation of the iridium metallotecton employed throughout this chapter.	190
Scheme 6.2: Increasing complexity and/or steric bulk of 4-pyridyl ligands employed in metallocryptophane formation.	217

List of Equations:

Equation 1.1: Stokes-Einstein equation.	196
---	-----

List of Abbreviations:

Å	Angstrom
ASU	Asymmetric unit
bpy	2, 2'-bipyridine
CIE	Comission Internationale D'Eclairage
COSY	Correlation spectroscopy
Cp*	Pentamethyl-cyclopentadiene
CTC	Cylcotricatechylene
CTG	Cyclotriguaiacylene
CTV	Cyclotrimeratrylene
DCL	Dynamic Combinatorial Library
DCM	Dichloromethane
dfppy	Difluorophenylpyridine
DFT	Density Functional Theory
dmb	Dimethyl bipyridine
DMSO	Dimethyl sulphoxide
DOSY	Diffusion ordered spectroscopy
dppp	1,2-bis(diphenylphosphino)propane
En	Ethylenediamine
ET	Energy transfer
<i>et al.</i>	<i>Et Alia.</i> (and others)
<i>Fac</i>	<i>Facial</i> (Coordination mode)
HEE	High energy emission
HOMO	Highest occupied molecular orbital
HPLC	High pressure liquid chromatography
HR ESI-MS	High resolution electro-spray ionisation mass spectrometry
Hz	Hertz
IC	Internal conversion
IR	Infra red
ISC	Intersystem crossing
<i>J</i>	Coupling constant (NMR)
K	Kelvin

LEE	Low energy emission
LEEC	Light emitting electrochemical cell
LUMO	Lowest unoccupied molecular orbital
m/z	Mass to charge ratio
MHz	Megahertz
MLCT	Metal to ligand charge transfer
MOF	Metal-organic framework
MRI	Magnetic resonance imaging
NaH	Sodium hydride
NHC	N-Heterocyclic carbene
NMR	Nuclear magnetic resonance
NOESY	Nuclear Overhauser Effect spectroscopy
OLED	Organic light emitting diode
OTf	Trifluoro-methane sulphonate
PET	Positron emission tomography
PLQY	Photoluminescent quantum yield
PMMA	Poly(methyl methacrylate)
ppy	2-phenylpyridine
SCXRD	Single crystal x-ray diffraction
THF	Tetrahydrofuran
tpy	Terpyridine
TRES	Time resolved emission spectroscopy
UoL	University of Leeds
UV-Vis	Ultra-violet visible light absorption
Δ	Capital delta, helical chirality
δ	Small delta, chemical shift (NMR)
Λ	Capital lambda, helical chirality
λ_{em}	Small lambda, emission wavelength
λ_{ex}	Small lambda, excitation wavelength
λ_{max}	Small lambda, maximum emission wavelength
^1H	Proton NMR
$^{13}\text{C}\{^1\text{H}\}$	Proton de-coupled Carbon NMR

1 Chapter 1

Introduction

1.1 Overview

This thesis contains work that combines targeted, rational design of metallo-supramolecular complexes with a view towards a functional output, in this case, the emission of light. This chapter will introduce the fields of luminescent emission, the application of the resultant emissive complexes in a wider context, as well as the vast area of supramolecular chemistry and the subset of metallo-supramolecular assemblies, with a focus on the cyclotrimeratriene family of compounds. This research will be placed in the context of current literature, providing evidence for the relevance and significance to the aforementioned fields.

1.2 Luminescence

In the most fundamental terms, luminescence is the emission of light. The emission of light is usually induced through an external factor, such as absorption of a specific wavelength of light or the passing of an electric charge across the sample. These two processes are sometimes split into photoluminescence and electroluminescence, but both processes involve the excitation of an electron from the ground state into an excited state, and it is the subsequent relaxation of the excited state electron that is concomitant with the emission of a photon of light, in order to balance the energy of the system.

Photoluminescence requires the use of a photon source, either a lamp or laser, to generate photons of a complementary wavelength to the energy level separations in a particular molecule. A photon is a quantised unit, thus depending on the wavelength applied it delivers a known quanta of energy to the system, and therefore the excitation wavelength is determined by energy levels of each complex.

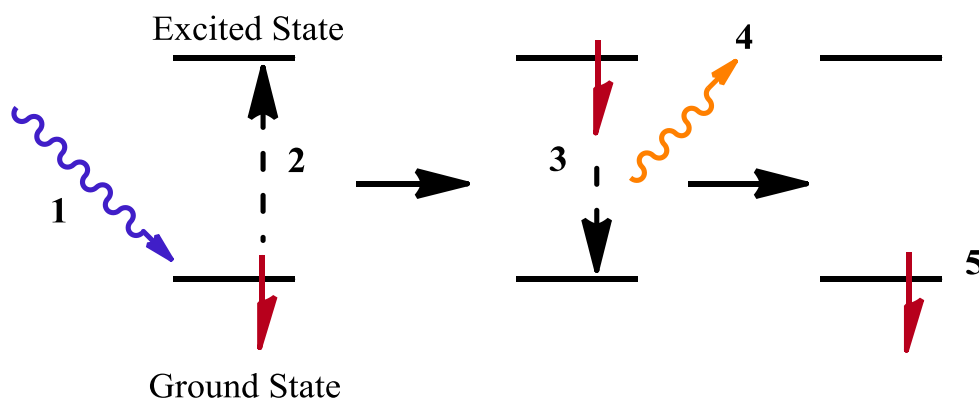


Figure 1.1: Simplified schematic to show the basic premise of photoluminescence.

As demonstrated in Figure 1.1, the absorption of a photon of light (1) induces the excitation of an electron in the ground state to its corresponding excited state (2). As that excited state electron relaxes back down to the lower energy ground state (3) the system must get rid of the excess energy through the emission of light (4), thus reforming the ground state (5). Due to vibrational relaxation, occurring in the excited state, and non-radiative decay pathways, the energy of the emitted light will always be lower than that which was absorbed, this phenomena is known as the Stokes Shift.

Electroluminescence is an analogous process, whereby an electric current is passed through the luminescent complex, leading the generation of ‘hole carriers’, electron poor regions, and ‘electron carriers’, electron rich regions.^{1,2} This is essentially a redox process, whereby simultaneous reduction and oxidation occur. When these two regions recombine, they re-form the ground state but also generate an exciton, which can be thought of as analogous to the excited state formed in photoluminescence. This exciton subsequently undergoes a similar relaxation process whereby it releases excess energy to return to the ground state through emission of light.

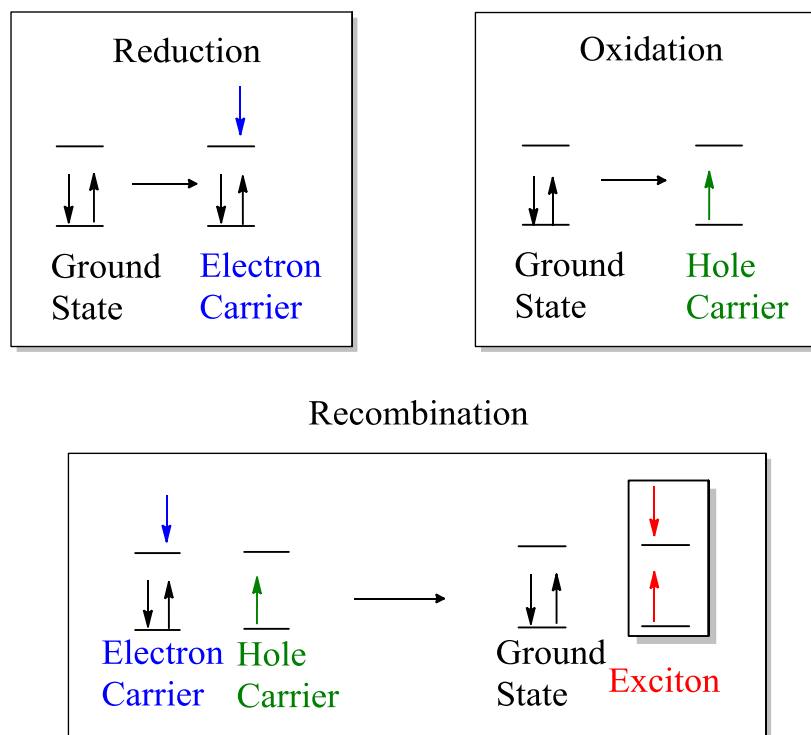


Figure 1.2: Simplified schematic to show the basic premise of electroluminescence.

The energy gap of the excited and ground state electrons in the exciton can be thought of as analogous to the HOMO (highest-occupied-molecular-orbital)-LUMO (lowest-unoccupied-molecular-orbital) gap of the molecule, therefore judicious ligand design incorporating electron withdrawing/donating groups can lead to high-fidelity control over the energy gap and thus the emission wavelength.

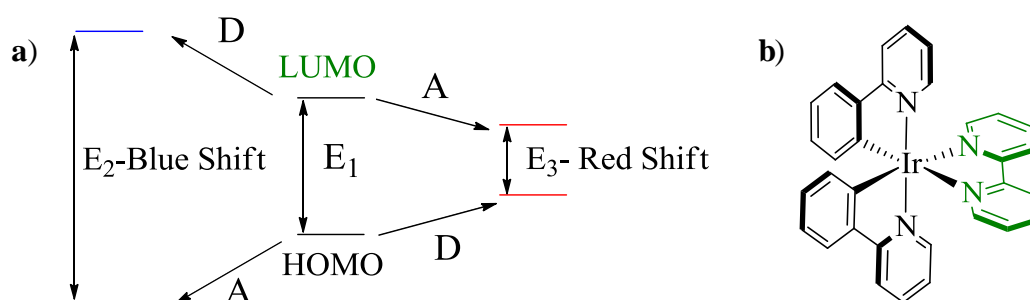


Figure 1.3: (a) Simplified schematic depicting the HOMO-LUMO energy gap, (b) colour-coded chemical structure of a model iridium complex.

Thus, if the locations of the HOMO and LUMO within the complex are known, or can be inferred from previous density functional theory (DFT) studies, then control over the emission wavelength is possible. The structure of the model iridium

complex $[\text{Ir}(\text{ppy})_2(\text{bpy})]$ is shown in Figure 1.3. Through extensive DFT studies and previous experimental evidence,³⁻⁹ the LUMO on this molecule is known to reside mainly on the bipyridine ligand, whilst the HOMO is mainly iridium with some phenylpyridine character. Therefore, by functionalising the phenylpyridine ligand with electron withdrawing groups, such as fluorine, the energy of the HOMO is lowered leading to a larger energy gap between the HOMO and LUMO, which in turn leads to a blue shift in emission. The converse is also true; if the bipyridine is functionalised with electron withdrawing groups, the energy of the LUMO is lowered and the emission red shifted.

1.2.1 Phosphorescence

Phosphorescence is a subset of luminescence, whereby the emission of light is delayed due to a series of energy level conversions occurring within the molecule before the final relaxation step.

As shown in Figure 1.4, a simplified Jablonski diagram, both fluorescence and phosphorescence are the emission of light due to an excited state electron relaxing to the ground state. However, fluorescence only involves the singlet energy levels; an electron is promoted to the excited singlet state (S_n) through absorption of a photon of light, this decays to the lowest excited singlet state (S_1) through internal conversion (vibrational relaxation) before decaying back to the electronic ground state through fluorescent emission of light. The wavelength of the emitted light will be longer, due to the inverse relationship between wavelength and energy, as some of the absorbed energy is lost during internal conversion. Fluorescent lifetimes are usually of the order of nanoseconds due to the spin-allowed nature of the transitions resulting in emission.^{10,11}

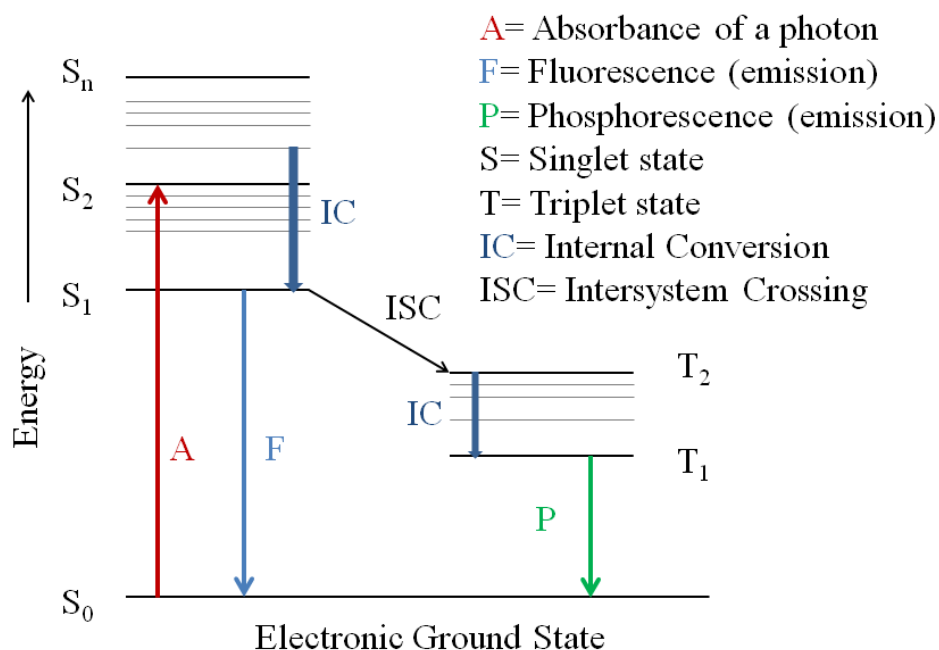


Figure 1.4: Simplified Jablonski diagram, showing both fluorescence and phosphorescence processes.

Phosphorescence, however, is a more convoluted process. An analogous absorption process occurs, promoting an electron to an excited singlet state which decays to the lowest excited singlet state through internal conversion. However, instead of undergoing fluorescence at that point, inter-system crossing can occur. ISC is formally spin-forbidden, as the spin selection rule states that transitions between states of a different multiplicity cannot occur. Nonetheless the presence of a heavy metal can often lead to strong spin-orbit coupling, as observed with late transition metal complexes discussed in this thesis. The coupling of spin and orbital angular momentum leads to mixing of the singlet and triplet states, therefore relaxing the spin-forbidden nature of the ISC transition. Once the electron has populated the excited triplet state it once again undergoes internal conversion to the lowest excited triplet state (T_1) before relaxing to the electronic ground state, however, as this transition ($S_0 \leftarrow T_1$) is also spin-forbidden, the lifetime of phosphorescent emission is often much longer than the corresponding fluorescent emission.¹²

The focus of this thesis will be the phosphorescent properties of the low-spin d^6 metals; Re(I), Ru(II) and Ir(III). These metals, when supported by polypyridyl ligand scaffolds, are known to possess strong phosphorescent emission that has found applications in a wide range of fields.¹³⁻²⁴

1.2.2 Applications

As mentioned in the overview of this chapter, the aim of this project is to design a system that possesses a specific function. This function, the emission of light, has many end-use applications that as such dictate the type and specificity of emission required.

Whilst there are numerous applications for phosphorescent metal-complexes, the main categories are bio-medical imaging,^{14,18,23,25-27} the formation of organic light emitting diodes (OLEDs)^{2,20,22,28-30} and light emitting electrochemical cells (LEECs)³¹⁻³⁶ and dye-sensitised solar cells (DSSCs).^{3,37}

1.2.2.1 Biomedical Imaging

Bio-medical imaging is a vast field in itself, encompassing positron emission tomography (PET), magnetic resonance imaging (MRI) and fluorescence microscopy, to name but a few. The most relevant to this body of work is clearly fluorescence microscopy, whereby cells and/or tissue samples are injected with a solution containing a luminescent emitter. This imaging agent is taken up by the cells and will localise in specific areas preferentially, after excitation by a precise wavelength the imaging agent will emit light, giving a visual representation of the cell itself. The localisation of the imaging agent can be controlled through targeted design of the chromophore, to give information about a particular area of interest.^{23,27,38}

Rhenium(I) systems containing polypyridyl ligand supports have been widely explored in this setting.^{25,39-42} The synthesis of systems of the form $[\text{Re}(\text{CO})_3(\text{N}^{\wedge}\text{N})]\text{X}$, where $\text{N}^{\wedge}\text{N}$ is any bis-imine bidentate ligand, and X^- is any anion, from the rhenium pentacarbonyl halogen precursor is relatively facile. The latent bound anion can subsequently be exchanged for a functionalised pyridyl unit; this pyridyl is generally considered the driving force towards specific cell localisation.²⁷ Judicious functionalisation of this unit can lead to targeted uptake; such as that exhibited by Lo *et al* whereby they appended a fructose moiety to target the mitochondria,⁴⁰ or Coogan *et al* whereby they mimicked a thiol receptor to target cysteine residues also present in the mitochondria.³⁸

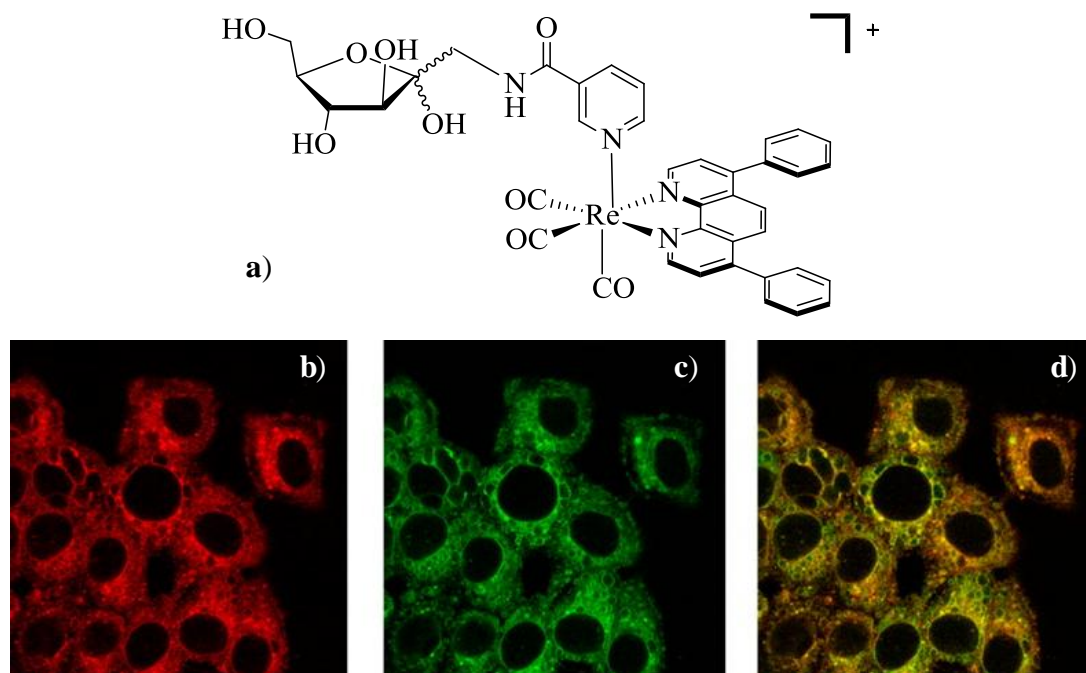


Figure 1.5: Chemical structure (a) and confocal microscopy images of a fructose appended imaging agent, (b) MCF-7 breast cancer cells incubated with the agent shown in a, (c) a known mitochondrial imaging agent, (d) overlay of both imaging agents depicting co-localisation of the two imaging agents. {Reprinted with permission from *Organometallics*, 2013, 32 (18), pp 5098–5102. Copyright 2013 American Chemical Society⁴⁰}.

There are also instances of iridium(III) polypyridyl complexes of the form $[\text{Ir}(\text{N}^{\wedge}\text{N})(\text{C}^{\wedge}\text{N})_2]$ being employed in con-focal cell imaging,^{18,43} with the Lo group once again providing many examples.^{14,18}

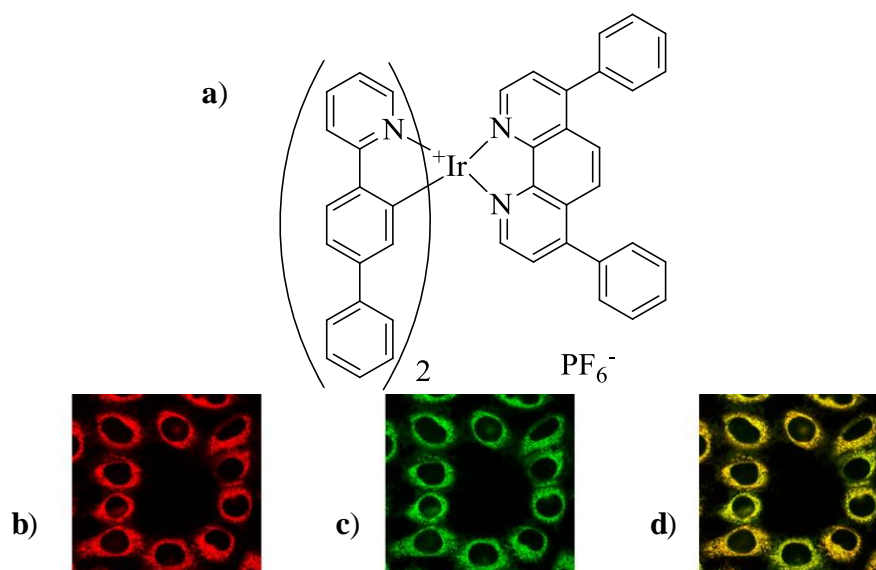


Figure 1.6: Chemical structure (a) of Iridium(III) imaging agent, (b) HeLa cells incubated with the imaging agent shown in a, (c) a known mitochondrial imaging agent, (d) overlay of both imaging agents depicting co-localisation of the two imaging agents {Reprinted with permission from *Inorg. Chem.*, 2015, 54 (13), pp 6582–6593. Copyright 2013 American Chemical Society.¹⁴}.

One of the advantages of employing the aforementioned low-spin d^6 metal complexes as luminescent cell imaging agents, other than their relatively large Stokes Shifts, is the generally longer lifetimes seen when compared to organic fluorophores.^{12,14,23,25,44,45} This phenomenon means that time-gated collections can be performed, whereby any short-lived emission from endogenous fluorophores present in cells can be allowed to decay before the collection is begun. This leads to a more accurate representation of the localisation of the imaging agent.

Whilst the application in biomedical imaging employing the complexes discussed in this thesis has not been explored, there is no reason why it could not be in the future. The tri-metallic nature of the emissive complexes synthesised herein, particularly the heteroleptic and heteronuclear systems, could lead to ratiometric probes, self-calibrating the concentration of a particular target molecule or the imaging agent itself.

1.2.2.2 OLEDs and LEECs

Rather than exploiting the photoluminescence of these types of metal complexes, the electrochemical luminescence can also be harnessed.

Organic light emitting diode devices have been around for many years; however the incorporation of transition metal complexes as the emissive layer is a more recent development.

Tang and VanSlyke developed one of the first OLED devices in 1987 containing a *tris*-chelated aluminium centre,⁴⁶ whilst Burroughes developed the first OLED containing polymeric poly(*p*-phenylene vinylene) in 1990.⁴⁷ It took 8 years before the incorporation of an emissive transition metal component, namely a platinum porphine,⁴⁸ leading to a new series of OLEDs containing phosphorescent metal complexes as the emissive layer.⁴⁹

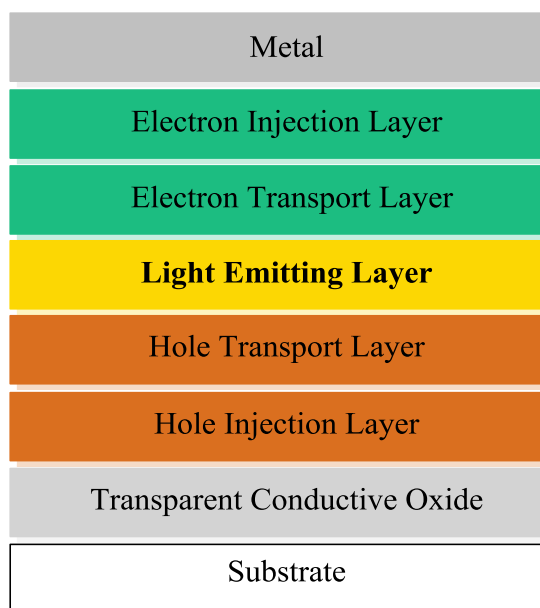


Figure 1.7: General schematic depicting the multitude of layers required for OLED fabrication. Adapted from reference ⁵⁰.

Despite the array of transition metal complexes that could potentially be incorporated into the OLED design, the fabrication of such devices is nowhere near facile. Many of the sublimation/deposition processes for the individual layers need to be performed under a rigorously controlled inert atmosphere or indeed a high-vacuum environment. The difficulty in fabrication leads to high cost, which in turn limits the real-world applications.

Light emitting electrochemical cells, on the other hand, have a much simpler construction, as shown in Figure 1.8.

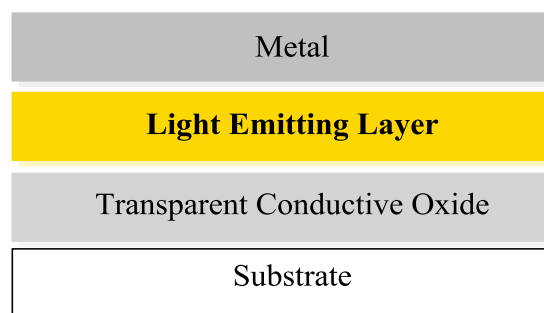


Figure 1.8: General schematic depicting the set-up of LEEC formation. Adapted from reference ³⁵.

The emissive layer in LEECs is generally a positively charged transition metal complex, such that when an electric charge is applied, the counter-ions and metal centre are separated towards the appropriate cathode/anode. This design gives rise to easily accessible hole/electron carriers without the need for external transport/injection layers.

LEECs were first reported by Pei *et al.* in 1995, whereby a highly conjugated fluorescent polymer was used as the emissive layer.⁵¹ Ionic transition metal complex containing LEECS, commonly referred to as iTMC-LEECs, were then subsequently reported by Lee *et al.* in 1996, when a ruthenium polypyridyl complex was employed.⁵² The ruthenium *tris*-chelate complex, containing three sulfonate-appended phenanthroline ligands, was spun into a thin film before incorporation into the device. This marked the first example of combining the well-established field of transition metal luminescence into electroluminescent devices. Since that seminal example, many groups have reported LEECs formed from both ruthenium⁵³ and iridium⁵⁴ *tris*-chelate complexes, with a recent review highlighting almost 40 iridium complexes that have been included in light-emitting electrochemical cells.⁵⁵ The sheer volume and variety of ionic iridium complexes employed in the formation of LEECs means that emission over a wide array of the colour spectrum can be achieved. For example, blue light emission can be achieved through employing bis-imidazole type ligands as the N^N component,⁵⁶ yellow emission employing difluorophenylpyridine and a spirobifluorene ligand system⁵⁷ and red emission employing a *tert*-butyl appended phenylpyrazole and a biquinoline ligand combination.⁵⁸

1.3 Supramolecular Chemistry

Supramolecular chemistry is a vast field, with a wide range of potentially contentious definitions. The most commonly applied definition is that coined by the pioneer of the field, Jean-Marie Lehn when he described it as ‘chemistry beyond the molecule’.⁵⁹ Although, the precise definition of a ‘molecule’ itself has recently been the subject of much contention, with the distinction between molecule, complex and supra-molecule being hotly debated, particularly with respect to mechanically interlocked species such as [*n*]-catenanes and rotaxanes.

The generally accepted designation is an assembly held together through non-covalent interactions; that is not covalently bound through the sharing of electrons. These non-covalent interactions can be categorised into sub-sections; electrostatic, Van Der Waals, π -effects, hydrogen bonds and the hydrophobic effect. These interactions lead to synergistic and complementary assembly and disassembly processes, whereby a complex mixture of sub-components can re-arrange into the most favourable thermodynamic product over time.^{59–62} This phenomenon is sometimes termed self-organisation or molecular recognition and can lead to the formation of enantiomerically pure structures from racemic precursors or the formation of two distinct assemblies through a parallel self-sorting process.⁶³ The assembly-disassembly process can be exploited through the formation of dynamic combinatorial libraries (DCLs), whereby hundreds of potential assemblies form in solution rapidly, under kinetic control, and over time the stability of the resultant architectures governs the preferred thermodynamic product. This approach, relying on the energy levels of the dynamic system, can allow access to highly complex assemblies that could otherwise be unobtainable.

1.3.1 Metallo-supramolecular Chemistry

Metallo-supramolecular chemistry is a sub-set of supramolecular chemistry that exclusively deals with the formation of metal-containing assemblies. Over the years, there have been numerous examples of strikingly complex supramolecular assemblies formed through use of metal centres and carefully designed ligand systems.^{64–78} One of the main aspects of these metallo-systems is the idea of self-repair; whereby the covalent bonds between metal and ligand-donor group are

sufficiently labile to facilitate self-correction, the breaking and reforming of bonds towards a favoured product.

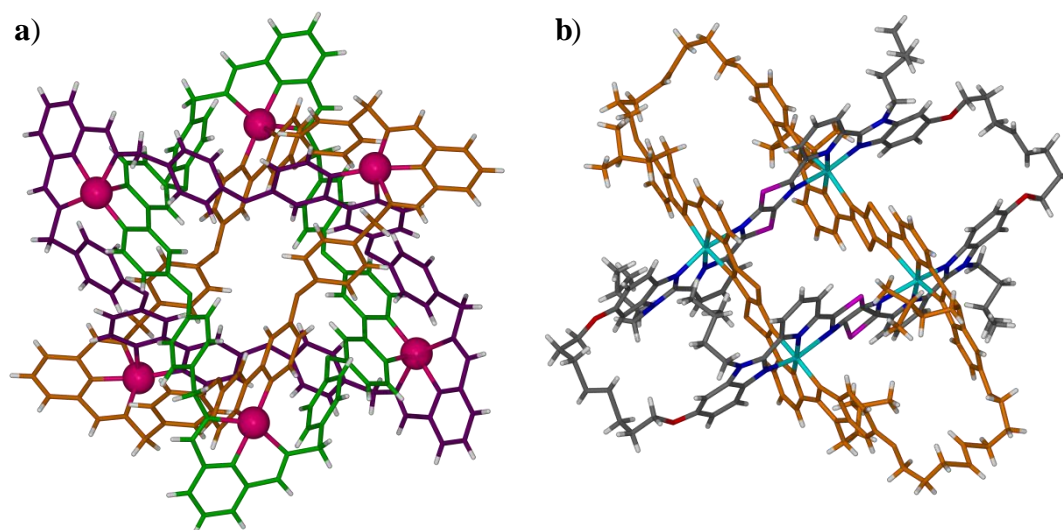


Figure 1.9: (a) Stoddart's Molecular Borromean rings,⁷² each mechanically interlocked ligand shown in a different colour, and (b) Leigh's Solomon Link,⁶⁸ one ligand shown in orange to highlight the interlocked nature of the assembly.

Examples of assemblies that can be accessed through self-assembly, but were previously difficult to access through classical step-wise organic synthesis are topologically complex architectures. Topological complexity is just one of the ways further complexity can be imbued to the resulting assemblies, whereby complex knots and mechanically interlocked molecules are formed, sometimes with a degree of templating. For example, both topologically complex assemblies, shown in Figure 1.9, are formed through the self-assembly of zinc(II) cations and nitrogen donor ligand scaffolds. Stoddart's Borromean rings form through the concomitant formation of 12 imine bonds along with metal binding events, whilst Leigh's Solomon link starts by forming a metal-bound interwoven grid array, then undergoes alkene metathesis to ring close the ligands, leading to a mechanically interlocked arrangement.

Examples of the type of topological complexity that can be imparted through metal-directed self-assembly are shown in Figure 1.10.

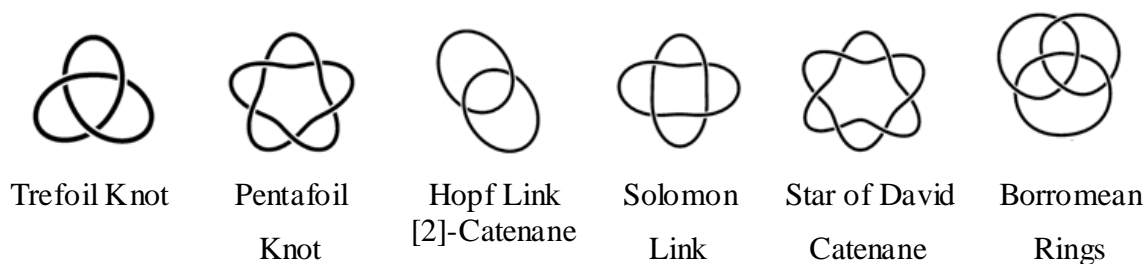


Figure 1.10: Examples of topologically complex interlocked molecules with the topological name underneath.{Reprinted with permission of Chem. Rev., 2011, 111 (9), pp 5434–5464. Copyright 2011, American Chemical Society}

There have been numerous examples of topologically complex assemblies since the initial pioneering report by Sauvage of an interlocked catenane motif⁷⁹ and the subsequent molecular trefoil knot; the general structure of both knots are shown in Figure 1.10.⁸⁰ The Hopf Link, or Catenane, is the simplest of the topologically complex knots, whereby two rings are interlocked mechanically, with no chemical bonds holding the assembly together.

Other examples include Borromean rings;^{72,77,81–83} where three distinct rings are interwoven, but no two rings are catenated. Solomon links,^{68,75,84} where two cyclic ligands are interwoven such that there are four crossing points, and the analogous cubes⁸⁵ have also been synthesised by the groups of Leigh, Severin and Trabolsi. Further examples of catenanes^{74,84,86–97} and trefoil knots^{84,98} have also been formed. Many of these syntheses rely on either dynamic imine formation, to allow for self-correction, or templation effects to pre-arrange the individual components. Sauvage employed the well-defined tetrahedral geometry of a Cu(I) salt to direct the formation of the first [2]-catenane, exploiting the orthogonal nature of two chelating phenanthroline ligands, from which the interlocked arrangement could be ‘closed’. Whilst Stoddart has employed metal-directed templation effects, such as the chelation of metal ions,⁷² his group have also formed highly complex organic interlocked systems that exploit π - π stacking and electrostatic interactions of charged pyridinium units.^{88,99–101}

Apart from the aesthetic appeal of these complex, interwoven assemblies, they provide possible routes to molecular devices that could potentially mimic processes that occur in nature, such as cargo transport.^{60,102–104}

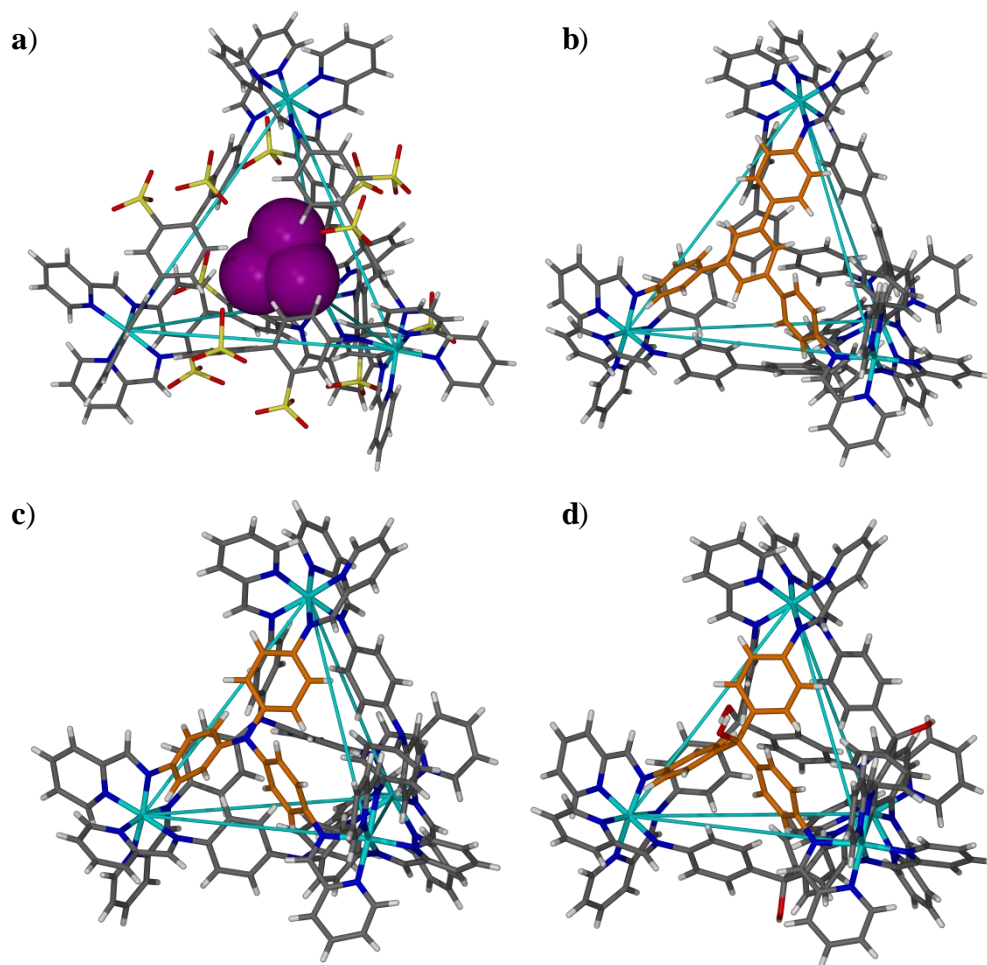


Figure 1.11: A series of Fe(II) tetrahedra from the Nitschke group, including (a) an Fe_4L_6 cage¹⁰⁵ that stabilises P_4 and (b-d) Fe_4L_4 face-capped tetrahedra that can encapsulate various guest molecules, with one ligand highlighted in orange.^{65,106}

The reversible nature of dynamic imine bond formation has been utilised extensively by the Nitschke group. By employing the *in situ* imine bond formation in conjunction with various iron salts, a whole library of tetrahedral cages have been formed, some of which are shown in Figure 1.11. Both linear linkers, Figure 1.11 (a), and trigonal face-capping ligands, Figure 1.11 (b-d), have been utilised to form Fe_4L_6 and Fe_4L_4 assemblies.^{65,105–108} Through modulation of the ligand component, the size of the internal cavity of the cage can be controlled, thus leading to selective uptake of specific guests dependant on their size or shape.^{106,107,109,110} This approach leans towards “molecular container” design, whereby a guest, potentially a volatile or hazardous compound, can be contained within a cage structure.^{111–113} To build upon this, cages could be designed such that a specific reaction could occur within

through restriction of the size or shape of an intermediate, such as those designed by Fujita *et al.*,¹¹⁴ or even control the chirality of the product.¹¹⁵

Of the discussed metallo-supramolecular assemblies, many are formed from labile transition metal salts, generally with non-coordinating anions. The lack of geometrically directing ligands pre-bound to the metal centre means that a greater variety of resultant structures are possible. A particularly common motif is square planar palladium(II) salts with N-donor ligands, leading to a host of open framework structures, cages and larger assemblies.^{85,90,116-127} By employing ambi-dentate N-donor ligands with defined binding angles, the formation of predictable libraries of assemblies are possible. This iso-structural arrangement can be achieved through elongating the linker-ligand through use of a spacer group, or to favour a particular assembly through use of more sterically bulky ligand scaffolds.^{124,128}

However, in recent times there has been a concerted effort to move towards directed assembly; targeting specific structures by employing either rigid linker ligands or geometrically directing metallo-tectons, or in fact a combination of both. The use of metallo-tectons leads to more predictable outcomes with respect to self-assembly, and the ability to target a specific desired 3D structure.

Two of the most common tectons towards geometrically targeted structures are the palladium ethylenediamine $[\text{Pd}(\text{en})]^{2+}$,^{94,116,129} and palladium *bis*-diphenylphosphinopropane units,^{93,130} as shown in Figure 1.12. These *cis*-protected metallo-tectons provide strong geometric direction; with two of the *cis*-sites on the square-planar metal blocked by the chelating ligand, the only accessible binding sites that remain are the opposite *cis*-sites. This approach leads to metallo-assemblies of a predictable geometry, simply through consideration of the angles in the linker-ligand and the angles of the available binding sites on the metal.

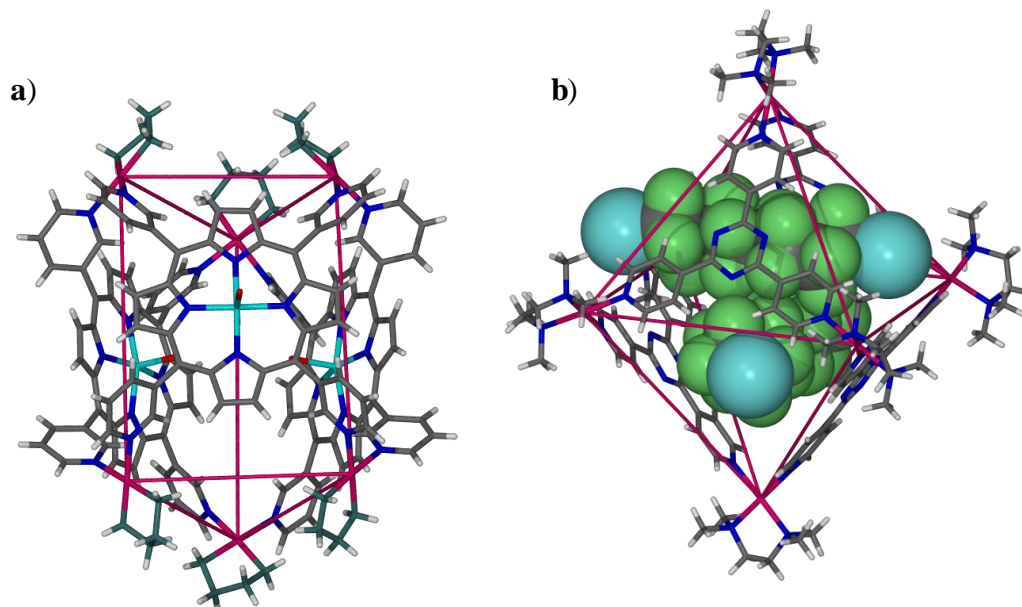


Figure 1.12: SCXRD structures of (a) a porphyrin-panelled trigonal prism¹³¹ and (b) Pd₆L₄ octahedron¹³² from the Fujita group, both directed by the Pd(en) tecton. Counter-ions removed for clarity.

As evidenced in Figure 1.12, *cis*-protected palladium tectons can result in diverse 3D structures dependant on the shape, binding angle and number of binding sites available at the ligand. The assembly in Figure 1.12 (a) describes a triangular prism, with three porphyrin ‘panels’ describing the rectangular faces of the prism, and the Pd(II) centres describing the vertices.¹³¹ Whilst Figure 1.12 (b) displays an octahedral assembly where half of the faces are capped by the tripodal tri-pyridyltriazine ligand and the six vertices are described by the Pd(II) centres.¹³²

The ability to design 3D structures through use of metallo-tectons is by no means restricted to square planar Pd(II); there are numerous examples of octahedral metals where one tripodal face has been capped to leave three orthogonal binding sites. As this thesis is concerned exclusively with low-spin d^6 metal centres, a sub-set of directed assemblies that are highly pertinent are the metalla-rectangles and metalla-cages formed through combination of face-capped ‘piano-stool’ Ir(III), Rh(III) and Ru(II) metallotectons.

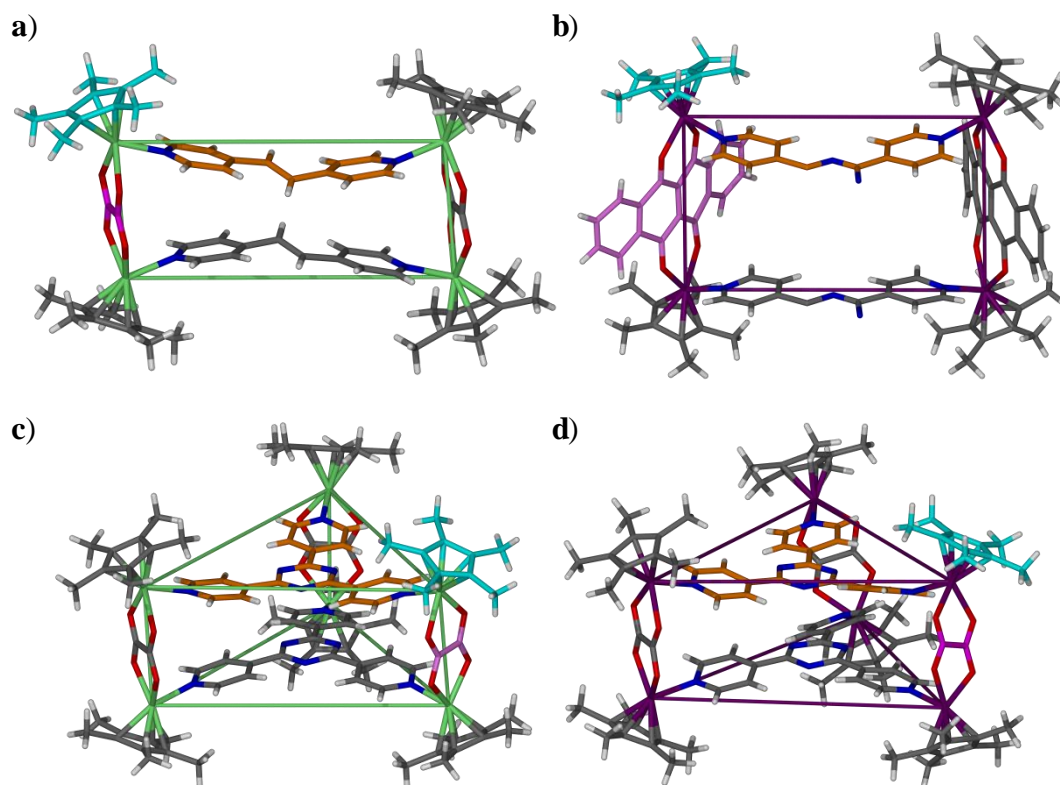


Figure 1.13: *Cp**-capped metalla-assemblies, (a) *Ir metalla-rectangle*¹³³ (b) *Rh metalla-rectangle*¹³⁴ (c) *Ir metalla-cage*¹³⁵ (d) *Rh metalla-cage*.¹³⁵ *Ir atoms are shown in green, Rh atoms in purple, one linking or face-capping ligand is highlighted in orange, one bidentate bridging ligand is highlighted in pink and a Cp* ligand is highlighted in cyan. Solvent and counterions removed for clarity.*

The types of assemblies as shown in Figure 1.13, are generally formed in a two-step procedure whereby two of the geometrically restricted metallotectons are bridged by a bidentate *O,O*-donor ligand; this “metallo-clip” provides two almost parallel binding sites onto which planar linking ligands can be bound. Directly analogous to the aforementioned *Cp**-M(III) systems, assemblies containing the ruthenium *p*-cymene metallotecton can also be formed.^{70,136–140} Metalla-assemblies of this type are not just visually attractive; they also possess promising anti-cancer activities, particularly examples from Therrien.^{137–139} The highly charged assemblies, one of which is displayed in Figure 1.14, (b), show good cell uptake and promising cytotoxicity towards cancerous cell lines. Another example from Dyson *et al*, formed from the tri-pyridyl triazine planar ligand, has been shown to encapsulate both Cisplatin and other platinum compounds, increasing their cytotoxicity towards ovarian cancer cell lines.¹³⁷

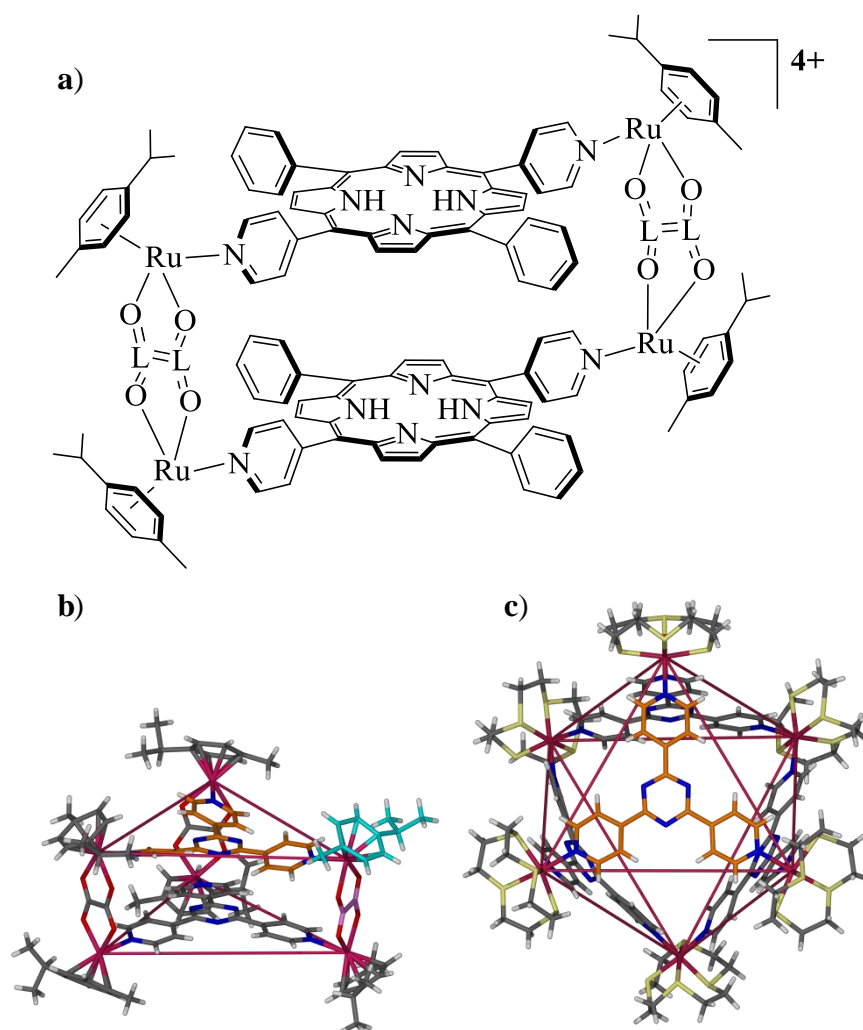


Figure 1.14: Ruthenium cage assemblies (a) Chemical structure of Therrien's pyridyl-porphyrin metalla-cage¹³⁸, where L is a linking bridging oxalato ligand (b) ruthenium p-cymene capped metalla-cage¹³⁶ (c) ruthenium thia-crown capped Ru₆L₄ metalla-capsule.¹⁴¹ Ru atoms shown in fuchsia, one p-cymene highlighted in cyan, face-capping ligands shown in orange. Solvent and counter ions removed for clarity.

Also shown in Figure 1.14, (c), is the ruthenium congener of Fujita's Pd₆L₄ octahedral assembly, directed through the use of tetra-thiacyclododecane. The Ru₆L₄ capsule was shown to be a host for an adamantane-based guest, displaying a visual chromic shift upon inclusion of the guest.¹⁴¹

Conversely there are much fewer Re(I), Ru(II) and Ir(III) supramolecular assemblies containing the emissive polypyridyl motif employed throughout this thesis, the general structure of that motif is shown in Figure 1.15.

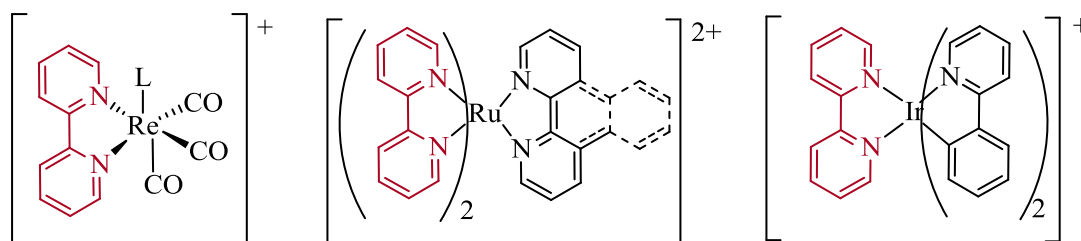


Figure 1.15: Chemical structure of the emissive polypyridyl motif in combination with Re(I), Ru(II) and Ir(III) d^6 metal centres.

The above motif can be expanded upon through functionalisation at numerous positions, or even expansion to other N^N-donor groups such as pyridylpyrazoles or C^N groups such as N-heterocyclic carbenes.^{6,142–145} One method of exploiting the emissive polypyridyl motif in a supramolecular setting is to incorporate it into a metal organic framework (MOF).

MOFs are a significant sub-set of metallosupramolecular chemistry; they consist of rigid linker ligands and metal centres or clusters bound together into 1, 2 or 3 dimensional assemblies. There are examples of iridium-containing MOFs that exploit the catalytic activity of bipyridine-bound iridium centres from the group of Wenbin Lin, whilst these systems do not contain the phenylpyridine ancillary ligands, they do exploit iridium centres in catalysis.^{146,147} The Lin group have also synthesised a phosphorescent MOF employing *tris*-cyclometallated iridium that is capable of sensing molecular oxygen through emission quenching,¹⁴⁸ as well as incorporating emissive iridium coordination polymers into nano-particles for use in biomedical imaging.¹⁴⁹

There are examples of MOFs incorporating other emissive centres into their design; such as the [Ru(bpy)₃]-Zn cluster MOF and [Ir(ppy)₂(bpy)]-Zn cluster MOF shown in Figure 1.16.^{149,150}

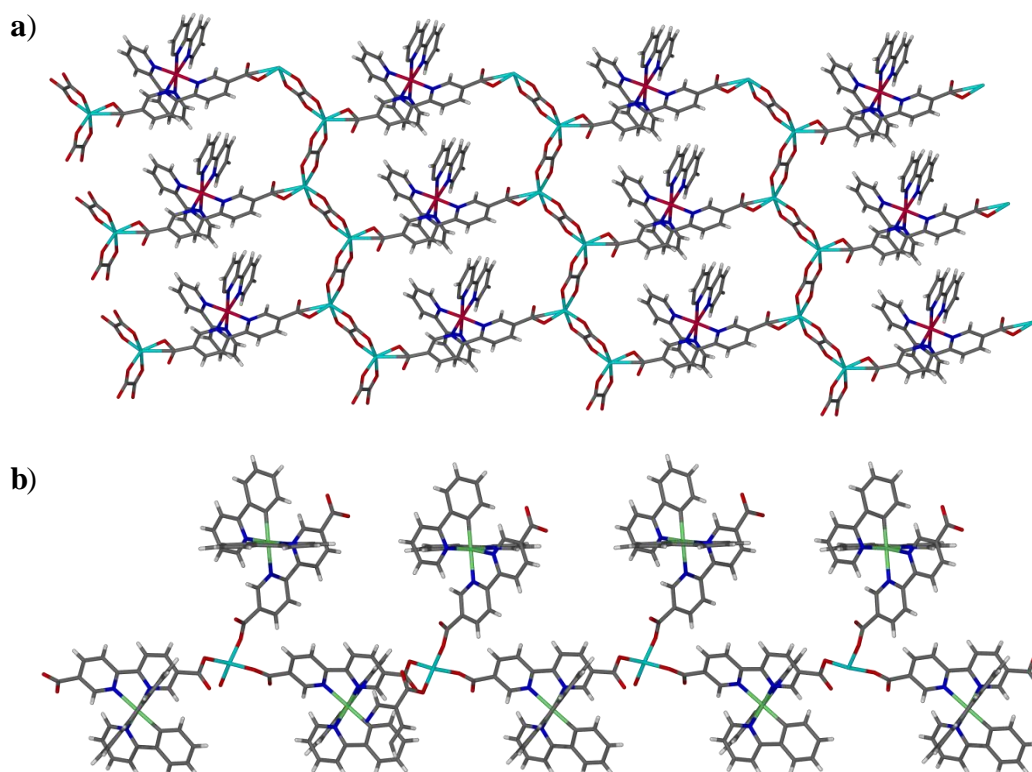


Figure 1.16: Emissive MOFs incorporating (a) Ruthenium centres¹⁴⁹ and (b) Iridium centres.¹⁵⁰

Most often, these emissive MOFs incorporate a bidentate N[^]N ligand already bearing carboxylate groups, through which the zinc atoms or clusters can bind. The design of these systems allows for well-established MOF chemistry to be employed whilst also retaining the desired emission properties of the employed metallotectons. Retention of the photophysical emission leads to potential applications as solid-state sensors for small molecules and guests.

Discrete examples of supramolecular systems employing emissive polypyridyl metallotectons are rarer still, with relevant examples shown in Figure 1.17.

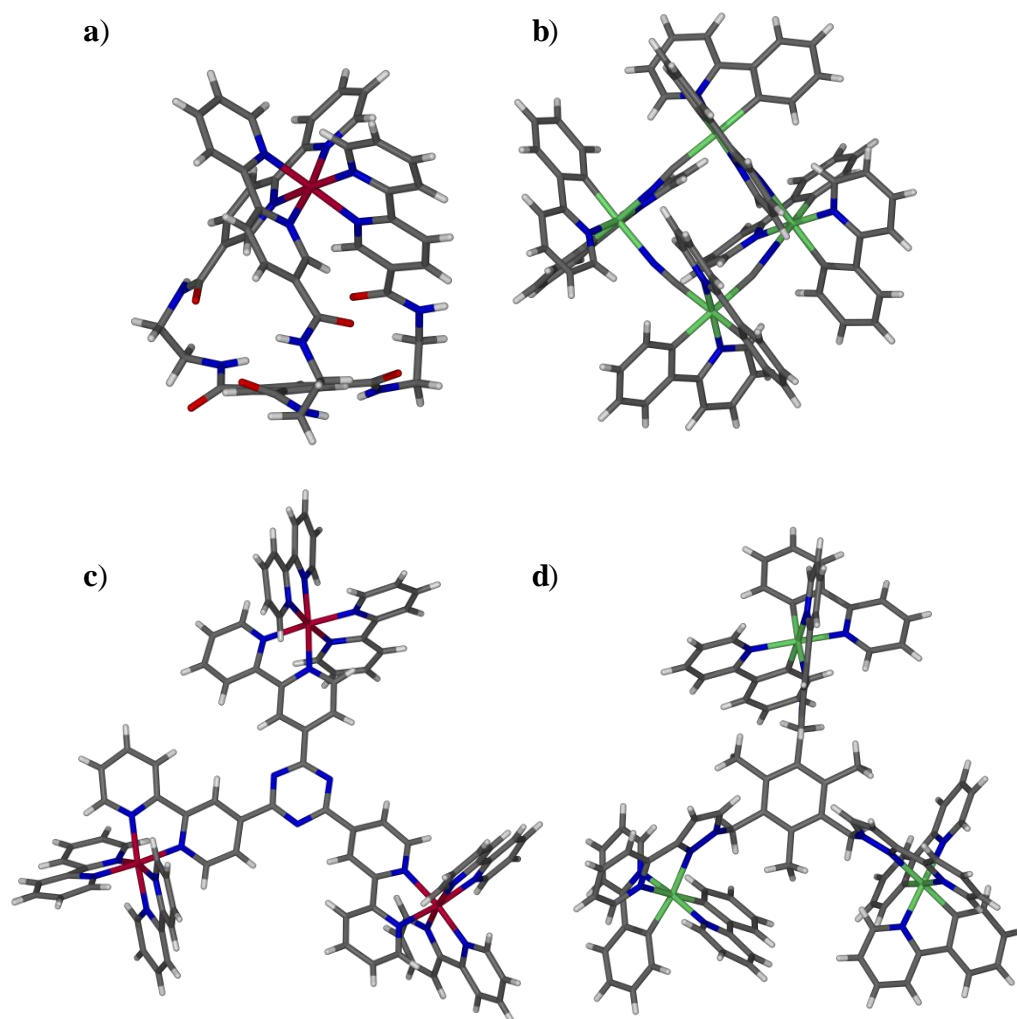


Figure 1.17: (a) Ruthenium cryptate¹⁵¹ (b) $\text{Ir}_4(\text{CN})_4$ tetramer,¹⁵² where $\text{Ir}=[\text{Ir}(\text{ppy})_2]$ (c) Ru_3L tri-nuclear assembly¹⁵³ where $\text{Ru}=[\text{Ru}(\text{bpy})_2]$, $\text{L}=\text{tri}(\text{bipyridyl})\text{triazine}$ (d) Ir_3L where $\text{Ir}=[\text{Ir}(\text{ppy})_2]$ $\text{L}=\text{tri}[3-(2\text{-pyridyl})\text{pyrazolylmethyl}]\text{-trimethylbenzene}$.¹⁵⁴ All solvent and counter-ions removed for clarity.

Figure 1.17 highlights a discrete ruthenium cryptate from the Fletcher group in (a), where one ligand provides all three *tris*-chelating sites for a single ruthenium centre.¹⁵¹ Baranoff *et al*, also report an iridium tetramer, Figure 1.17 (b), employing bridging ambidentate cyano/nitrile ligands in combination with an $[\text{Ir}(\text{ppy})_2]$ metallotecton.¹⁵² Both of these examples exhibit bright luminescent emission. The ruthenium cryptate selectively binds nitrate anions and subsequently displays a concomitant decrease in luminescence emission intensity, whilst the iridium tetramer exhibits bright green emission with a noteworthy photoluminescent quantum yield.

The two tri-nuclear examples (c and d) depicted in Figure 1.17, are the most closely related complexes to the work presented in Chapters 3, 4 and 5 of this thesis. The synthesis of the tri-nuclear ruthenium species, containing the tris-4-(2,2'-bipyridine)-1,3,5-triazine ligand, was extended to both the di- and mono-nuclear ruthenium complexes as well.¹⁵³ All of the ruthenium complexes based upon this ligand were reported to show phosphorescent emission around the 700 nm region. Whilst the tri-nuclear iridium system, based upon the tri[3-(2-pyridyl)pyrazolylmethyl]-trimethylbenzene ligand scaffold, exhibits yellow luminescent emission around 500 nm.¹⁵⁴ However, direct comparisons cannot be drawn between the complexes discussed in Chapters 3 and 4 and the example above due to the pyridylpyrazole binding motif, as opposed to bipyridyl, displayed in Figure 1.17.

Another subtly distinct group of assemblies are the macro-cyclic supramolecular assemblies involving emissive d^6 metals. Macro-cyclic assemblies have been reported by the groups of Thomas,^{155–157} Hupp¹⁵⁸ and Lees;¹⁵⁹ of most relevance are the heteronuclear assemblies whereby one or more emissive metal centre is incorporated into the assembly in combination with either another emissive centre or a non-emissive transition metal acting as a geometric director.

Metallomacrocycles can retain the luminescent emission of the fluorophore, although only the Re_4Os_4 example from Lees was emissive in acetonitrile solution. Through combination of a tri-dentate terpyridyl ligand also appended with a 4-pyridyl binding site, Lees formed a series of $[(\text{Re})_4(\text{M})_4]$ metalla-squares, where the second metal was either iron, ruthenium or osmium. The $[\text{M}(\text{tpy})_2]^{2+}$ fragment was pre-formed and employed as a linear linker, however upon formation neither the iron or ruthenium assemblies displayed any identifiable emission.

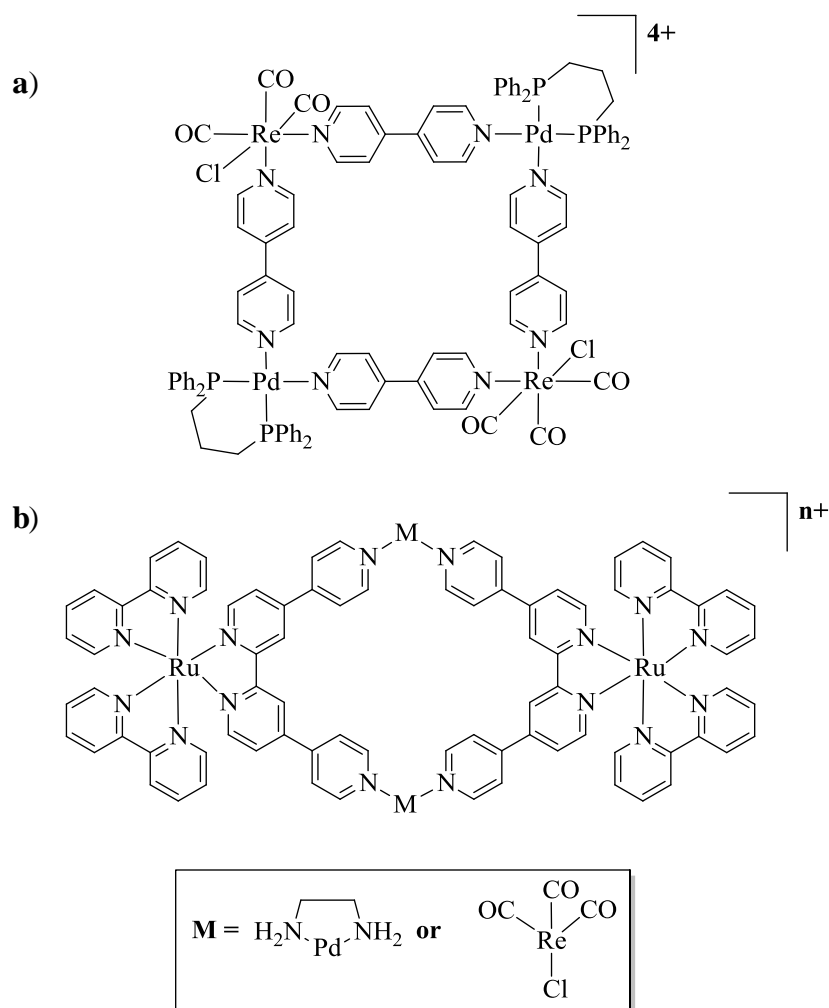


Figure 1.18: (a) Chemical structure of emissive Re_2Pd_2 metalla-square,¹⁵⁸ where $\text{Re}=[\text{Re}(\text{CO})_3\text{Cl}]$ and $\text{Pd}=[\text{Pd}(\text{dppp})]^{2+}$ (b) Ru_2M_2 metallomacrocycle,¹⁵⁵ where $\text{Ru}=[\text{Ru}(\text{bpy})_2]^{2+}$ and $\text{M}=[\text{Pd}(\text{en})]^{2+}$ or $[\text{Re}(\text{CO})_3\text{Cl}]$.

Hupp's Re_2Pd_2 square, Figure 1.18 (a), was found to retain the strong rhenium-based emission at around 625 nm, regardless of incorporation into the supramolecular assembly.¹⁵⁸ The folded metallomacrocycles of Thomas *et al*, have been investigated thoroughly with regards to not only the intrinsic emission properties,¹⁵⁵ but also as a host-guest sensor^{155,156} and in biologically relevant settings.¹⁵⁷ The rhenium congener retains the 70° angle imparted by the bipyridine bite-angle, leading to a 'folded-in' macrocyclic arrangement. Both the palladium and rhenium containing congeners gave remarkably similar phosphorescent emission profiles, 665 nm for the Re(I) and 670 nm for the Pd(II) analogue, supporting the conclusion that the majority of the observed emission is due to transitions associated with the ruthenium centre.

1.4 Cyclotrivenatrylene

The cyclotrivenatrylene (CTV) family of ligands, namely cyclotricatechylene (CTC), cyclotrivenatrylene (CTV) and cyclotriguaiacylene (CTG), represent a class of cavitands that possess a well-defined, hydrophobic cavity when in their “crown” form.

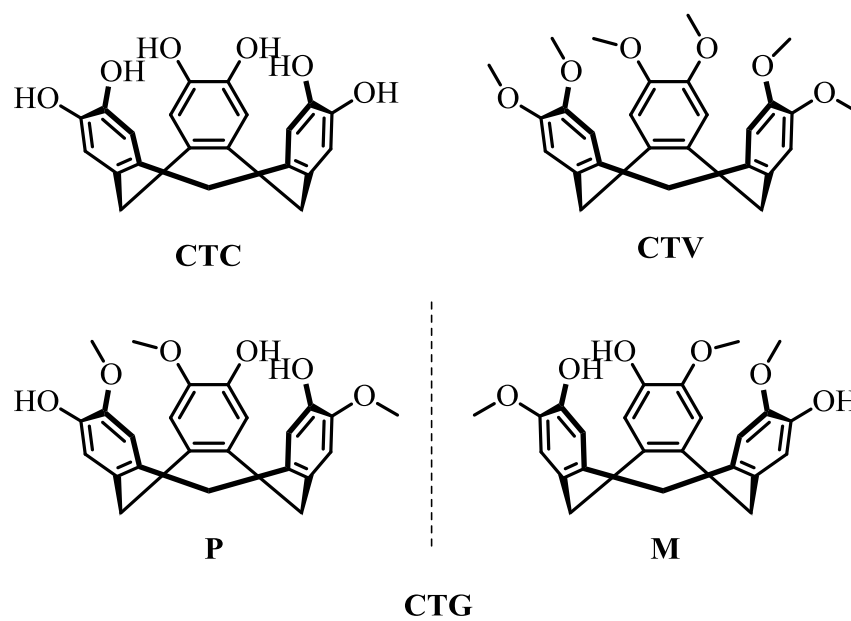


Figure 1.19: Chemical structure of the tri-benzo cyclononatriene family of ligands, including the chiral cyclotriguaiacylene molecule.

Due to the hexa-methoxy arrangement around the upper-rim, CTV itself is mainly restricted to use as a host for large, globular guests such as fullerenes and carboranes. These host-guest assemblies generally form through a ‘ball-and-socket’ type interaction of a spherical guest with the bowl-shaped cavity.^{160,161}

CTC has been employed as a ligand scaffold for both tri-nuclear M_3L systems^{162,163} and in supramolecular self-assembly towards the formation of larger architectures, both metallo-¹⁶⁴ and organic,¹⁶⁵ as well as forming clathrate inclusion complexes in the solid state.¹⁶⁶

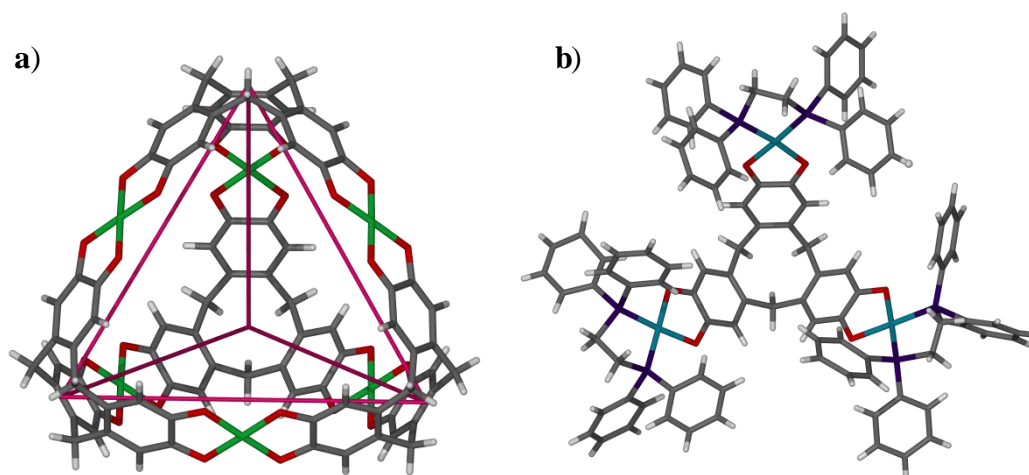
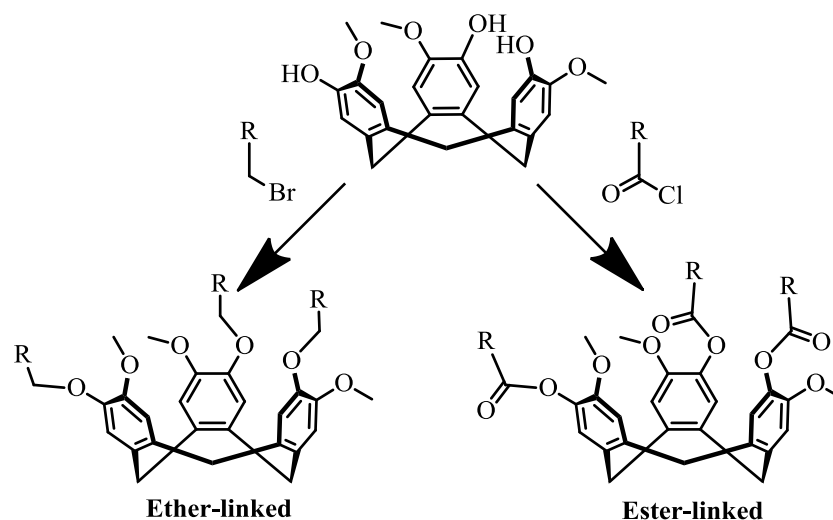


Figure 1.20: (a) Cu_4L_4 CTC tetrahedron,¹⁶⁴ face-capping sodium clusters removed for clarity (b) Pt_3L redox-active tri-nuclear CTC complex,¹⁶³ where $Pt=[Pt(dppe)]$.

A common feature to most CTC complexes is de-protonation of the phenolic positions to provide a pair of chelating binding sites, as demonstrated in Figure 1.20. The platinum example, Figure 1.20 (b), was first reported in 1998 by Bohle and Stasko,¹⁶² but the interesting redox properties were not investigated until 2015 by Halcrow *et al.*¹⁶³

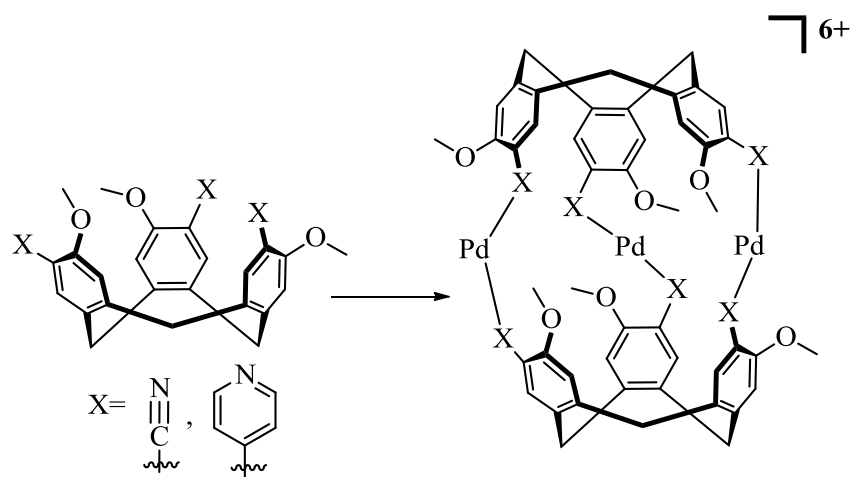
However, the most widely employed congener by far, in a supramolecular setting, is the chiral CTG ligand. Due to the alternating methoxy- hydroxyl arrangement around the upper rim, the molecule exhibits helical chirality, giving rise to the *M* and *P* isomers, as demonstrated in Figure 1.19. Tris-substitution of the hydroxyl groups through either halo-methyl or acid chloride appended groups leads to formation of ether or ester-linked ligand scaffolds.



Scheme 1.1: Formation of both ether- and ester-linked CTG ligand families.

Generally, in the effort towards metallo-supramolecular assemblies, the R-group appended contains a metal-binding unit such as pyridyl,^{85,95,126,127,167–169} carboxylate¹⁷⁰ or N-oxide.^{171,172} There are, of course, many examples of organic CTG-containing molecules, such as organic cryptophanes;^{173–177} where two CTG cavita nd ligands are covalently bound in a head-to-head fashion, as well as hemi-cryptophanes;^{178–183} where a cavita nd ligand is capped by another tripodal ligand motif. Organic cryptophanes were first synthesised in the 1980's by Collet *et al*, and the subsequent SCXRD data showed the inclusion of a tightly bound dichloromethane solvent guest.^{173,184} Hemi-cryptophanes have also found use in both catalysis, where a Zn(II) hemi-cryptophane enhanced the rate of reaction,^{178,181,185} and as host-molecules for biologically relevant small molecules.^{182,186}

There are elegant examples of metallo-supramolecular assemblies derived from alternative CTG-type ligands that are not functionalised through the route described in Scheme 1.1. The ligands synthesised by Shinkai¹⁸⁷ and Schaly,¹³⁰ directly attached pyridyl units and nitrile appended CTG, have been employed in combination with the *cis*-protected palladium source [Pd(dppp)], lead to Pd₃L₂ metallocryptophane assemblies, as demonstrated in Scheme 1.2.



Scheme 1.2: Formation of palladium Pd_3L_2 metallocryptophane assemblies from Shinkai¹⁸⁷ and Schaly.¹³⁰ Where $Pd=[Pd(dppp)][OTf]_2$.

As highlighted in Figure 1.19, CTG-derived ligands are formed as racemic mixtures of *M* and *P* isomers, depending on the substitution position around the upper-rim of the bowl. Thus when combining these ligands to form metallocryptophanes there are two potential outcomes; chiral *anti*-cages comprised of two ligands of the same enantiomer, or the meso *syn*-cages, where one ligand of each enantiomer is included.

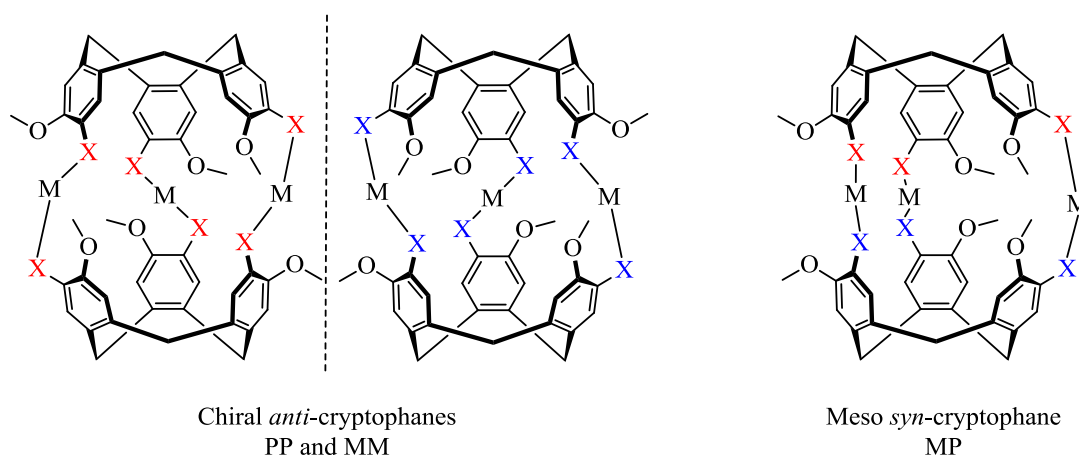


Figure 1.21: Enantiomeric description of metallocryptophane cages. *M*= any bridging metal, *X*= any metal-binding group.

Figure 1.21 shows the possible enantiomeric combinations of a metallocryptophane assembly, the red and blue X-group indicates the chirality of that ligand. The chiral *MM* and *PP* arrangements are enantiomers of each other, whilst the meso form is achiral.

Although the metallotecton employed and resultant structure achieved by both Shinkai and Schaly are similar, the enantiomeric result is different; Shinkai forms a

mixture of both *anti*- and *syn*-cages, whilst Schaly forms the *anti*-cages quantitatively and immediately. Shinkai did however find that adding an excess of the racemic ligand into the reaction drove the formation of the *syn*-cage.

Whilst there are numerous examples of coordination-polymers prepared from functionalised CTG ligands, incorporating a myriad of metals, counter-ions and solvent systems,^{171,172,188–190} the current drive is towards predictable, targeted, discrete assemblies.^{169,191,192}

The largest discrete CTG assembly to date is the stella octangular; a palladium assembly containing eight ligands and six palladium centres, describing the shape of a stellated octahedron, Figure 1.22 (a).¹²⁶ This structure was predicted due to the rigid ligand and well-defined square planar geometry of the Pd(II) metal precursor; it is repeatable and reliable, and has been seen to form in a variety of solvents, from numerous ‘naked’ palladium precursors in combination with 4-pyridyl containing ligands. The facile nature of formation has led to in depth studies of both the chirality contained within the assembly^{127,191,192} and the host-guest properties.¹⁹³

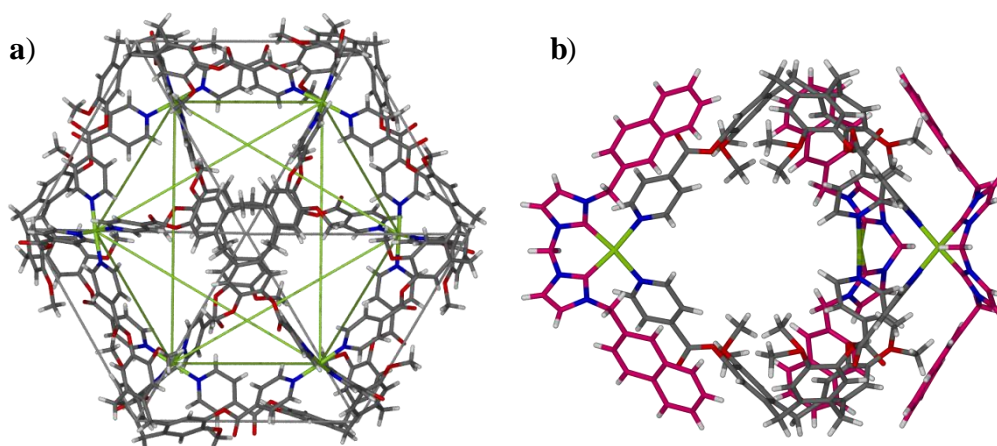


Figure 1.22: SCXRD structures of (a) the stella octangular Pd_6L_8 assembly and (b) an NHC-directed Pd_3L_2 metallocryptophane, where $Pd=[Pd(\text{bis-NHC})]$.

In an effort to achieve a higher degree of control over the self-assembly process, geometrically directing metallotectons were employed by Hardie *et al.* in the form of a strongly *cis*-protected palladium source.¹⁶⁹ An extended *bis*-N-heterocyclic ligand scaffold was utilised to not only favour *cis*-coordination, but also exploit π - π stacking to ‘lock’ the M_3L_2 assembly into place.¹⁶⁹

Relative to the number of metallo-supramolecular assemblies with CTG based ligands, there are notably fewer discrete, tri-nuclear metal-complexes. One such

example is a $[\text{Pd}(\text{Cl}_2)]_3\text{L}$ complex where PdCl_2 has been employed in combination with the hexa-substituted 2-pyridyl ligand, to give rise to an inter-veratrole chelating system, as seen in Figure 1.23 (a).¹⁹⁴ This hexa-pyridyl ligand also forms tri-nuclear complexes with $\text{Ag}(\text{I})$ and $\text{Cu}(\text{II})$, although these examples could not be elucidated crystallographically. Another hexa-substituted ligand system of interest is the hexakis(bipyridyl)-CTV system of Wytko, Figure 1.23 (b), whereby binding of different copper salts induced structural changes. When tetrahedral $\text{Cu}(\text{I})$ salts were employed a single isomer of the resultant Cu_3L complex was observed to exist in solution, despite a variety of possible isomers resulting from both inter-veratrole and intra-veratrole binding; the conformation shown below.¹⁹⁵ In addition to the possibility of inter- versus intra-veratrole binding, there are both Λ and Δ helical isomers possible as well.

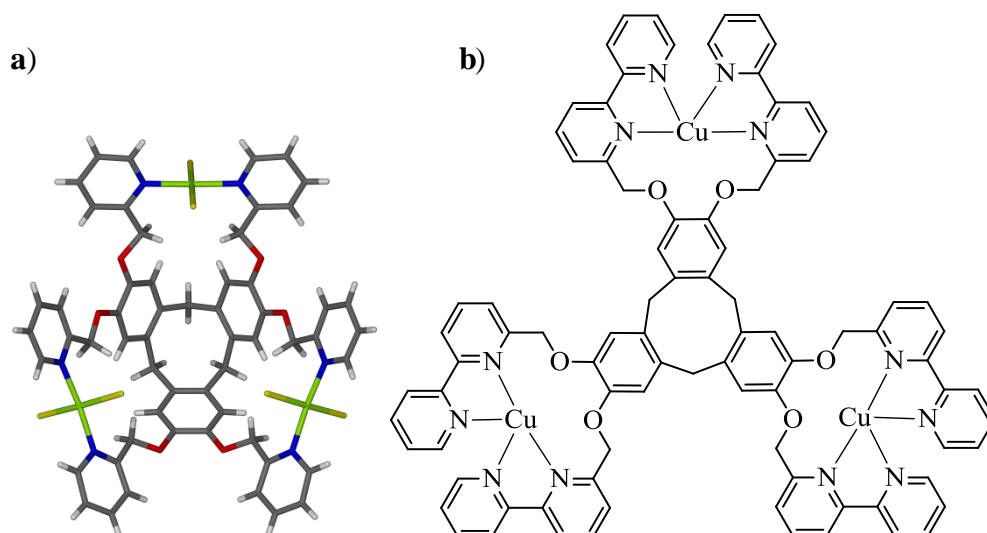


Figure 1.23: SCXRD structure of (a) $[\text{Pd}(\text{Cl})_2]_3\text{L}$ ¹⁹⁴ displaying inter-veratrole metal binding and the chemical structure of Wytko's copper-binding hexakis(bipyridyl)-CTV¹⁹⁵ displaying intra-veratrole metal binding.

Tris-substituted CTV-type ligands have also been synthesised bearing alternative metal-binding groups to the common N-donor motif. A few examples of these are shown in Figure 1.24. Verboom exploited the mercury binding properties of the azobenzene unit to not only form the $\text{Hg}(\text{II})$ complex, but also to act as a colorimetric sensor for its presence; when $\text{Hg}(\text{II})$ is present in solution, it binds to the azo unit and induces a colour change from yellow to red.¹⁹⁶

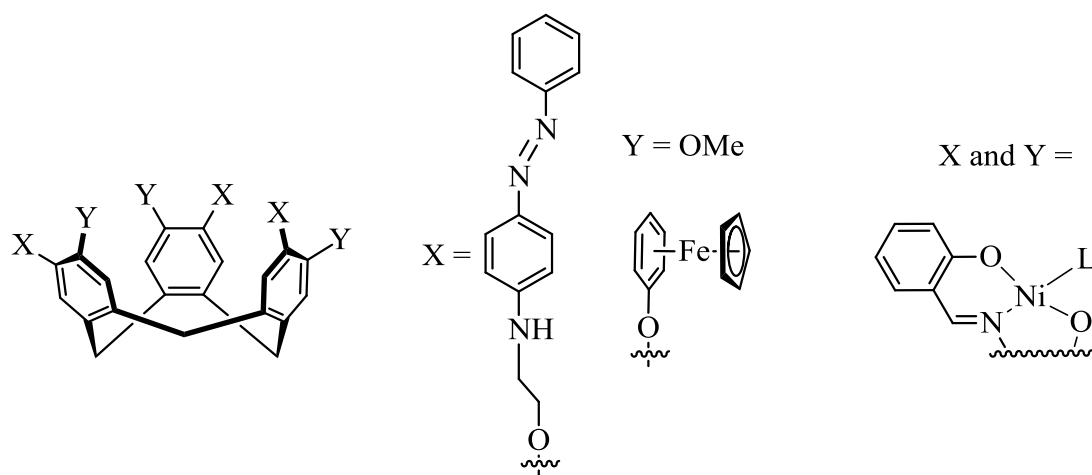


Figure 1.24: Tris-substituted CTV-type ligands from Verboom,¹⁹⁶ Atwood¹⁹⁷ and Bohle.¹⁹⁸

Bohle and Stasko have functionalised a CTV core through appending a salicylaldimine group that can chelate a nickel(II) centre in addition to the catechol moiety on the upper-rim of the cavitand core.¹⁹⁸ This methodology was found to be easily applied to a whole series of Schiff base ligands.

In a different approach, Atwood *et al.*, have appended three ferrocene-type units to the upper-rim of a CTG ligand to synthesise a host-molecule that can selectively extract perrhenate and pertechnetate anions from aqueous solution.¹⁹⁷ The removal of pertechnetate anions from solution is an important ecological task given their presence in nuclear waste material, and the ability to selectively bind pertechnetate in the presence of other anions is a notable achievement.

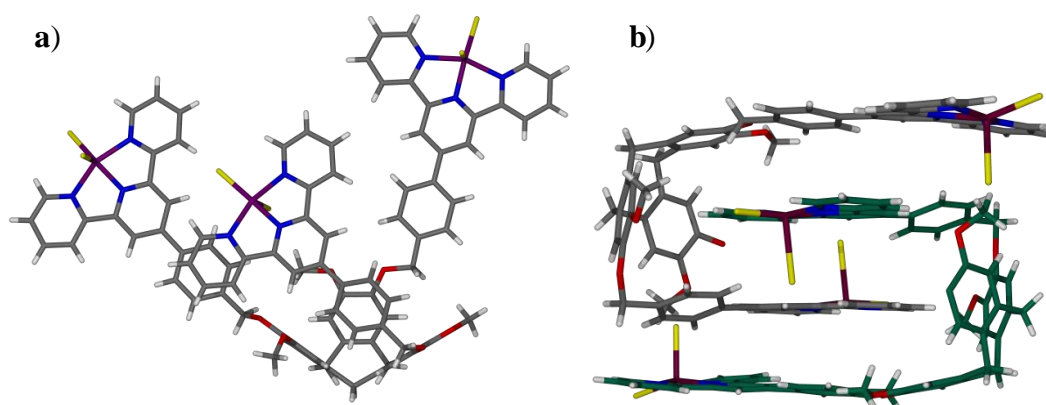


Figure 1.25: SCXRD structure of $[\text{Cu}(\text{Cl})_2]_3\text{L}$ and the self-inclusion 'hand-shake' motif exhibited. One ligand shown in green.¹⁹⁹

Possibly the most similar previous example to the work presented herein, is the $[\text{Cu}(\text{Cl})_2]_3\text{L}$ complex depicted in Figure 1.25 (a), where the ligand utilised is an extended terpyridine CTG scaffold.¹⁹⁹ This ligand provides a tri-dentate binding site for a copper(II) centre, whilst also exhibiting a ‘hand-shake’ motif, Figure 1.25 (b), whereby one ligand arm acts as the guest for a second molecule of the complex, which in turn acts as the guest for the first molecule in a reciprocal fashion. However, this copper complex was formed under solvothermal conditions, and as such only solid-state analysis could be obtained.

The solution-state stability and processability of the complexes discussed within this thesis mark them apart from the majority of the previously synthesised assemblies.

1.5 Project Outline

The primary aim of this research is to combine luminescent metal centres with the cyclotrimeratrylene ligand scaffold. Previously, primarily kinetically labile metal centres have been employed in combination with the aforementioned cyclotrimeratrylene family of ligands, employing supramolecular self-assembly and the ability of the labile metals to make and break bonds repeatedly towards a thermodynamically favourable outcome. Through rational design and consideration of both low-spin d^6 metal binding geometries and ligand complexation angles, a library of emissive supramolecular complexes will be targeted, formed from a wide range of seemingly inert metal centres and easily functionalisable ancillary ligands from which to impart varying emissive outcomes, ideally with a high-degree of control.

Initially a range of tri-metallic, discrete complexes are targeted with a view to understanding the relationship between emissive metallotecton and supramolecular scaffold. Once the properties of the tri-metallic systems are known, further investigation will concern means of colour tuning through careful and considered alteration of the three distinct metallotectons.

The ability of emissive systems to be easily tuned with a high-degree of control over the resultant emission wavelength is still non-facile. This research is aiming to develop a novel, modular approach towards tuneable colour emission, which could be applied to an almost infinite range of metallotectons. Expansion of this approach can be achieved through investigation of homo-*metallic* systems; by incorporation of

diverse, pre-functionalised ancillary ligands into the coordination sphere of the same metal centre, or homo-*nuclear* approaches; through inclusion of metallotectons containing different metal centres into the same tri-metallic complex.

Secondary aims of this project are concerned with the formation of self-assembled metallo-supramolecular assemblies, containing similar emissive metallotectons as geometrically directing metal sub-units. Through this work a range of hemi-cryptophane, metallo-cryptophane and cubic supramolecular assemblies will be discussed. The incorporation of luminescent metallotectons could allow for the sensing of subtle host-guest interactions through examination of the resultant emission changes.

1.6 Bibliography

- 1 *Electroluminescence I*, Academic Press, 1999.
- 2 Z. H. Kafafi, *Organic Electroluminescence*, CRC Press, 2005.
- 3 S. Fantacci and F. De Angelis, *Coord. Chem. Rev.*, 2011, **255**, 2704–2726.
- 4 K. P. S. Zaroni, B. K. Kariyazaki, A. Ito, M. K. Brennaman, T. J. Meyer and N. Y. Murakami Iha, *Inorg. Chem.*, 2014, **53**, 4089–4099.
- 5 M. Tavasli, T. N. Moore, Y. Zheng, M. R. Bryce, M. A. Fox, G. C. Griffiths, V. Jankus, H. A. Al-Attar and A. P. Monkman, *J. Mater. Chem.*, 2012, **22**, 6419–6428.
- 6 P.-H. Lanoë, J. Chan, G. Gontard, F. Monti, N. Armaroli, A. Barbieri and H. Amouri, *Eur. J. Inorg. Chem.*, 2016, **2016**, 1631–1634.
- 7 X. Shang, D. Han, Q. Zhan, G. Zhang and D. Li, *Organometallics*, 2014, **33**, 3300–3308.
- 8 C.-C. Wang, Y.-M. Jing, T.-Y. Li, Q.-L. Xu, S. Zhang, W.-N. Li, Y.-X. Zheng, J.-L. Zuo, X.-Z. You and X.-Q. Wang, *Eur. J. Inorg. Chem.*, 2013, **2013**, 5683–5693.
- 9 S. Ladouceur and E. Zysman-Colman, *Eur. J. Inorg. Chem.*, 2013, **2013**, 2985–3007.

- 10 S. W. Botchway, M. Charnley, J. W. Haycock, A. W. Parker, D. L. Rochester, J. A. Weinstein and J. A. G. Williams, *Proc. Natl. Acad. Sci.*, 2008, **105**, 16071–16076.
- 11 A. Beeby, S. W. Botchway, I. M. Clarkson, S. Faulkner, A. W. Parker, D. Parker and J. A. G. Williams, *J. Photochem. Photobiol. B*, 2000, **57**, 83–89.
- 12 X.-Q. Guo, F. N. Castellano, L. Li, H. Szmecinski, J. R. Lakowicz and J. Sipior, *Anal. Biochem.*, 1997, **254**, 179–186.
- 13 R.-R. Ye, C.-P. Tan, M.-H. Chen, L. Hao, L.-N. Ji and Z.-W. Mao, *Chem. – Eur. J.*, 2016, DOI: 10.1002/chem.201505160.
- 14 K. Y. Zhang, H.-W. Liu, M.-C. Tang, A. W.-T. Choi, N. Zhu, X.-G. Wei, K.-C. Lau and K. K.-W. Lo, *Inorg. Chem.*, 2015, **54**, 6582–6593.
- 15 K. P. S. Zanoni, R. L. Coppo, R. C. Amaral and N. Y. M. Iha, *Dalton Trans.*, 2015, **44**, 14559–14573.
- 16 R. O. Reithmeier, S. Meister, A. Siebel and B. Rieger, *Dalton Trans.*, 2015, **44**, 6466–6472.
- 17 K. Qiu, B. Yu, H. Huang, P. Zhang, L.-N. Ji and H. Chao, *Dalton Trans.*, 2015, **44**, 7058–7065.
- 18 S.-J. Liu, H. Liang, K. Y. Zhang, Q. Zhao, X. Zhou, W.-J. Xu and W. Huang, *Chem. Commun.*, 2015, **51**, 7943–7946.
- 19 R. Davidson, L. E. Wilson, A. Duckworth, D. S. Yufit, A. Beeby and P. Low, *Dalton Trans.*, 2015, **44**, 11368–11379.
- 20 G. Velmurugan and P. Venuvanalingam, *Dalton Trans.*, 2014, **44**, 8529–8542.
- 21 S. Mandal, D. K. Poria, R. Ghosh, P. S. Ray and P. Gupta, *Dalton Trans.*, 2014, **43**, 17463–17474.
- 22 J. Jayabharathi, V. Thanikachalam and R. Sathishkumar, *New J. Chem.*, 2014, **39**, 235–245.
- 23 M. C. Gimeno, V. Fernández-Moreira and I. Marzo, *Chem. Sci.*, 2014, **5**, 4443–4446.

-
- 24 B. Tong, Q. Mei, D. Chen and M. Lu, *Synth. Met.*, 2012, **162**, 1701–1706.
- 25 A. W.-T. Choi, V. M.-W. Yim, H.-W. Liu and K. K.-W. Lo, *Chem. – Eur. J.*, 2014, **20**, 9633–9642.
- 26 H. Komatsu, K. Yoshihara, H. Yamada, Y. Kimura, A. Son, S. Nishimoto and K. Tanabe, *Chem. – Eur. J.*, 2013, **19**, 1971–1977.
- 27 V. Fernández-Moreira, F. L. Thorp-Greenwood, A. J. Amoroso, J. Cable, J. B. Court, V. Gray, A. J. Hayes, R. L. Jenkins, B. M. Kariuki, D. Lloyd, C. O. Millet, C. F. Williams and M. P. Coogan, *Org. Biomol. Chem.*, 2010, **8**, 3888–3901.
- 28 X. Yang, X. Xu, J. Dang, G. Zhou, C.-L. Ho and W.-Y. Wong, *Inorg. Chem.*, 2016, **55**, 1720–1727.
- 29 D. Kourkoulos, C. Karakus, D. Hertel, R. Alle, S. Schmeding, J. Hummel, N. Risch, E. Holder and K. Meerholz, *Dalton Trans.*, 2013, **42**, 13612–13621.
- 30 R. Tao, J. Qiao, G. Zhang, L. Duan, L. Wang and Y. Qiu, *J. Phys. Chem. C*, 2012, **116**, 11658–11664.
- 31 K. Hasan, L. Donato, Y. Shen, J. D. Slinker and E. Zysman-Colman, *Dalton Trans.*, 2014, **43**, 13672–13682.
- 32 S. Evariste, M. Sandroni, T. W. Rees, C. Roldán-Carmona, L. Gil-Escrig, H. J. Bolink, E. Baranoff and E. Zysman-Colman, *J. Mater. Chem. C*, 2014, **2**, 5793–5804.
- 33 A. M. Bünzli, E. C. Constable, C. E. Housecroft, A. Prescimone, J. A. Zampese, G. Longo, L. Gil-Escrig, A. Pertegás, E. Ortí and H. J. Bolink, *Chem. Sci.*, 2015, **6**, 2843–2852.
- 34 E. C. Constable, C. E. Housecroft, G. E. Schneider, J. A. Zampese, H. J. Bolink, A. Pertegás and C. Roldan-Carmona, *Dalton Trans.*, 2014, **43**, 4653–4667.
- 35 R. D. Costa, E. Ortí, H. J. Bolink, F. Monti, G. Accorsi and N. Armaroli, *Angew. Chem. Int. Ed.*, 2012, **51**, 8178–8211.
- 36 R. D. Costa, G. Fernández, L. Sánchez, N. Martín, E. Ortí and H. J. Bolink, *Chem. – Eur. J.*, 2010, **16**, 9855–9863.
-

- 37 E. Baranoff, J.-H. Yum, M. Graetzel and M. K. Nazeeruddin, *J. Organomet. Chem.*, 2009, **694**, 2661–2670.
- 38 A. J. Amoroso, R. J. Arthur, M. P. Coogan, J. B. Court, V. Fernández-Moreira, A. J. Hayes, D. Lloyd, C. Millet and S. J. A. Pope, *New J. Chem.*, 2008, **32**, 1097–1102.
- 39 H. C. Bertrand, S. Clède, R. Guillot, F. Lambert and C. Policar, *Inorg. Chem.*, 2014, **53**, 6204–6223.
- 40 K. Yin Zhang, K. Ka-Shun Tso, M.-W. Louie, H.-W. Liu and K. Kam-Wing Lo, *Organometallics*, 2013, **32**, 5098–5102.
- 41 A. Leonidova, V. Pierroz, R. Rubbiani, J. Heier, S. Ferrari and G. Gasser, *Dalton Trans.*, 2013, **43**, 4287–4294.
- 42 V. Fernández-Moreira, M. L. Ortego, C. F. Williams, M. P. Coogan, M. D. Villacampa and M. C. Gimeno, *Organometallics*, 2012, **31**, 5950–5957.
- 43 W. Jiang, Y. Gao, Y. Sun, F. Ding, Y. Xu, Z. Bian, F. Li, J. Bian and C. Huang, *Inorg. Chem.*, 2010, **49**, 3252–3260.
- 44 M. P. Coogan and V. Fernández-Moreira, *Chem. Commun.*, 2013, **50**, 384–399.
- 45 F. Lu and T. Nabeshima, *Dalton Trans.*, 2014, **43**, 9529–9536.
- 46 C. W. Tang and S. A. VanSlyke, *Appl. Phys. Lett.*, 1987, **51**, 913–915.
- 47 J. H. Burroughes, D. D. C. Bradley, A. R. Brown, R. N. Marks, K. Mackay, R. H. Friend, P. L. Burns and A. B. Holmes, *Nature*, 1990, **347**, 539–541.
- 48 M. A. Baldo, D. F. O'Brien, Y. You, A. Shoustikov, S. Sibley, M. E. Thompson and S. R. Forrest, *Nature*, 1998, **395**, 151–154.
- 49 M. A. Baldo, S. Lamansky, P. E. Burrows, M. E. Thompson and S. R. Forrest, *Appl. Phys. Lett.*, 1999, **75**, 4–6.
- 50 S. B. Meier, D. Tordera, A. Pertegás, C. Roldán-Carmona, E. Ortí and H. J. Bolink, *Mater. Today*, 2014, **17**, 217–223.
- 51 Q. Pei, G. Yu, C. Zhang, Y. Yang and A. J. Heeger, *Science*, 1995, **269**, 1086–1088.

- 52 J.-K. Lee, D. S. Yoo, E. S. Handy and M. F. Rubner, *Appl. Phys. Lett.*, 1996, **69**, 1686–1688.
- 53 J. Slinker, D. Bernardis, P. L. Houston, H. D. Abruña, S. Bernhard and G. G. Malliaras, *Chem. Commun.*, 2003, 2392–2399.
- 54 L. Flamigni, A. Barbieri, C. Sabatini, B. Ventura and F. Barigelletti, in *Photochemistry and Photophysics of Coordination Compounds II*, eds. V. Balzani and S. Campagna, Springer Berlin Heidelberg, 2007, pp. 143–203.
- 55 T. Hu, L. He, L. Duan and Y. Qiu, *J. Mater. Chem.*, 2012, **22**, 4206–4215.
- 56 L. He, J. Qiao, L. Duan, G. Dong, D. Zhang, L. Wang and Y. Qiu, *Adv. Funct. Mater.*, 2009, **19**, 2950–2960.
- 57 H.-C. Su, Y.-H. Lin, C.-H. Chang, H.-W. Lin, C.-C. Wu, F.-C. Fang, H.-F. Chen and K.-T. Wong, *J. Mater. Chem.*, 2010, **20**, 5521–5526.
- 58 A. B. Tamayo, S. Garon, T. Sajoto, P. I. Djurovich, I. M. Tsyba, R. Bau and M. E. Thompson, *Inorg. Chem.*, 2005, **44**, 8723–8732.
- 59 J.-M. Lehn, *Angew. Chem. Int. Ed. Engl.*, 1988, **27**, 89–112.
- 60 J.-M. Lehn, *Science*, 1985, **227**, 849–856.
- 61 J.-M. Lehn, *Angew. Chem. Int. Ed. Engl.*, 1990, **29**, 1304–1319.
- 62 J.-M. Lehn, *Science*, 2002, **295**, 2400–2403.
- 63 R. Kramer, J. M. Lehn and A. Marquis-Rigault, *Proc. Natl. Acad. Sci.*, 1993, **90**, 5394–5398.
- 64 G. F. S. Whitehead, F. Moro, G. A. Timco, W. Wernsdorfer, S. J. Teat and R. E. P. Winpenny, *Angew. Chem. Int. Ed.*, 2013, **52**, 9932–9935.
- 65 R. A. Bilbeisi, T. K. Ronson and J. R. Nitschke, *Angew. Chem. Int. Ed.*, 2013, **52**, 9027–9030.
- 66 N. Mittal, M. L. Saha and M. Schmittel, *Chem. Commun.*, 2015, **51**, 15514–15517.
- 67 M. L. Saha, N. Mittal, J. W. Bats and M. Schmittel, *Chem. Commun.*, 2014, **50**, 12189–12192.

- 68 J. E. Beves, J. J. Danon, D. A. Leigh, J.-F. Lemonnier and I. J. Vitorica-Yrezabal, *Angew. Chem. Int. Ed.*, 2015, **54**, 7555–7559.
- 69 J.-F. Ayme, J. E. Beves, D. A. Leigh, R. T. McBurney, K. Rissanen and D. Schultz, *Nat. Chem.*, 2012, **4**, 15–20.
- 70 A. Mishra, S. C. Kang and K.-W. Chi, *Eur. J. Inorg. Chem.*, 2013, **2013**, 5222–5232.
- 71 B. Sun, M. Wang, Z. Lou, M. Huang, C. Xu, X. Li, L.-J. Chen, Y. Yu, G. L. Davis, B. Xu, H.-B. Yang and X. Li, *J. Am. Chem. Soc.*, 2015, **137**, 1556–1564.
- 72 K. S. Chichak, S. J. Cantrill, A. R. Pease, S.-H. Chiu, G. W. V. Cave, J. L. Atwood and J. F. Stoddart, *Science*, 2004, **304**, 1308–1312.
- 73 A. M. Johnson, C. A. Wiley, M. C. Young, X. Zhang, Y. Lyon, R. R. Julian and R. J. Hooley, *Angew. Chem. Int. Ed.*, 2015, **54**, 5641–5645.
- 74 T. Gunnlaugsson, C. Lincheneau and B. Jean-Denis, *Chem. Commun.*, 2014, **50**, 2857–2860.
- 75 C. Schouwey, J. J. Holstein, R. Scopelliti, K. O. Zhurov, K. O. Nagornov, Y. O. Tsybin, O. S. Smart, G. Bricogne and K. Severin, *Angew. Chem. Int. Ed.*, 2014, **53**, 11261–11265.
- 76 S. Roche, C. Haslam, S. L. Heath and J. A. Thomas, *Chem. Commun.*, 1998, 1681–1682.
- 77 S.-L. Huang, Y.-J. Lin, Z.-H. Li and G.-X. Jin, *Angew. Chem. Int. Ed.*, 2014, **53**, 11218–11222.
- 78 D. V. Kondratuk, J. K. Sprafke, M. C. O’Sullivan, L. M. A. Perdigo, A. Saywell, M. Malfois, J. N. O’Shea, P. H. Beton, A. L. Thompson and H. L. Anderson, *Chem. – Eur. J.*, 2014, **20**, 12826–12834.
- 79 C. O. Dietrich-Buchecker, J. P. Sauvage and J. P. Kintzinger, *Tetrahedron Lett.*, 1983, **24**, 5095–5098.
- 80 C. O. Dietrich-Buchecker and J.-P. Sauvage, *Angew. Chem. Int. Ed. Engl.*, 1989, **28**, 189–192.

- 81 F. L. Thorp-Greenwood, A. N. Kulak and M. J. Hardie, *Nat. Chem.*, 2015, **7**, 526–531.
- 82 N. C. Seeman, in *Molecular Catenanes, Rotaxanes and Knots*, eds. J.-P. Sauvage and C. Dietrich-Buchecker, Wiley-VCH Verlag GmbH, 1999, pp. 323–356.
- 83 S.-L. Huang, Y.-J. Lin, T. S. A. Hor and G.-X. Jin, *J. Am. Chem. Soc.*, 2013, **135**, 8125–8128.
- 84 T. Prakasam, M. Lusi, M. Elhabiri, C. Platas-Iglesias, J.-C. Olsen, Z. Asfari, S. Cianférani-Sanglier, F. Debaene, L. J. Charbonnière and A. Trabolsi, *Angew. Chem. Int. Ed.*, 2013, **52**, 9956–9960.
- 85 T. K. Ronson, J. Fisher, L. P. Harding, P. J. Rizkallah, J. E. Warren and M. J. Hardie, *Nat. Chem.*, 2009, **1**, 212–216.
- 86 C. Heim, D. Udelhofen and F. Vögtle, in *Molecular Catenanes, Rotaxanes and Knots*, eds. J.-P. Sauvage and C. Dietrich-Buchecker, Wiley-VCH Verlag GmbH, 1999, pp. 177–222.
- 87 D. A. Leigh, R. G. Pritchard and A. J. Stephens, *Nat. Chem.*, 2014, **6**, 978–982.
- 88 I. C. Gibbs-Hall, N. A. Vermeulen, E. J. Dale, J. J. Henkelis, A. K. Blackburn, J. C. Barnes and J. F. Stoddart, *J. Am. Chem. Soc.*, 2015, **137**, 15640–15643.
- 89 O. Gidron, M. Jirásek, N. Trapp, M.-O. Ebert, X. Zhang and F. Diederich, *J. Am. Chem. Soc.*, 2015, **137**, 12502–12505.
- 90 C. Browne, T. K. Ronson and J. R. Nitschke, *Angew. Chem. Int. Ed.*, 2014, **53**, 10701–10705.
- 91 Z. Meng, Y. Han, L.-N. Wang, J.-F. Xiang, S.-G. He and C.-F. Chen, *J. Am. Chem. Soc.*, 2015, **137**, 9739–9745.
- 92 C. S. Wood, T. K. Ronson, A. M. Belenguer, J. J. Holstein and J. R. Nitschke, *Nat. Chem.*, 2015, **7**, 354–358.
- 93 R. Hovorka, G. Meyer-Eppler, T. Piehler, S. Hytteballe, M. Engeser, F. Topić, K. Rissanen and A. Lützen, *Chem. – Eur. J.*, 2014, **20**, 13253–13528.

-
- 94 E. M. López-Vidal, M. D. García, C. Peinador and J. M. Quintela, *Chem. – Eur. J.*, 2014, **21**, 2259–2267.
- 95 J. J. Henkelis, T. K. Ronson, L. P. Harding and M. J. Hardie, *Chem. Commun.*, 2011, **47**, 6560–6562.
- 96 A. Westcott, J. Fisher, L. P. Harding, P. Rizkallah and M. J. Hardie, *J. Am. Chem. Soc.*, 2008, **130**, 2950–2951.
- 97 M. Fujita, in *Molecular Catenanes, Rotaxanes and Knots*, eds. J.-P. Sauvage and C. Dietrich-Buchecker, Wiley-VCH Verlag GmbH, 1999, pp. 57–76.
- 98 J.-F. Ayme, G. Gil-Ramírez, D. A. Leigh, J.-F. Lemonnier, A. Markevicius, C. A. Muryn and G. Zhang, *J. Am. Chem. Soc.*, 2014, **136**, 13142–13145.
- 99 D. B. Amabilino, P. R. Ashton, A. S. Reder, N. Spencer and J. F. Stoddart, *Angew. Chem. Int. Ed. Engl.*, 1994, **33**, 1286–1290.
- 100 E. J. Dale, N. A. Vermeulen, A. A. Thomas, J. C. Barnes, M. Juríček, A. K. Blackburn, N. L. Strutt, A. A. Sarjeant, C. L. Stern, S. E. Denmark and J. F. Stoddart, *J. Am. Chem. Soc.*, 2014, **136**, 10669–10682.
- 101 N. Hafezi, J. M. Holcroft, K. J. Hartlieb, E. J. Dale, N. A. Vermeulen, C. L. Stern, A. A. Sarjeant and J. F. Stoddart, *Angew. Chem. Int. Ed.*, 2014, **54**, 456–461.
- 102 R. S. Forgan, J.-P. Sauvage and J. F. Stoddart, *Chem. Rev.*, 2011, **111**, 5434–5464.
- 103 J.-M. Lehn, in *Supramolecular Chemistry*, Wiley-VCH Verlag GmbH & Co. KGaA, 1995, pp. 69–80.
- 104 N. Ahmad, H. A. Younus, A. H. Chughtai and F. Verpoort, *Chem. Soc. Rev.*, 2014, **44**, 9–25.
- 105 P. Mal, B. Breiner, K. Rissanen and J. R. Nitschke, *Science*, 2009, **324**, 1697–1699.
- 106 R. A. Bilbeisi, J. K. Clegg, N. Elgrishi, X. de Hatten, M. Devillard, B. Breiner, P. Mal and J. R. Nitschke, *J. Am. Chem. Soc.*, 2012, **134**, 5110–5119.

- 107 A. Jiménez, R. A. Bilbeisi, T. K. Ronson, S. Zarra, C. Woodhead and J. R. Nitschke, *Angew. Chem. Int. Ed.*, 2014, **53**, 4556–4560.
- 108 J. L. Bolliger, T. K. Ronson, M. Ogawa and J. R. Nitschke, *J. Am. Chem. Soc.*, 2014, **136**, 14545–14553.
- 109 W. Meng, B. Breiner, K. Rissanen, J. D. Thoburn, J. K. Clegg and J. R. Nitschke, *Angew. Chem. Int. Ed.*, 2011, **50**, 3479–3483.
- 110 A. M. Castilla, T. K. Ronson and J. R. Nitschke, *J. Am. Chem. Soc.*, 2016, **138**, 2342–2351.
- 111 C. J. Bruns, D. Fujita, M. Hoshino, S. Sato, J. F. Stoddart and M. Fujita, *J. Am. Chem. Soc.*, 2014, **136**, 12027–12034.
- 112 P. Ballester, M. Fujita and J. Rebek, *Chem. Soc. Rev.*, 2014, **44**, 392–393.
- 113 Y. Jiao, J. Wang, P. Wu, L. Zhao, C. He, J. Zhang and C. Duan, *Chem. – Eur. J.*, 2014, **20**, 2224–2231.
- 114 T. Murase, Y. Nishijima and M. Fujita, *J. Am. Chem. Soc.*, 2012, **134**, 162–164.
- 115 C. Zhao, Q.-F. Sun, W. M. Hart-Cooper, A. G. DiPasquale, F. D. Toste, R. G. Bergman and K. N. Raymond, *J. Am. Chem. Soc.*, 2013, **135**, 18802–18805.
- 116 M. Yoshizawa, M. Nagao, K. Kumazawa and M. Fujita, *J. Organomet. Chem.*, 2005, **690**, 5383–5388.
- 117 K. Yamashita, A. Hori and M. Fujita, *Tetrahedron Prize Creat. Org. Chem. New React. Catal. Dev. Appl.*, 2007, **63**, 8435–8439.
- 118 Q.-F. Sun, T. Murase, S. Sato and M. Fujita, *Angew. Chem. Int. Ed.*, 2011, **50**, 10318–10321.
- 119 J. E. M. Lewis, E. L. Gavey, S. A. Cameron and J. D. Crowley, *Chem. Sci.*, 2012, **3**, 778–784.
- 120 M. Yoneya, T. Yamaguchi, S. Sato and M. Fujita, *J. Am. Chem. Soc.*, 2012, **134**, 14401–14407.

- 121 C. Klein, C. Gütz, M. Bogner, F. Topić, K. Rissanen and A. Lützen, *Angew. Chem. Int. Ed.*, 2014, **53**, 3739–3742.
- 122 J. Lewis, A. B. S. Elliott, C. J. McAdam, K. C. Gordon and J. D. Crowley, *Chem. Sci.*, 2014, **5**, 1833–1843.
- 123 G. Meyer-Eppler, F. Topić, G. Schnakenburg, K. Rissanen and A. Lützen, *Eur. J. Inorg. Chem.*, 2014, **2014**, 2495–2501.
- 124 D. Samanta and P. S. Mukherjee, *Chem. – Eur. J.*, 2014, **20**, 12483–12492.
- 125 Q.-F. Sun, S. Sato and M. Fujita, *Angew. Chem. Int. Ed.*, 2014, **53**, 13510–13513.
- 126 T. K. Ronson, J. Fisher, L. P. Harding and M. J. Hardie, *Angew. Chem. Int. Ed.*, 2007, **46**, 9086–9088.
- 127 T. K. Ronson, C. Carruthers, J. Fisher, T. Brotin, L. P. Harding, P. J. Rizkallah and M. J. Hardie, *Inorg. Chem.*, 2010, **49**, 675–685.
- 128 A. Peuronen, S. Forsblom and M. Lahtinen, *Chem. Commun.*, 2014, **50**, 5469–5472.
- 129 M. Fujita, S. Nagao and K. Ogura, *J. Am. Chem. Soc.*, 1995, **117**, 1649–1650.
- 130 A. Schaly, Y. Rousselin, J.-C. Chambron, E. Aubert and E. Espinosa, *Eur. J. Inorg. Chem.*, 2016, **2016**, 832–843.
- 131 N. Fujita, K. Biradha, M. Fujita, S. Sakamoto and K. Yamaguchi, *Angew. Chem. Int. Ed.*, 2001, **40**, 1718–1721.
- 132 H. Takezawa, T. Murase, G. Resnati, P. Metrangolo and M. Fujita, *Angew. Chem. Int. Ed.*, 2015, **54**, 8411–8414.
- 133 Y.-F. Han, Y.-J. Lin, W.-G. Jia, G.-L. Wang and G.-X. Jin, *Chem. Commun.*, 2008, 1807–1809.
- 134 Y.-F. Han, H. Li, Z.-F. Zheng and G.-X. Jin, *Chem. – Asian J.*, 2012, **7**, 1243–1250.
- 135 P. Govindaswamy, D. Linder, J. Lacour, G. Süß-Fink and B. Therrien, *Dalton Trans.*, 2007, 4457–4463.

- 136 P. Govindaswamy, D. Linder, J. Lacour, G. Süß-Fink and B. Therrien, *Chem. Commun.*, 2006, 4691–4693.
- 137 B. Therrien, G. Süß-Fink, P. Govindaswamy, A. K. Renfrew and P. J. Dyson, *Angew. Chem.*, 2008, **120**, 3833–3836.
- 138 N. P. E. Barry, O. Zava, J. Furrer, P. J. Dyson and B. Therrien, *Dalton Trans.*, 2010, **39**, 5272–5277.
- 139 B. Therrien, *CrystEngComm*, 2014, **17**, 484–491.
- 140 R. Pettinari, F. Marchetti, C. Pettinari, F. Condello, B. W. Skelton, A. H. White, M. R. Chierotti and R. Gobetto, *Dalton Trans.*, 2016, **45**, 3974–3982.
- 141 K. Yamashita, M. Kawano and M. Fujita, *Chem. Commun.*, 2007, 4102–4103.
- 142 T. Sajoto, P. I. Djurovich, A. Tamayo, M. Yousufuddin, R. Bau, M. E. Thompson, R. J. Holmes and S. R. Forrest, *Inorg. Chem.*, 2005, **44**, 7992–8003.
- 143 S. Gülcemal, A. G. Gökçe and B. Çetinkaya, *Inorg. Chem.*, 2013, **52**, 10601–10609.
- 144 J. G. Vaughan, B. L. Reid, S. Ramchandani, P. J. Wright, S. Muzzioli, B. W. Skelton, P. Raiteri, D. H. Brown, S. Stagni and M. Massi, *Dalton Trans.*, 2013, **42**, 14100–14114.
- 145 T.-Y. Li, X. Liang, L. Zhou, C. Wu, S. Zhang, X. Liu, G.-Z. Lu, L.-S. Xue, Y.-X. Zheng and J.-L. Zuo, *Inorg. Chem.*, 2014, **54**, 161–173.
- 146 K. Manna, T. Zhang and W. Lin, *J. Am. Chem. Soc.*, 2014, **136**, 6566–6569.
- 147 C. Wang, J.-L. Wang and W. Lin, *J. Am. Chem. Soc.*, 2012, **134**, 19895–19908.
- 148 Z. Xie, L. Ma, K. E. deKrafft, A. Jin and W. Lin, *J. Am. Chem. Soc.*, 2010, **132**, 922–923.
- 149 D. Liu, R. C. Huxford and W. Lin, *Angew. Chem. Int. Ed.*, 2011, **50**, 3696–3700.

- 150 L. Li, S. Zhang, Y. Xu, S. Zhao, Z. Sun and J. Luo, *Inorg. Chem.*, 2015, **54**, 8872–8874.
- 151 N. C. A. Baker, N. C. Fletcher, P. N. Horton and M. B. Hursthouse, *Dalton Trans.*, 2012, **41**, 7005–7012.
- 152 E. Baranoff, E. Orselli, L. Allouche, D. D. Censo, R. Scopelliti, M. Grätzel and M. K. Nazeeruddin, *Chem. Commun.*, 2011, **47**, 2799–2801.
- 153 B. Laramee-Milette, F. Lussier, I. Ciofini and G. Hanan, *Dalton Trans.*, 2015, **44**, 11551–11561.
- 154 T. Hajra, J. K. Bera and V. Chandrasekhar, *Inorganica Chim. Acta*, 2011, **372**, 53–61.
- 155 P. de Wolf, S. L. Heath and J. A. Thomas, *Chem. Commun.*, 2002, 2540–2541.
- 156 H. Ahmad, B. W. Hazel, A. J. H. M. Meijer, J. A. Thomas and K. A. Wilkinson, *Chem. – Eur. J.*, 2013, **19**, 5081–5087.
- 157 H. Ahmad, D. Ghosh and J. A. Thomas, *Chem. Commun.*, 2014, **50**, 3859–3861.
- 158 R. V. Slone, D. I. Yoon, R. M. Calhoun and J. T. Hupp, *J. Am. Chem. Soc.*, 1995, **117**, 11813–11814.
- 159 S.-S. Sun and A. J. Lees, *Inorg. Chem.*, 2001, **40**, 3154–3160.
- 160 J. L. Atwood, M. J. Barnes, M. G. Gardiner and C. L. Raston, *Chem. Commun.*, 1996, 1449–1450.
- 161 M. J. Hardie, P. D. Godfrey and C. L. Raston, *Chem. – Eur. J.*, 1999, **5**, 1828–1833.
- 162 D. Scott Bohle and D. Stasko, *Chem. Commun.*, 1998, 567–569.
- 163 J. J. Loughrey, N. J. Patmore, A. Baldansuren, A. J. Fielding, E. J. L. McInnes, M. J. Hardie, S. Sproules and M. A. Halcrow, *Chem. Sci.*, 2015, **6**, 6935–6948.
- 164 B. F. Abrahams, B. A. Boughton, N. J. FitzGerald, J. L. Holmes and R. Robson, *Chem. Commun.*, 2011, **47**, 7404–7406.

- 165 B. F. Abrahams, N. J. FitzGerald, T. A. Hudson, R. Robson and T. Waters, *Angew. Chem. Int. Ed.*, 2009, **48**, 3129–3132.
- 166 J. J. Loughrey, C. A. Kilner, M. J. Hardie and M. A. Halcrow, *Supramol. Chem.*, 2012, **24**, 2–13.
- 167 M. J. Hardie, R. M. Mills and C. J. Sumbly, *Org. Biomol. Chem.*, 2004, **2**, 2958–2964.
- 168 C. J. Sumbly and M. J. Hardie, *Angew. Chem. Int. Ed.*, 2005, **44**, 6395–6399.
- 169 J. J. Henkelis, C. J. Carruthers, S. E. Chambers, R. Clowes, A. I. Cooper, J. Fisher and M. J. Hardie, *J. Am. Chem. Soc.*, 2014, **136**, 14393–14396.
- 170 T. K. Ronson, H. Nowell, A. Westcott and M. J. Hardie, *Chem. Commun.*, 2011, **47**, 176.
- 171 J. J. Henkelis, S. A. Barnett, L. P. Harding and M. J. Hardie, *Inorg. Chem.*, 2012, **51**, 10657–10674.
- 172 J. J. Henkelis, T. K. Ronson and M. J. Hardie, *CrystEngComm*, 2013, **16**, 3688–3693.
- 173 A. Collet, *Tetrahedron*, 1987, **43**, 5725–5759.
- 174 T. Brotin, T. Devic, A. Lesage, L. Emsley and A. Collet, *Chem. – Eur. J.*, 2001, **7**, 1561–1573.
- 175 T. Brotin and J.-P. Dutasta, *Chem. Rev.*, 2009, **109**, 88–130.
- 176 K. T. Holman, S. D. Drake, J. W. Steed, G. W. Orr and J. L. Atwood, *Supramol. Chem.*, 2010, **22**, 870–890.
- 177 M. A. Little, J. Donkin, J. Fisher, M. A. Halcrow, J. Loder and M. J. Hardie, *Angew. Chem. Int. Ed.*, 2012, **51**, 764–766.
- 178 Y. Makita, K. Sugimoto, K. Furuyoshi, K. Ikeda, S. Fujiwara, T. Shin-ike and A. Ogawa, *Inorg. Chem.*, 2010, **49**, 7220–7222.
- 179 P. D. Raytchev, O. Perraud, C. Aronica, A. Martinez and J.-P. Dutasta, *J. Org. Chem.*, 2010, **75**, 2099–2102.
- 180 B. Chatelet, E. Payet, O. Perraud, P. Dimitrov-Raytchev, L.-L. Chapellet, V. Dufaud, A. Martinez and J.-P. Dutasta, *Org. Lett.*, 2011, **13**, 3706–3709.

- 181 Y. Makita, K. Sugimoto, K. Furuyoshi, K. Ikeda, T. Fujita, S.-I. Fujiwara and A. Ogawa, *Supramol. Chem.*, 2011, **23**, 269–272.
- 182 O. Perraud, S. Lefevre, V. Robert, A. Martinez and J.-P. Dutasta, *Org. Biomol. Chem.*, 2012, **10**, 1056–1059.
- 183 A. Martinez, D. Zhang, J.-C. Mulatier, J. R. Cochrane, L. Guy, J.-P. Dutasta and G. Gao, *Chem. – Eur. J.*, 2016, n/a–n/a.
- 184 J. Canceill, M. Cesario, A. Collet, J. Guilhem, C. Riche and C. Pascard, *J. Chem. Soc. Chem. Commun.*, 1986, 339–341.
- 185 Y. Makita, K. Ikeda, K. Sugimoto, T. Fujita, T. Danno, K. Bobuatong, M. Ehara, S. Fujiwara and A. Ogawa, *J. Organomet. Chem.*, 2012, **706–707**, 26–29.
- 186 O. Perraud, V. Robert, A. Martinez and J.-P. Dutasta, *Chem. – Eur. J.*, 2011, **17**, 13405–13408.
- 187 Z. Zhong, A. Ikeda, S. Shinkai, S. Sakamoto and K. Yamaguchi, *Org. Lett.*, 2001, **3**, 1085–1087.
- 188 M. J. Hardie and C. J. Sumby, *Inorg. Chem.*, 2004, **43**, 6872–6874.
- 189 T. K. Ronson and M. J. Hardie, *CrystEngComm*, 2008, **10**, 1731–1734.
- 190 M. A. Little, M. A. Halcrow, L. P. Harding and M. J. Hardie, *Inorg. Chem.*, 2010, **49**, 9486–9496.
- 191 J. J. Henkelis and M. J. Hardie, *Chem. Commun.*, 2015, **51**, 11929–11943.
- 192 J. J. Henkelis, J. Fisher, S. L. Warriner and M. J. Hardie, *Chem. – Eur. J.*, 2014, **20**, 4117–4125.
- 193 N. J. Cookson, J. J. Henkelis, R. J. Ansell, C. W. G. Fishwick, M. J. Hardie and J. Fisher, *Dalton Trans.*, 2014, **43**, 5657–5661.
- 194 C. J. Sumby, K. C. Gordon, T. J. Walsh and M. J. Hardie, *Chem. – Eur. J.*, 2008, **14**, 4415–4425.
- 195 J. A. Wytko, C. Boudon, J. Weiss and M. Gross, *Inorg. Chem.*, 1996, **35**, 4469–4477.

- 196 Nuriman, B. Kuswandi and W. Verboom, *Anal. Chim. Acta*, 2009, **655**, 75–79.
- 197 J. A. Gawenis, K. T. Holman, J. L. Atwood and S. S. Jurisson, *Inorg. Chem.*, 2002, **41**, 6028–6031.
- 198 D. S. Bohle and D. J. Stasko, *Inorg. Chem.*, 2000, **39**, 5768–5770.
- 199 C. Carruthers, T. K. Ronson, C. J. Sumby, A. Westcott, L. P. Harding, T. J. Prior, P. Rizkallah and M. J. Hardie, *Chem. – Eur. J.*, 2008, **14**, 10286–10296.

2 Chapter 2

Synthesis of cyclotriguaiacylene derived ligands and the resultant rhenium(I) complexes

2.1 Introduction

Through appending a variety of functional groups to a cyclononatriene core, numerous ligands have previously been prepared. The functionality appended to these ligands includes; carboxylate groups,^{1,2} *N*-oxides,^{2,3} bipyridines⁴ and terpyridines,⁵ however by far the most common is pyridyl.⁶⁻¹¹ In general, most of the prepared ligands were combined with a plethora of metal salts to give rise to self-assembled metallo-structures. The resultant structures vary from the simplest, yet far from the most facile to prepare, M_3L_2 metallocryptophanes¹²⁻¹⁴ and their interlocked congeners, catenanes,^{4,8} through topological knots¹⁰ and rings¹⁵ to large, discrete stellated assemblies comprised of up to eight ligand molecules.^{9,11} The majority of these structures are the result of labile metal salts self-assembling with the desired ligand over the course of weeks, in contrast to the work presented herein which represents a shift towards more kinetically stable metal centres and a move away from self-assembly.

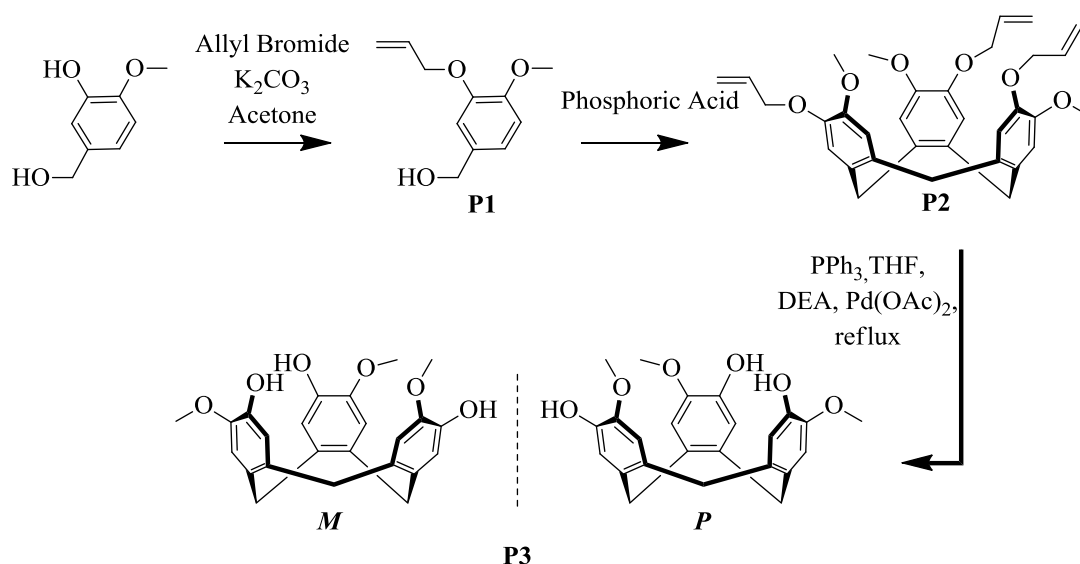
This thesis looks solely at the combination of low-spin d^6 metal ions in combination with cyclotriguaiacylene supramolecular building blocks. As discussed in the introductory chapter, low-spin d^6 metals are some of the most stable, with a large Δ_{oct} , which makes them ideally suited for incorporation into functional materials and devices. The most notable and relevant subset of d^6 containing complexes are those bound to bidentate polypyridyl ligands, as these systems are known to possess luminescent properties. The incorporation of a functional component, in this case luminescent metallotectons, leads to a more directed synthesis, targeting a specific, desired outcome. Rational design of ligand scaffolds and geometrical consideration towards the binding angles of metallotectons allow for a predictable route towards functional metal complexes.

To provide a more complete encapsulation of any ‘internal’ void space, and thus increase the likelihood of host-guest interactions, formation of cryptophane¹⁶⁻²³ and hemi-cryptophane²⁴⁻²⁸ systems have often been employed. Through “capping” the

cavitand species, the distinction between peripheral association and internal host-guest interactions between complex and guest is increased, and through judicious substitution or functionalisation the internal cavity can be made a more attractive prospect to specific potential guest molecules.^{16,29–31}

2.2 Ligand synthesis

The basic scaffold motif upon which all of the discussed ligands are based is the tripodal cavitand cyclotriguaiacylene. This chiral molecule is formed in a well-defined three-step procedure; protection of the phenolic alcohol on either vanillyl or *iso*-vanillyl alcohol, acid-catalysed cyclisation and subsequent de-protection of the phenol group to furnish a racemic mixture of *M* and *P* cyclotriguaiacylene, Scheme 2.1.

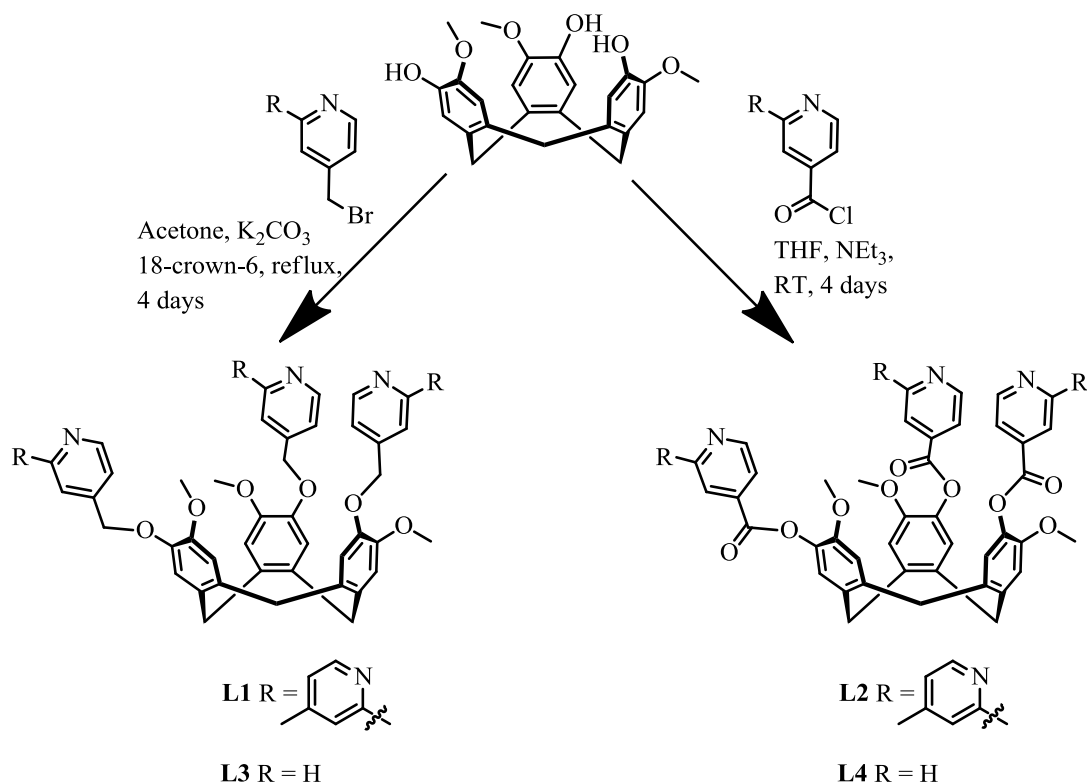


Scheme 2.1: Full synthetic route towards racemic *M* and *P* cyclotriguaiacylene.

Either vanillyl alcohol or the isomeric form *iso*-vanillyl alcohol can be used in this synthesis, as when cyclised into the trimeric ligand motif the alternating methoxy-allylether arrangement simply forms both isomers of the resultant cavitand. The protection of the phenolic group is essentially quantitative and the allylether alcohol can be formed on the tens-of-grams scale. The dry-melt approach to the cyclisation step furnishes **P2** in ~40-50% yield; this is due to solidification of the product over the course of the reaction. Palladium catalysed de-protection of the allylic groups relies on the *in situ* formation of palladium *tetrakis*-triphenylphosphine to give **P3** in

>70% yields. Cyclotriguaiacylene itself is always formed as a racemic mixture, and therefore all the subsequent ligands formed from **P3** are also racemic.

The tripodal cyclotriguaiacylene derived ligands employed in this thesis were synthesised by literature,³² or modified literature,^{4,11} procedures, except for the novel **L2**. The general procedure can be split into two categories; the synthetic route towards ether-linked ligands systems **L1/L3** and the route towards ester-linked systems **L2/L4**.



Scheme 2.2: General synthetic route towards L1-L4.

The reaction of 4-methyl-2,2'-bipyridine-4'-carbonylchloride or *iso*-nicotinoyl chloride hydrochloride and cyclotriguaiacylene, in anhydrous THF in the presence of triethylamine base furnished pure **L2** and **L4** respectively in yields >80%.

The bipyridyl components of both **L1** and **L2** were synthesised from the readily available 4,4'-dimethyl-2,2'-bipyridine. Selenium dioxide was employed to furnish 4-methyl-4'-formyl-2,2'-bipyridine, from which the hydroxymethyl appended **L1** precursor and the carboxylic acid appended **L2** precursor can both be formed. The synthesised 2,2'-bipyridyl-4-methyl-4'-carboxylic acid precursor was converted to the acyl chloride analogue through reaction with thionyl chloride and subsequently reacted *in situ* as described in Scheme 2.2.

The synthetic route towards **L1** and **L3** was modified slightly from literature procedures; previously forcing conditions of NaH base and anhydrous dimethylformamide solvent were employed under rigorously anaerobic conditions in order to obtain acceptable yields of pure product. The modified procedure requires only K_2CO_3 base, in conjunction with a catalytic amount of 18-crown-6, in hydrous acetone solvent. The bromomethyl-containing ligand arm, 4-methyl-2,2'-bipyridine-4'-bromomethyl or 4-bromomethylpyridine hydrobromide, was added in a single portion and immediately gave a dark brown colour to the solution, however over a period of days the solution mixture bleached to leave a pale orange tinge. The remaining solvent was removed *in vacuo*, and the resultant residue extracted with chloroform before drying with $MgSO_4$. The chloroform solution was then concentrated and the desired ligands isolated through precipitation with excess methanol and filtration. The ethereal **L1** and **L3** were reliably furnished in >75% yields, giving identical analytical characterisation as previously reported.^{4,11}

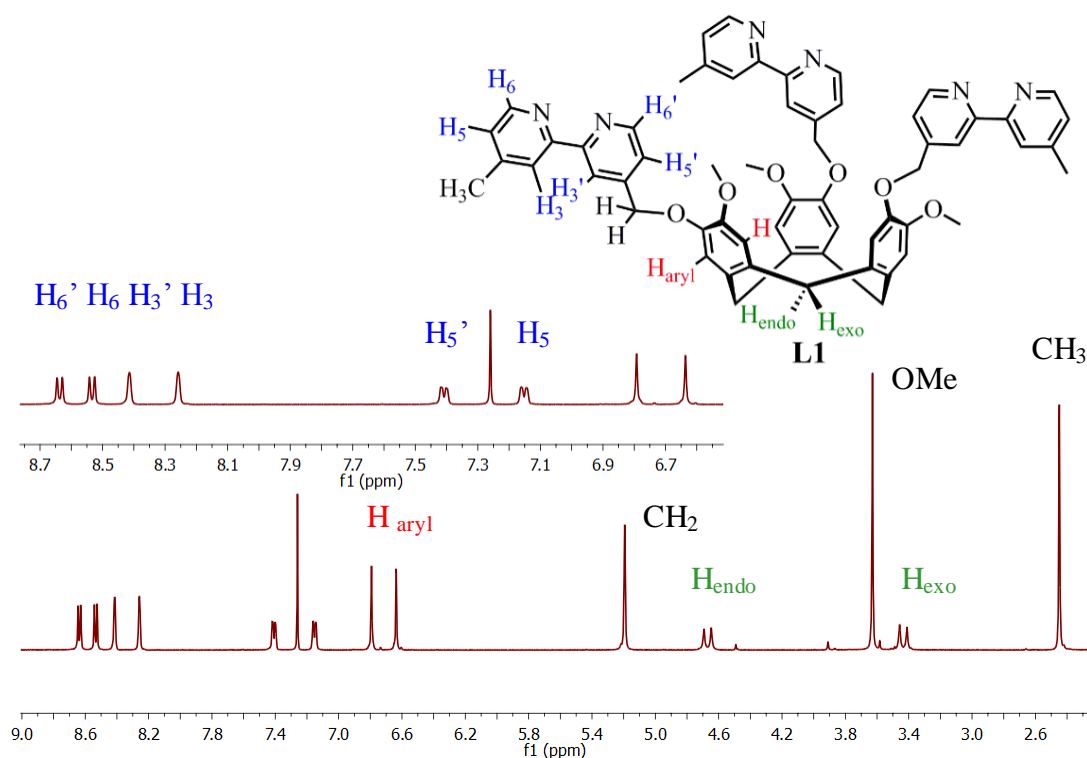


Figure 2.1: Interpreted 1H NMR spectrum of **L1** in $CDCl_3$ solvent.

Precise proton assignments were based on 1H - 1H COSY NMR spectra, where correlations between the H' -bearing ring and the CH_2 of the ethereal linking group can be seen, as well as correlations between the protons on the other pyridyl ring and

the protons on the methyl group in the 4 position. The diastereotopic *endo* and *exo* protons of the methylene bridge are also visible, and diagnostic of clean tri-substituted ligand formation.

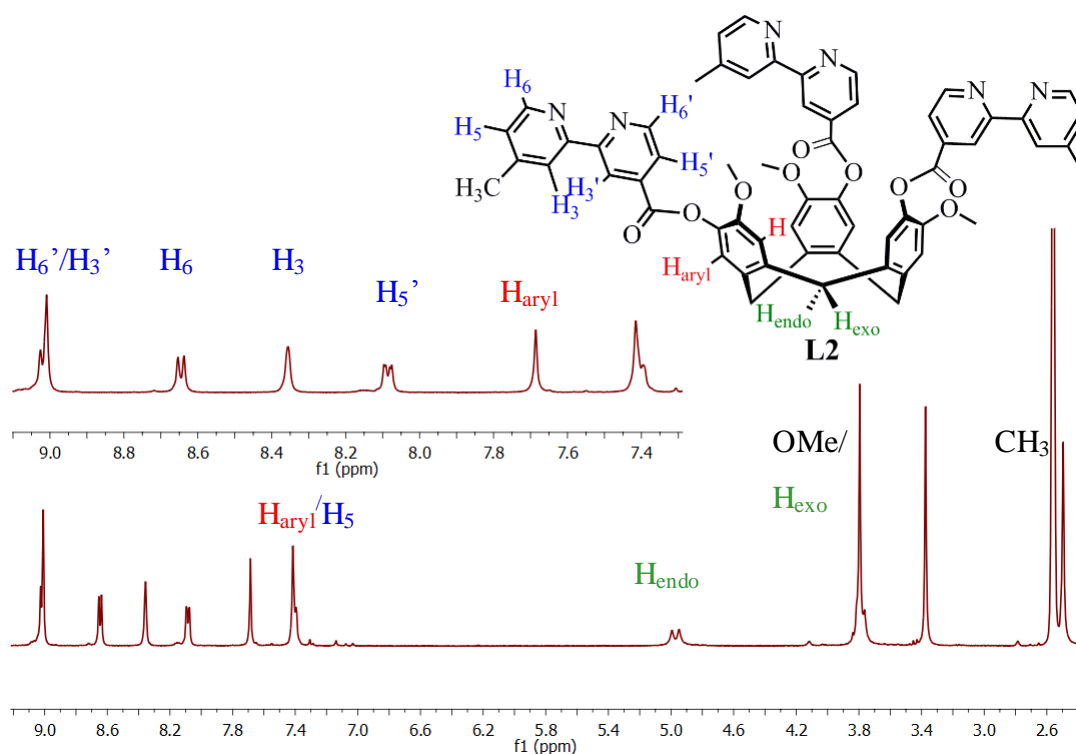


Figure 2.2: Interpreted ^1H NMR spectrum of **L2 in d_6 -DMSO.**

Again, ^1H - ^1H COSY NMR spectra, Figure 2.3, were used to assign the aromatic bipyridyl protons. **L2** shows overlap of the *exo* proton peak with the peak belonging to the methoxy group; however the total integration of the broad peak amounts to the correct 4H.

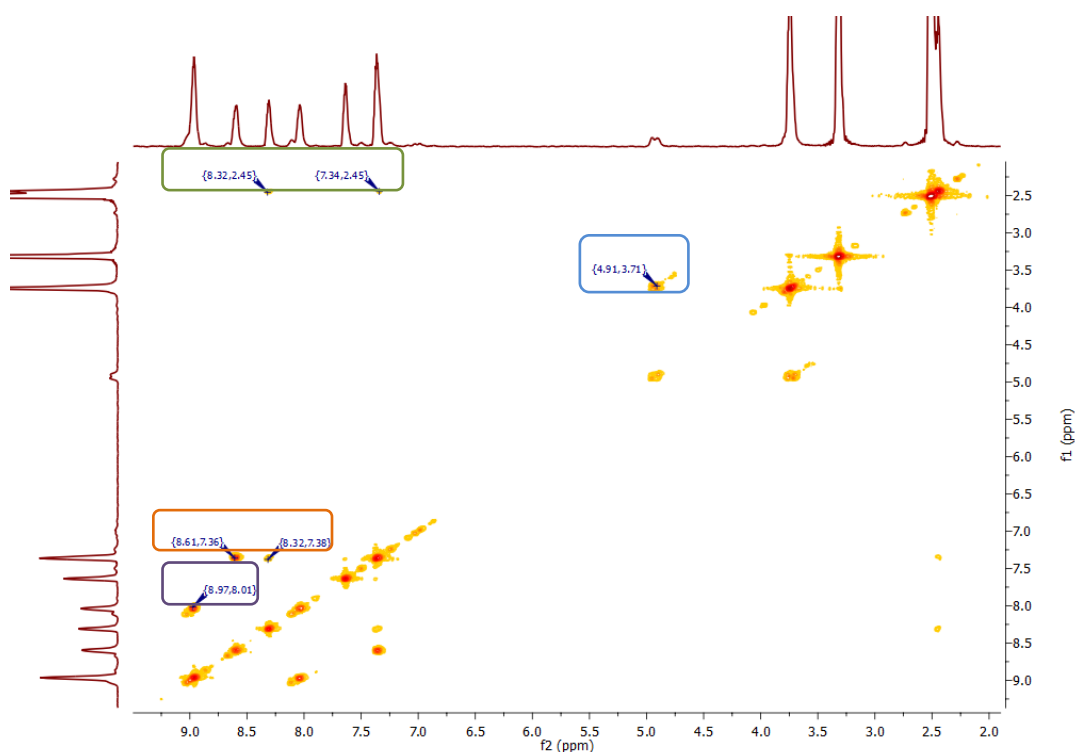


Figure 2.3 : Interpreted ^1H - ^1H COSY NMR spectrum of L2, with pertinent coupling highlighted.

Coupling between the *endo/exo* methylene bridge protons can be seen, highlighted in the blue box, confirming the presence of the *exo* protons underneath the larger peak belonging to the protons of the methoxy group at 3.7 ppm. The coupling between the methyl protons in the 4 position of the bipyridine arm at 2.4 ppm, and the adjacent H^3 and H^5 are highlighted in the green box, allowing discrimination between protons on the two inequivalent pyridyl rings making up the bipyridyl moiety. The coupling between H^5 and H^3/H^6 , as highlighted in the orange box, confirms the presence of H^5 underneath the peak assigned to the aryl CTG proton at 7.3 ppm. The analogous coupling between H^5 at 8.0 ppm and the overlapping H^6/H^3 at 8.9 ppm is shown in the purple box, again confirming the presence of both peaks and the corresponding assignments.

The novel ligand **L2** was fully characterised, with the HR ESI-MS, Figure 2.4, displaying peaks at 997, 499 and 333 m/z , assigned to the mono-, bis- and tris-protonated **L2**. The IR spectrum of **L2** also exhibits a strong ester carbonyl stretch at $\sim 1750\text{ cm}^{-1}$, as well as strong C-O stretches at ~ 1170 and 1280 cm^{-1} .

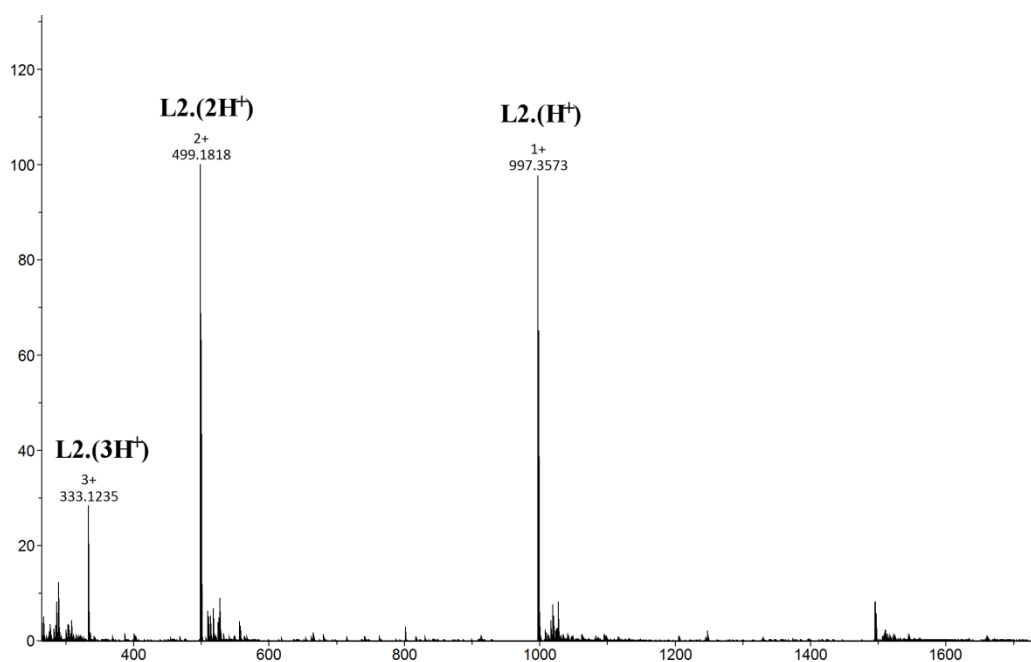
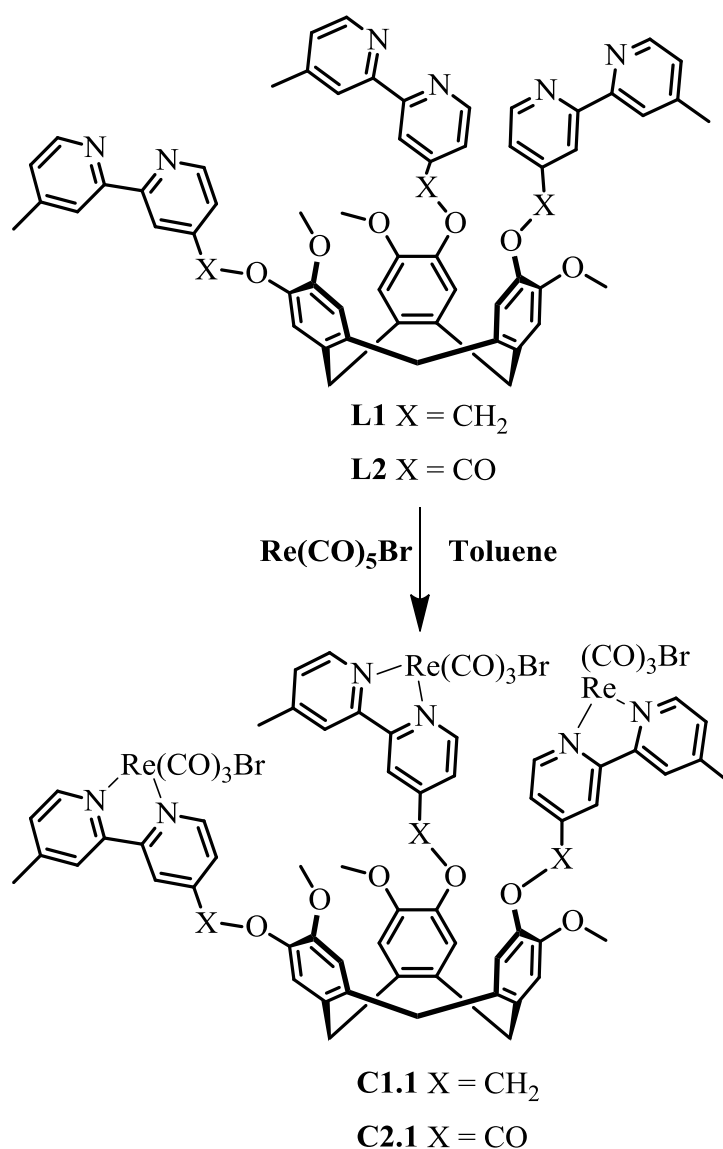


Figure 2.4 : Assigned HR ESI-MS of L2.

The metal complexes resulting from **L1** and **L2** will be discussed in Chapters 2-5. The supramolecular assemblies formed from **L3** and **L4** will be discussed in Chapters 5-6.

2.3 Rhenium(I) complexes of L1 and L2

The initial reasoning behind the synthesis of **L1** and **L2** was to mimic the reactivity of conventional mono-nuclear bipyridine chemistry to form complexes with luminescent low-spin d^6 metal centres. The first metal explored was rhenium(I) in the form of the rhenium pentacarbonyl bromide, which can be easily synthesised from the commercially available dirheniumdecarbonyl.



Scheme 2.3: General synthetic route towards C1.1 and C2.1.

Following generally analogous synthetic procedures to the mono-nuclear systems; namely suspending **L1/L2** in toluene in the presence of 3.1 equivalents of rhenium pentacarbonyl bromide and heating to reflux for 12 hours, both **C1.1** and **C2.1** were furnished in >80% yields as bright yellow powders. **C1.1** is soluble in a range of solvents, including acetonitrile, nitromethane and DMSO, whilst the more rigid **C2.1** is far less soluble, with DMSO being the main solvent employed throughout characterisation.

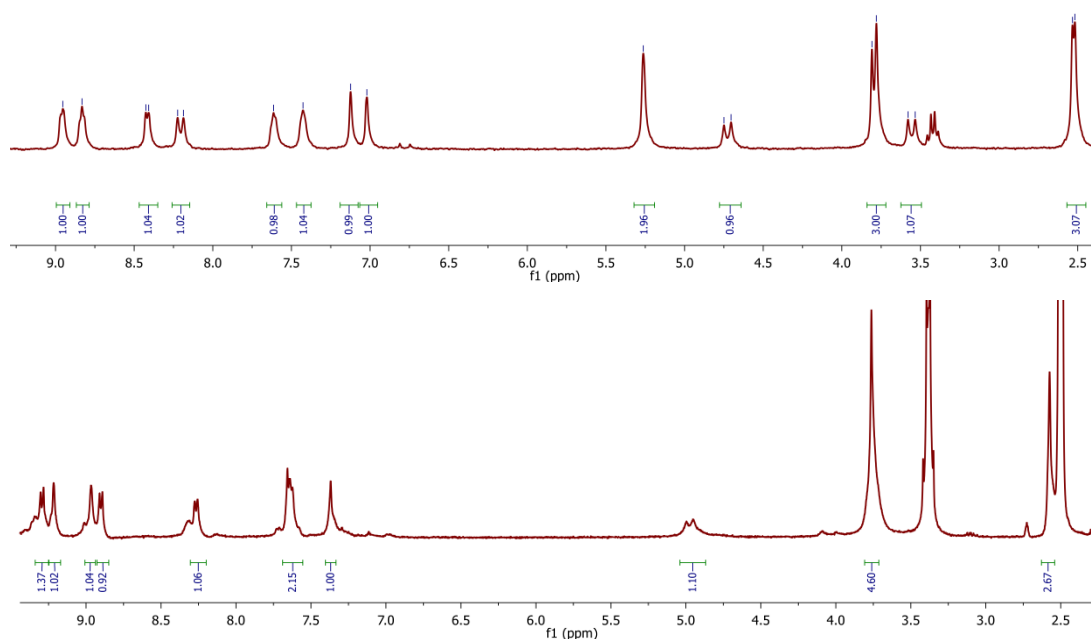


Figure 2.5: ^1H NMR spectra of **C1.1** in $d_3\text{-MeCN}$ (top) and **C2.1** in $d_6\text{-DMSO}/d_3\text{-MeCN}$ (bottom).

As evidenced in Figure 2.5 the ^1H NMR spectra of the resultant complexes are relatively similar to those of the free ligands **L1** and **L2**, however there is a degree of peak broadening due to the reduced rotation around the ether/ester linkage respectively. This broadening can be seen to a greater degree in **C2.1** which bears the more rigid ester linking group between the cyclononatriene core and the bipyridyl arm. The precise proton assignments of **C1.1** and **C2.1** were determined through 2D ^1H - ^1H COSY NMR spectroscopy (see ESI chapter S2), whereby coupling between protons adjacent to the methyl group and those adjacent to the methyl ether linking group can be distinguished.

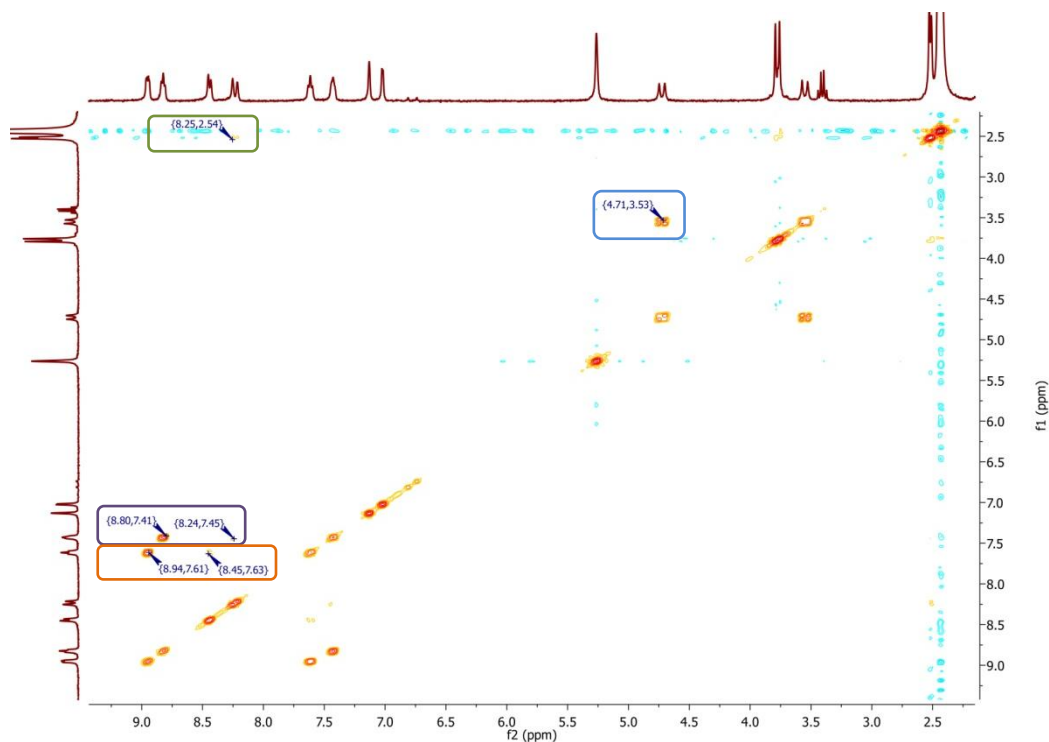


Figure 2.6: Assigned ^1H - ^1H COSY NMR spectrum of **C1.1**.

The ^1H - ^1H COSY NMR spectrum of **C1.1** is shown in Figure 2.6, where coupling between the *endo/exo* protons is highlighted in the blue box. The cross-peak highlighted in green corresponds to coupling between the methyl protons on the bipyridine arm at 2.5 ppm and the adjacent H^3 peak at 8.2 ppm, thus allowing discrimination between the two pyridyl rings on the bipyridine arm. The cross-peak in purple shows the strong coupling between H^5 at 7.4 ppm and H^6 at 8.8 ppm, and to a lesser extent between H^5 and H^3 at 8.2 ppm. The analogous coupling between $\text{H}^{5'}$ at 7.6 ppm and $\text{H}^{6'}$ at 8.9 ppm, and thus $\text{H}^{5'}$ and $\text{H}^{3'}$ at 8.4 ppm can be seen highlighted in orange.

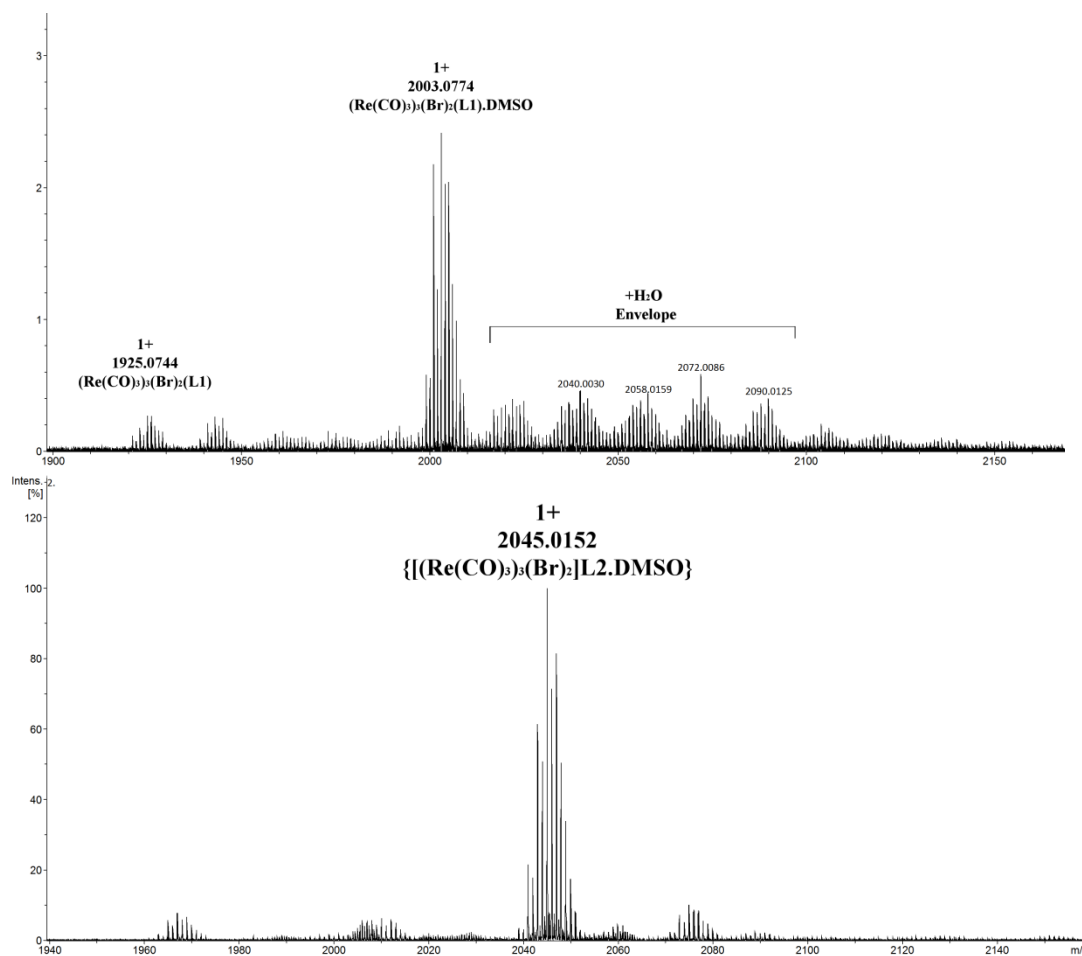
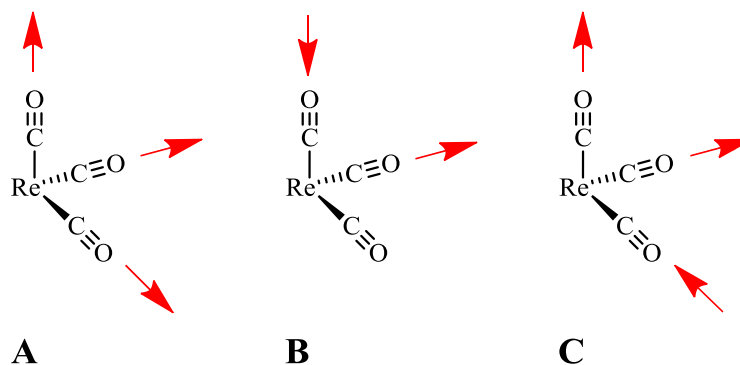


Figure 2.7: HR ESI-MS of C1.1 (top) and C2.1 (bottom) showing the expected rhenium isotope pattern.

Due to the strongly coordinated bromide counter-ions, both species did not ionise well, however assignable peaks could be located. The expected peak at 1925 m/z assigned to $\{[(\text{Re}(\text{CO})_3)_3(\text{Br})_2]\mathbf{L1}\}^+$ was visible, however the main peak observed was assigned to $\{[(\text{Re}(\text{CO})_3)_3(\text{Br})_2]\mathbf{L1}\}^+\cdot\text{DMSO}$ at 2003 m/z ; **C1.1** having lost one bromide counter-ion and gained one associated DMSO solvent molecule. There is also a clear H_2O envelope; whereby a succession of water molecules are ionised along with **C1.1**. **C2.1** can be seen at the expected molecular mass of 2045 m/z , however, once again this is due to the loss of one bromide anion and the gain of one molecule of DMSO solvent, $\{[(\text{Re}(\text{CO})_3)_3(\text{Br})_2]\mathbf{L2}\}^+\cdot\text{DMSO}$. The presence of a mass peak at the expected $[\text{M}+\text{H}^+]$ value is coincidental, due to the equivalent mass of one bromine atom and one DMSO molecule, isotope pattern analysis confirms the presence of only two bromine atoms in the molecular ion peak in each case.

The IR spectra of both species show the requisite strong C≡O stretches at 2017/1883 cm⁻¹ and 2029/1889 cm⁻¹ respectively. *Fac*-tricarbonyl species possess highly characteristic IR stretches due to the geometrically locked *facial* arrangement around the metal centre.



Scheme 2.4: Symmetric and un-symmetric stretches of C≡O ligands, with respect to their IR stretching bands, A) Symmetric B)/C) un-symmetric stretches.

Scheme 2.4 shows the symmetric stretch, A), which is assigned to the higher frequency band at 2017 and 2029 cm⁻¹ in **C1.1** and **C2.1** respectively, whereas the un-symmetric stretches B and C, which are often seen as broad overlapping bands, are assigned to the broad bands at 1883 and 1889 cm⁻¹.^{33,34} The fundamental organic IR stretches are also exhibited by both **C1.1** and **C2.1**, displaying C=C stretches at 1616 and 1618 cm⁻¹ and C-O stretches at 1180 and 1178 cm⁻¹ respectively. **C2.1** also displays an additional stretch at 1748 cm⁻¹, assigned as the organic ester carbonyl. Microanalysis of both complexes confirmed purity.

2.4 Photophysical properties of **C1.1** and **C2.1**

Despite the exceptionally similar molecular structure of **C1.1** and **C2.1**, the photophysical properties are markedly different. Due to the low solubility of **C2.1** in most common laboratory solvents, DMSO was used for all photophysical characterisation to allow for reliable comparison between both complexes without any undesired solvatochromic shifts.

The UV-visible spectra of both complexes were first obtained, in DMSO. Both **C1.1** and **C2.1** show high energy intra-ligand transitions, with smaller, broader shoulders at around 300 nm, tentatively ascribed to MLCT absorption. There is also significant absorption between 350-450 nm, although slightly more so in **C1.1**.

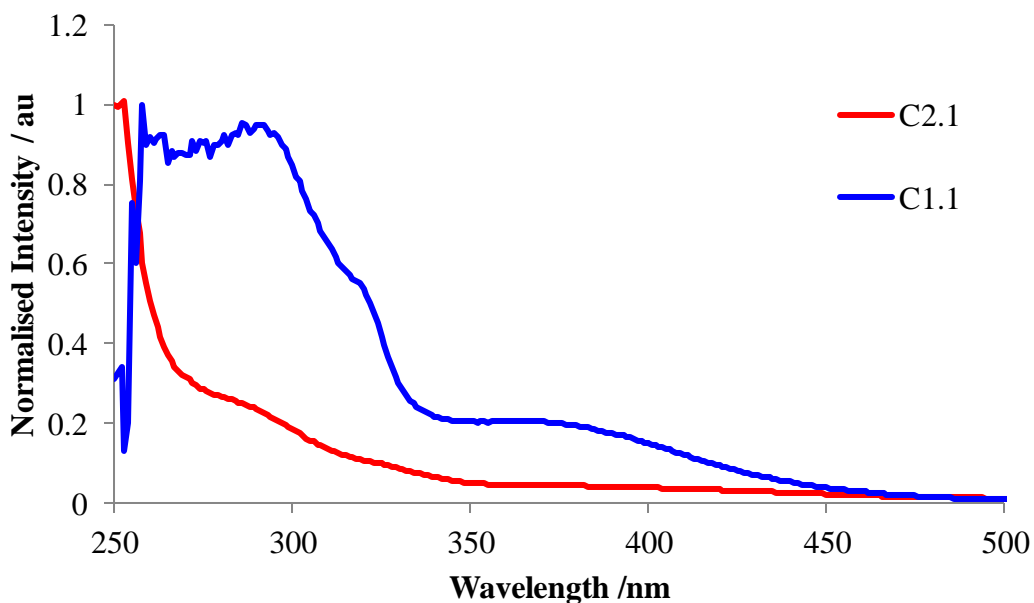
UV-Vis spectra of C1.1 and C2.1 in DMSO

Figure 2.8: Overlaid UV-Visible spectra of C1.1 and C2.1 in DMSO solution.

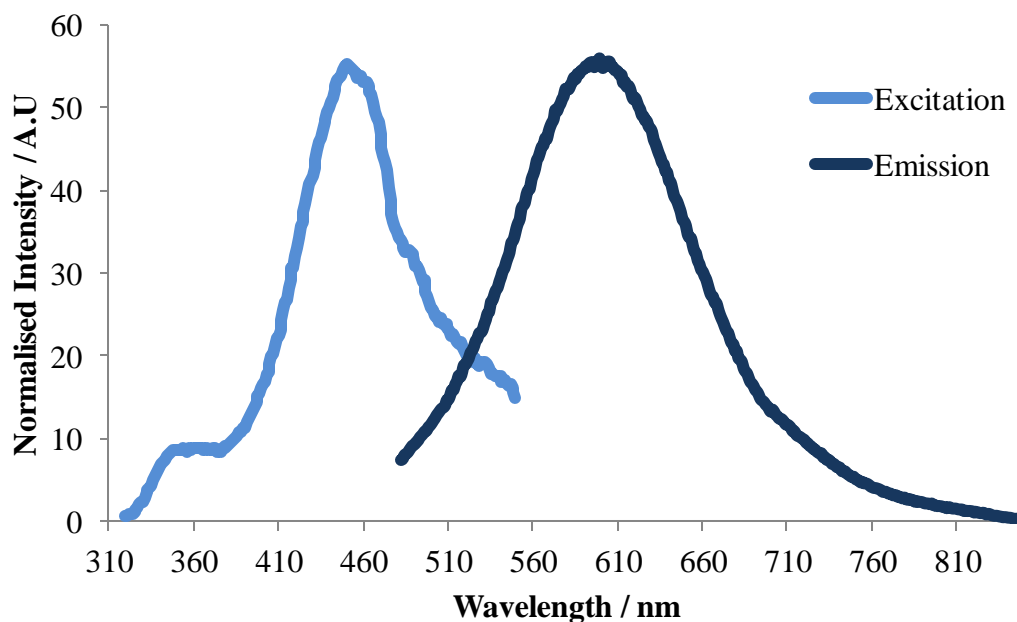
2.4.1 Photophysical properties of C1.1**Excitation and Emission of C1.1**

Figure 2.9: Overlaid excitation and emission profiles of C1.1 in DMSO.

C1.1 possesses an emission maximum of 598 nm and an excitation maximum of 451 nm. The emission profile is similar to many mono-nuclear $\text{Re}(\text{CO})_3\text{Br}(\text{N}^{\wedge}\text{N})$ systems in general appearance;³⁵⁻³⁹ the broad unstructured emission is characteristic of $^3\text{MLCT}$ between the $\text{Re-d}\pi$ centre and the π^* -cloud of the bis-imine ligand. The extent of the emission above 700 nm is noteworthy however, as any emission in this region is verging on infrared. Infrared emission is particularly favoured in biomedical applications due to the deep tissue penetration provided in combination with lower energy wavelengths being far less damaging to the surrounding cells.⁴⁰ The relatively low energy emission is concomitant with a decrease in excitation energy, again moving away from the necessity of using damaging UV light.

The lifetime of **C1.1** is remarkably long at 467 ns, which would make this complex ideal for any biomedical imaging applications in terms of time-gated image collection. There are many endogenous fluorophores present in human body, such as large conjugated organic molecules and DNA itself, therefore in confocal fluorescence microscopy the administered phosphorescent complex is excited and the image collection delayed by ~ 10 ns to allow any quickly decaying fluorescence to die out before the collection is initiated. A long luminescent lifetime such as **C1.1** is thus ideal for this application.⁴¹⁻⁴⁴

2.4.2 Photophysical properties of C2.1

Excitation and Emission of C2.1

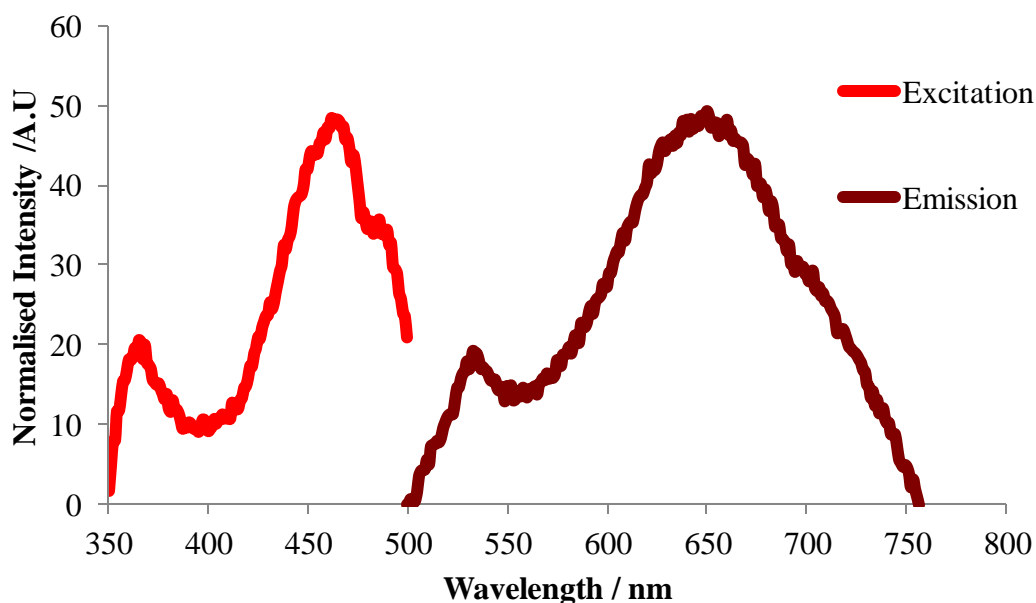


Figure 2.10: Overlaid excitation and emission profiles of C2.1 in DMSO.

C2.1 displays markedly different excitation and emission profiles to the ether congener **C1.1**, exhibiting dual bands in both excitation and emission. The emission maxima are situated at 533 and 650 nm, with the corresponding excitation maxima at 365 and 460 nm. This profile suggests two distinct but complementary processes are occurring at the same time, with the broad emission band at 650 nm most likely due to $^3\text{MLCT}$, analogous to that seen in **C1.1**. The MLCT emission displays a bathochromic shift with respect to **C1.1**, with the increased conjugation between metal and ligand due to the ester linkage probably playing a significant role.

Despite the structural similarity to **C1.1**, **C2.1** displays an average lifetime over 25 times shorter at 19 ns. This is made up of two distinct lifetime components as measured through time resolved emission spectroscopy (TRES), one belonging to each emission band; the high energy band has a lifetime of 3 ns, whereas the lifetime of the lower energy band is 21 ns. Both of these lifetimes are much shorter than **C1.1** (467 ns), and suggest that the ester linked complex must possess a pathway towards non-radiative decay, leading to the shorter lifetimes seen. Whilst the shorter lifetimes are less desirable from a time-gated standpoint, the bathochromic shift towards the infra-red region is extremely favourable.

2.4.3 Comparison of C1.1 and C2.1

Regardless of the almost identical molecular structure of **C1.1** and **C1.2**, the photophysics of the two systems are remarkably different. **C2.1** is red-shifted with respect to both the excitation and emission, showing markedly different dual-emission, whereas **C1.1** shows single emission peaks with slight hypsochromic shifts. Whilst the high energy emission peak in **C2.1** could be due to a highly emissive impurity in the solution, further work suggests that the two peaks are related, as by changing the excitation wavelength, the intensity of each peak can be favoured. This relationship suggests that the two emissive processes are occurring in the same complex, whereby different wavelength excitation preferentially favours one of the transitions.

One of the most notable features of these two complexes is the level of susceptibility they display to relatively minor structural alterations; changing an ether linkage to an ester produces a Stokes shift of over 50 nm. This sensitivity suggests that further alterations, be it to the linking group between bipyridyl and cyclononatriene core or functionalisation on the bipyridine arm, could produce dramatic shifts in the resultant emission.

2.5 Crystallographic analysis of L1 and C1.1

2.5.1 Solid state structure of L1

Single crystals of **L1**•[(EtO)₂] were obtained through the diffusion of diethyl ether vapours into a solution of **L1** in chloroform. The resultant needles were of poor quality and did not diffract to high angles. The structure was solved in the *Pbna* space group, giving the asymmetric unit (ASU) as one molecule of **L1** and one molecule of diethyl ether anti-solvent. The ether solvent is well resolved due to its trapped position in this clathrate arrangement. The ligand molecules pack bowl-in-bowl as alternating enantiomers to form racemic columns propagating through the crystal lattice. Each column is surrounded by four closest neighbours facing in the opposing direction.

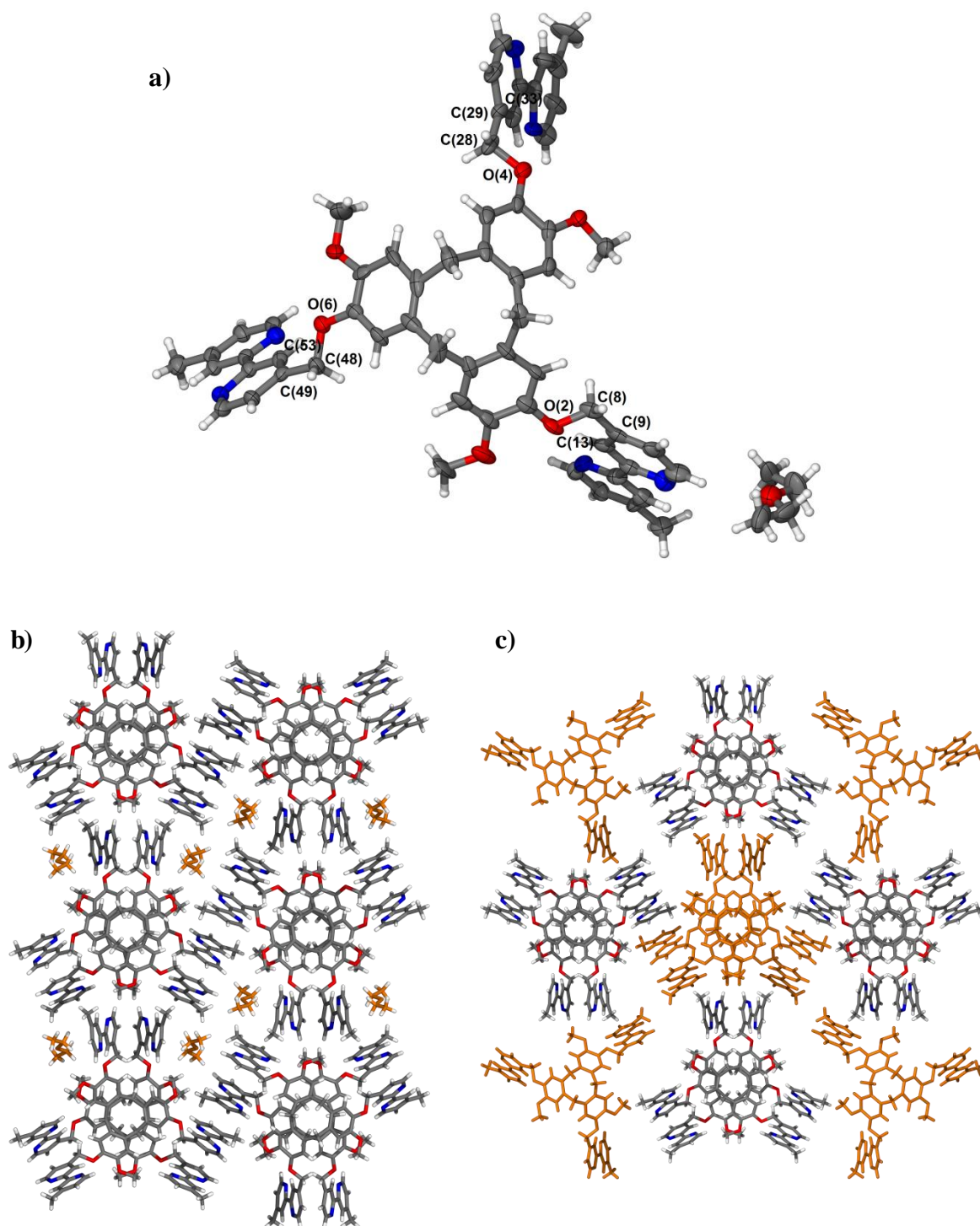


Figure 2.11: a) Labeled ASU of $L1 \cdot [(Et)_2O]$ anisotropic displacement parameters set at 30% b) clathrate structure of the trapped diethyl ether anti-solvent, shown in orange c) head-up/head-down arrangement of the ligand stacks.

Figure 2.11 shows the asymmetric unit of $L1 \cdot [(Et)_2O]$ looking down the crystallographic a axis. Whilst solution state data gives rise to C_3 symmetry, the

SCXRD data shows that **L1** does not present in a C_3 symmetric space group in the solid state; each bipyridyl arm is twisted with respect to the cyclononatriene core by between 48 and 53°, leading to breakdown of the symmetry through the centre of the cavitand. The bipyridyl arm O6-C48-C49-C53 possesses a torsion angle of 53.5°, O2-C8-C9-C13 an angle of 50.9° and O4-C28-C29-C33 an angle of 48.9°. As expected, the two nitrogen atoms in each bipyridyl arm twist away from each other, to relieve any strain caused by the interactions of their lone pairs

2.5.2 Solid state structure of **C1.1**

X-ray quality crystals of **C1.1**•*n*[MeNO₂] were achieved through the slow diffusion of diethyl ether vapours into a concentrated solution of **C1.1** in nitromethane solvent. The structure solved in the $R\bar{3}$ space group; trigonal space groups of this are not uncommon for these C_3 symmetric ligand scaffolds.^{4,7,8,11,32,45–47} The asymmetric unit contains one third of each enantiomeric M_3L unit and one nitromethane solvent molecule.

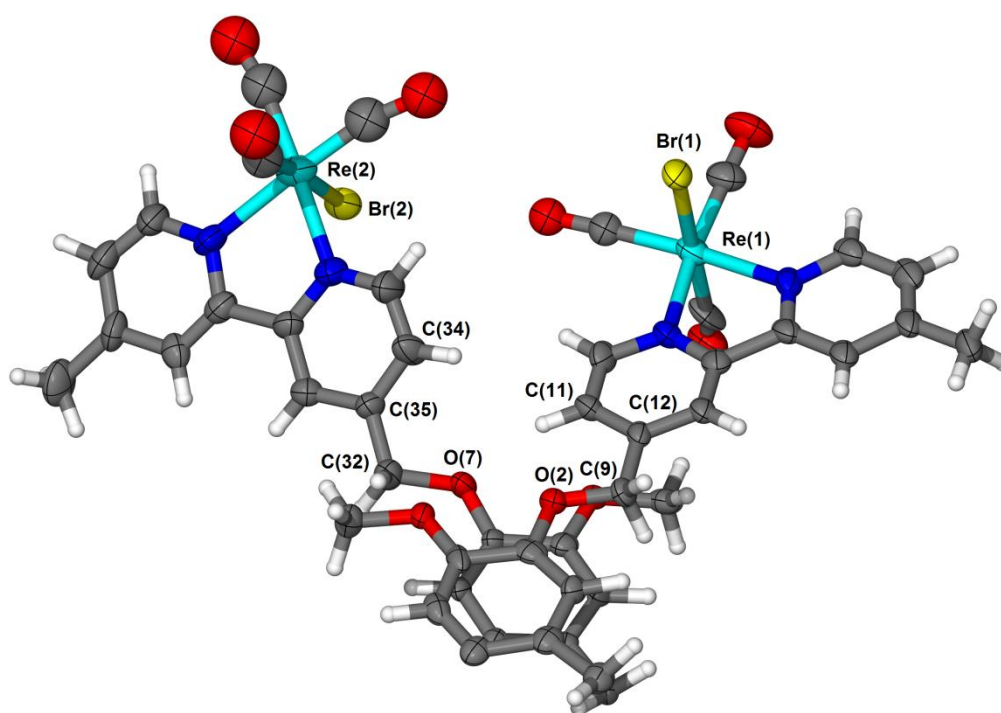


Figure 2.12: ASU of C1.1, ellipsoids shown at 30% probability, nitromethane solvent excluded for clarity.

As expected, the coordination environment around the rhenium centres is of octahedral geometry, displaying minor distortion from idealised angles due to the

restricted bite angle of the bipyridine ligand. The restriction of the bidentate ligand leads to bite angles of 74.8° (N4-Re2-N3) and 73.1° (N1-Re1-N2), giving a concomitant increase in N-Re-C bond angles of $102\text{-}103^\circ$ around Re2 and 98° around Re1, due to the *facial* arrangement of C \equiv O ligands. The coordinated bromide anion completes the opposing *facial* arrangement in collaboration with the bipyridine moiety.

The *M* enantiomer is that containing Re1, and thus the Re2 containing fragment belongs to the *P* enantiomer. The two enantiomers stack ‘bowl-in-bowl’ as a racemic pair of molecules, however the distance between the two central benzene rings of the cyclononatriene core is 4.6 \AA , and thus too long to suggest any $\pi\text{-}\pi$ interactions. The three carbonyl ligands on the *P* enantiomer were refined isotropically as well as one on the *M* isomer. The two enantiomeric fragments are not crystallographically equivalent, with each isomer displaying a markedly different torsion angle through the methyl ether linkage; *M* (O2-C9-C12-C11 = 11.5°) versus *P* (O7-C32-C35-C34 = 41.8°). The *M* isomer displays an almost planar torsion angle with respect to the benzene ring of the cavitand core, whilst the *P* isomer is strongly distorted, to allow the Re(CO) $_3$ Br unit to twist outwards away from the centre of the cavitand, presumably to relieve any steric stress between neighbouring carbonyl groups within the enantiomeric pair stack.

Re1-Br1	2.5974(19)	Re2-Br2	2.587(2)
Re1-N1	2.176(11)	Re2-N3	2.170(13)
Re1-N2	2.209(11)	Re2-N4	2.221(14)
Re1-C21	1.86(2)	Re2-C44	1.87(3)
Re1-C22	1.862(16)	Re2-C45	1.74(3)
Re1-C23	2.04(2)	Re2-C46	1.90(3)
N1-Re1-N2	73.4(5)	N3-Re2-N4	74.9(5)
O2-C9-C12-C11	11.5	O7-C32-C35-C34	41.8

Table 2.1: Selected bond lengths (Å) and angles (°) from the crystal structure of *C1.1*.

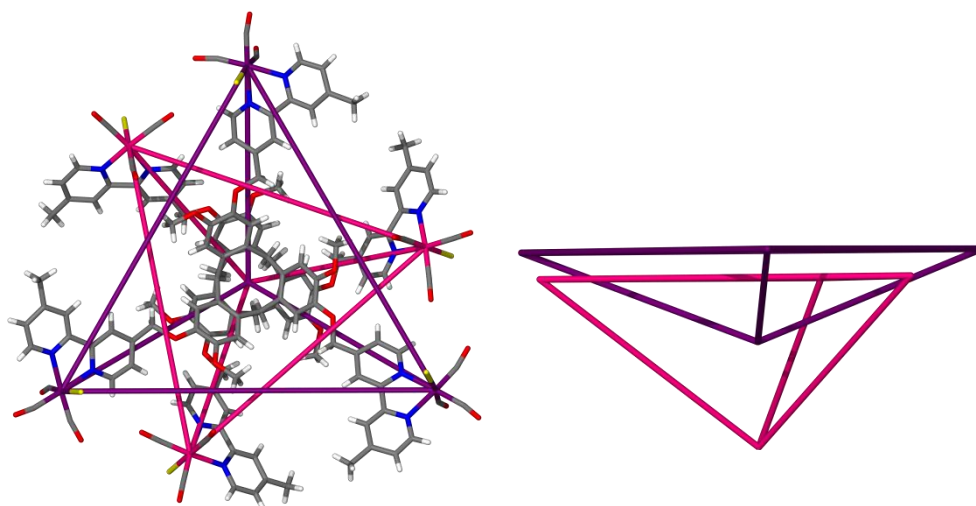


Figure 2.13: a) viewing the enantiomeric pair-stack looking down the crystallographic *c* axis b) the difference in the triangular pyramid described by each enantiomer.

The inequivalence between the two M_3L enantiomers can also be seen in the relative depths of the bowls described by the three metal centres and a centroid taken from the centre of the methylene bridge carbons.

Enantiomer	Bowl depth [‡]	Re-Re
<i>M</i>	7.584	17.396
<i>P</i>	4.105	20.781

Table 2.2: selected inter-atomic and topological distances of *C1.1* in Å, [‡] = measured from the centre of the triangle described by the three *Re* centres and the centre of the cyclonatriene core.

The *M* isomer, shown by the pink triangular pyramid, has a much deeper bowl with an intra-metallic distance of 17.396 Å, compared to the *P* isomer describing a much shallower bowl, but correspondingly longer intra-metallic distances. The *P* enantiomer has thus been compressed in the *c* axis.

The enantiomeric stack-pairs propagate out into alternating infinite up-down zigzag sheets. As demonstrated in Figure 2.14, the enantiomeric pairs tessellate together through stacking of complementary adjacent bipyridine arms in an *MM-PP* arrangement. However, at 4.2-4.9 Å apart the interaction cannot be called true π - π stacking.

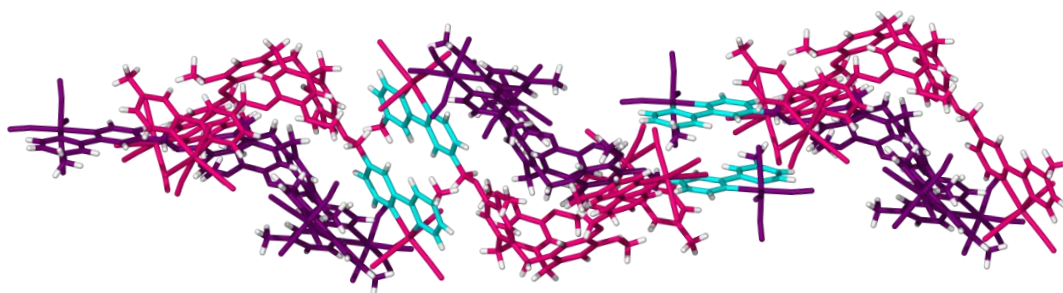


Figure 2.14: Packing structure of *C1.1* showing the enantiomeric pairs, *M* and *P* shown in pink and purple respectively, with stacking interactions shown in cyan.

This arrangement leads to layers of 2D zigzag sheets, however due to the ill-fitting nature of the separate sheets there is significant space between the layers leading to over 40% void space throughout the crystal lattice, as calculated through PLATON.⁴⁸

2.6 Towards heteroleptic ambidentate metallocryptophanes

The rationale behind appending luminescent functionality to a supramolecular building block was first as a proof of principle exercise; that the presence of the central cavitated scaffold did not negatively impact the emission properties, and secondly in an effort towards a functional molecule; working as a luminescent sensor in a host-guest capacity. Whilst there are examples of large spherical guests, such as fullerenes,⁴⁹ sitting in the open hydrophobic cavity, to provide more of a driving force for encapsulation a common method is to “cap” the open bowl to form

a hemi-cryptophane,^{22,24,27,31,50–52} cryptophane^{19,20,23,53,54} or metallocryptophane,^{12–14} depending on the nature of the “cap”.

It was envisaged that a *tris*-pyridyl donor based off of a central benzene ring could act as the appropriate capping ligand, as initial consideration of *tris*-(2-aminoethyl)amine suggested that the size discrepancy was too large to overcome. However, rather than attempt to form a hemi-cryptophane with a dissimilar tripodal ligand, **L4** was employed to form a metallocryptophane due to the exact size match and ideal binding geometries presented.

From analysis of the SCXRD data of both separate components, **C1.1** and **L4**, the complementarity in size and binding geometries can clearly be seen.

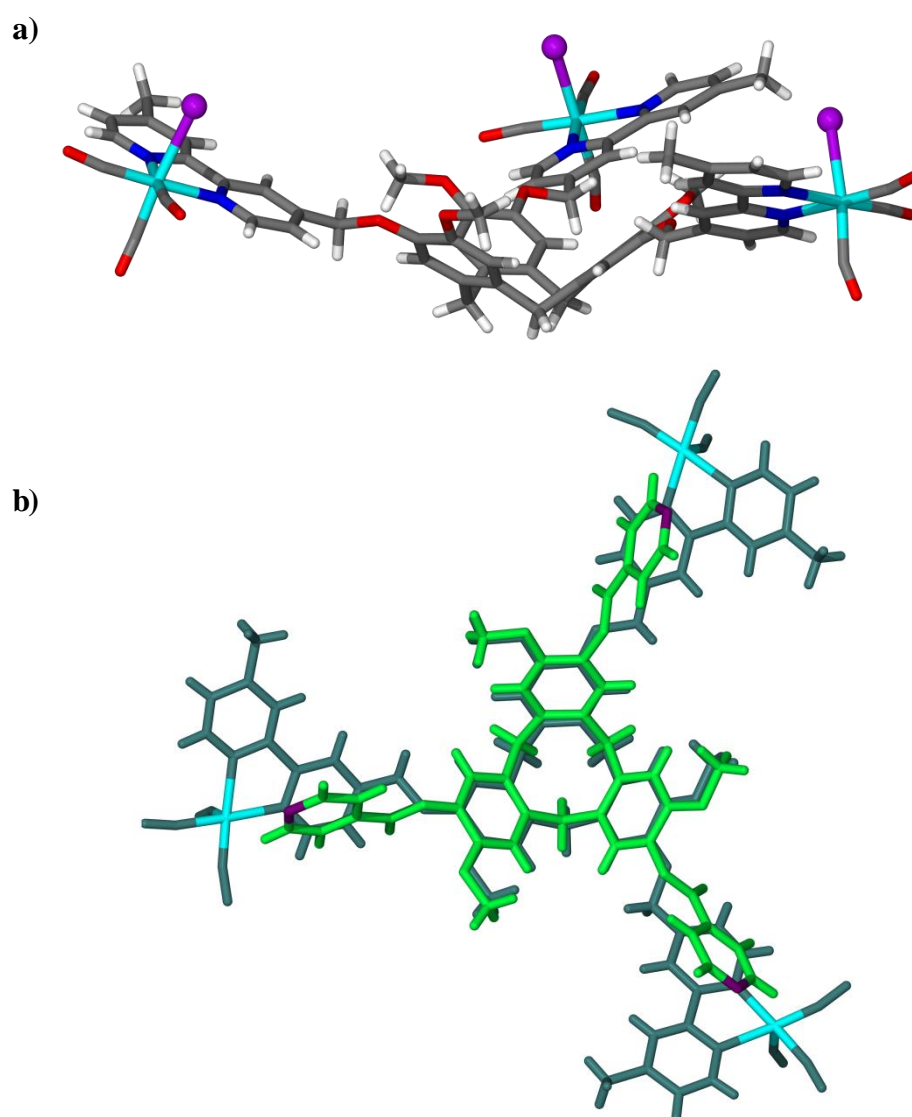


Figure 2.15: a) side-view of **C1.1** highlighting the advantageous positions of the vacant coordination sites, Br atoms shown as spheres b) overlay of **C1.1** (teal) and **L4** (green) highlighting the complementary structural motifs.

Initially the coordinated bromide counter ion on **C1.1** was removed through halide abstraction using silver triflate *in situ*, to generate intermediate **C1.1B** and then combined with a stoichiometric amount of **L4** in non-coordinating nitromethane solvent. **C1.1B** was subjected to HR ESI-MS to confirm the removal of all three bromide counter-ions before use.

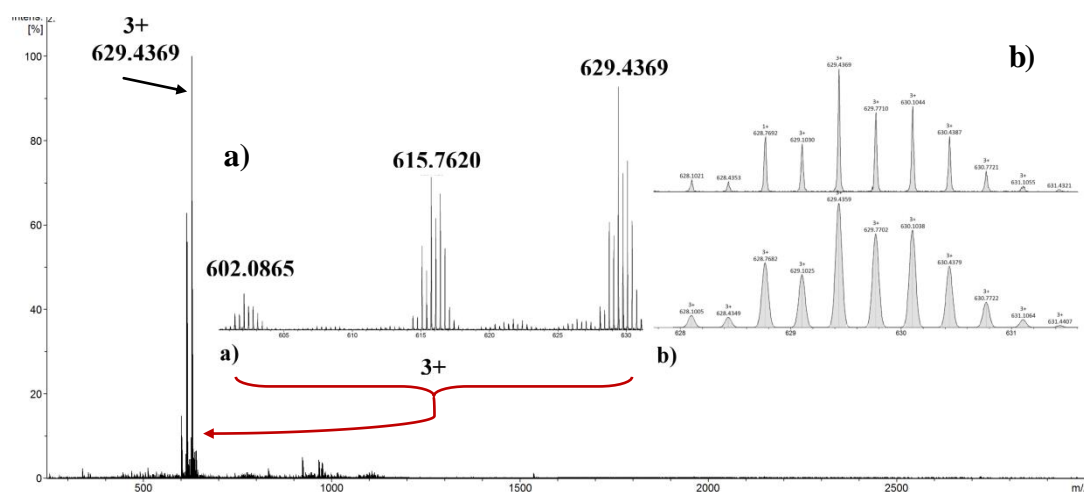
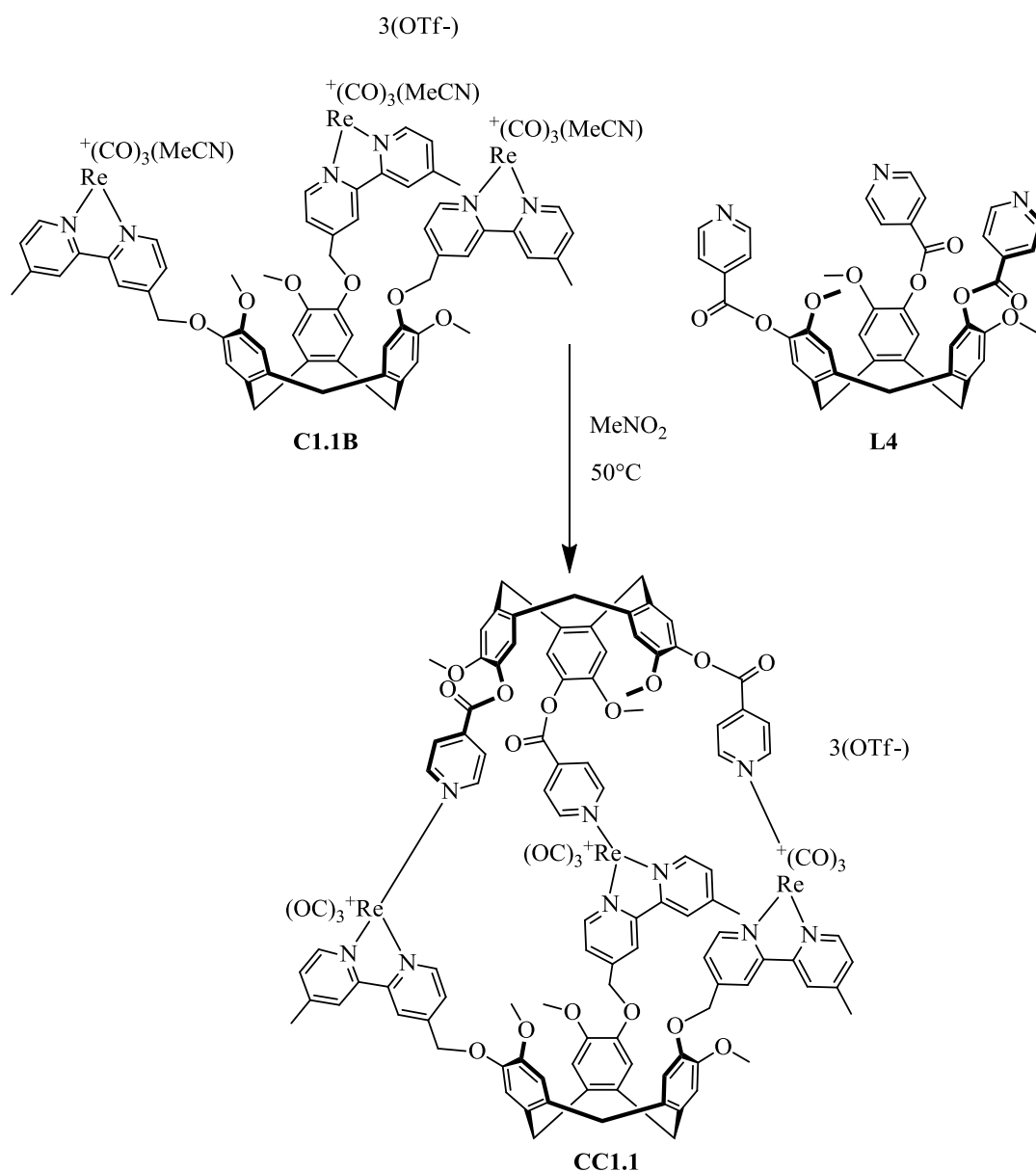


Figure 2.16: HR ESI-MS of **C1.1B** to confirm formation, a) the sequential loss of bound MeCN ligands b) measured (top) and calculated (bottom) isotope pattern of the 3+ peak of **C1.1B**.

Figure 2.16 shows the clean formation of **C1.1B**, with the only appreciable peak at 629 m/z assignable to $\{[\text{Re}(\text{CO})_3(\text{MeCN})_3\text{L1}]\}^{3+}$, the smaller peaks at 615 and 602 m/z are due to sequential loss of previously coordinated acetonitrile. The distinctive isotope pattern of **C1.1B** can be seen inset in Figure 2.16, along with the predicted theoretical pattern.

As shown in Figure 2.15, the positions of the coordinated bromide anions in **C1.1**, and thus the vacant coordination sites in **C1.1B**, are pre-organised into a beneficial arrangement for further binding. The exact size-match of **L4**, due to the cyclononatriene core, means both components are pre-arranged into complementary geometries favouring the formation of the first heteroleptic ambidentate metallocryptophane **CC1.1**



Scheme 2.5: Formation of heteroleptic metallocryptophane CC1.1.

The use of non-coordinating solvent is required to drive the formation of the metallocryptophane, whereby the only by-product of assembly construction is displaced acetonitrile solvent.

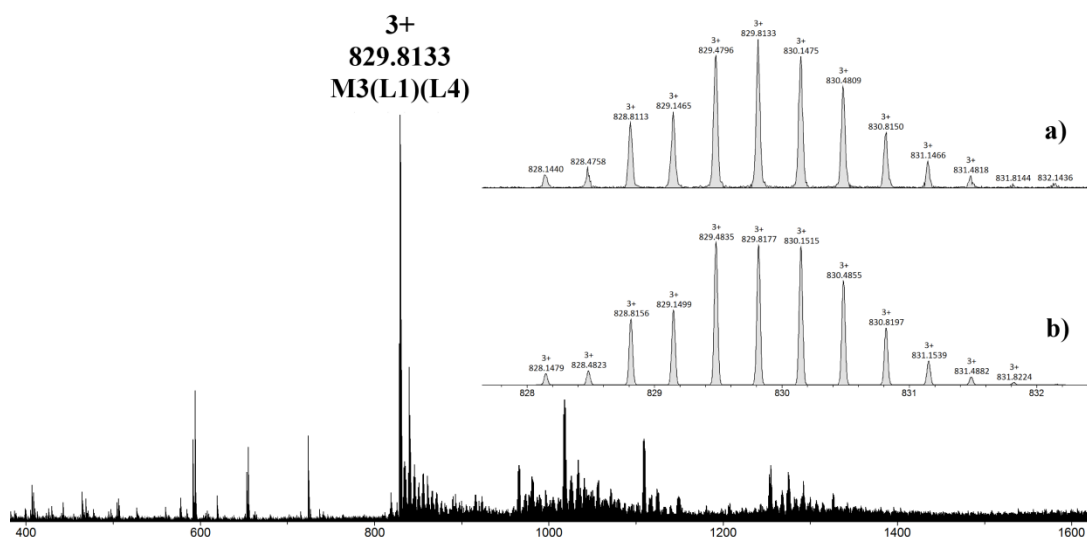


Figure 2.17: HR ESI-MS of CC1.1, seen without non-coordinating triflate anions, $M=[\text{Re}(\text{CO})_3]$, a) measured isotope pattern b) calculated isotope pattern for CC1.1, shown inset.

The main m/z peak visible after twelve hours heating was attributed to the 3+ charge state of CC1.1, flying without the associated non-coordinated triflate counterions. There is some fragmentation into smaller assemblies, as it to be expected. The measured isotope pattern matches exactly with the calculated pattern, shown inset in Figure 2.17, supporting the conclusion that the heteroleptic cage CC1.1 has been formed.

The formation of CC1.1 was followed by ^1H NMR spectroscopy in d_3 -MeNO₂, shown in Figure 2.18.

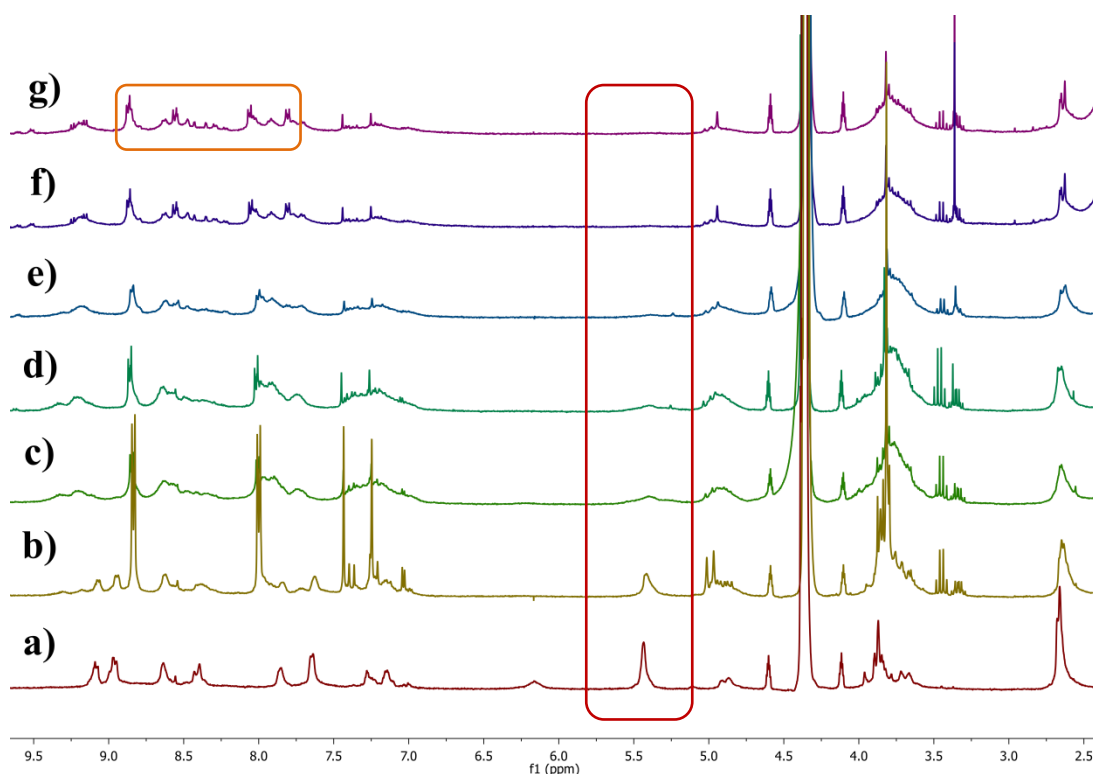


Figure 2.18: Stacked ^1H NMR spectra following the formation of **C1.1** a) **C1.1B** b) after addition of a stoichiometric amount of **L4** c) 4 hrs RT d) 6 hrs e) 8hrs f) 10hrs g) 12hrs.

The dynamic library of species formed immediately after the addition of **L4** leads to a broad spectrum that gradually sharpens up to a degree over time, as the reaction progresses towards a major product. The most significant change observed, highlighted in the red box, is the gradual disappearance of the peak at 5.4 ppm belonging to the ethereal bridging protons. In **C1.1B** the flexibility and free-rotation of the bipyridine arm leads to a relatively sharp singlet. However, as the free-rotation of that arm is restricted due to the formation of a cage species, the geometry becomes locked in place. The peak at 5.4 ppm initially broadens out, as the protons become more and more diastereotopic, and eventually broadens out to infinity. Another point of note is the splitting of the previously equivalent pyridyl protons; in the **L4** both *ortho* protons and both *meta* protons on the pyridyl ring are equivalent, displaying two doublets at 8.7 ppm and 8.1 ppm. However, in the final spectrum **g**), highlighted in the orange box, there are two sets of doublets, suggesting that the pyridyl ring can no longer freely rotate, leading to splitting of the pyridyl proton resonances.

This reaction was conducted on an NMR scale, and thus far attempts to crystallise the resultant heteroleptic ambidentate metallocryptophane have been unsuccessful.

2.7 Conclusions and future direction

The formation of **C1.1** and **C2.1** demonstrate the applicability of combining luminescent motifs with a supramolecular scaffold. The vast difference between the photophysical properties of the two complexes also reveals the sensitivity to structural changes that can be achieved through modulation of not only the basic ligand scaffold, but also through judicious functionalisation throughout the molecule. The degree of conjugation between the metal-binding bipyridine arm and the central cavitand has also been shown to have a profound effect on the luminescent lifetimes of the resultant complexes; the conjugated complex **C2.1** shows an average lifetime of just 19 ns, compared to the non-conjugated ether complex **C1.1** possessing a lifetime of 467 ns, 25 times longer.

The clear expansion of this work lead to the formation of the first heteroleptic ambidentate metallocryptophane **CC1.1**, by capping the acetonitrile adduct of **C1.1**, **C1.1B** with **L4**. The pre-organised nature of the two components and the exact size-match leads to the facile formation of the head-to-head cage. Future work on this system could explore the host-guest properties of cage complex **CC1.1** along with the photophysical attributes, as well as the combination of these two facets towards the development of a luminescent supramolecular sensor assembly.

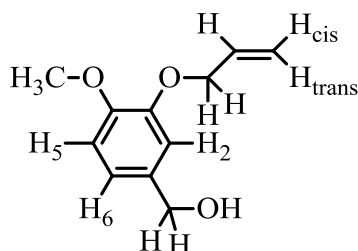
2.8 Experimental

2.8.1 General Considerations

NMR spectra were recorded by automated procedures on Bruker Avance 500 or DPX 300 MHz NMR spectrometers. All deuterated solvents were purchased from commercial sources. All ^1H and ^{13}C spectra were referenced relative to the residual solvent peak. High resolution electrospray mass spectra (ESI-MS) were measured on a Bruker MaXis Impact spectrometer in either positive or negative ion mode. FT-IR spectra were recorded as solid phase samples on a Bruker ALPHA Platinum-ATR spectrometer. Samples for microanalysis were dried under vacuum before analysis and the elemental composition determined by Ms Tanya Marinko-Covell of the University of Leeds Microanalytical Service using a Carlo Erba elemental analyser MOD 1106 spectrometer. Steady state emission and excitation spectra were recorded on an Agilent Technologies Cary Eclipse. Time-resolved spectra were recorded on a PicoQuant FluoTime 300 exciting with an LDH-P-C-375 and decays analysed with the program FluoFit. A 0.4 mg mL^{-1} solution in aerated DMSO was made to 5 mL in a volumetric flask, the solution was then transferred to a quartz cuvette and the experiments run at ambient temperature. Photophysical studies were performed in DMSO (to ensure full dissolution of the solids). All chemicals were purchased from commercial sources and used as received. All ligands were synthesised as racemic mixtures and employed as such in complexation studies.

Preparation of cyclotriguaiacylene (CTG):⁵⁵

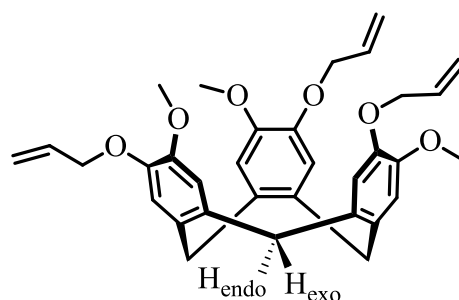
Step 1: Synthesis of 4-methoxy-3-(propen-2-yl)-oxybenzyl alcohol PI



Iso-vanillyl alcohol (30.0 g, 194 mmol), allyl bromide (20.3 mL, 233 mmol) and potassium carbonate (26.8 g, 194 mmol) were heated to reflux in acetone (60 mL) for 24 hrs under an Argon atmosphere. The solvent was removed *in vacuo* and the residue taken up in dichloromethane (2 x 200 mL), the organic layer was washed with H_2O (100 mL) and brine (60 mL). The combined organic layers were then

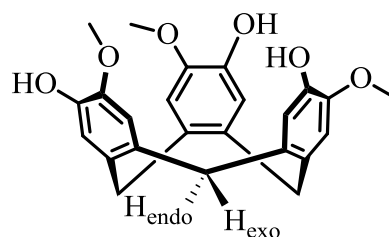
dried over magnesium sulphate. Removal of the solvent *in vacuo* gave the product as an off white solid (33.87 g, 96.8%) that was used in the subsequent reaction. ^1H NMR (300 MHz, CDCl_3) δ 6.93 (s, 1H, H_6), 6.85 (d, $J = 0.9$ Hz, 2H, H_5/H_2), 6.08 (ddt, $J = 17.2, 10.7, 5.4$ Hz, 1H, CHCH_2), 5.40 (dd, $J = 17.3, 1.5$ Hz, 1H, H_{trans}), 5.28 (dd, $J = 10.4, 1.3$ Hz, 1H, H_{cis}), 4.66 – 4.52 (m, 4H, $\text{CH}_2\text{OH}/\text{CH}_2\text{O}$), 3.88 (s, 3H, OMe). $^{13}\text{C}\{^1\text{H}\}$ NMR (75 MHz, CDCl_3) δ 149.63, 147.58, 134.05, 133.38, 119.37, 118.11, 113.37, 110.88, 70.01, 65.37, 55.98. TOF-MS ESI: $m/z = 177.0916$ (M-OH) All data are consistent with the literature.⁵⁵

Step 2: Synthesis of tris(propen-2-yloxy)cyclotriguaiacylene P2



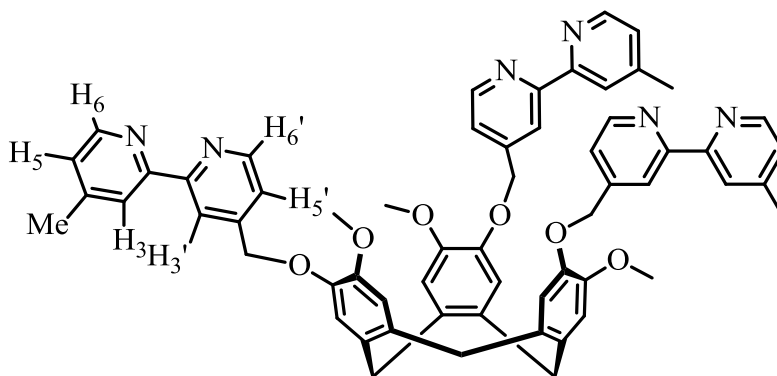
4-methoxy-3-(propen-2-yl)-oxybenzyl alcohol (15 g, 77 mmol) was heated with stirring at 80°C . A catalytic amount of superphosphoric acid (spatula tip) was added and stirring was continued for 8 hrs, during which time the mixture turned beige and solidified. Sonication in methanol (200 mL) afforded a fine white solid that was collected by filtration, washed with further methanol and dried *in vacuo* to give the product as a white solid (7.72 g, 56.7%) ^1H NMR (300 MHz, CDCl_3) δ 6.85 (s, 1H, aryl CTG), 6.79 (s, 1H, aryl CTG), 6.06 (ddt, $J = 17.3, 10.5, 5.2$ Hz, 1H, CHCH_2), 5.37 (dq, $J = 17.3, 1.6$ Hz, 1H, H_{trans}), 5.24 (dq, $J = 10.5, 1.4$ Hz, 1H, H_{cis}), 4.74 (d, $J = 13.7$ Hz, 1H, H_{endo}), 4.59 (qd, $J = 3.4, 1.5$ Hz, 2H, OCH_2CH_2), 3.84 (d, $J = 3.4$ Hz, 3H, OMe), 3.51 (d, $J = 13.9$ Hz, 1H, H_{exo}). $^{13}\text{C}\{^1\text{H}\}$ NMR (126 MHz, CDCl_3) δ 148.37, 146.92, 133.90, 132.49, 131.91, 117.64, 115.77, 113.81, 70.37, 56.27, 36.68. TOF-MS ESI: $m/z = 546.2858$ (M+ H_2O) All data are consistent with the literature.⁵⁵

Step 3: Synthesis of cyclotriguaiacylene P3



Tris(propen-2-yloxy)cyclotriguaiacylene (3 g, 5.47 mmol) and triphenyl phosphine (300 mg, 1.14 mmol) were refluxed under an Argon atmosphere for 2 hrs in dry THF (100 mL), diethylamine (29 mL) and H₂O (25 mL). Palladium acetate (100 mg, 0.44 mmol) was then added and the solution left to heat for 18 hrs. The solution was filtered hot, through celite, and the solvent removed. The resulting off-white solid was triturated in methanol, filtered and washed with ether to give the product as a fine white powder (1.68g, 75.7%) ¹H NMR (300 MHz, CDCl₃) δ 6.88 (s, 1H, aryl CTG), 6.79 (s, 1H, aryl CTG), 5.39 (s, 1H, OH), 4.71 (d, *J* = 13.7 Hz, 1H, H_{endo}), 3.85 (s, 3H, OMe), 3.50 (d, *J* = 13.8 Hz, 1H, H_{exo}). ¹³C{¹H} NMR (126 MHz, DMSO-d₆) δ 145.94, 144.86, 132.56, 130.41, 116.77, 113.99, 55.97, 35.01. TOF-MS ESI: *m/z* = 426.1918 (M+H₂O) All data are consistent with the literature.²¹

Preparation of (±)-2,7,12-trimethoxy-3, 8, 13-tris(4-(4'-methyl-2, 2'-bipyridyl)methyl)-10, 15-dihydro-5H-tribenzo[a, d, g]cyclononatriene (L1)

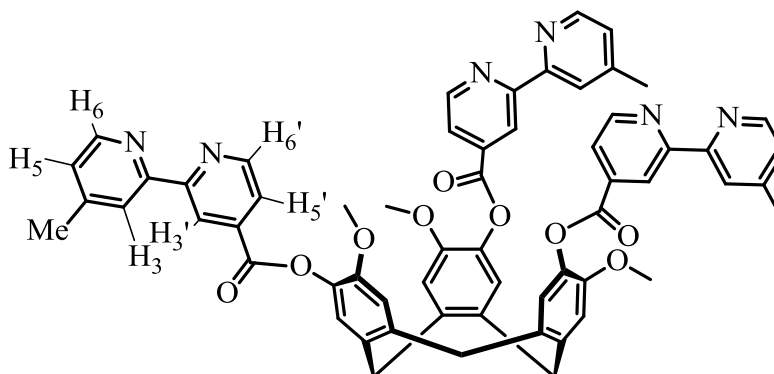


L1 was prepared in accordance with a modified literature procedure, all data are consistent.⁴

Under an inert atmosphere, potassium carbonate (1.10 g, 7.97 mmol), a catalytic amount of 18-crown-6 and a suspension of CTG (0.200 g, 0.490 mmol) were stirred at reflux in acetone (30 mL) for 30 minutes. 4-bromomethyl-4'-methyl-2,2'-bipyridine (0.900 g, 3.43 mmol) was then added to the deprotonated CTG solution and the mixture left to stir at reflux for 48 hours. After cooling the acetone was removed *in vacuo*, water (50 mL) added and the suspension extracted with dichloromethane (3 × 50 mL). The combined extracts were dried over magnesium sulphate and taken to dryness to give an oily substance that was triturated with

methanol to give an off-white solid (0.364 g, 77.7 %) ^1H NMR (300 MHz, CDCl_3) δ (ppm) 8.65 (d, $J = 5.0$ Hz, 1H, $\text{H}^{\delta'}$), 8.55 (d, $J = 4.9$ Hz, 1H, H^{δ}), 8.45 (s, 1H, $\text{H}^{\delta'}$), 8.28 (s, 1H, H^{δ}), 7.43 (d, $J = 4.7$ Hz, 1H, $\text{H}^{\delta'}$), 7.18 (d, $J = 4.6$ Hz, 1H, H^{δ}), 6.80 (s, 1H, aryl CTG), 6.65 (s, 1H, aryl CTG), 5.20 (s, 2H, OCH_2), 4.67 (d, $J = 13.7$ Hz, 1H, H_{endo}), 3.64 (s, 3H, OMe), 3.44 (d, $J = 13.7$ Hz, 1H, H_{exo}), 2.46 (s, 3H, Me) $^{13}\text{C}\{^1\text{H}\}$ NMR (126 MHz, CDCl_3) δ 156.50, 155.72, 149.75, 149.09, 148.72, 148.41, 148.10, 146.70, 133.29, 131.69, 125.04, 122.16, 121.48, 118.58, 116.49, 113.76, 70.44, 56.21, 36.59, 21.34 TOF-MS ESI: $m/z = 977.4002$ ($\text{M}+\text{Na}^+$) Analysis for $\text{C}_{60}\text{H}_{54}\text{N}_6\text{O}_6 \cdot 0.5(\text{H}_2\text{O})$ (% calculated, found) C (74.75, 74.60) H (5.75, 5.70) N (8.72, 8.70)

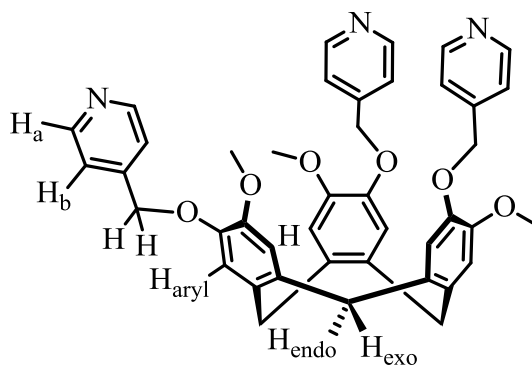
Preparation of (\pm)-2,7,12-trimethoxy-3, 8, 13-tris(4-(4'-methyl-2, 2'-bipyridyl)carboxy)-10, 15-dihydro-5H-tribenzo[a, d, g]cyclononatriene (L2)



Cyclotriguaiacylene (0.369 g, 0.97 mmol) was dissolved in dry THF (60 mL) under a nitrogen atmosphere and cooled to -78°C . Triethylamine (2 mL) was added to the solution and stirred for 1 hour at -78°C . 4'-methyl-2,2'-bipyridine-4-carboxyl chloride (0.800 g, 0.76 mmol) was added to the reaction flask and the solution stirred for a further 2 hours at -78°C , then allowed to come to room temperature and stirred for a further 3 days. The solvent was then removed *in vacuo* to give a pale off-pink solid that was triturated with EtOH to give the title compound as an off-white solid (0.655 g, 0.687 mmol, 76%). ^1H NMR (300 MHz, DMSO) δ 9.02 (s, 1H, $\text{H}^{\delta'}$), 9.00 (s, 1H, $\text{H}^{\delta'}$), 8.64 (d, $J = 4.8$ Hz, 1H, H^{δ}), 8.35 (s, 1H, H^{δ}), 8.03 (d, $J = 5.4$ Hz, 1H, $\text{H}^{\delta'}$), 7.68 (s, 1H, aryl CTG), 7.41 (s, 1H, aryl CTG), 7.39 (s, 1H, H^{δ}), 4.96 (d, $J = 13.8$ Hz, 1H, H_{endo}), 3.79 (m, $J = 9.1$ Hz, 4H, $\text{H}_{\text{exo}}/\text{OMe}$), 2.49 (s, 3H, Me). $^{13}\text{C}\{^1\text{H}\}$ NMR (126 MHz, DMSO- d_6) δ (ppm) 163.04, 156.78, 153.88, 150.83, 149.34, 149.19, 148.39, 138.97, 137.60, 137.17, 131.97, 125.62, 124.07, 123.07,

121.40, 119.57, 114.58, 56.29, 35.04, 20.71. TOF-MS ESI: $m/z = 997.3569$ ($M+H^+$)
 Analysis for $C_{60}H_{48}N_6O_9 \cdot 2(H_2O)$ (% calculated, found) C (69.76, 69.90) H (5.07, 4.75) N (8.13, 7.80)

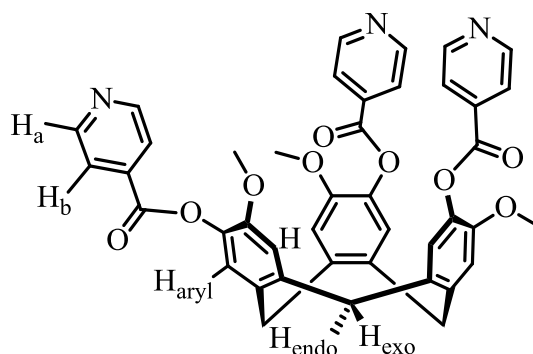
Preparation of (\pm)-2,7,12-trimethoxy-3, 8, 13-tris(4-pyridylmethoxy)-10, 15-dihydro-5H-tribenzo[a, d, g]cyclononatriene (L3)



L3 was prepared in accordance with a modified literature procedure¹¹ all data are consistent.

Under an inert atmosphere, potassium carbonate (2.0 g, 14.5 mmol), a catalytic amount of 18-crown-6 and a suspension of CTG (0.200 g, 0.490 mmol) were stirred at reflux in acetone (150 mL) for 30 minutes. 4-bromomethylpyridine hydrobromide (0.500 g, 1.98 mmol) was then added to the deprotonated CTG solution and the mixture left to stir at reflux for 3 days. After cooling the acetone was removed *in vacuo*, water (50 mL) added and the suspension extracted with dichloromethane (3 × 50 mL). The combined extracts were dried over magnesium sulphate and taken to dryness to give an oily substance that was triturated with methanol to give an off-white solid (0.290 g, 87.5 %) 1H NMR (300 MHz, $CDCl_3$) δ 8.60 (dd, $J = 6.2, 2.8$ Hz, 2H, H_a), 7.34 (dd, $J = 6.4, 2.6$ Hz, 2H, H_b), 6.78 (s, 1H, aryl CTG), 6.67 (s, 1H, aryl CTG), 5.11 (s, 2H, CH_2), 4.70 (d, $J = 13.8$ Hz, 1H, H_{endo}), 3.71 (s, 3H, OMe), 3.46 (d, $J = 13.8$ Hz, 1H, H_{exo}). $^{13}C\{^1H\}$ NMR (126 MHz, $CDCl_3$) δ 150.18, 148.77, 146.82, 146.75, 133.40, 131.83, 121.38, 116.60, 113.97, 70.22, 56.30, 36.61. TOF-MS ESI: $m/z = 682.2911$ ($M+H^+$)

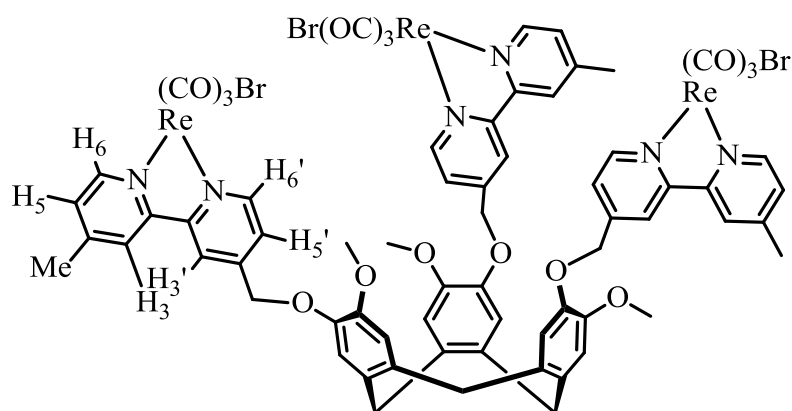
Preparation of (\pm)-2,7,12-trimethoxy-3, 8, 13-tris(4-carboxypyridyl)-10, 15-dihydro-5H-tribenzo[a, d, g]cyclononatriene (L4)



L4 was prepared in accordance with literature procedure, all data are consistent.⁷

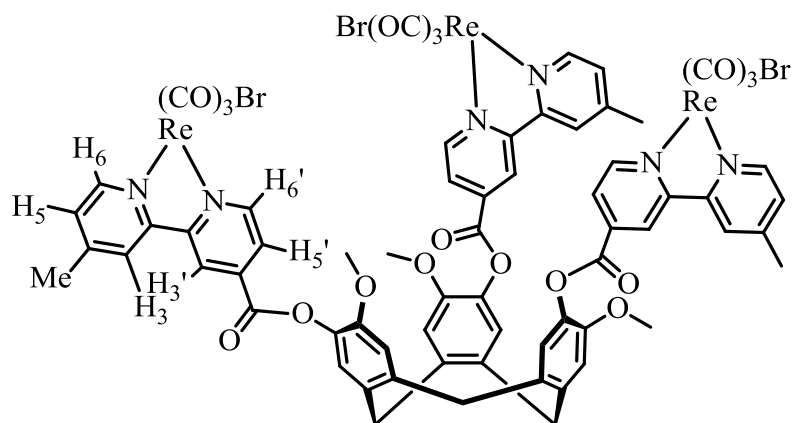
Cyclotriguaiacylene (0.300 g, 0.74 mmol) was dissolved in dry THF (50 mL) under a nitrogen atmosphere and cooled to -78°C . Triethylamine (2.5 mL) was added to the solution and stirred for 1 hour at -78°C . Isonicotinoyl chloride hydrochloride (0.527 g, 2.96 mmol) was added to the reaction flask and the solution stirred for a further 2 hours at -78°C , then allowed to come to room temperature and stirred for a further 2 days. The solvent was then removed *in vacuo* to give an off- white solid that was triturated with MeOH to give the title compound as a white solid (0.461 g, 86 %). ^1H NMR (300 MHz, CD_3NO_2) δ 8.85 (dd, $J = 6.1, 2.9$ Hz, 2H, H_a), 7.99 (dd, $J = 6.0, 2.8$ Hz, 2H, H_b), 7.44 (s, 1H, aryl CTG), 7.26 (s, 1H, aryl CTG), 5.01 (d, $J = 13.8$ Hz, 1H, H_{endo}), 3.92 – 3.76 (m, 4H, H_{exo} /OMe). $^{13}\text{C}\{^1\text{H}\}$ NMR (126 MHz, DMSO) δ 162.99, 151.02, 149.12, 138.87, 137.53, 135.86, 131.90, 123.99, 122.89, 114.52, 56.25, 34.94. TOF-MS ESI: $m/z = 724.2288$ ($\text{M}+\text{H}^+$)

Preparation of complex [(Re(Br)(CO)₃)₃(tris(4-[4'-methyl-2, 2'-bipyridyl]methyl)CTG)] (C1.1):



Re(CO)₅Br (67.9 mg, 0.167 mmol) was added to **L1** (50 mg, 0.05 mmol) in toluene (15 mL) and heated to reflux for 24 hours to form an orange solution and bright yellow precipitate. The precipitate was isolated through sinter filtration, and washed with cold toluene (15 mL) and diethyl ether (10 mL) to give a crystalline yellow solid (101 mg, 96 %); ¹H NMR (300 MHz, CD₃CN) δ 8.95 (s, 1H, H^{6'}), 8.83 (s, 1H, H⁶), 8.42 (d, *J* = 5.3 Hz, 1H, H^{3'}), 8.21 (d, *J* = 11.0 Hz, 1H, H³), 7.61 (s, 1H, H^{5'}), 7.43 (s, 1H, H⁵), 7.12 (s, 1H, aryl CTG), 7.02 (s, 1H, aryl CTG), 5.26 (s, 2H, OCH₂), 4.73 (d, *J* = 13.5 Hz, 1H, H_{endo}), 3.79 (d, *J* = 8.6 Hz, 3H, OMe), 3.56 (d, *J* = 13.6 Hz, 1H, H_{exo}), 2.53 (d, *J* = 4.5 Hz, 3H, Me), ¹³C{¹H} NMR (126 MHz, DMSO) δ 197.50, 189.69, 155.41, 154.76, 153.19, 152.60, 152.43, 151.68, 148.22, 145.96, 134.02, 132.23, 128.65, 125.56, 125.36, 125.01, 122.11, 117.22, 114.49, 69.37, 56.19, 35.23, 21.06; TOF-MS ESI: *m/z* = 2003.0774 {[(Re(CO)₃)₃(Br)₂]**L1**}⁺•DMSO, calculated for 2003.0772; Analysis for C₆₉H₅₄Br₃N₆O_{15.2}(H₂O) (% calculated, found) C (40.59, 40.40) H (2.86, 2.80) N (4.12, 4.10); IR (solid state): ν_{max} = 2017 (C≡O), 1883 (C≡O), 1616 (C=C), 1505, 1487, 1416, 1273, 1180 (C-O), 1088, 1031, 973, 888, 826, 646. UV-visible absorption maxima (DMSO, nm) 293, 318, 368.

Preparation of complex [(Re(Br)(CO)₃)₃(tris(4-[4'-methyl-2', 2'-bipyridoyl] CTG)] (C2.1):



Re(CO)₅Br (0.131 g, 0.321 mmol) was added to **L2** (0.100 g, 0.100 mmol) in toluene (15 mL) and heated to reflux for 24 hours to form an orange solution and bright yellow precipitate. The precipitate was removed through sinter filtration, and washed with cold toluene (15 mL) and diethyl ether (10 mL) to give a crystalline yellow solid (193 mg, 94%); ¹H NMR (300 MHz, DMSO-d₆) δ (ppm) 9.30 (d, *J* = 6.0 Hz, 1H, H^{6'}), 9.21 (s, 1H, H^{3'}), 8.97 (s, 1H, H³), 8.90 (d, *J* = 5.7 Hz, 1H, H⁶), 8.26 (d, *J* = 5.6 Hz, 1H, H^{5'}), 7.66 (s, 1H, CTG aryl), 7.63 (d, *J* = 5.2 Hz, 1H, H⁵), 7.37 (s, 1H, CTG aryl), 4.97 (d, *J* = 13.9 Hz, 1H, H_{endo}), 3.76 (s, 4H, OMe/H_{exo}), 2.58 (s, 3H, Me); ¹³C{¹H} NMR (126 MHz, DMSO) δ 197.28, 197.02, 189.08, 161.42, 157.11, 154.52, 153.90, 152.62, 152.43, 149.00, 139.18, 138.95, 137.43, 131.99, 128.93, 126.62, 126.00, 123.94, 123.29, 114.53, 56.28, 35.04, 20.72.; TOF-MS ESI: *m/z* = 2045.0152 {[(Re(CO)₃)₃(Br)₂]**L2**}⁺•DMSO, calculated for 2045.0150; Analysis for C₆₉H₄₈Br₃N₆O₁₆ (% calculated, found) C (40.48, 40.20) H (2.36, 2.60) N (4.10, 4.10); IR (solid state): ν_{max} = 2020 (C≡O), 1889 (C≡O), 1748 (OC=O) 1618 (C=C), 1505, 1409, 1324, 1302, 1251, 1232, 1205, 1176 (C-O), 1140, 1101, 1070, 991, 895, 833, 767, 645. UV-visible absorption maxima (DMSO, nm) 252, 290, 330, 377.

Preparation of cage [C1.1B(L4)] (CC1.1):

C1.1 (0.020 g, 0.009 mmol) was dissolved in MeCN (5 mL) in the presence of AgOTf (0.008 g, 0.032 mmol) in the absence of light. The resultant solution was heated to 60 °C for 12 hours then allowed to cool. The solution was filtered through a pad of Celite to removed AgBr and concentrated in vacuo to ~1 mL, diethyl ether was added to precipitate a pale yellow powder (**C1.1B**) in approximately quantitative yield. {TOF-MS ESI: *m/z* = 629.4369 (M-3(OTf))} A stoichiometric amount of **C1.1B** was dissolved immediately in combination with L4 (0.0062 g, 0.008 mmol) in d₃-nitromethane (0.5 mL), and the resultant solution heated to 50 °C for 24 hours. The formation of **CC1.1** was followed by ¹H NMR and HR ESI-MS over time. TOF-MS ESI: *m/z* = 829.8133{(Re(CO)₃)₃(**L1**)(**L4**)}³⁺, calculated for 829.8175.

2.8.2 X-ray crystallography

Crystals were mounted under inert oil on a MiTeGen tip and flash frozen to 100(1) K using an OxfordCryosystems low temperature device. X-ray diffraction data were collected using Cu- K_{α} radiation ($\lambda = 1.54184 \text{ \AA}$) or Mo- K_{α} radiation ($\lambda = 0.71073 \text{ \AA}$) using an Agilent Supernova dual-source diffractometer with Atlas S2 CCD detector and fine-focus sealed tube generator. Data were corrected for Lorentzian and polarization effects and absorption corrections were applied using multi-scan methods. The structures were solved by direct methods using SHELXS-97 and refined by full-matrix on F^2 using SHELXL-97.⁵⁶ Unless otherwise specified, all non-hydrogen atoms were refined as anisotropic, and hydrogen positions were included at geometrically estimated positions. Crystals of **L1**·(Et₂O) were of poor quality, with poor internal consistency ($R_{int} = 0.1955$) and only exhibited weak diffraction, with no diffraction at high angles. Attempts to grow higher quality crystals were not successful. For complex **C1.1**·n(CH₃NO₂) solvent CH₃NO₂ and some CO ligands were refined isotropically and one C=O bond length restrained. The crystal lattice contained significant void space that could not be meaningfully modelled as solvent. The SQUEEZE routine of PLATON was therefore employed.⁴⁸

Compound	L1 ·(Et ₂ O)	C1.1 ·n(CH ₃ NO ₂)
Formula	C ₆₄ H ₆₄ N ₆ O ₇	C ₁₄₁ H ₁₁₇ Br ₆ N ₁₅ O ₃₆ Re ₆
<i>Mr</i>	1029.21	4194.16
Crystal color and shape	Colorless, plate	Yellow, polyhedral
Crystal size (mm)	0.20 x 0.10 x 0.01	0.10 x 0.10 x 0.20
Crystal system	Orthorhombic	Trigonal (hexagonal axes)
Space group	<i>Pbna</i>	<i>R-3</i>
<i>a</i> (Å)	9.308(2)	29.1454(12)
<i>b</i> (Å)	34.568(10)	29.1454(12)
<i>c</i> (Å)	33.811(9)	42.570(3)
α (°)	90	90
β (°)	90	90
γ (°)	90	120
<i>V</i> (Å ³)	10879(5)	31317(3)
<i>Z</i>	8	6
ρ_{calc} (g·cm ⁻³)	1.257	1.334
θ range (°)	4.68 – 45.0	3.65-58.99
No. data collected	23412	16678
No. unique data	4392	9929
<i>R</i> _{int}	0.1955	0.0382
No. obs. Data (<i>I</i> > 2σ(<i>I</i>))	2045	6101
No. parameters	704	553
No. restraints	0	1
<i>R</i> _{<i>I</i>} (obs data)	0.1251	0.0950
<i>wR</i> ₂ (all data)	0.3706	0.2583
<i>S</i>	1.003	1.458

Photophysical studies

UV-vis spectra were recorded on an Agilent Technologies Cary 60. Steady state emission and excitation spectra were recorded on an Agilent Technologies Cary Eclipse. Time-resolved spectra were recorded on a PicoQuant FluoTime 300 exciting with an LDH-P-C-375 and decays analysed with the program FluoFit. A 0.4 mgmL⁻¹ solution in aerated DMSO was made to 5 mL in a volumetric flask, the solution was then transferred to a quartz cuvette and the experiments run at ambient temperature. Photophysical studies were performed in DMSO (to ensure full

dissolution of the solids). The lifetime of the complex is defined as the time at which the emission intensity has dropped to e^{-1} times the initial intensity I_0 . To calculate this value the dark counts must be taken into account, as the intensity of the emission does not drop to 0, but plateaus at ~ 2000 a.u. The data must be normalised to reflect the baseline dark count. Therefore the average dark count value is subtracted from all recorded intensities to give an I_0 of 8000 a.u. As stated, $I_\tau = I_0 \times e^{-1}$, leading to an I_τ value of 2943 a.u., which corresponds to a τ value of 0.467 μs , or 467 ns for **C1.1** and a two component lifetime of 3 ns and 23 ns for complex **C2.1** as confirmed by TRES measurements and analysis with FluoroFit.

2.9 Bibliography

- 1 T. K. Ronson, H. Nowell, A. Westcott and M. J. Hardie, *Chem. Commun.*, 2011, **47**, 176.
- 2 J. J. Henkelis, T. K. Ronson and M. J. Hardie, *CrystEngComm*, 2013, **16**, 3688–3693.
- 3 J. J. Henkelis, S. A. Barnett, L. P. Harding and M. J. Hardie, *Inorg. Chem.*, 2012, **51**, 10657–10674.
- 4 A. Westcott, J. Fisher, L. P. Harding, P. Rizkallah and M. J. Hardie, *J. Am. Chem. Soc.*, 2008, **130**, 2950–2951.
- 5 C. Carruthers, T. K. Ronson, C. J. Sumby, A. Westcott, L. P. Harding, T. J. Prior, P. Rizkallah and M. J. Hardie, *Chem. – Eur. J.*, 2008, **14**, 10286–10296.
- 6 C. J. Sumby and M. J. Hardie, *Angew. Chem. Int. Ed.*, 2005, **44**, 6395–6399.
- 7 M. J. Hardie and C. J. Sumby, *Inorg. Chem.*, 2004, **43**, 6872–6874.
- 8 J. J. Henkelis, T. K. Ronson, L. P. Harding and M. J. Hardie, *Chem. Commun.*, 2011, **47**, 6560–6562.
- 9 T. K. Ronson, J. Fisher, L. P. Harding and M. J. Hardie, *Angew. Chem. Int. Ed.*, 2007, **46**, 9086–9088.

-
- 10 T. K. Ronson, J. Fisher, L. P. Harding, P. J. Rizkallah, J. E. Warren and M. J. Hardie, *Nat. Chem.*, 2009, **1**, 212–216.
- 11 T. K. Ronson, C. Carruthers, J. Fisher, T. Brotin, L. P. Harding, P. J. Rizkallah and M. J. Hardie, *Inorg. Chem.*, 2010, **49**, 675–685.
- 12 J. J. Henkelis, C. J. Carruthers, S. E. Chambers, R. Clowes, A. I. Cooper, J. Fisher and M. J. Hardie, *J. Am. Chem. Soc.*, 2014, **136**, 14393–14396.
- 13 A. Schaly, Y. Rousselin, J.-C. Chambron, E. Aubert and E. Espinosa, *Eur. J. Inorg. Chem.*, 2016, **2016**, 832–843.
- 14 Z. Zhong, A. Ikeda, S. Shinkai, S. Sakamoto and K. Yamaguchi, *Org. Lett.*, 2001, **3**, 1085–1087.
- 15 F. L. Thorp-Greenwood, A. N. Kulak and M. J. Hardie, *Nat. Chem.*, 2015, **7**, 526–531.
- 16 K. T. Holman, S. D. Drake, J. W. Steed, G. W. Orr and J. L. Atwood, *Supramol. Chem.*, 2010, **22**, 870–890.
- 17 G. K. Seward, Y. Bai, N. S. Khan and I. J. Dmochowski, *Chem. Sci.*, 2011, **2**, 1103–1110.
- 18 L. Garel, J.-P. Dutasta and A. Collet, *Angew. Chem. Int. Ed. Engl.*, 1993, **32**, 1169–1171.
- 19 T. Brotin and J.-P. Dutasta, *Chem. Rev.*, 2009, **109**, 88–130.
- 20 J. M. Chambers, P. A. Hill, J. A. Aaron, Z. Han, D. W. Christianson, N. N. Kuzma and I. J. Dmochowski, *J. Am. Chem. Soc.*, 2009, **131**, 563–569.
- 21 A. Collet, *Tetrahedron*, 1987, **43**, 5725–5759.
- 22 B. Chatelet, E. Payet, O. Perraud, P. Dimitrov-Raytchev, L.-L. Chapellet, V. Dufaud, A. Martinez and J.-P. Dutasta, *Org. Lett.*, 2011, **13**, 3706–3709.
- 23 M. A. Little, J. Donkin, J. Fisher, M. A. Halcrow, J. Loder and M. J. Hardie, *Angew. Chem. Int. Ed.*, 2012, **51**, 764–766.
- 24 P. D. Raytchev, O. Perraud, C. Aronica, A. Martinez and J.-P. Dutasta, *J. Org. Chem.*, 2010, **75**, 2099–2102.

- 25 Y. Makita, K. Sugimoto, K. Furuyoshi, K. Ikeda, S. Fujiwara, T. Shin-ike and A. Ogawa, *Inorg. Chem.*, 2010, **49**, 7220–7222.
- 26 Y. Makita, K. Ikeda, K. Sugimoto, T. Fujita, T. Danno, K. Bobuatong, M. Ehara, S. Fujiwara and A. Ogawa, *J. Organomet. Chem.*, 2012, **706–707**, 26–29.
- 27 O. Perraud, S. Lefevre, V. Robert, A. Martinez and J.-P. Dutasta, *Org. Biomol. Chem.*, 2012, **10**, 1056–1059.
- 28 Y. Makita, K. Sugimoto, K. Furuyoshi, K. Ikeda, T. Fujita, S.-I. Fujiwara and A. Ogawa, *Supramol. Chem.*, 2011, **23**, 269–272.
- 29 R. M. Fairchild and K. T. Holman, *J. Am. Chem. Soc.*, 2005, **127**, 16364–16365.
- 30 O. Perraud, V. Robert, H. Gornitzka, A. Martinez and J.-P. Dutasta, *Angew. Chem. Int. Ed.*, 2012, **51**, 504–508.
- 31 A. Schmitt, V. Robert, J.-P. Dutasta and A. Martinez, *Org. Lett.*, 2014, 2374–2377.
- 32 M. J. Hardie, R. Ahmad and C. J. Sumby, *New J. Chem.*, 2005, **29**, 1231–1240.
- 33 A. V. Jr, in *Photophysics of Organometallics*, ed. A. J. Lees, Springer Berlin Heidelberg, 2009, pp. 115–158.
- 34 H. Kvapilová, A. Vlček, V. Barone, M. Biczysko and S. Záliš, *J. Phys. Chem. A*, 2015, **119**, 10137–10146.
- 35 J. H. Mecchia Ortiz, F. E. Morán Vieyra, C. D. Borsarelli, I. Romero, X. Fontrodona, T. Parella, N. D. Lis de Katz, F. Fagalde and N. E. Katz, *Eur. J. Inorg. Chem.*, 2014, **2014**, 3359–3369.
- 36 A. W.-T. Choi, V. M.-W. Yim, H.-W. Liu and K. K.-W. Lo, *Chem. – Eur. J.*, 2014, **20**, 9633–9642.
- 37 M. C. Gimeno, V. Fernández-Moreira and I. Marzo, *Chem. Sci.*, 2014, **5**, 4443–4446.
- 38 V. Fernández-Moreira, F. L. Thorp-Greenwood, A. J. Amoroso, J. Cable, J. B. Court, V. Gray, A. J. Hayes, R. L. Jenkins, B. M. Kariuki, D. Lloyd, C. O.

- Millet, C. F. Williams and M. P. Coogan, *Org. Biomol. Chem.*, 2010, **8**, 3888–3901.
- 39 A. J. Amoroso, M. P. Coogan, J. E. Dunne, V. Fernández-Moreira, J. B. Hess, A. J. Hayes, D. Lloyd, C. Millet, S. J. A. Pope and C. Williams, *Chem. Commun.*, 2007, 3066–3068.
- 40 A. E. Pierri, A. Pallaoro, G. Wu and P. C. Ford, *J. Am. Chem. Soc.*, 2012, **134**, 18197–18200.
- 41 X.-Q. Guo, F. N. Castellano, L. Li, H. Szmecinski, J. R. Lakowicz and J. Sipior, *Anal. Biochem.*, 1997, **254**, 179–186.
- 42 M. P. Coogan and V. Fernández-Moreira, *Chem. Commun.*, 2013, **50**, 384–399.
- 43 J. R. Lakowicz, *Principles of fluorescence spectroscopy*, Springer, 2006.
- 44 Q. Zhao, C. Huang and F. Li, *Chem Soc Rev*, **40**, 2508–2524.
- 45 M. J. Hardie, R. M. Mills and C. J. Sumbly, *Org. Biomol. Chem.*, 2004, **2**, 2958–2964.
- 46 T. K. Ronson and M. J. Hardie, *CrystEngComm*, 2008, **10**, 1731–1734.
- 47 M. J. Hardie, P. D. Godfrey and C. L. Raston, *Chem. – Eur. J.*, 1999, **5**, 1828–1833.
- 48 A. L. Spek, *Acta Crystallogr. A*, 1990, **46**, 34–34.
- 49 J. L. Atwood, M. J. Barnes, M. G. Gardiner and C. L. Raston, *Chem. Commun.*, 1996, 1449–1450.
- 50 Y. Makita, K. Sugimoto, K. Furuyoshi, K. Ikeda, S. Fujiwara, T. Shin-ike and A. Ogawa, *Inorg. Chem.*, 2010, **49**, 7220–7222.
- 51 T. Fujita, S. Fujiwara, Y. Makita, K. Sugimoto, K. Furuyoshi, K. Ikeda and A. Ogawa, *Supramol. Chem.*, **23**.
- 52 O. Perraud, V. Robert, A. Martinez and J.-P. Dutasta, *Chem. – Eur. J.*, 2011, **17**, 4177–4182.
- 53 T. Brotin, D. Cavagnat, E. Jeanneau and T. Buffeteau, *J. Org. Chem.*, 2013, 6143–6153.

- 54 T. Brotin, T. Devic, A. Lesage, L. Emsley and A. Collet, *Chem. – Eur. J.*, 2001, **7**, 1561–1573.
- 55 J. Canceill, A. Collet and G. Gottarelli, *J. Am. Chem. Soc.*, 1984, **106**, 5997–6003.
- 56 G. M. Sheldrick, *Acta Crystallogr. A*, 2008, **64**, 112–122.

3 Chapter 3

Tri- and mono- homometallic iridium complexes of CTG-type ligands

3.1 Introduction

Light emitting complexes are of great interest throughout chemistry, with potential applications in organic light emitting diode (OLED) and light emitting electrochemical cell (LEEC) systems,¹⁻⁴ in luminescent biomedical imaging⁵⁻⁷ and as sensors for drugs and explosives.⁸ There is a wealth of experimental research into the emission properties of both $[\text{Ir}(\text{C}^{\wedge}\text{N})_3]$ and $[\text{Ir}(\text{C}^{\wedge}\text{N})_2(\text{L}^{\wedge}\text{X})]^+$ iridium containing species, both into the resultant effect of altering the $\text{C}^{\wedge}\text{N}$ cyclometallating ligand and the $\text{L}^{\wedge}\text{X}$ ligand, which can be any combination of nitrogen, oxygen and sulphur containing bidentate ligand.^{1,3,6-20} Typical nomenclature when referring to iridium complexes dictates that *homoleptic* denotes an iridium centre bound to three identical cyclometallating ligands, whereas *heteroleptic* refers to an iridium centre bound to two cyclometallating ligands and one chelating ligand, i.e. *intra-metallic* similarity descriptor.

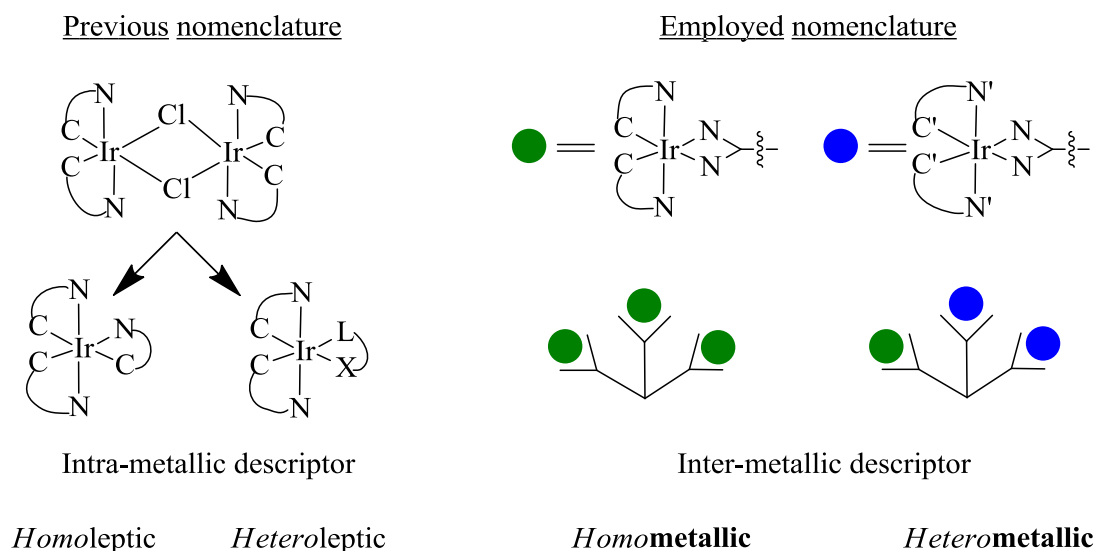


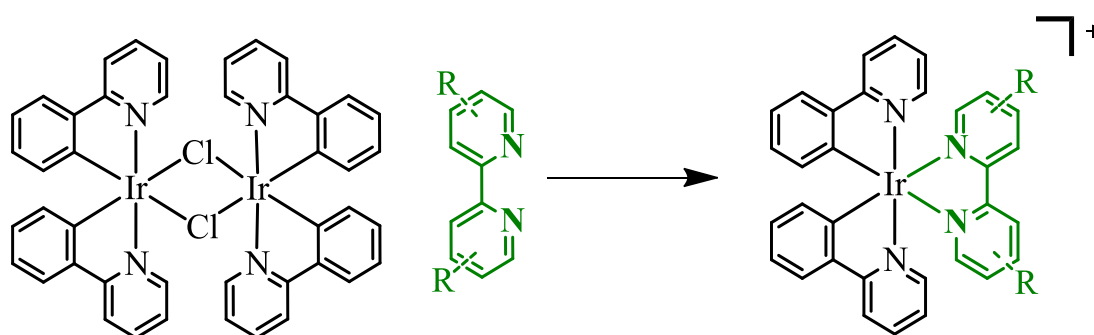
Figure 3.1 : Nomenclature relating to iridium complexes in the literature and in this work.

In this thesis, due to the tripodal nature of the ligand, and thus the presence of more than one iridium centre, the nomenclature adopted refers to both intra- and inter-metallic similarity. This work refers to the relative similarity of the ancillary cyclometallating ligands on distinct iridium centres, commonly referred to as a metallotecton, within the same metallo-complex i.e. *inter*-metallic similarity. Hence, *homo-metallic* in the title of this chapter refers to complexes where the same iridium metallotecton is bound to the cyclotriguaiacylene ligand multiple times. Whereas in Chapter 4, mixed systems are formed through the use of both phenylpyridine-containing and di-fluorophenylpyridine-containing metallotectons, leading to *hetero-metallic* metallo-complexes. All of the complexes discussed are heteroleptic, as two ancillary phenylpyridine ligands, and the bipyridine arm of the tripodal cavitant ligands are bound to the iridium centre.

This work will look exclusively at cationic iridium complexes bearing various C^N cyclometallating phenylpyridine ligands, and N^N chelating bipyridine ligands which are all part of larger tripodal cyclotriguaiacylene ligand scaffolds.

3.2 Preparation of homo tri-metallic iridium species

Although ubiquitous in the field of light-emitting devices, a common method for the preparation of bis-cyclometallated iridium species of the form $[\text{Ir}(\text{C}^{\text{N}})_2(\text{N}^{\text{N}})]\text{X}$, is through the reaction of a μ -chlorobridged iridium dimer and two equivalents of an N^N chelating ligand, as seen in Scheme 3.1.^{9,13,15,16,18,21}



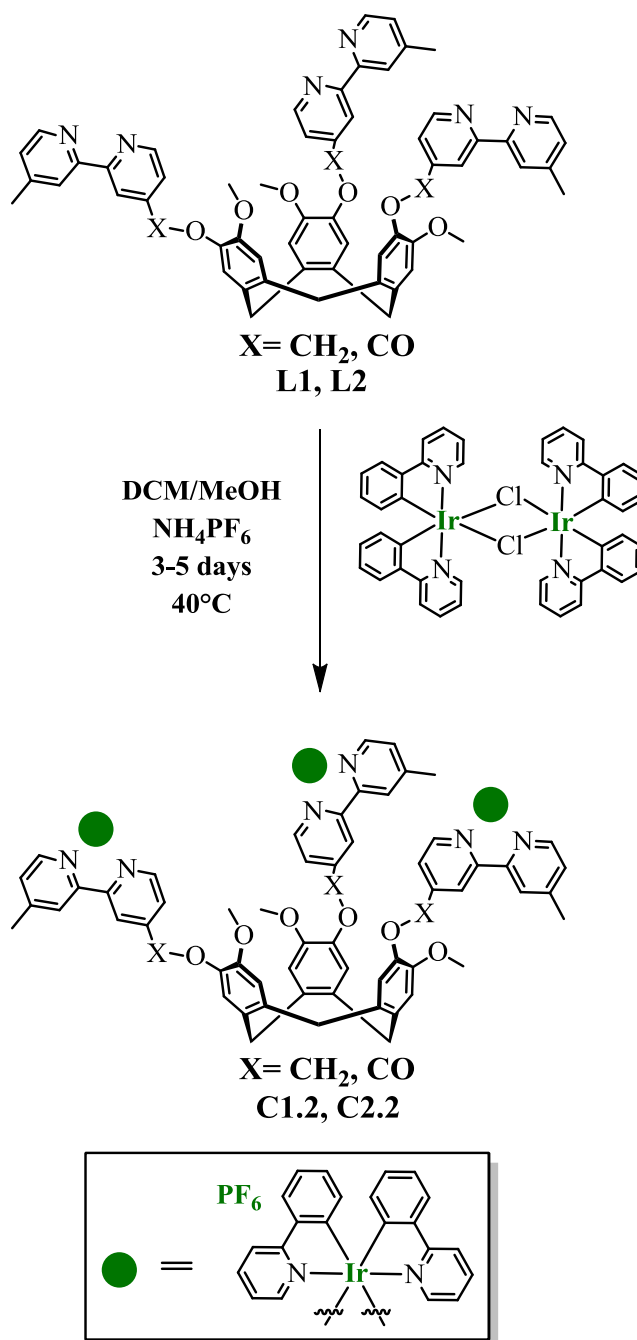
Scheme 3.1: The general route to formation of $[\text{Ir}(\text{C}^{\text{N}})_2(\text{N}^{\text{N}})]$ species.

In combination with the tripodal bipyridine ligands **L1** and **L2** discussed in the previous chapters, the above general route was applied in an effort to form homo tri-metallic iridium complexes **C1.2** and **C2.2**. In this case, the phrase ‘*homometallic*’ is

used in reference to similarity of the ancillary ligands around each discrete metal centre, in so much as each of the three distinct iridium centres in the subsequent complexes are structurally equivalent.

The formation of these species was initially explored employing high-boiling point solvents, such as diglyme and ethoxyethanol in an effort to drive the reaction towards the desired homo tri-metallic products, **C1.2** and **C2.2**. However, during reaction at elevated temperatures the bipyridine arm can be cleaved from the central tribenzo[*a, d, g*]cyclononatriene core, leading to irreversible degradation of the ligands.

To preclude the observed breakdown of the ligands, a milder synthetic route was investigated. The route is adapted from recent procedures,¹⁰ employing a DCM/MeOH solvent mixture and prolonged reaction times of up to five days, described in Scheme 3.2.



Scheme 3.2: Formation of C1.2 and C2.2, homo tri-metallic iridium species.

The status of the reaction, and thus the formation of the desired product, can easily be followed by use of HR ESI-MS, with the distinctive iridium isotope pattern being diagnostic of complex formation.

The resultant species **C1.2** and **C2.2** are seen at 818 and 832 m/z respectively as the +3 cation, Figure 3.2, without their non-coordinated chloride, or subsequently hexafluorophosphate, anions. Once the reaction has gone to completion, the latent chloride anions are exchanged for hexafluorophosphate anions through precipitation

of **C1.2** and **C2.2** with a saturated aqueous solution of ammonium hexafluorophosphate.

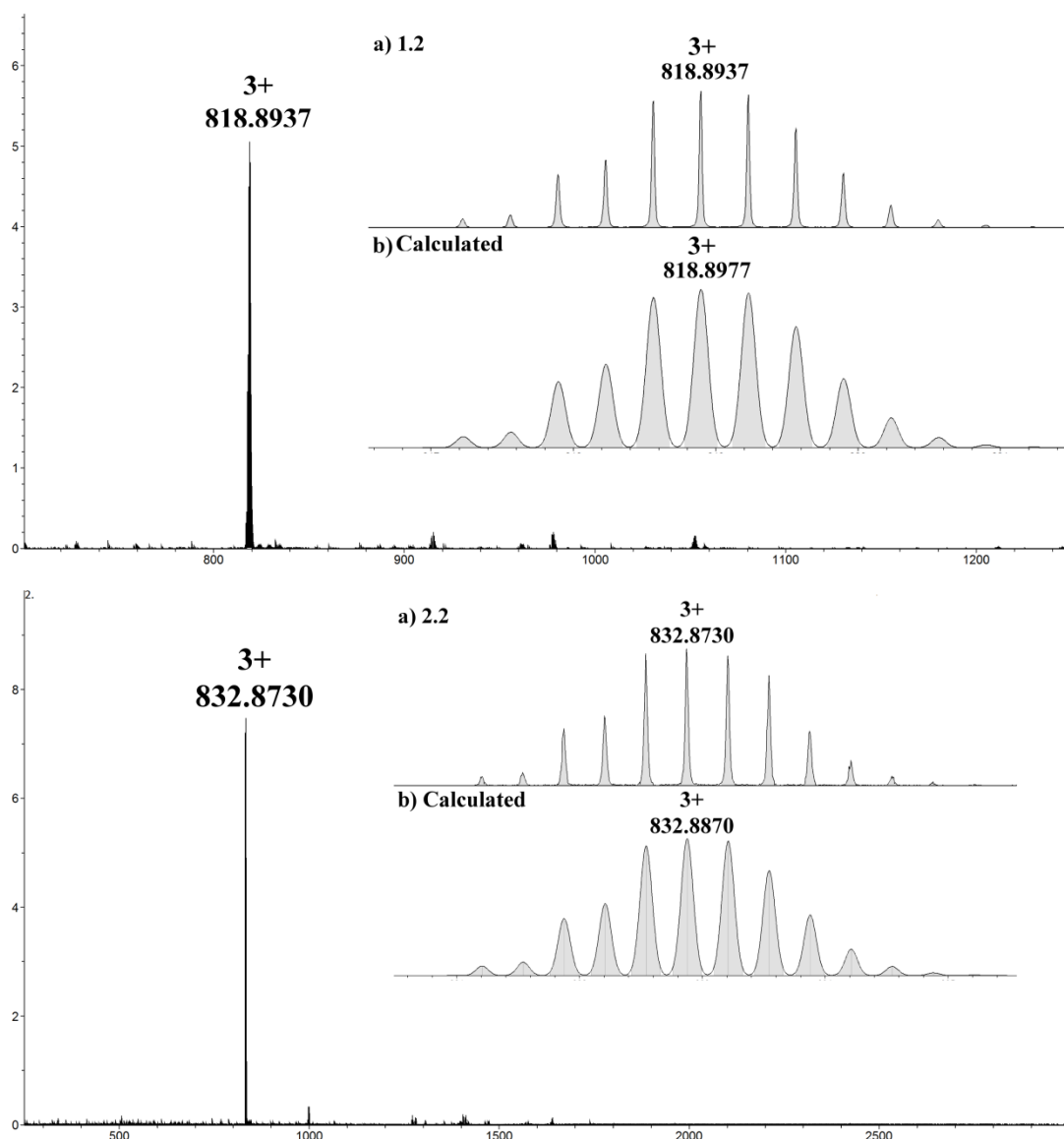


Figure 3.2: Expanded HR-ESI-MS of **C1.2** (top) and **C2.2** (bottom) with the isotope pattern of the 3+ peak and corresponding calculated spectrum of the M^{3+} peak, inset.

As evidenced in Figure 3.2, **C1.2** and **C2.2** can be formed cleanly through this mild synthetic route, with negligible side-products and no ligand degradation observed. The three iridium centres in these systems, **C1.2** and **C2.2**, are structurally equivalent, giving rise to the ‘homometallic’ systems; however they are not chemically equivalent as there are a number of diastereomers. As discussed in Chapter 2, cyclotriguaiacylene ligands are always formed as a racemic mixture of *M* and *P* enantiomers, thus **L1** and **L2** are present throughout as a mixture of

enantiomers. Furthermore, due to the *tris*-chelate nature of the ligand binding motif around the iridium centres, there are also Δ and Λ helical isomers present. The combination of these factors leads to a complex mixture of isomers in solution, exacerbated by the chirality around each bipyridine arm being independent of the other binding sites within the same complex, thus both Δ and Λ isomers can exist in the same complex. There are eight unique permutations that can arise from the combination of ligand and metal chirality, as shown in Figure 3.3.

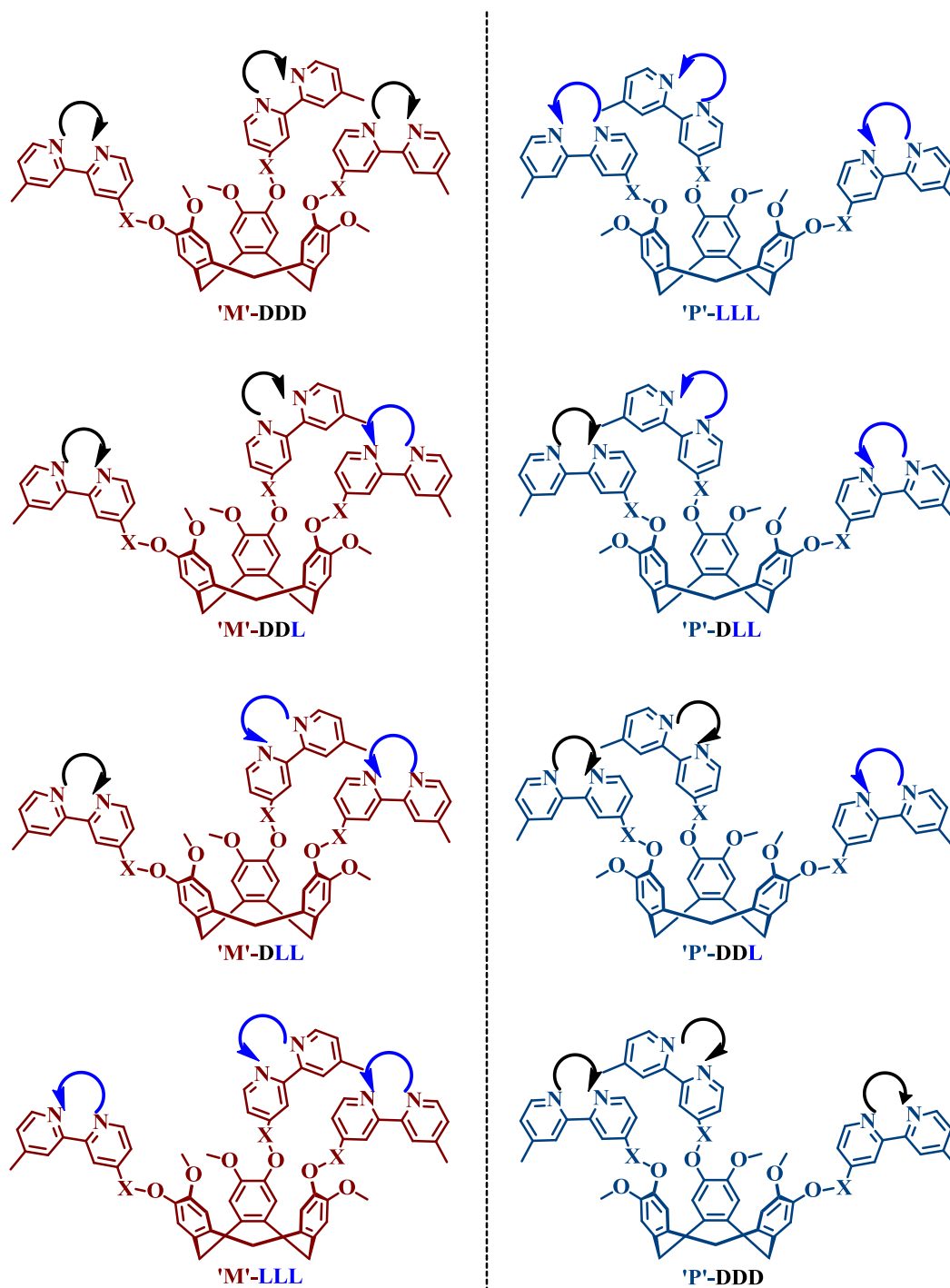
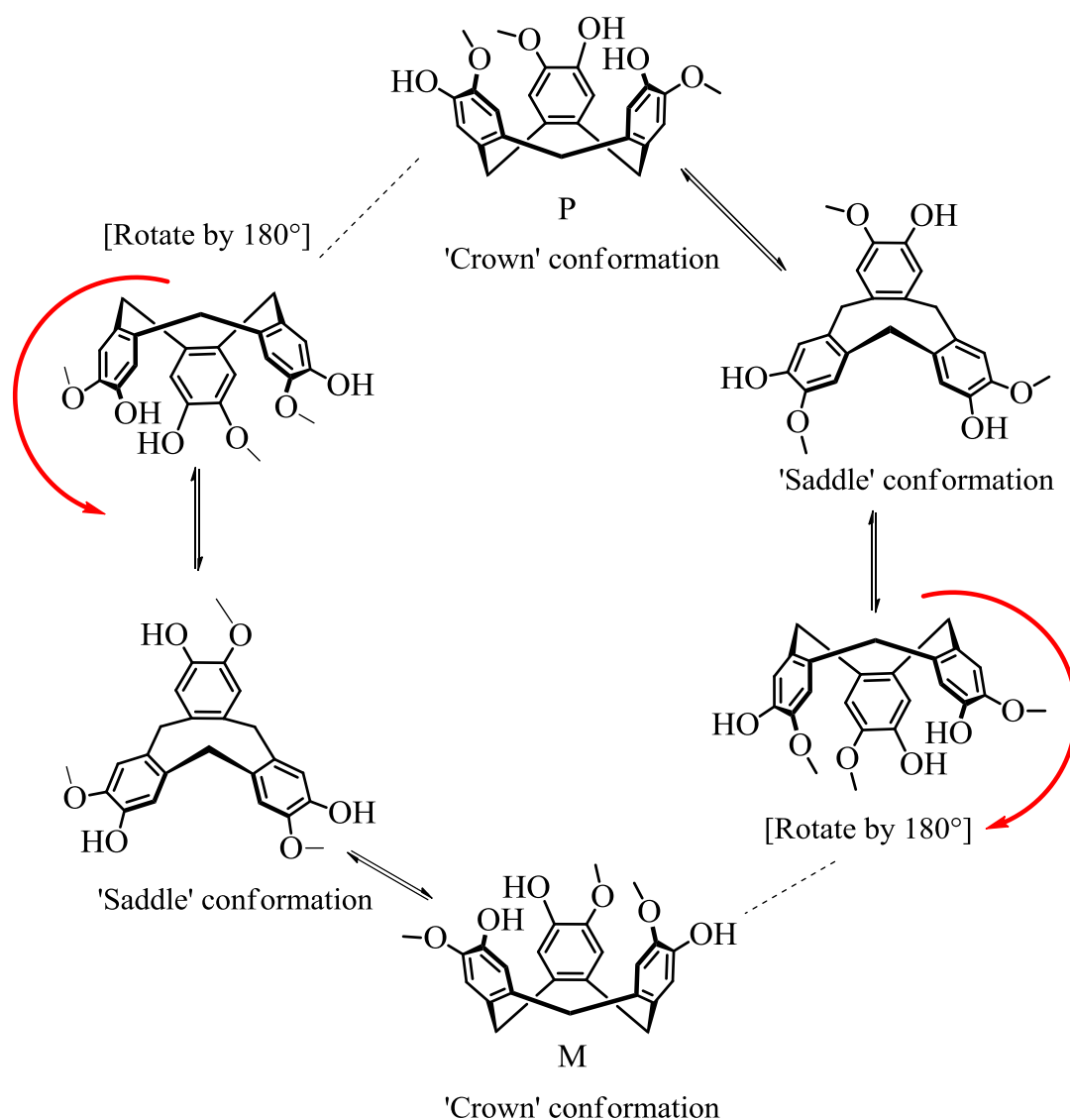


Figure 3.3: Possible stereoisomers of C1.2/C2.2; the *M* isomer shown in red and the *P* isomer in blue, with octahedral chirality represented by the curved arrows.

This assortment of stereoisomers could be simplified somewhat through chiral resolution of either the cyclotriguaiacylene ligands,^{22–24} or the metal precursor.^{13,25,26} However, chiral resolution of this ligand system is not facile; all previous attempts in the Hardie group to separate the *M* and *P* isomers of cyclotriguaiacylene ligands employing chiral HPLC facilities available at the UoL, have failed to isolate either

enantiomer cleanly. An additional obstacle to resolving the ligand enantiomers is the presence of the saddle conformation of the central cyclononatriene core. All ligands synthesised from CTG will adopt the lower-energy crown conformation, but the existence of the saddle form gives rise to a potential route to enantiomeric inter-conversion, as evidenced in Scheme 3.3.



Scheme 3.3: Potential inter-conversion cycle for all cyclotriguaiacylene ligands.

Starting from the crown conformation of the *P* isomer, the saddle form can be accessed through an outwards flexing motion of two of the substituted benzene rings, the opposite *M* enantiomer can then be formed through the same flexing outwards of the remaining benzene ring to re-form the crown conformation. This effect will clearly be dependent on the substituent groups around the upper-rim of

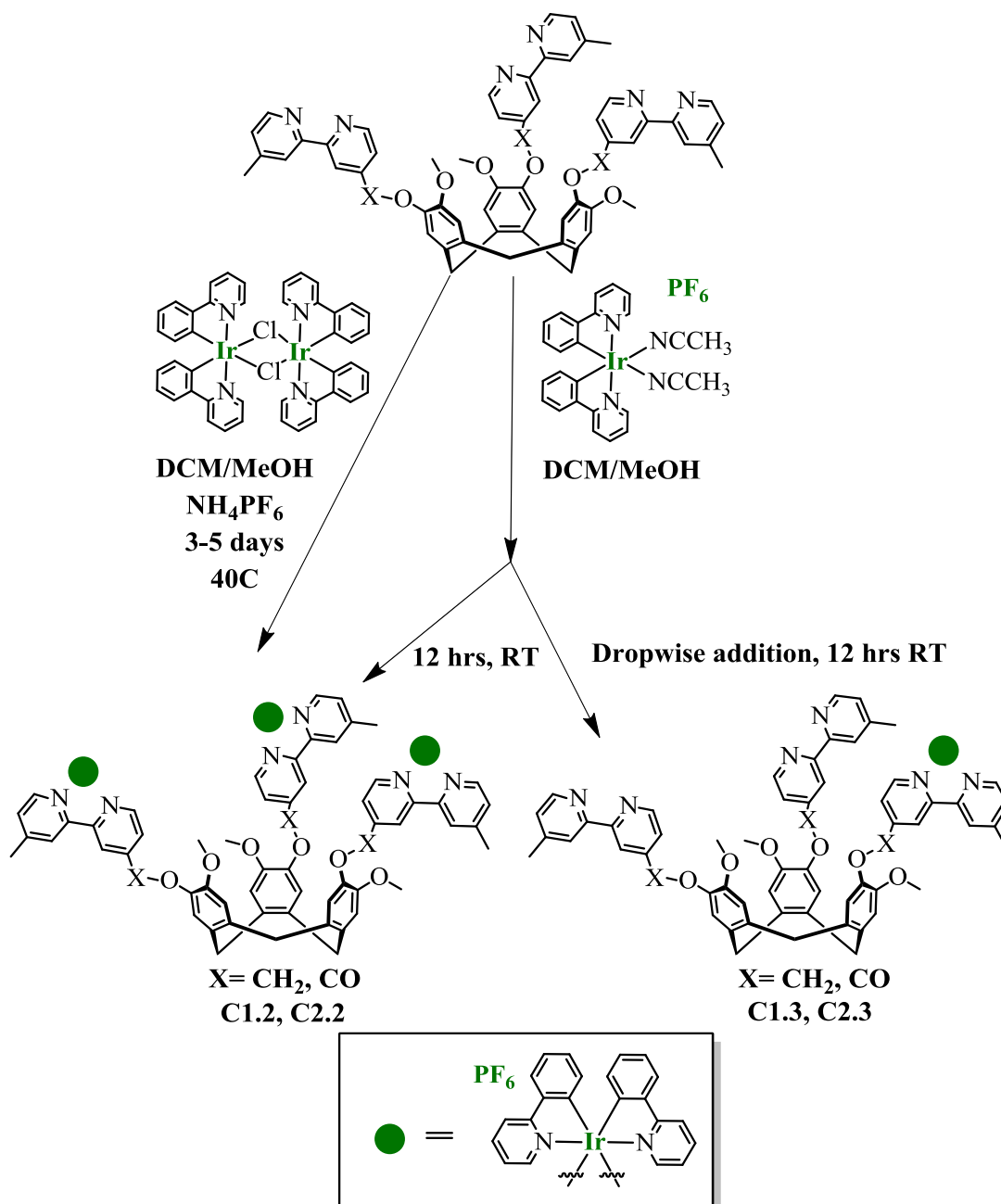
the cavitand, thus ligands containing more sterically demanding groups will possess a higher inter-conversion barrier, whereas cyclotrimeratrylene, the hexa-methoxy variant, has an isomerisation half-life of one day at room temperature.²⁷ Therefore, due to the relatively long reaction times, as well as the slightly elevated temperature the reaction is run at, chiral resolution of **L1** and **L2** is not a suitable approach in this instance.

The complexity induced through the stereoisomer contributions lead to complicated, but reproducible, ¹H NMR spectra, as discussed in more detail in section 3.4. As such, mass spectrometry was the main method employed to follow the formation of homo tri-metallic **C1.2** and **C2.2**.

3.3 Preparation of mono-metallic iridium species

Despite the success and ease of formation of the homo tri-metallic complexes, the aim of this work was to provide '*proof-of-principle*' that the tripodal ligand system herein could afford a suitable and stable ligand scaffold for the iridium complexes without impeding the desired photophysical properties. To build on and expand upon the functional output of this system, an effort towards the mono-metallic analogues was undertaken. Formation of a mono-metallic iridium system gives rise to two vacant coordination sites on the remaining bipyridine arms, and therefore gives a potential route to heterometallic or heteronuclear complexes.

Initial attempts to form the mono-metallic species employing the previously utilised μ -chlorobridged iridium dimer, as depicted in Scheme 3.4, all lead to over-metallation of the ligand binding sites, regardless of the high-dilution conditions and drop-wise addition employed. It is surmised that the very fact that the metal precursor is dimeric is the cause of this over-metallation, as when the bridging chloro-ligands are dissociated to enable binding to one bipyridine arm, the remaining iridium counterpart is also 'activated' towards ligand binding, whilst being in close proximity to a second bipyridine arm on the same ligand molecule. Thus, even if high-dilution conditions are rigorously implemented in the bulk solution, the local concentration on an individual molecular level around the discrete ligand arms is much higher. A monomeric metallotecton was therefore synthesised to overcome this obstacle and the resultant synthetic route shown in Scheme 3.4.



Scheme 3.4: Formation routes to homo tri-metallic C1.2 and C2.2 and their mono-metallic congeners C1.3 and C2.3.

Formation of the monomeric iridium precursor is facile, and proceeds in acetonitrile solvent in the presence of halide abstracting agent silver hexafluorophosphate. Gentle heating of the system gives rise to the acetonitrile adduct, already bearing a hexafluorophosphate anion. Reaction of the iridium monomer with an appropriate amount of **L1** or **L2** in a DCM:MeOH (9:1) solvent mixture, again employing high-dilution and drop-wise addition, furnished complexes **C1.3** and **C2.3** respectively in good yields. Through use of 0.9 equivalents of iridium precursor, the probability of

over-metallation is further decreased, and the only other species present in solution would be excess ligand, which can easily be removed through the drastic differences in solubility between uncomplexed, free ligand and any metallated species.

The formation of both mono-metallic species, **C1.3** and **C2.3**, can also be followed by *in situ* qualitative monitoring of the emission properties. The organic ligands **L1** and **L2** show negligible visible emission when excited at 405 nm, as does the monomeric iridium precursor. The mono-metallic products, however, both possess a *bis*-cyclometallated, N[^]N chelated iridium centre and are therefore emissive under the conditions described above. Consequently, formation of the desired product, **C1.3** or **C2.3**, can be qualitatively followed through the bright yellow or orange emission respectively, Figure 3.4.

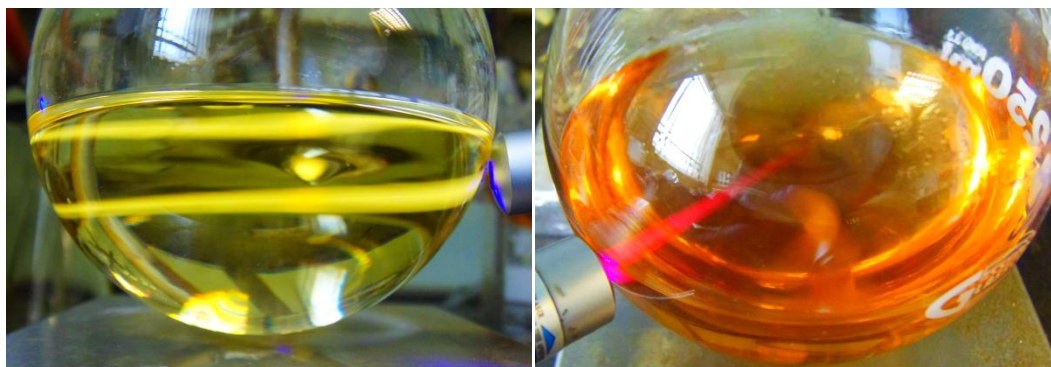


Figure 3.4: *In situ* emission of mono-metallic **C1.3** (left) and **C2.3** (right) with excitation at 405 nm.

Although only qualitative in nature, the difference “by-eye” of the emitted colour from the *in situ* emission demonstrates the versatility of this system, as seemingly minor structural alterations can lead to dramatic shifts in emission wavelength.

Homo tri-metallic **C1.2** and **C2.2** can of course also be formed through use of the monomeric precursor, reducing the required reaction time to only twelve hours, and allowing the reaction to proceed at room temperature when the correct stoichiometries are implemented. This approach leads to marginal increase in the achieved yields, presumably due to the negated need for an anion exchange step.

The HR ESI-MS for **C1.3** and **C2.3**, Figure 3.5, show the clean formation of the desired mono-metallic species, with the M⁺ peak of the cationic complex observed at 1455 and 1487 *m/z* respectively.

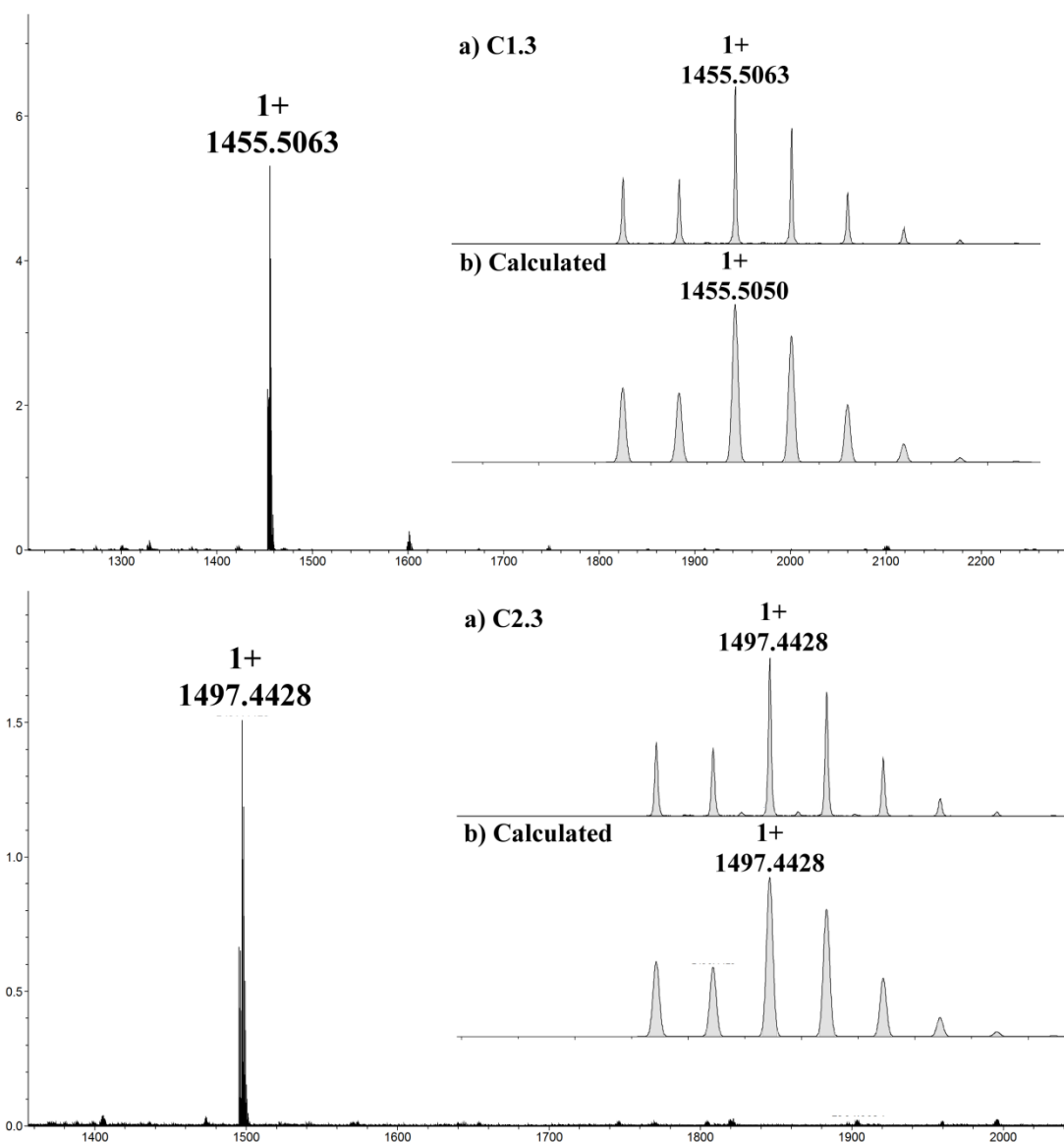


Figure 3.5: Expanded HR-ESI-MS of mono-metallic C1.3 (top) and C2.3 (bottom) with the isotope pattern of the 1+ peak and corresponding calculated spectrum of the M^+ peak, inset.

Although both C1.3 and C2.3 are commonly detected as the naked cation, without the associated hexafluorophosphate anion, the availability of the basic nitrogen donors on the vacant bipyridine arms gives a route to further protonation in the gas phase. Thus, C1.3 can be observed as [(1.3)], [(1.3)•H⁺] and [(1.3)•2(H⁺)] at 1455, 728 and 485 m/z respectively.

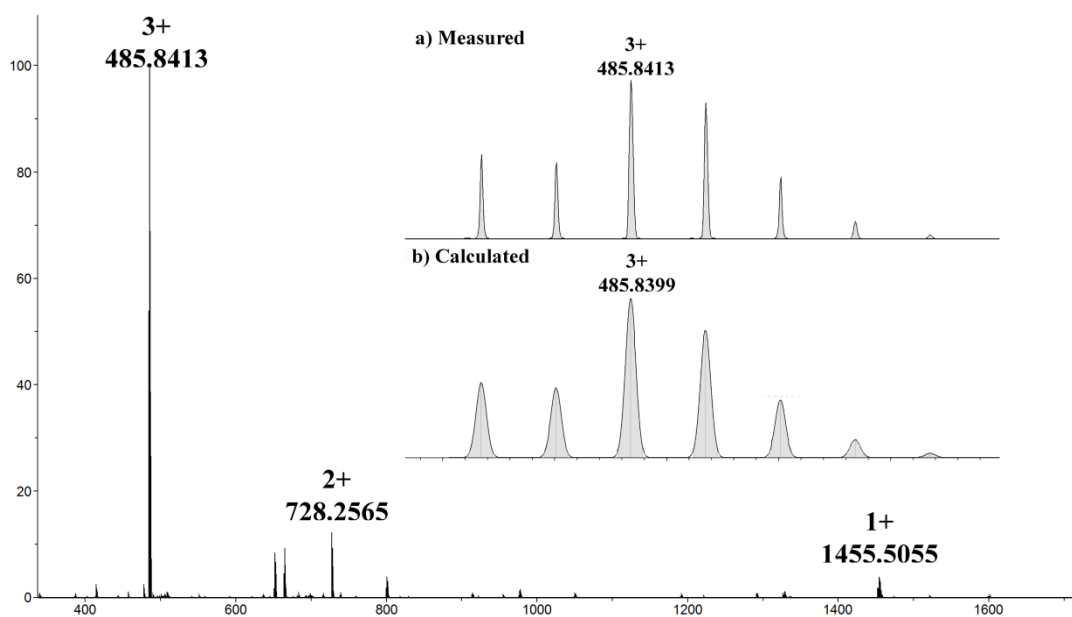


Figure 3.6: Expanded HR ESI-MS of mono-metallic C1.3 showing the variety of protonated species observed in the gas phase.

This phenomenon also occurs with C2.3 although not as cleanly, and is thus observed as [(2.3)], [(2.3)•H⁺] and [(2.3)•2(H⁺)] at 1497, 749 and 499 *m/z* respectively, as shown in Figure 3.7.

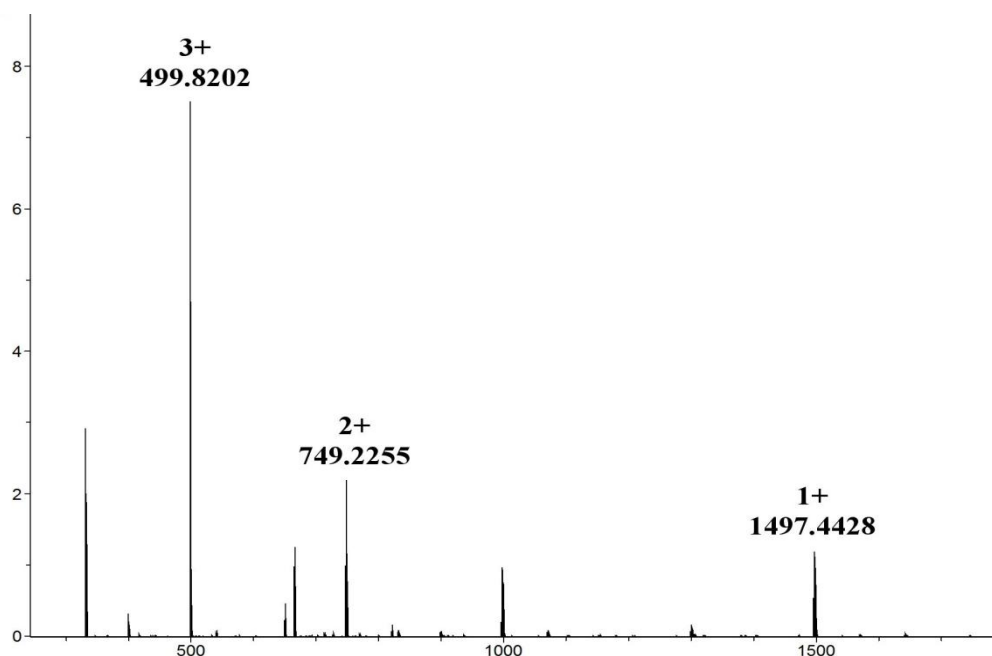


Figure 3.7 : Expanded HR-ESI MS of mono-metallic C2.3 showing the variety of protonated species observed in the gas phase.

3.4 Spectroscopic analysis of tri- and mono-metallic iridium complexes

The synthesis of all the previously discussed tri- and mono-metallic iridium complexes heavily relies on the use of high resolution mass spectrometry, to follow reaction progress and to ascertain when a reaction has gone to completion. The stability of these types of species is evidenced through the negligible degree of fragmentation observed, even throughout the ESI process, negating the need for specialist direct-injection techniques, and allowing for standard pre-programmed ESI methods to be implemented with ease. This is particularly advantageous as the ^1H NMR spectra of both the tri- and mono-metallic species are complicated. The complex enantiomeric mixtures of both ligand and metallotecton have previously been discussed in relation to the tri-metallic **C1.2** and **C2.2**, and although simplified in enantiomeric terms **C1.3** and **C2.3** show more complex spectra due to both vacant and metal-bound bipyridine arms existing in the same molecule.

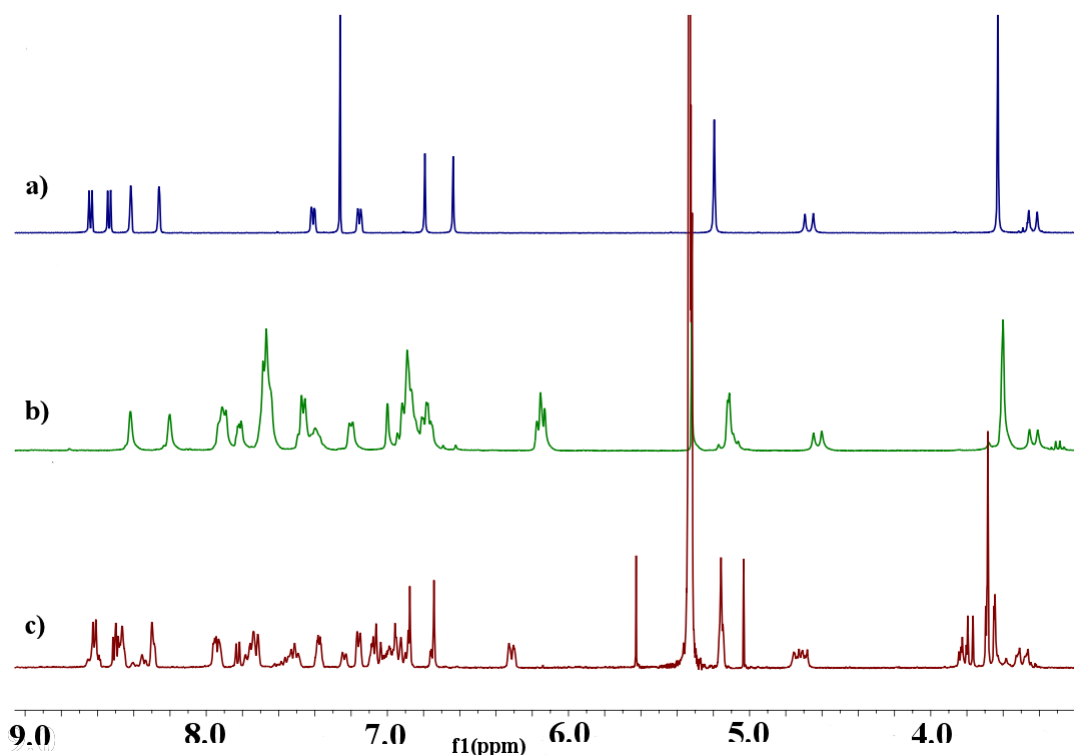


Figure 3.8: Stacked spectra exemplifying the complex ^1H NMR spectra recorded for a) *L1* in $d\text{-CHCl}_3$ b) tri-metallic **C1.2** in $d_2\text{-DCM}$ c) mono-metallic **C1.3** in $d_2\text{-DCM}$.

The ^1H NMR spectrum of **L1** in deuterated chloroform solvent, spectrum a) in Figure 3.8, demonstrates the C_3 symmetry of the free, un-complexed ligand, as one set of sharp peaks corresponding to the protons on all three equivalent bipyridine arms is observed.

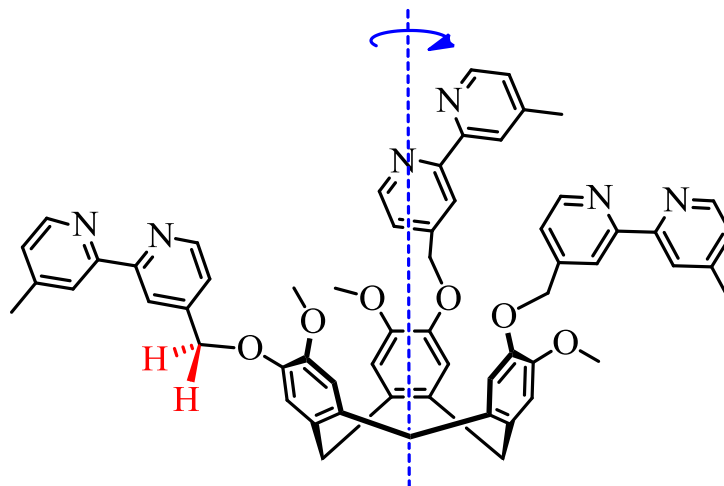


Figure 3.9: Structure of **L1**, with the methyl ether protons highlighted in red and the C_3 axis shown in blue.

The signal at 5.2 ppm corresponds to the two equivalent methylene protons on the methyl ether linking group between the cyclononatriene core and the bipyridine arm, shown in red in Figure 3.9. Due to free rotation on the NMR timescale they appear as a sharp singlet in the spectrum of **L1**. The observed spectrum of tri-metallic **C1.2**, by comparison, possesses noticeably broader peaks, due to the increase in steric bulk around each ligand arm, leading to more hindered rotation. This is most clearly evidenced through broadening of the previously discussed methyl ether peak at 5 ppm; the aforementioned sharp singlet starts to split into two, becoming *pseudo*-diastereomeric, as the chemical environment of the two protons represented therein becomes distinct.

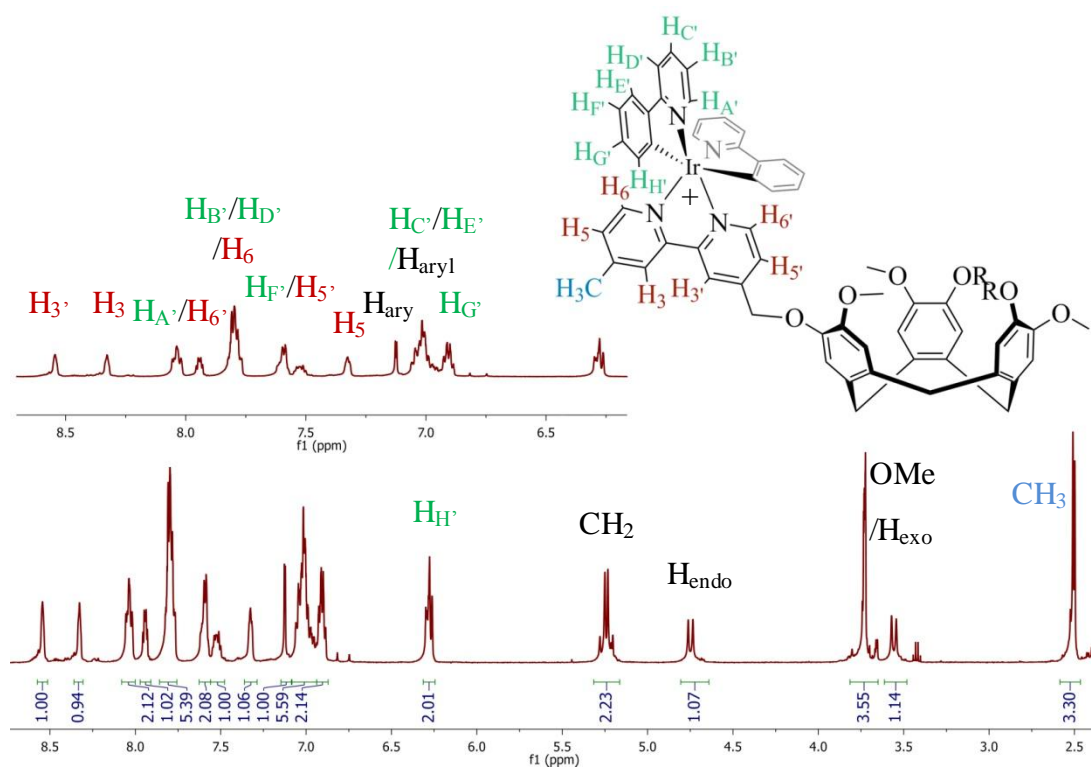


Figure 3.10: Expanded ^1H NMR spectrum of **C1.2** in CD_3CN with the aromatic region expanded for clarity and the chemical structure relating to the proton assignments inset (only one metallated arm shown for clarity, and anions not shown).

The precise assignments were derived from a 2D COSY NMR spectrum. The methyl, methoxy and *endo/exo* doublets are all seen at the expected chemical shifts of 2.5, 3.7, 3.5 and 4.6 ppm respectively. The previously sharp methylene CH_2 protons have become diastereomeric, displaying a roofed doublet at 5.2 ppm. Each of the resonances assigned to phenylpyridine-based protons has an integration of two, due to the two ancillary ligands bound to each iridium centre. The highest-field peak at 6.2 ppm is assigned to $\text{H}_{\text{H}'}$ on the phenylpyridine ligand, whilst the other phenylpyridine protons are assigned in green.

The spectrum of mono-metallic **C1.3** is thus even more complex. **C1.3** possesses two free bipyridine arms, which appear as sharp, well resolved peaks in the spectrum, and one iridium-bound bipyridine arm giving rise to broader peaks.

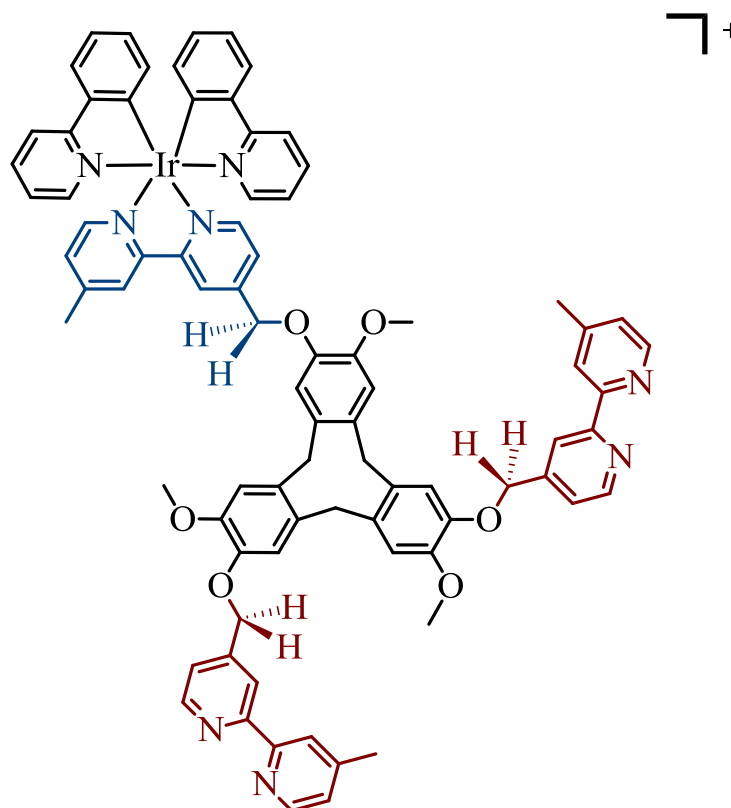


Figure 3.11: Expanded structure of mono-metallic C1.3 to demonstrate the inequivalence of the bound and un-bound bipyridine arms.

Again, this inequivalence is demonstrated through the splitting of the peak belonging to the methyl ether protons at 5.2 ppm; displaying a sharp singlet assigned to the four protons bound to the free-bipyridine arms (shown in red, Figure 3.11), and a smaller, broader peak assigned to the two protons on the methyl ether bridge of the bipyridine arm bound to the lone iridium centre (shown in blue, Figure 3.11). Binding of one ligand arm to the iridium metallotecton also generates inequivalence between protons on different bipyridine arms.

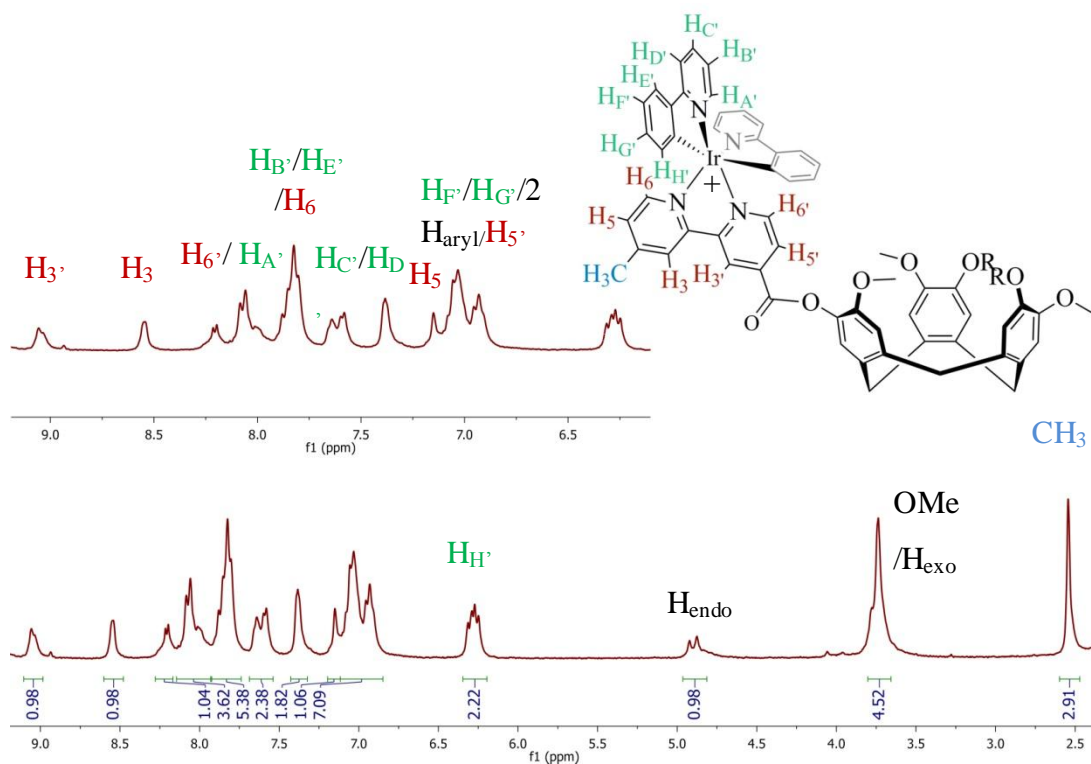


Figure 3.12: Expanded ^1H NMR spectrum of **C2.2** in CD_3CN with the aromatic region expanded for clarity and the chemical structure relating to the proton assignments inset (only one metallated arm shown for clarity).

Again, COSY NMR was employed to assign the complex aromatic region, as shown in Figure 3.12. The methyl, methoxy and *endo/exo* doublets are all seen at the expected chemical shifts. Once again, the highest field aromatic resonance, at 6.7 ppm, is assigned to $\text{H}_{\text{H}'}$ of the phenylpyridine ancillary ligand. The phenylpyridine protons are assigned in green, whilst those belonging to the aromatic ligand scaffold are assigned in red. As with **C1.2**, the aromatic region of **C2.2** can be rationalised through consideration of the total peak integrals; those peaks assigned to protons on the ligand scaffold should integrate to one proton, whilst those on the ancillary ligand should integrate to two protons each. The complex multiplet around 7 ppm thus integrates to seven protons, assigned to two from each of $\text{H}_{\text{F}'}$ and $\text{H}_{\text{G}'}$, two aryl protons from the ligand scaffold and $\text{H}_{\text{5}'}$ from the bipyridine arm, totalling seven protons.

The equivalent complexity is seen in the spectra of **L2**, tri-metallic **C2.2** and mono-metallic **C2.3**.

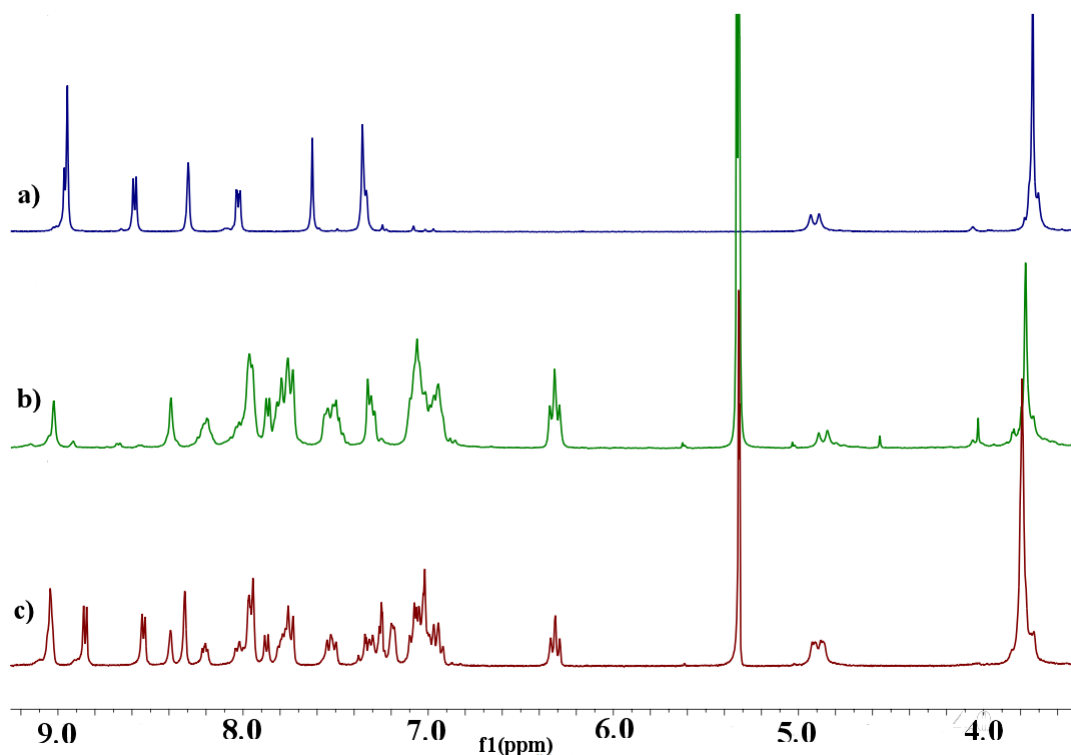


Figure 3.13: Stacked spectra exemplifying the complex ¹H NMR spectra recorded for a) **L2** in *d*₆-DMSO b) tri-metallic **C2.2** in *d*₂-DCM c) mono-metallic **C2.3** in *d*₂-DCM.

The ¹H NMR spectrum of **L2** was recorded in deuterated dimethyl sulphoxide solvent, due to the very low solubility of the ligand. Once again, the C₃ symmetry of the free ligand is evidenced through one set of sharp peaks belonging to the aromatic protons on the equivalent bipyridine arms. The resonance assigned to the *exo*-proton on the central methylene-bridge is hidden under the resonance of the methoxy group, and therefore seen as a shoulder at 3.7 ppm. Analogous to **C1.2**, **C2.2** displays slightly broadened peaks due to the increased steric bulk around the bipyridine arm. The ¹H NMR spectrum of mono-metallic **C2.3** is essentially a superposition of spectra *a* and *b*, possessing sharp peaks assignable to the protons on the unbound bipyridine arms, and broader peaks of the metal-bound arm.

3.5 Photophysical properties of tri- and mono-metallic Ir species

The photophysical spectra were run at the University of St Andrews by PhD student Diego Rota Martir in collaboration with the group of Dr Eli Zysman-Colman. The photophysical properties of both tri-metallic species **C1.2** and **C2.2**, and mono-

metallic species **C1.3** and **C2.3**, were investigated in deaerated acetonitrile solvent, at 298 K. The complexes were also incorporated into poly(methyl methacrylate) (PMMA) doped thin-films at 5 wt %.

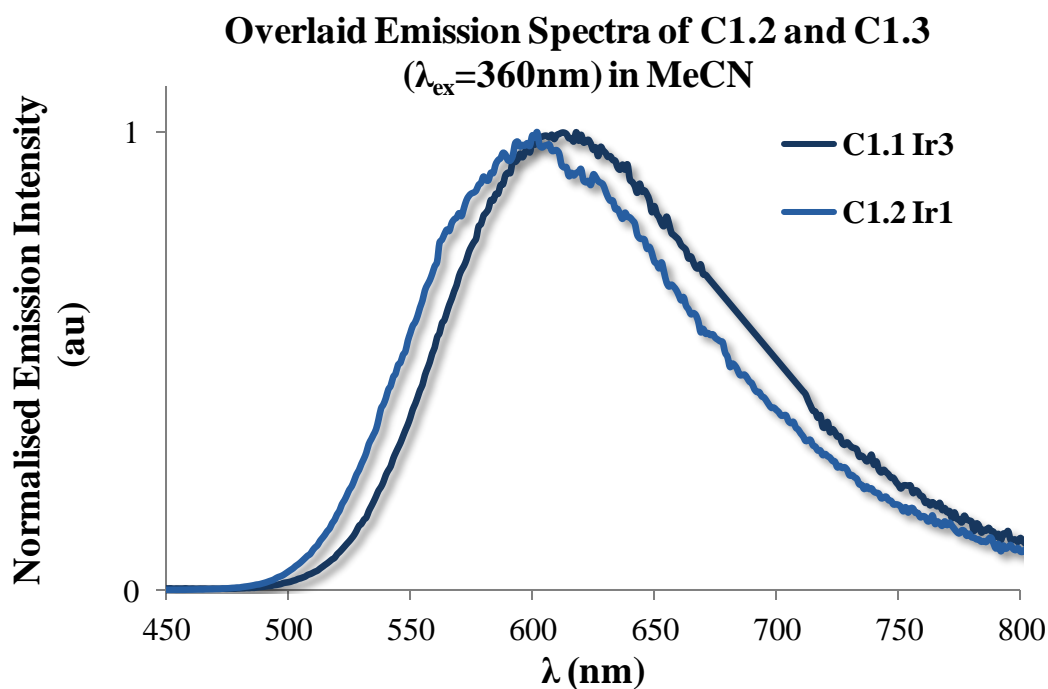


Figure 3.14: Overlaid emission spectra for C1.2 and C1.3 recorded in deaerated acetonitrile.

The two complexes, both tri- and mono-metallic **C1.2** and **C1.3**, comprised of the ether-linked **L1**, both show very similar emission profiles. Tri-metallic **C1.2** possesses a λ_{max} when excited at 360 nm of 615 nm that trails off in a traditional bell-shaped curve. Mono-metallic **C1.3** shows a similar λ_{max} of 601 nm, displaying a hypsochromic shift to higher-energy than **C1.2** by just 14 nm. The mono-nuclear analogue, $[\text{Ir}(\text{ppy})_2(\text{dmb})]^+$ where dmb=dimethylbipyridine, possess a λ_{max} of 580 nm in analogous deaerated acetonitrile.²⁸ Thus, the emission profiles of the tri- and mono-metallic systems both show a slight bathochromic shift by ~20-30 nm. Analysis of the resultant emission lifetimes associated with **C1.2** and **C1.3**, presented in Table 3.1, indicates similar values for the emission peaks, of 586 and 530 ns respectively, displaying a significant improvement to the reported value of 310 ns for the mono-nuclear system.

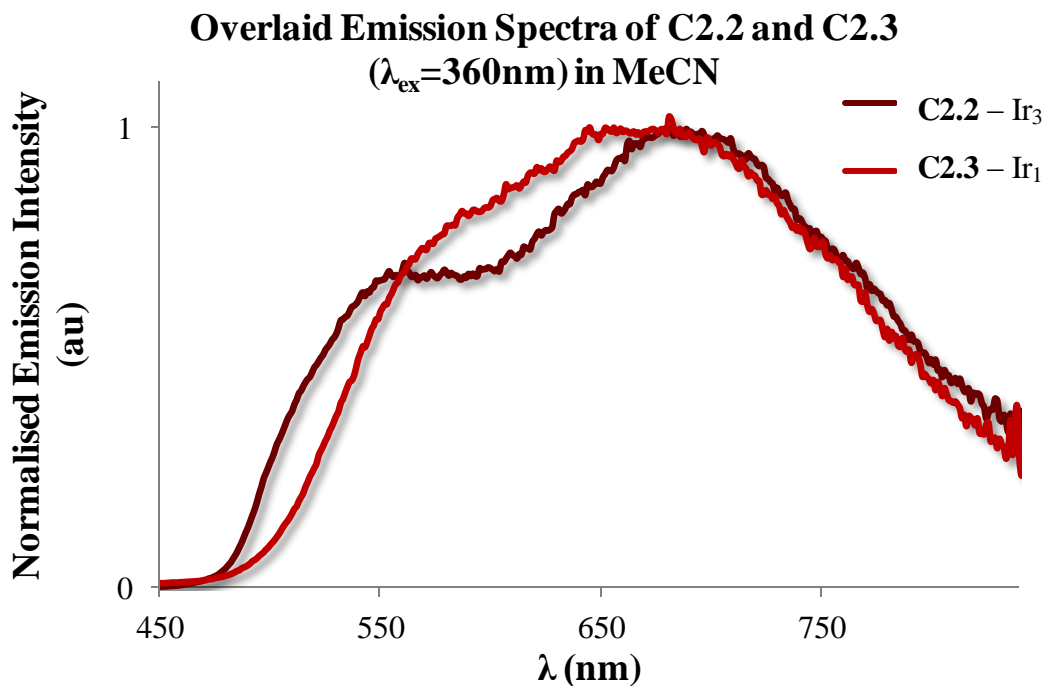


Figure 3.15: Overlaid emission spectra of C2.2 and C2.3 recorded in deaerated acetonitrile.

Conversely, ester-linked systems tri- and mono-metallic **C2.2** and **C2.3**, display markedly different emission profiles, both in regards to each other and to **C1.2-3**. As is evidenced in Figure 3.15, the emission profiles of **C2.2** and mono-metallic **C2.3** include two distinct emission peaks, comprising of one peak centred on 560 nm, and another peak at lower energy, around 680 nm.

Tri-metallic **C2.2** possesses a strong high energy emission peak (λ_{em}) at 563 nm, blue shifted from the analogous single emission of **C1.2**. Nonetheless, emission of **C2.2** “by-eye” is substantially red-shifted; this is due to the significant proportion of light emitted above ~ 650 nm. The second λ_{em} at 686 nm dominates the observed emission, with the ratio of high-energy emission (HEE) to low-energy emission (LEE) approximately 0.79:1. Mono-metallic **C2.3** also shows dual-emission, however the peaks are less distinct, with the high energy peak (λ_{em} 566 nm) appearing almost as a shoulder to the lower energy peak at 686 nm. The ratio of emission intensities, HEE:LEE, is 0.7:1, whereby the LEE peak dominates the emission intensity.

The observed dual-emission of **C2.2** and **C2.3**, and conversely the lack of dual emission seen in **C1.2** and **C1.3**, is attributed to the increased conjugation within the **L2** ligand scaffold. The presence of the ester linking group between central

cyclononatriene core and bipyridine arm gives rise to a potential conjugation route, allowing for a fully conjugated ligand motif, one that is not possible with the analogous **L1**. Thus, it follows that organic-type ligand-centred or intra-ligand transitions are responsible for the HEE peaks, whereas the more familiar triplet metal-to-ligand charge-transfer, ³MLCT, is responsible for the LEE peaks. Previous examples have shown that highly conjugated systems, such as those containing extended phenanthroline and phenylbenzoquinoline analogues as both N[^]N and cyclometallating ligands, display similar dual emission, in this case in the near IR region.²⁹ Whilst the precise contributions to the HOMO/LUMO levels from the two chelating and cyclometallating ligands are reasonably complex, the result is an emission profile showing clear dual-emission and a strong bathochromic shift with respect to less conjugated analogues.

Complex	λ_{em} (nm) ^b	Φ_{PL} (%) ^c	t_e (ns) ^d
1.2	615	9.8	586
1.3	601	14.4	530
2.2	563 (0.79), 686 (1)	1.4	20 (0.07), 558 (0.93)
2.3	566 (0.7), 686 (1)	1.0	22 (0.82), 498 (0.18)

Table 3.1: Emission maxima, quantum yield and lifetime analysis of C1.2-3 and C2.2-3 in deaerated acetonitrile solution.

Lifetime analysis of the distinct emission peaks substantiates this assignment. Emission peaks at 563 and 566 nm in **C2.2** and **C2.3** respectively, possess lifetimes of just 20 and 22 ns, indicative of short-lived organic-based transitions, whereas the lower-energy peaks at 686 nm show much longer lifetimes of 558 and 498 ns, suggesting a longer-lived phosphorescence process is responsible. Relative intensity values are shown in brackets, both with regards to the emission maxima and the lifetimes. The lifetime of tri-metallic **C2.2** is dominated by the 686 nm emission peak, giving rise to a lifetime of 558 ns that accounts for 93% of the overall lifetime. Conversely, the lifetime of mono-metallic **C2.3** is dominated by the ligand-based

566 nm peak, giving rise to a short 22 ns lifetime that accounts for 82% of the overall lifetime. This disparity can be rationalised through consideration of the molecular structure; tri-metallic **C2.2** contains three times as many iridium centres as **C2.3**, therefore it follows that the resultant lifetime would be more heavily dominated by iridium-based MLCT emission. The inverse effect can also be recognised as the lifetime attributable to **C2.3**, containing two un-bound ligand arms, is dominated by emission from ligand-centred peaks, with the lower-energy 686 nm peak only responsible for 18% of the overall lifetime.

The resultant photoluminescent quantum yield, Φ_{PL} , of the four complexes also demonstrates the distinction between the two ligand sub-sets. Both complexes containing **L1** display photoluminescent quantum yields (PLQY) larger than the **L2** analogues by a factor of ten. This suggests that the decisive factor in determining the emission efficiency is the ligand scaffold itself, and not the degree of metallation. Accordingly, there must be a route towards non-radiative decay present in **L2** that is not present in **L1**, leading to the observed quenching of the PLQY.

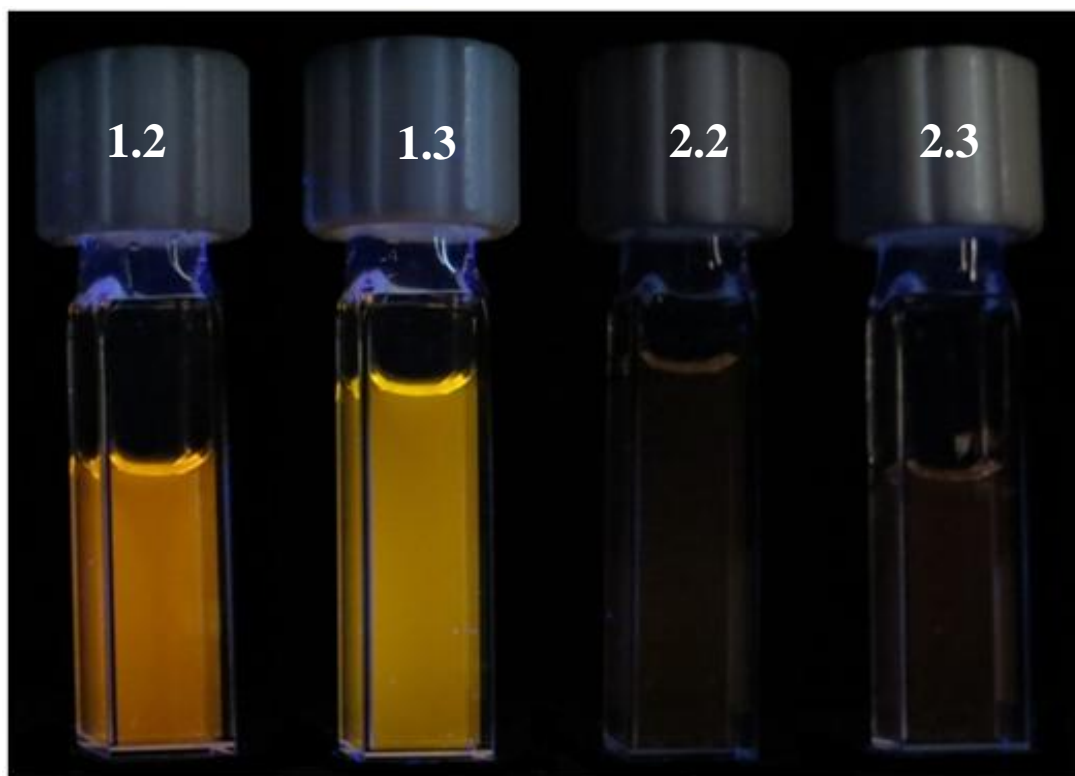


Figure 3.16: Dark-room image revealing the contrast in emission properties between L1 and L2 containing complexes.

The improved PLQY of mono-metallic **C1.3** versus tri-metallic **C1.2** can be speculatively rationalised through consideration of the concentration of chromophores. **C1.3** contains just one emissive centre, whereas **C1.2** contains three chromophore units, held in close proximity to each other, thus giving rise to potential energy transfer mechanisms which may be non-radiative, therefore leading to the observed decrease in PLQY. Conversely, the opposite is true for tri-metallic **C2.2** versus **C2.3**; the mono-metallic **C2.3** displays a smaller PLQY. However, this may be due in part to the previously mentioned quenching effect of **L2** itself, since mono-metallic **C2.3** can be thought of as containing more ligand character than tri-metallic **C2.2**.

The photophysics of all four complexes were also investigated when incorporated into doped PMMA thin films at 5 weight %. The rationale behind this is to examine the photophysics where collisional and vibrational quenching is less of a factor; this is achieved through constraint in an inert matrix.

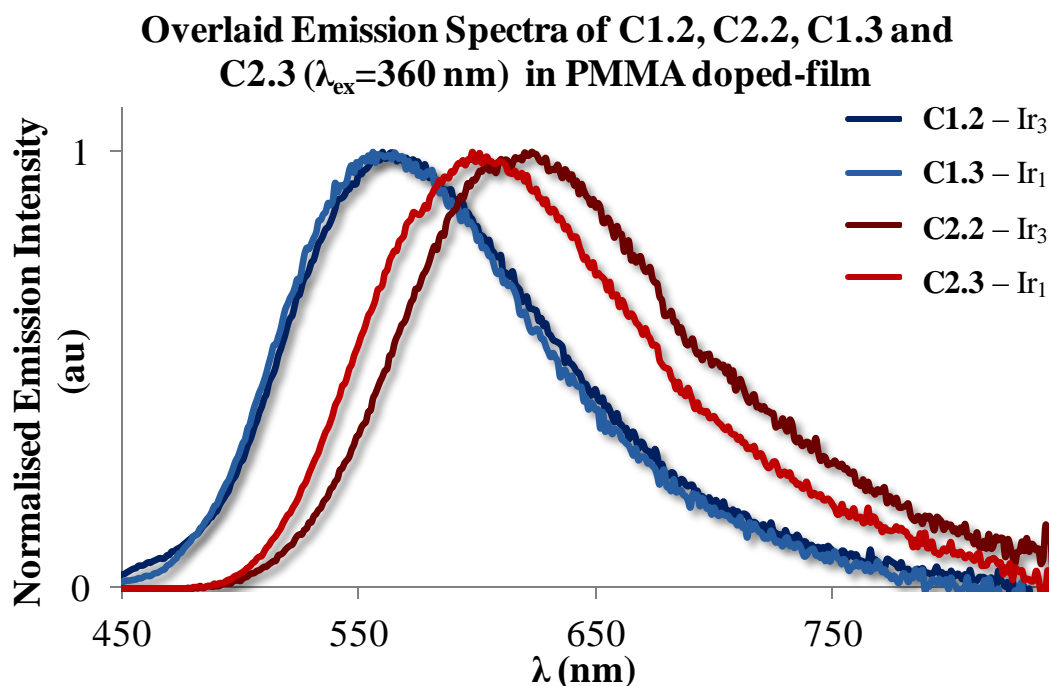


Figure 3.17: Overlaid emission spectra of C1.2, 2.2, 1.3 and 2.3 when incorporated into a doped PMMA thin-film.

As evidenced above in Figure 3.17, the λ_{max} for all four complexes are blue-shifted to higher energy, regardless of the ligand employed. This can be rationalised by consideration of the vibrational energy of the emissive transitions; when a complex is incorporated into a thin-film it is essentially restrained and thus experiences less

vibrational quenching. If less energy is lost through vibrations, then more energy remains to be emitted, leading to the higher energy emission observed in the PMMA films.

Complex	λ_{em} (nm)	Φ_{PL} (%)	t_e (ns)
1.2	565	17.7	194 (0.6), 960 (0.6)
1.3	566	26.4	376 (0.26), 1210 (0.74)
2.2	625	13.9	248 (0.35), 1003 (0.65)
2.3	601	21.3	291 (0.21), 1032 (0.79)

Table 3.2: Emission maxima, quantum yield and lifetime analysis of C1.2-3 and C2.2-3 in PMMA doped thin-films.

The general trends observed for both mono- and tri-metallic iridium complexes are; significant blue-shifts in emission peak, larger PLQY and much longer lifetimes or lifetime components. Again, the longer lifetimes can be explained through incarceration of the complex in an inert medium which retards vibrational and non-radiative emission.

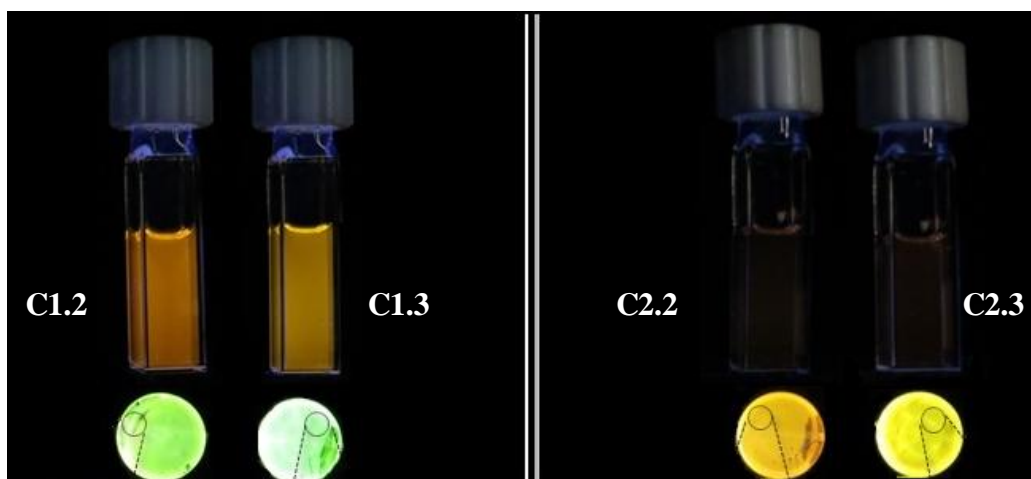


Figure 3.18 : Dark-room images of **C1.2**, **1.3**, **2.2** and **2.3**. Emission in deaerated acetonitrile solution is shown (top) for comparison, emission in PMMA doped thin-films shown underneath. [$\lambda_{ex}=360$ nm].

The visible blue-shift from acetonitrile solution to PMMA thin-film can be seen in Figure 3.18, particularly for complexes **C1.2** and **C1.3**. Whilst the greatly increased PLQY is most obvious in the dark-room images of complexes **C2.2** and **C2.3**; where in solution there is barely any visible emission, whilst under irradiation from the same source, there is significant emission from the PMMA thin films.

3.6 Conclusions and further direction

A novel route to homo tri-metallic iridium systems **C1.2** and **C2.2** has been reported, ultimately utilising a more reactive iridium monomer as a precursor to shorten reaction times and allow the reaction to proceed at ambient temperatures. The mono-metallic congeners **C1.3** and **C2.3** have also been synthesised employing high-dilution conditions to preclude over-metallation.

The remarkably clean formation of all systems was extensively followed by HR ESI-MS, due to the distinctive iridium isotope pattern and owing to the complex ^1H NMR spectra obtained.

Photophysical analysis leads to some interesting conclusions about the relative importance of ligand structure versus degree of metallation. There is a clear divide between complexes derived from **L1** as opposed to **L2**; those formed from **L2** show dual-emission from both ligand-centred and $^3\text{MLCT}$ transitions, whereas **L1**-based complexes exhibit a singular emission peak with PLQYs improved by a factor of ten.

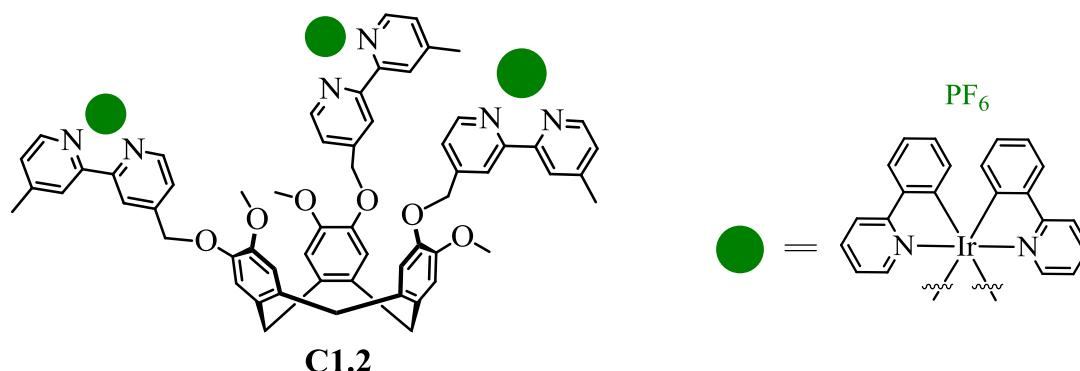
When the complexes are incorporated into PMMA doped thin-films the emission is blue-shifted, and the both the PLQY and lifetimes improved. This is most likely due to decreased vibrational quenching in the PMMA matrix. Incorporation into a thin film also lead to significant improvements in the photophysical properties of the ester-linked **C2.2** and **C2.3**.

The reliable formation of mono-metallic **C1.3** and **C2.3** opens the avenue of exploration towards heteroleptic complexes; whereby sequential addition of varied iridium metallotectons could lead to formation of complexes where the iridium centres bear distinct ancillary ligands. The functionality already present on the ancillary phenylpyridine ligands bound to the iridium metallotecton can be modified with ease, and thus pertinent combinations can be incorporated into a single complex in order to tune the resultant photophysics.^{1,4,21,28,30-32}

The vacant binding sites on mono-metallic **C1.3** and **C2.3** by no means have to be subsequently reacted with the same metal; heteronuclear complexes are also a possibility, leading to an even wider range of potential photophysical properties.

3.7 Experimental

3.7.1 Synthesis

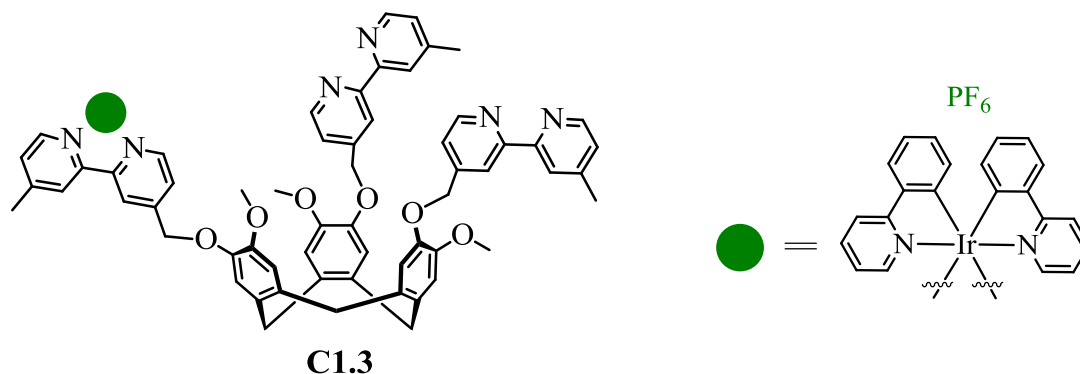


Preparation of complex [(Ir(III)(2-phenylpyridine)₂]₃(tris(4-[4'-methyl-2, 2'-bipyridyl]methyl)CTG)₃(PF₆⁻) (C1.2):

[Ir(ppy)₂(Cl)]₂ (0.084 g, 0.078 mmol) and (±)-**L1** (0.050 g, 0.052 mmol) were combined in a mixture of DCM/MeOH (10:1) (9 mL total) and heated to 40°C. The reaction was followed by MS, and heating was continued until the main peak seen was the [Ir(ppy)₂]₃(**L1**)³⁺ cationic complex. The reaction mixture was taken to dryness *in vacuo* and redissolved in MeCN (5 mL), halide exchange was accomplished by addition of an aqueous solution of NH₄PF₆. The soluble PF₆⁻ salt did not precipitate and the MeCN was removed *in vacuo*, leaving an aqueous residue that was extracted with DCM, dried over MgSO₄ and concentrated to ~1 mL *in vacuo*. Diethyl ether was added to the solution to give the title product as a bright yellow powder (0.130 g, 88%); ¹H NMR (300 MHz, CD₃CN) δ 8.52 (s, 1H), 8.30 (s, 1H), 8.00 (d, *J* = 6.6 Hz, 2H), 7.91 (d, *J* = 3.2 Hz, 1H), 7.78 (d, *J* = 5.5 Hz, 5H), 7.56 (d, *J* = 5.5 Hz, 2H), 7.50 (s, 1H), 7.30 (d, *J* = 5.3 Hz, 1H), 7.10 (s, 1H), 6.99 (t, *J* = 7.7 Hz, 5H), 6.88 (t, *J* = 7.0 Hz, 2H), 6.25 (t, *J* = 6.6 Hz, 2H), 5.22 (d, *J* = 3.1 Hz, 2H), 4.72 (d, *J* = 13.7 Hz, 1H), 3.70 (s, 3H), 3.53 (d, *J* = 13.6 Hz, 1H), 2.47 (s, 3H); ¹³C{¹H} NMR (75 MHz, CD₃CN) δ 168.43, 156.99, 156.15, 152.95, 151.96, 151.47, 151.41, 151.30, 150.88, 150.03, 150.00, 149.46, 147.06, 145.02, 144.96, 139.42, 134.81, 132.94, 132.54, 132.46, 131.31, 130.11, 126.93, 126.89, 126.31, 125.84, 124.36, 123.43, 123.10, 123.04, 120.79, 118.26, 114.94, 70.13, 56.78, 36.25, 21.44; TOF-MS ESI: *m/z* = 818.9015 (M³⁺); Analysis for C₁₂₆H₁₀₂F₁₈Ir₃N₁₂O₆P₃ (% calculated, found) C (52.33, 52.40) H (3.56, 3.60) N (5.81, 5.70); Infrared Analysis

(FT-IR, cm^{-1}) 556, 737, 756, 835, 1031, 1144, 1267, 1421, 1477, 1508, 1607 (s),
3044 (b)

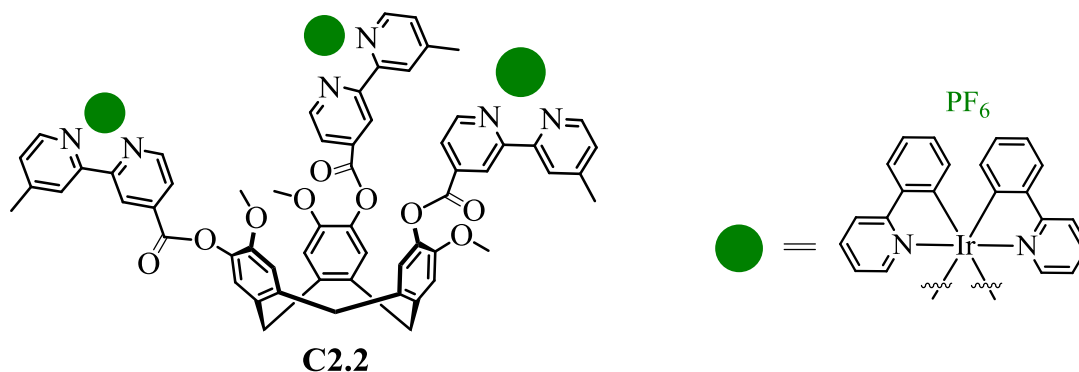
Preparation of complex [(Ir(III)(2-phenylpyridine)₂)(tris(4-[4'-methyl-2, 2'-bipyridyl]methyl)CTG)].(PF₆⁻) (C1.3):



[(ppy)₂(MeCN)₂].PF₆ (0.035 g, 0.048 mmol) in DCM (100 mL) was added dropwise over a period of 1 hour to a stirring solution of (±)-**L1** (0.046 g, 0.048 mmol) in a mixture of DCM/MeOH (10:1) (100 mL total) at room temperature. Over time, after addition of the pale yellow iridium precursor solution to the colourless ligand solution, the reaction mixture became bright yellow and was analysed by MS, stirring was continued until the main peak seen was the [Ir(ppy)₂](L1)⁺ cationic complex. The reaction mixture was taken to dryness *in vacuo*, re-dissolved in MeCN then filtered through celite to remove any unreacted **L1**. The MeCN solution was removed *in vacuo*, the complex re-dissolved in DCM and diethyl ether was added to the solution to give the title product as a bright yellow powder (0.063 g, 82.8%) ¹H NMR (300 MHz, CD₂Cl₂) δ 8.69 – 8.55 (m, 1H), 8.49 (dd, *J* = 9.6, 5.3 Hz, 1H), 8.32 (dd, *J* = 15.3, 5.7 Hz, 1H), 7.94 (d, *J* = 7.6 Hz, 1H), 7.83 (d, *J* = 5.6 Hz, 1H), 7.75 (dd, *J* = 12.6, 7.1 Hz, 1H), 7.51 (t, *J* = 5.6 Hz, 1H), 7.38 (d, *J* = 5.7 Hz, 1H), 7.24 (d, *J* = 5.4 Hz, 1H), 7.16 (d, *J* = 6.5 Hz, 1H), 7.12 – 6.91 (m, 2H), 6.88 (d, *J* = 2.7 Hz, 1H), 6.79 – 6.67 (m, 1H), 6.32 (d, *J* = 7.5 Hz, 1H), 5.15 (d, *J* = 3.0 Hz, 1H), 4.72 (dd, *J* = 14.0, 8.6 Hz, 1H), 3.91 – 3.74 (m, 1H), 3.67 (dd, *J* = 12.8, 2.6 Hz, 2H), 3.50 (dd, *J* = 14.0, 5.1 Hz, 1H), 2.58 (s, 1H), 2.44 (s, 2H); ¹³C{¹H} NMR (126 MHz, DMSO) δ 166.70, 166.61, 155.23, 154.63, 154.58, 151.37, 150.28, 149.12, 148.89, 148.78, 148.64, 147.86, 147.73, 147.53, 145.74, 143.63, 143.57, 138.50, 138.45, 132.74, 131.79, 131.69, 130.86, 130.01, 129.18, 124.85, 123.66, 122.02, 121.53, 121.10, 119.80, 118.11, 115.39, 113.81, 68.64, 55.88, 55.65, 34.95, 20.71, 20.53.; TOF-MS ESI: *m/z* = 1455.5051 (M⁺); Analysis for C₈₂H₇₀F₆IrN₈O₆P. (% calculated, found) C (61.53, 58.65) H (4.41, 4.30)

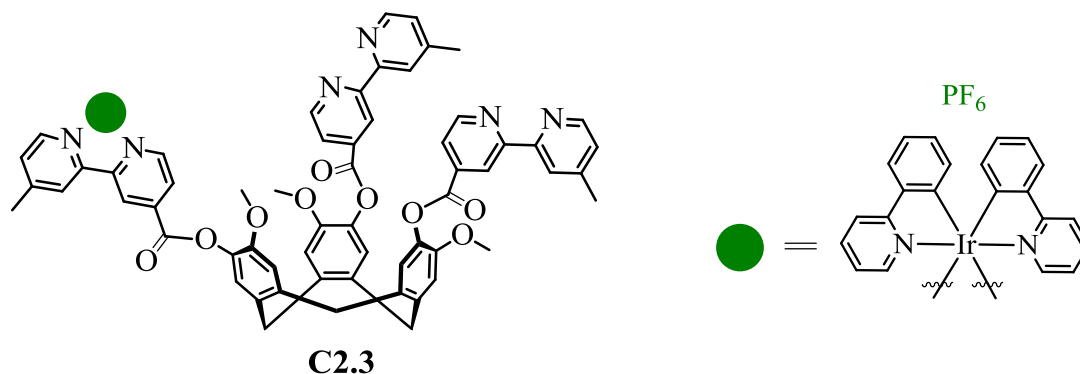
N (7.00, 6.70); Infrared Analysis (FT-IR, cm^{-1}) 556, 737, 756, 839, 1031, 1144, 1266, 1422, 1477, 1508, 1606 (s), 3052 (b)

Preparation of complex [Ir(III)(2-phenylpyridine)₂]₃(tris(4-[4'-methyl-2, 2'-bipyridyl]carboxy)CTG)]₃(PF₆⁻) (C2.2):



[Ir(ppy)₂(Cl)]₂ (0.080 g, 0.074 mmol) and (±)-**L2** (0.050 g, 0.050 mmol) were combined in a mixture of DCM/MeOH (10:1) (9 mL total) and heated to 40°C. The reaction was followed by MS, and heating was continued until the main peak seen was the [Ir(ppy)₂]₃(**L2**)³⁺ cationic complex. The reaction mixture was taken to dryness *in vacuo* and re-dissolved in MeCN (5 mL), halide exchange was accomplished by addition of an aqueous solution of NH₄PF₆. The soluble PF₆⁻ salt did not precipitate and the MeCN was removed *in vacuo*, leaving an aqueous residue that was extracted with DCM, dried over MgSO₄ and concentrated to ~1 mL *in vacuo*. Diethyl ether was added to the solution to give the title product as a bright orange powder (0.092 g, 62%) ¹H NMR (300 MHz, DMSO-d₆) δ 9.29 (d, *J* = 5.3 Hz, 1H), 9.06 (d, *J* = 5.5 Hz, 1H), 8.24 (dd, *J* = 18.3, 7.7 Hz), 8.12 (d, *J* = 5.8 Hz), 7.94 (t, *J* = 8.4 Hz), 7.78 (dd, *J* = 12.3, 5.8 Hz), 7.71 (d, *J* = 5.7 Hz), 7.59 (dd, *J* = 12.0, 5.4 Hz), 7.51 (s, 1H), 7.32 – 7.21 (m), 7.20 – 7.09 (m), 7.03 (t, *J* = 7.2 Hz), 6.91 (t, *J* = 7.1 Hz), 6.18 (dd, *J* = 12.4, 7.5 Hz) [8.24-6.18, m, 26H], 4.94 (d, *J* = 14.4 Hz, 0H), 3.72 (d, *J* = 18.9 Hz, 3H), 2.54 (s, 6H); ¹³C{¹H} NMR (75 MHz, DMSO-d₆) δ 166.95, 166.72, 161.69, 157.32, 154.31, 152.05, 151.59, 151.57, 151.50, 150.32, 150.25, 150.22, 149.27, 149.19, 149.17, 149.08, 149.04, 143.98, 143.80, 139.00, 138.98, 138.94, 138.36, 137.52, 131.26, 131.08, 130.45, 126.71, 125.25, 125.23, 124.29, 124.09, 124.04, 122.55, 120.20, 56.31, 55.03, 30.81, 20.83; TOF-MS ESI: *m/z* = 832.8768 (M³⁺); Analysis for C₁₂₆H₉₆F₁₈Ir₃N₁₂O₉P₃ (% calculated, found) C (51.58, 48.73) H (3.30, 3.13) N (5.73, 5.55); Infrared Analysis (FT-IR, cm⁻¹) 556, 738, 756, 837, 1031, 1138, 1177, 1250, 1417, 1478, 1608, 1750 (s), 3050 (b)

Preparation of complex [(Ir(III)(2-phenylpyridine)₂)(tris(4-[4'-methyl-2, 2'-bipyridyl]carboxy)CTG)].(PF₆⁻) (C2.3):



[Ir(ppy)₂(MeCN)₂].PF₆ (0.036 g, 0.050 mmol) in DCM (100 mL) was added dropwise over a period of 1 hour to a stirring solution of (±)-**L2** (0.050 g, 0.050 mmol) in a mixture of DCM/MeOH (10:1) (100 mL total) at room temperature. Over time, after addition of the pale yellow iridium precursor solution to the colourless ligand solution, the reaction mixture became bright orange and was analysed by MS, stirring was continued until the main peak seen was the **Ir(L2)⁺** cationic complex. The reaction mixture was taken to dryness *in vacuo*, re-dissolved in MeCN then filtered through celite to remove any unreacted **L2**. The MeCN solution was removed *in vacuo*, the complex re-dissolved in DCM and diethyl ether was added to the solution to give the title product as a pale orange powder (0.062 g, 75%) ¹H NMR (300 MHz, CD₂Cl₂) δ 9.02 (d, *J* = 4.1 Hz, 1H), 8.84 (d, *J* = 5.6 Hz, 1H), 8.54 (d, *J* = 4.6 Hz, 1H), 8.38 (s, 1H), 8.30 (s, 1H), 8.22 (d, *J* = 6.7 Hz, 1H), 8.12 – 7.90 (m, 2H), 7.88 (d, *J* = 6.0 Hz, 1H), 7.77 (dd, *J* = 17.2, 8.1 Hz, 2H), 7.52 (dd, *J* = 9.4, 5.8 Hz, 1H), 7.42 – 7.19 (m, 2H), 7.14 – 6.88 (m, 3H), 6.32 (t, *J* = 7.8 Hz, 1H), 4.89 (d, *J* = 14.8 Hz, 1H), 3.78 (t, *J* = 10.1 Hz, 4H), 2.60 (s, 1H), 2.48 (s, 2H); ¹³C{¹H} NMR (126 MHz, CD₂Cl₂) δ 168.28, 168.08, 164.10, 164.05, 162.02, 158.10, 157.64, 155.36, 155.08, 152.91, 152.31, 150.77, 150.63, 150.53, 150.14, 149.59, 149.16, 144.28, 144.17, 139.89, 139.57, 139.11, 138.90, 138.51, 138.34, 132.54, 132.30, 132.16, 132.04, 131.41, 131.28, 130.15, 128.38, 126.40, 125.84, 125.55, 125.45, 124.55, 124.46, 124.08, 123.99, 123.56, 123.48, 122.49, 121.26, 120.44, 114.85, 114.69, 56.81, 56.77, 36.94, 36.81, 21.86, 21.55.; TOF-MS ESI: *m/z* = 1497.4428 (M⁺); Analysis for C₈₂H₆₄F₆IrN₈O₉P (% calculated, found) C (59.96, 57.80) H (3.93, 3.70) N (6.82, 6.35); Infrared Analysis (FT-IR, cm⁻¹) 557, 755, 840, 1031, 1138, 1178, 1237, 1418, 1478, 1608, 1747 (s), 3028 (b)

3.7.2 Photophysical studies

All samples were prepared at the University of St Andrews by Diego Rota Martir, in HPLC grade acetonitrile with varying concentrations in the order of 10^{-4} - 10^{-6} M. Absorption spectra were recorded at room temperature using a Shimadzu UV-1800 double beam spectrophotometer. Molar absorptivity determination was verified by linear least-squares fit of values obtained from at least four independent solutions at varying concentrations with absorbance ranging from 6.05×10^{-5} to 2.07×10^{-5} M. The sample solutions for the emission spectra were prepared in HPLC-grade MeCN and degassed via freeze-pump-thaw cycles using a quartz cuvette designed in-house. Steady-state emission and excitation spectra and time-resolved emission spectra were recorded at 298 K using an Edinburgh Instruments F980. All samples for steady-state measurements were excited at 360 nm, while samples for time-resolved measurements were excited at 378 nm using a PDL 800-D pulsed diode laser. Emission quantum yields were determined using the optically dilute method.³³ A stock solution with absorbance of ca. 0.5 was prepared and then four dilutions were prepared with dilution factors between 2 and 20 to obtain solutions with absorbances of ca. 0.095, 0.065, 0.05 and 0.018, respectively. The Beer-Lambert law was found to be linear at the concentrations of these solutions. The emission spectra were then measured after the solutions were rigorously degassed via three freeze-pump-thaw cycles prior to spectrum acquisition. For each sample, linearity between absorption and emission intensity was verified through linear regression analysis and additional measurements were acquired until the Pearson regression factor (R^2) for the linear fit of the data set surpassed 0.9. Individual relative quantum yield values were calculated for each solution and the values reported represent the slope value. The equation $\Phi_s = \Phi_r (A_r/A_s)(I_s/I_r)(n_s/n_r)^2$ was used to calculate the relative quantum yield of each of the sample, where Φ_r is the absolute quantum yield of the reference, n is the refractive index of the solvent, A is the absorbance at the excitation wavelength, and I is the integrated area under the corrected emission curve. The subscripts s and r refer to the sample and reference, respectively. A solution of quinine sulfate in 0.5 M H₂SO₄ ($\Phi_r = 54.6\%$) was used as external references.³⁴

PMMA doped films were prepared by spin coating the samples from a solution of 2-methoxyethanol (HPLC grade) containing 5 % w/w of the desired sample. Steady-

state emission and excitation spectra and time-resolved emission spectra of both powders and doped films were recorded at 298 K using an Edinburgh Instruments F980. Solid-state PLQY measurements of thin films were performed in an integrating sphere under a nitrogen purge in a Hamamatsu C9920-02 luminescence measurement system.³⁵

3.8 Bibliography

- 1 M. Tavasli, T. N. Moore, Y. Zheng, M. R. Bryce, M. A. Fox, G. C. Griffiths, V. Jankus, H. A. Al-Attar and A. P. Monkman, *J. Mater. Chem.*, 2012, **22**, 6419–6428.
- 2 E. Baranoff, J.-H. Yum, M. Graetzel and M. K. Nazeeruddin, *J. Organomet. Chem.*, 2009, **694**, 2661–2670.
- 3 J. Jayabharathi, V. Thanikachalam and R. Sathishkumar, *New J. Chem.*, 2014, **39**, 235–245.
- 4 C.-C. Wang, Y.-M. Jing, T.-Y. Li, Q.-L. Xu, S. Zhang, W.-N. Li, Y.-X. Zheng, J.-L. Zuo, X.-Z. You and X.-Q. Wang, *Eur. J. Inorg. Chem.*, 2013, **2013**, 5683–5693.
- 5 W. Jiang, Y. Gao, Y. Sun, F. Ding, Y. Xu, Z. Bian, F. Li, J. Bian and C. Huang, *Inorg. Chem.*, 2010, **49**, 3252–3260.
- 6 F. Lu and T. Nabeshima, *Dalton Trans.*, 2014, **43**, 9529–9536.
- 7 K. Y. Zhang, H.-W. Liu, M.-C. Tang, A. W.-T. Choi, N. Zhu, X.-G. Wei, K.-C. Lau and K. K.-W. Lo, *Inorg. Chem.*, 2015, **54**, 6582–6593.
- 8 X. Hou, Y. Wu, H. Cao, H. Sun, H. Li, G. Shan and Z.-M. Su, *Chem. Commun.*, 2014, **50**, 6031–6034.
- 9 S. Ladouceur and E. Zysman-Colman, *Eur. J. Inorg. Chem.*, 2013, **2013**, 2985–3007.
- 10 S.-J. Liu, H. Liang, K. Y. Zhang, Q. Zhao, X. Zhou, W.-J. Xu and W. Huang, *Chem. Commun.*, 2015, **51**, 7943–7946.

-
- 11 L. Li, S. Zhang, L. Xu, L. Han, Z.-N. Chen and J. Luo, *Inorg. Chem.*, 2013, **52**, 12323–12325.
- 12 N. Zhao, Y.-H. Wu, R.-M. Wang, L.-X. Shi and Z.-N. Chen, *Analyst*, 2011, **136**, 2277–2282.
- 13 A. Auffrant, A. Barbieri, F. Barigelletti, J. Lacour, P. Mobian, J.-P. Collin, J.-P. Sauvage and B. Ventura, *Inorg. Chem.*, 2007, **46**, 6911–6919.
- 14 R. D. Costa, G. Fernández, L. Sánchez, N. Martín, E. Ortí and H. J. Bolink, *Chem. – Eur. J.*, 2010, **16**, 9855–9863.
- 15 A. M. Bünzli, E. C. Constable, C. E. Housecroft, A. Prescimone, J. A. Zampese, G. Longo, L. Gil-Escrig, A. Pertegás, E. Ortí and H. J. Bolink, *Chem. Sci.*, 2015, **6**, 2843–2852.
- 16 L. Donato, C. E. McCusker, F. N. Castellano and E. Zysman-Colman, *Inorg. Chem.*, 2013, **52**, 8495–8504.
- 17 T.-Y. Li, X. Liang, L. Zhou, C. Wu, S. Zhang, X. Liu, G.-Z. Lu, L.-S. Xue, Y.-X. Zheng and J.-L. Zuo, *Inorg. Chem.*, 2014, **54**, 161–173.
- 18 E. C. Constable, C. E. Housecroft, G. E. Schneider, J. A. Zampese, H. J. Bolink, A. Pertegás and C. Roldan-Carmona, *Dalton Trans.*, 2014, **43**, 4653–4667.
- 19 K. A. McGee and K. R. Mann, *Inorg. Chem.*, 2007, **46**, 7800–7809.
- 20 B. Tong, Q. Mei, D. Chen and M. Lu, *Synth. Met.*, 2012, **162**, 1701–1706.
- 21 X. Yang, X. Xu, J. Dang, G. Zhou, C.-L. Ho and W.-Y. Wong, *Inorg. Chem.*, 2016, **55**, 1720–1727.
- 22 B. Chatelet, L. Joucla, D. Padula, L. D. Bari, G. Pilet, V. Robert, V. Dufaud, J.-P. Dutasta and A. Martinez, *Org. Lett.*, 2015, **17**, 500–503.
- 23 Z. Zhong, A. Ikeda, S. Shinkai, S. Sakamoto and K. Yamaguchi, *Org. Lett.*, 2001, **3**, 1085–1087.
- 24 A. Schaly, Y. Rousselin, J.-C. Chambron, E. Aubert and E. Espinosa, *Eur. J. Inorg. Chem.*, 2016, **2016**, 832–843.

-
- 25 C. Xu, A. Guenet, N. Kyritsakas, J.-M. Planeix and M. W. Hosseini, *Inorg. Chem.*, 2015, **54**, 10429–10439.
- 26 O. Chepelin, J. Ujma, X. Wu, A. M. Z. Slawin, M. B. Pitak, S. J. Coles, J. Michel, A. C. Jones, P. E. Barran and P. J. Lusby, *J. Am. Chem. Soc.*, 2012, **134**, 19334–19337.
- 27 H. Zimmermann, P. Tolstoy, H.-H. Limbach, R. Poupko and Z. Luz, *J. Phys. Chem. B*, 2004, **108**, 18772–18778.
- 28 K. P. S. Zanoni, B. K. Kariyazaki, A. Ito, M. K. Brennaman, T. J. Meyer and N. Y. Murakami Iha, *Inorg. Chem.*, 2014, **53**, 4089–4099.
- 29 R. Tao, J. Qiao, G. Zhang, L. Duan, L. Wang and Y. Qiu, *J. Phys. Chem. C*, 2012, **116**, 11658–11664.
- 30 P.-H. Lanoë, J. Chan, G. Gontard, F. Monti, N. Armaroli, A. Barbieri and H. Amouri, *Eur. J. Inorg. Chem.*, 2016, n/a–n/a.
- 31 S. Kumar, Y. Hisamatsu, Y. Tamaki, O. Ishitani and S. Aoki, *Inorg. Chem.*, 2016.
- 32 K. Hasan, L. Donato, Y. Shen, J. D. Slinker and E. Zysman-Colman, *Dalton Trans.*, 2014, **43**, 13672–13682.
- 33 G. A. Crosby and J. N. Demas, *J. Phys. Chem.*, 1971, **75**, 991–1024.
- 34 A. M. Brouwer, *Pure Appl. Chem.*, 2011, **83**, 2213–2228.
- 35 N. C. Greenham, I. D. W. Samuel, G. R. Hayes, R. T. Phillips, Y. A. R. R. Kessener, S. C. Moratti, A. B. Holmes and R. H. Friend, *Chem. Phys. Lett.*, 1995, **241**, 89–96.

4 Chapter 4

Hetero Tri-metallic iridium complexes of CTG-type ligands

4.1 Introduction

In the previous chapter, the synthesis and photophysical behaviour of a series of homometallic iridium complexes were discussed, this chapter will look at their heterometallic congeners. In this case, heterometallic refers to the ancillary cyclometallating ligands bound to structurally distinct iridium centres, i.e. different metallotectons have been employed in the same complex.

Chapter Three highlighted the marked difference in emission properties of iridium complexes resulting from **L1** versus **L2**, whilst the differences between the mono- and tri-metallic species were much less pronounced. This chapter will look at fine-tuning the resultant emission through different combinations of metallotecton. By fine-tuning the emission, or even predicting the emission colour, the complexes become a much more attractive option in the effort towards functional devices, i.e. the formation of OLEDs or LEECs.¹⁻⁸

The three metal binding sites on the ligand scaffold can be thought of as distinct centres, thus the emission wavelength of a mono-nuclear analogue is likely to show strong similarities to the emission of bound ligand arm. Due to the wealth of previous research on mono-nuclear iridium systems, the resultant emission wavelength of the tri-metallic systems can be reasonably predicted.^{1,5,9,10} With this in mind, it may be possible to selectively metallate with a pre-chosen combination of metallotectons to give a desired resultant emission colour. Whilst there has been a significant amount of research into colour tuning the emission of mono-nuclear iridium systems, such that a high degree of control over the resultant emission properties is now possible, the disadvantage of this approach is the singular emission wavelength.^{3,6,7,10-16} When a mono-nuclear system is tuned to give rise to a desired energy gap, that energy gap gives rise to a specific wavelength emission, thus some emission colours are still out of reach due to their combinatorial nature. One of the most highly desired emission colours, with respect to real-world applicability, is white light. White light emitting devices can be employed in both domestic and commercial lighting situations, with the current drive towards replacing traditional

incandescent light bulbs. However ‘white’ light is not a singular emission wavelength, it is the result of over-reaching emission from many wavelengths combined together to appear white. The easiest way to visualise this is through use of a chromaticity chart, adapted from the Commission Internationale de L’Eclairage.

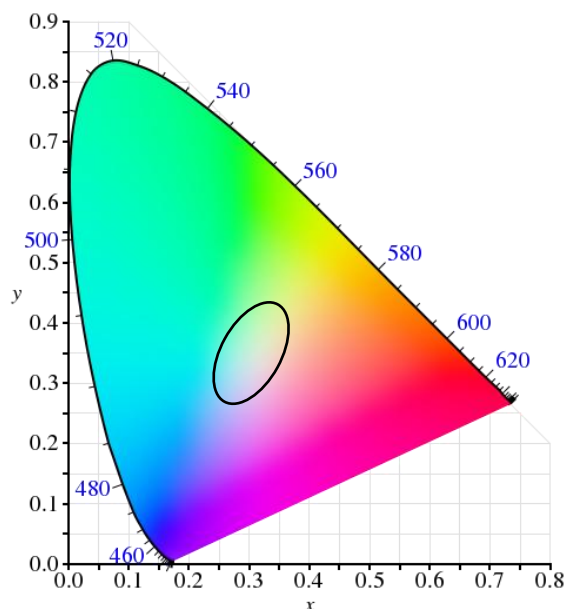


Figure 4.1: CIE chart highlighting the white-light containing central area.¹⁷

Emission that appears white to the human eye is simply emission to some degree covering the whole spectrum, hence the central positioning of true white-light in Figure 4.1. Therefore a multi-metallic, multi-emission system is ideally suited towards tailoring emission in the direction of white light. This could be achieved through a judicious choice of complementary metallotectons, through consideration of their individual emission properties and how they might relate to one another. Whilst there has been considerable research into the formation and emission properties of mono-nuclear systems, much less has been explored in relation to multi-nuclear systems. There are examples of chloro-, alkynyl or tetraacetylene linked dimers where the peripheral ancillary ligands have been rationally functionalised.^{18–20} However, multi-nuclear systems mainly consist of a linear bridging ligand linking two identical metal sites,^{21,22} whereas this chapter is concerned with the synthesis of multi-nuclear heteroleptic iridium systems. Conversely, there are examples of these types of linear bridging ligands being employed in the formation of heteronuclear complexes, whereby multiple metal

centres are combined with other luminescent metals such as ruthenium, osmium, rhenium and platinum.^{23–30}

4.2 Preparation of hetero tri-metallic iridium complexes

In the previous chapter, the synthesis, characterisation and photophysical properties of both tri- and mono- homometallic iridium complexes were discussed. This chapter will further build on the mono-metallic analogues, providing secondary functionalisation at the previously vacant bipyridine binding sites. The ability to form a mono-metallic system, with these vacant binding sites, leads to the possibility of additional synthetic modification; i.e. sequentially binding further metallotectons with a variety of functionalised phenylpyridine auxiliary ligands. The versatility of this modular approach allows fine tuning of the resultant photophysics. Therefore, as shown in Figure 4.2, there is a general scheme to alter the resultant emission wavelength, either through a hypso- or bathochromic shift, through judicious choices of electron withdrawing or electron donating groups on the phenylpyridine ancillary ligands or on the N[^]N ligand scaffold.

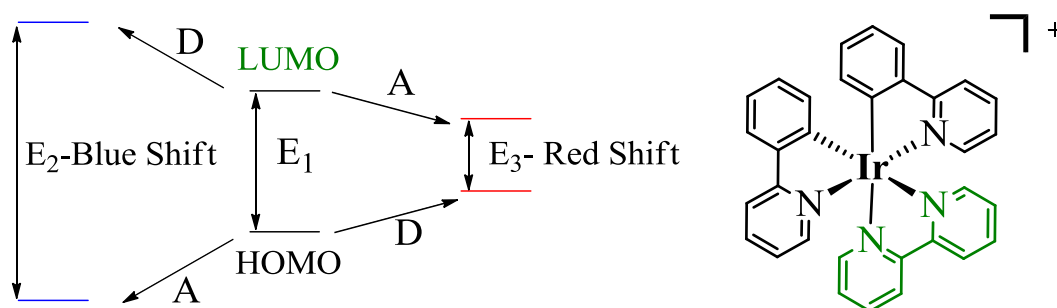
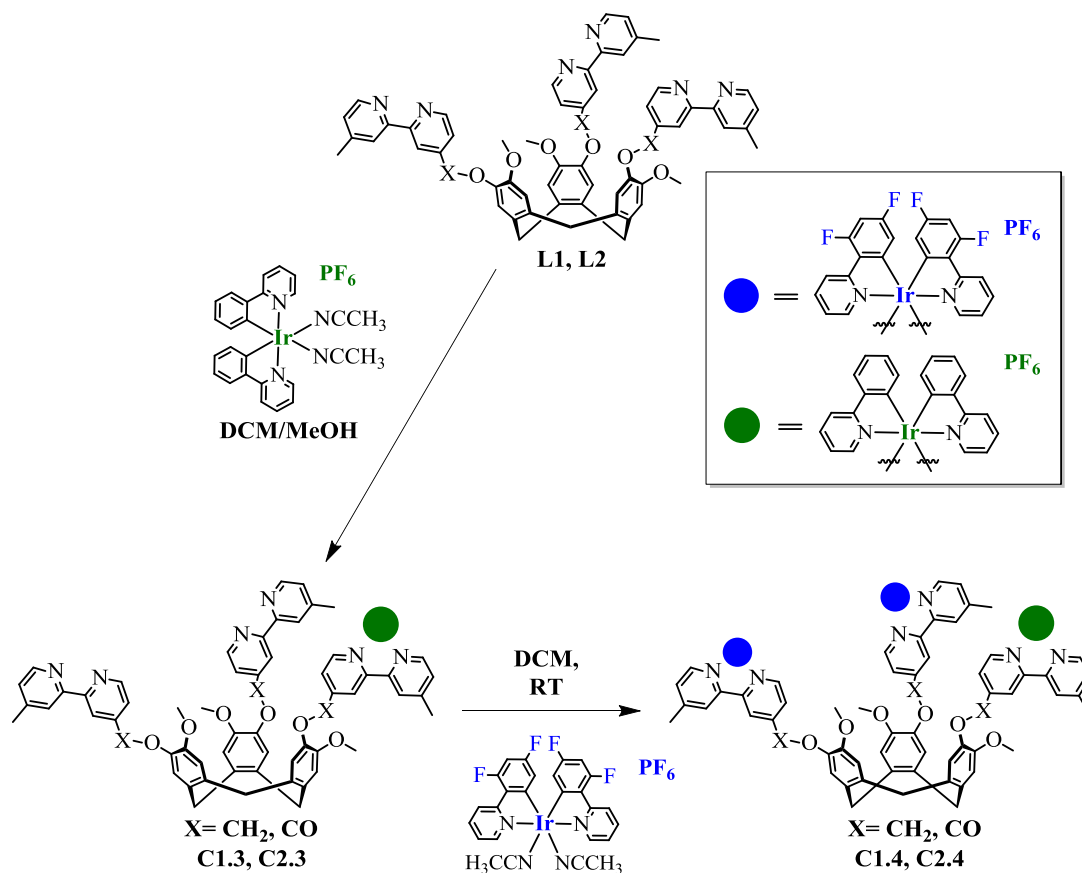


Figure 4.2: Generic HOMO-LUMO energy gap scheme related to the colour coded general $[Ir(C^N)_2(N^N)]$ structure.

To provide a diagnostic shift in emission, a heavily fluorinated phenylpyridine ancillary ligand was employed in formation of the secondary metallotecton. The electron withdrawing nature of the multi-fluorine moiety leads to a stabilisation of the associated energy level, and a blue-shift in emission, known through extensive previous density functional theory (DFT) calculations to make up the majority of the highest-occupied-molecular-orbital (HOMO) level.^{10,16,31} Conversely, fluorination of

the N^N ligand and/or synergistic substitution of the phenylpyridine ligand with electron donating moieties should lead to a noticeable red-shift in emission.

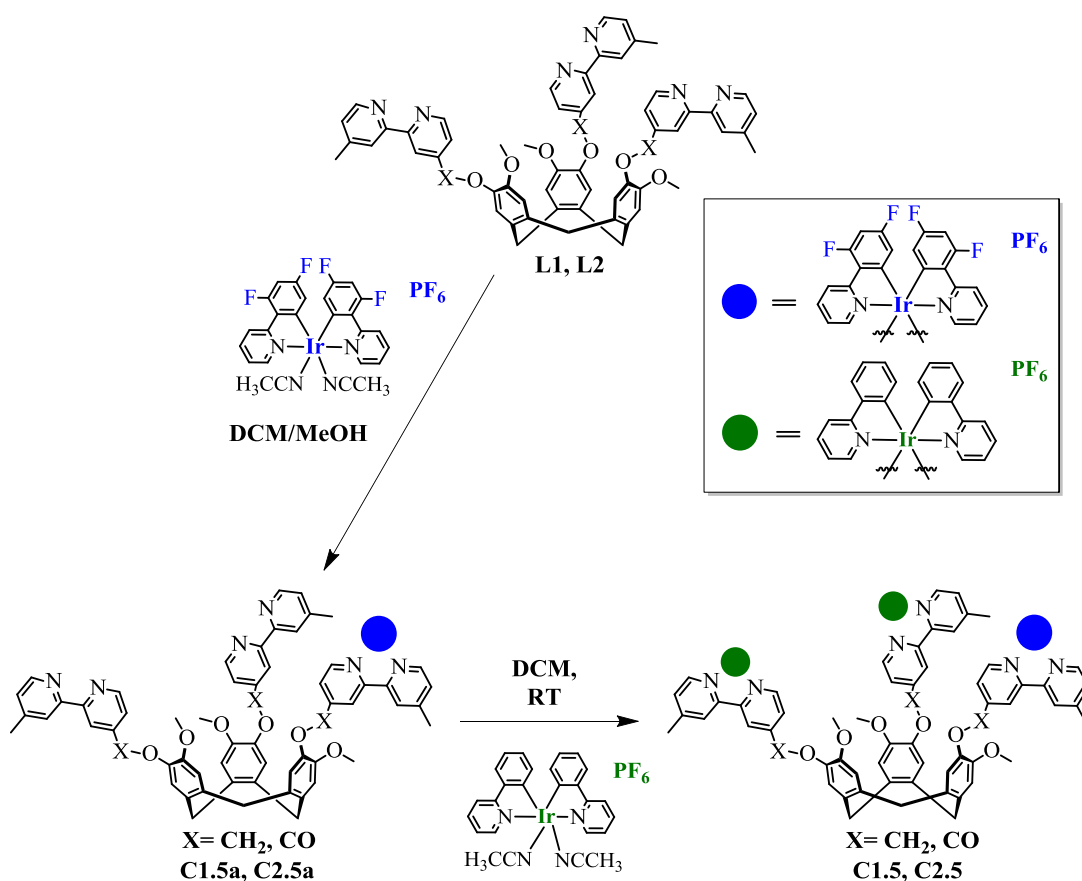


Scheme 4.1: Two-step route of heterometallic iridium complexes **C1.4** and **C2.4**.

The post-synthetic secondary and/or tertiary metallation steps are relatively facile, proceeding at room temperature in dichloromethane solvent when charged with the appropriate amount of secondary metallotecton, as exemplified in Scheme 4.1. The initial secondary metallotecton trialed in this modular approach was decorated with a heavily fluorinated phenylpyridine auxiliary ligand, 2,4-difluorophenyl-2-pyridine (dfppy), represented by the blue circle. By taking previously discussed mono-metallic **C1.3** and **C2.3**, and further metallating with the fluorinated metallotecton, heterometallic species **C1.4** and **C2.4** were formed, and given the designation (●●●) as a visual representation of the metallotectons contained within. The formation of these two complexes, **C1.4** and **C2.4**, proceeded at room temperature in DCM solvent with no need to exclude air or moisture from the reaction system. The progress of the reaction was followed mainly through HR ESI-MS, as discussed previously in Chapter Three; the three iridium isotope pattern is diagnostic of

complex formation. Complete formation was found to take approximately 12 hours, until the main peaks visible in the HR-MS were assigned to the tri-cationic **C1.4** and **C2.4** respectively. A precise 2:1 stoichiometry of $[\text{Ir}(\text{dfppy})_2(\text{MeCN})_2]\cdot\text{PF}_6$ metallotecton to ligand was employed leading to high isolated yields of between 85 and 95%, with complex yet reproducible ^1H NMR spectra, discussed in detail in Section 4.3.2., and strong C-F IR stretches around 1250 cm^{-1} .

However, this two-step approach whereby a mono-metallic system is further metallated is not confined to **C1/2.3**, the mono-metallic species employed as the vehicle for heterometallic complex formation can contain whichever iridium metallotecton is required. Hence the analogous species **C1.5** and **C2.5** (●●●) were synthesised by first forming the mono-metallic system using the fluorinated $[\text{Ir}(\text{dfppy})_2(\text{MeCN})_2]\cdot\text{PF}_6$ metallotecton, and further metallating with the original un-substituted metallotecton $[\text{Ir}(\text{ppy})_2(\text{MeCN})_2]\cdot\text{PF}_6$, as shown in Scheme 4.2.



Scheme 4.2: Two-step, in situ formation of heterometallic iridium complexes **C1.5** and **C2.5**.

In this instance the mono-metallic, fluorinated congeners **C1.5a** and **C2.5a** were not isolated, their formation was confirmed through HR ESI-MS and they were subsequently reacted on with the secondary metallotecton *in situ*.

Prolonged reaction of the fluorinated $[\text{Ir}(\text{dfppy})_2(\text{MeCN})_2]\cdot\text{PF}_6$ metallotecton with both **L1** and **L2** resulted in degradation and decomposition of the ligands. Evidence of bipyridine arm cleavage was observed, more so with the ester-linked **L2**, leading to concomitant over-metallation of the remaining metal-binding sites, thus the reaction required a careful balance of purity against yield. 0.85-0.9 equivalents of $[\text{Ir}(\text{dfppy})_2(\text{MeCN})_2]\cdot\text{PF}_6$ was employed to ensure no over-metallation was observed, however regardless of the resultant HR-MS the reaction was not left for more than 12 hours in solution, as after that point decomposition was seen to occur. The DCM solvent was removed *in vacuo*, and the residue re-dissolved in minimal acetonitrile then filtered through celite to remove any un-reacted ligand. This process gave rise to better purity of mono-metallic **C1.4a** and **C1.5a**, but also a slight decrease in yield.

As the target of this chapter was to form hetero tri-metallic complexes, the isolation of **C1.4a** and **C1.5a** was not a priority.

4.3 Spectroscopic analysis of heterometallic systems

4.3.1 High-resolution mass spectrometric analysis of heterometallic iridium complexes

The foremost method of analysis of the heterometallic systems was once again high resolution mass spectrometry, as the three-iridium isotope pattern is diagnostic of complex formation.

Mono-metallic **C1.3** displayed a distinctive molecular ion peak at 1455 m/z , thus the progress of the reaction towards **C1.4** (●●●) can be followed through HR-MS as the major product tends towards the molecular ion peak of **C1.4** at 866 m/z .

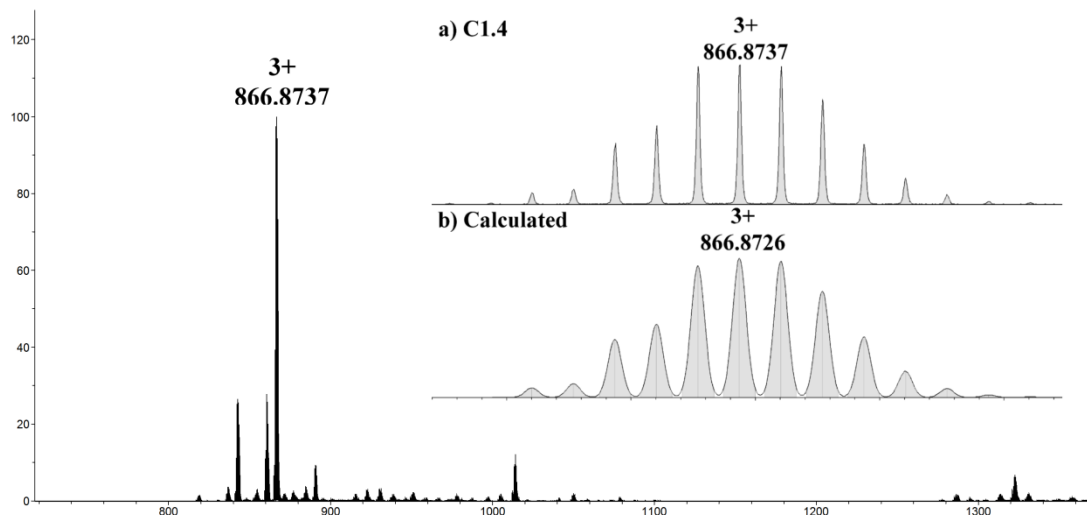


Figure 4.3: HR ESI-MS of C1.4 showing the 3+ molecular ion peak at 866 m/z, the measured a) and calculated b) isotope pattern of the 3+ peak of C1.4 is shown inset.

As demonstrated in Figure 4.3, formation of heterometallic **C1.4** is relatively clean, with the molecular ion peak at 866.8737 m/z assigned to $\{[\text{Ir}(\text{ppy})_2][\text{Ir}(\text{dfppy})_2]_2\text{L1}\}^{3+}$, observed without any associated hexafluorophosphate anions. The only other notable peaks belong to **C1.4** having lost successive fluorine atoms at 860.8674, 854.8800 and 842.8848 m/z, assigned to loss of 1, 2 and 4 fluorine atoms respectively. The measured isotope pattern for the 3+ peak is an exact match for the calculated pattern, shown inset in Figure 4.3.

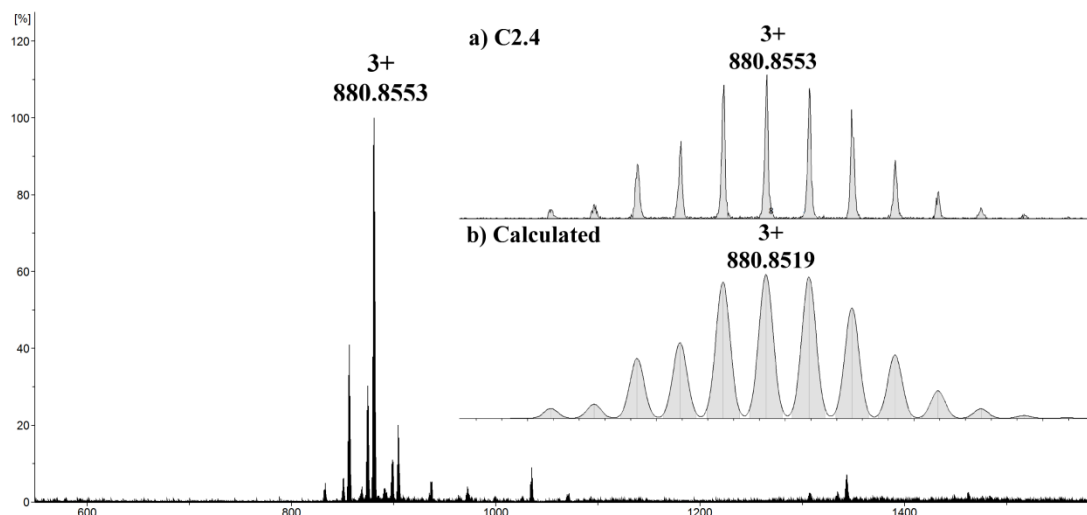


Figure 4.4: HR ESI-MS of C2.4 showing the 3+ molecular ion peak at 880 m/z, the measured a) and calculated b) isotope pattern of the 3+ peak of C2.4 is shown inset.

The HR-MS of **C2.4** (●●●) is directly analogous to **C1.4**, in that the 3+ molecular ion peak at 880.8553 m/z is assigned to $\{[\text{Ir}(\text{ppy})_2][\text{Ir}(\text{dfppy})_2]_2\text{L2}\}^{3+}$, once again observed without any associated hexafluorophosphate anions. Peaks seen at 874.8569, 868.8580 and 856.5318 m/z are assigned to sequential loss of 1, 2 and 4 fluorine atoms during the ionisation process. The measured and calculated isotope patterns for **C2.4** are essentially super-imposable.

The construction of **C1.5** and **C2.5** (●●●) proceed *via* the formation of **C1.5a** and **C2.5a**, the mono-metallic fluorinated congeners of **C1.3** and **C2.3**. As shown in Scheme 4.2, **C1.5a** and **C2.5a** were not isolated, the formation of the desired intermediate was confirmed through HR-MS and further reactions carried out *in situ*.

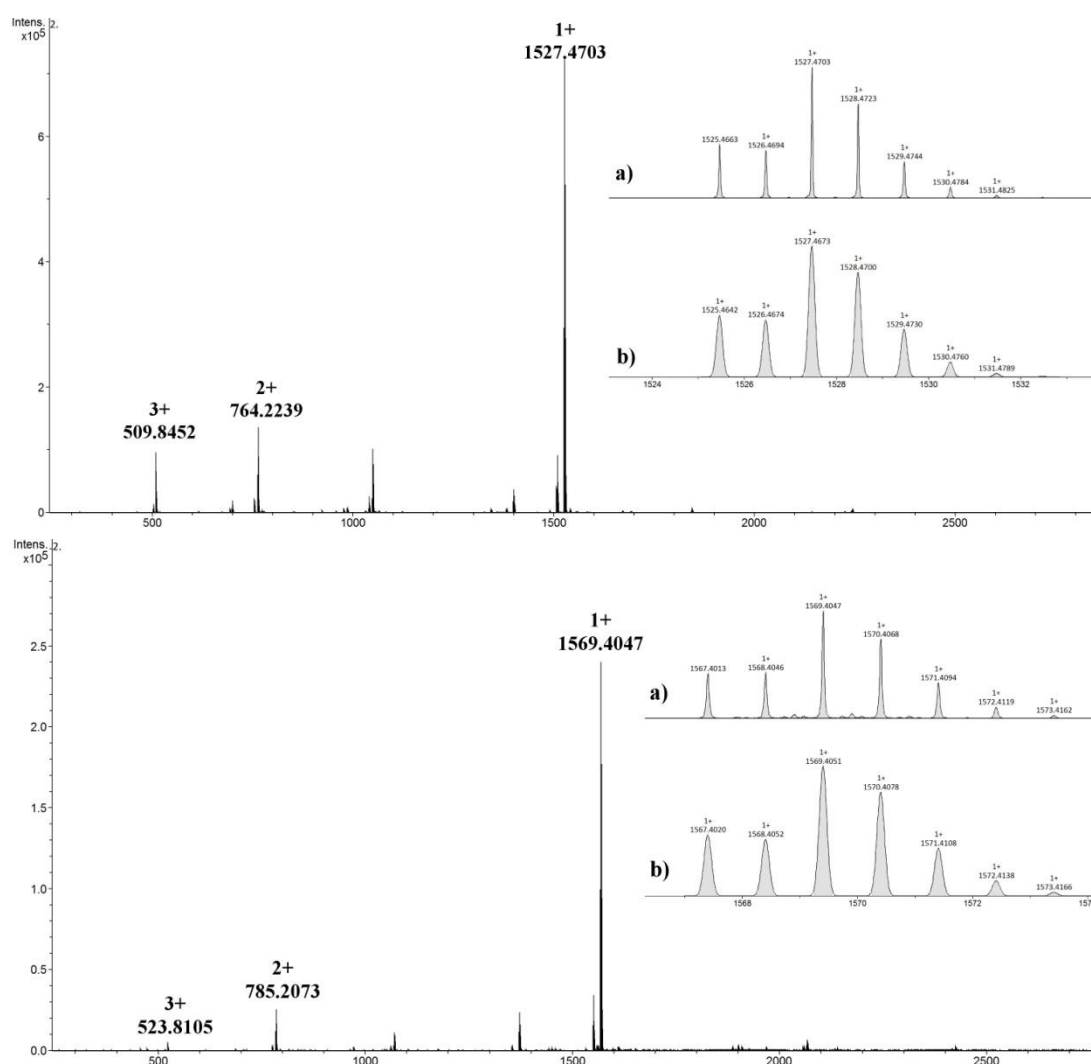


Figure 4.5: HR-MS of C1.5a (top) and C2.5a (bottom) displaying the 1+ molecular ion peak at 1527 and 1569 respectively, as well as the 2+ and 3+ charge states of the desired complexes. The measured isotope pattern a) and calculated pattern b) are shown inset on both spectra.

Figure 4.5 clearly demonstrates the applicability of this modular approach, as the formation of **C1.5a** and **C2.5a** proceeds in an analogous fashion to **C1.3** and **C2.3**. Through use of 0.9 equivalents of $[\text{Ir}(\text{dfppy})_2(\text{MeCN})_2]\cdot\text{PF}_6$ metallotecton, the likelihood of over-metallation is decreased and removal of any excess ligand precursor is facile due to the vastly differing solubilities of free ligand versus metallated products. The characteristic iridium isotope pattern can be seen in each expanded 1+ peak, inset in Figure 4.5.

Dichloromethane solutions of **C1.5a** and **C2.5a** were subsequently charged with two equivalents of the original un-substituted phenylpyridine iridium metallotecton, $[\text{Ir}(\text{ppy})_2(\text{MeCN})_2]\cdot\text{PF}_6$, and allowed to stir at room temperature for 12 hours. The formation of **C1.5** and **C2.5** (●●●) were again followed by use of HR-MS to confirm the presence of the desired product.

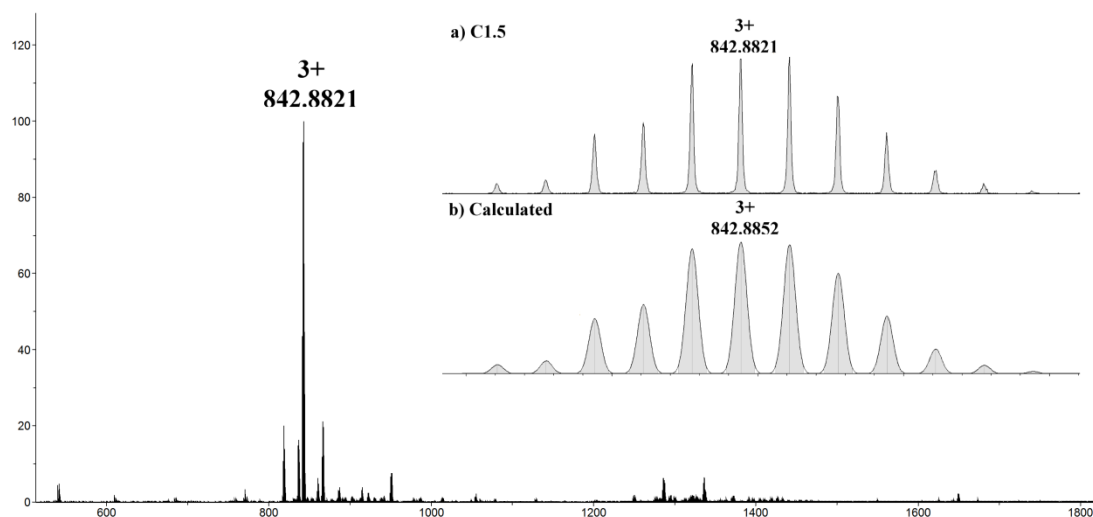


Figure 4.6: HR ESI-MS of C1.5 showing the 3+ molecular ion peak at 842 m/z, the measured a) and calculated b) isotope pattern of the 3+ peak of C1.5 is shown inset.

The 3+ molecular ion peak at 842.8821 m/z in Figure 4.6 is assigned as $\{[\text{Ir}(\text{ppy})_2]_2[\text{Ir}(\text{dfppy})_2]\text{L1}\}^{3+}$, observed without the associated hexafluorophosphate anions. Multiple mass peaks adjacent to the molecular ion peak are due to sequential loss of fluorine atoms, analogous to **C1.4**. The observed isotope pattern of **C1.5** matches the calculated pattern exactly, displaying the characteristic three iridium roofing.

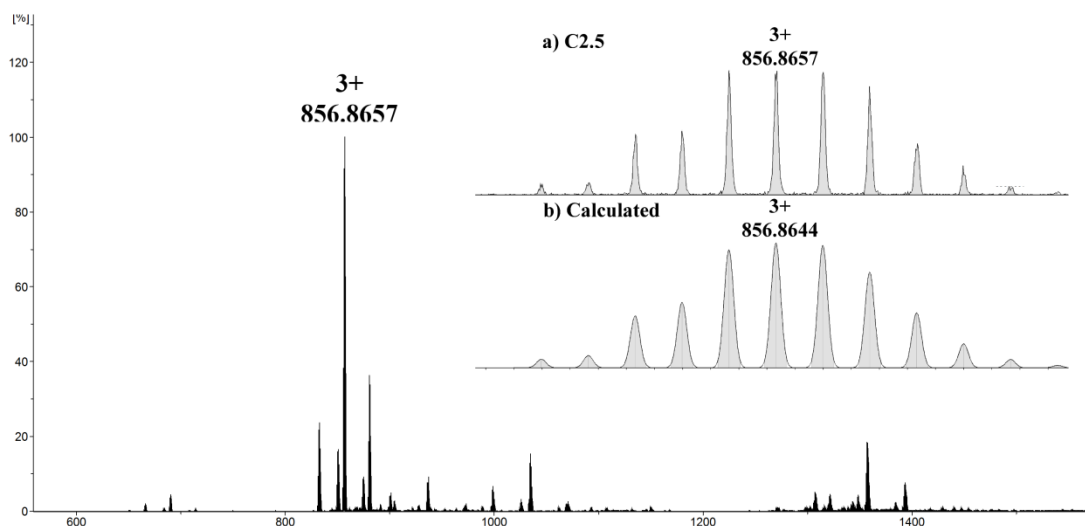


Figure 4.7: HR ESI-MS of C2.5 showing the 3+ molecular ion peak at 856 m/z, the measured a) and calculated b) isotope pattern of the 3+ peak of C2.5 is shown inset.

The 3+ molecular ion peak observed at 856.8657 m/z is assigned to $\{[\text{Ir}(\text{ppy})_2]_2[\text{Ir}(\text{dfppy})_2]\text{L2}\}^{3+}$ without any associated anions. As is the case with all of the fluorinated heterometallic species, sequential loss of fluorine atoms during the ionisation process is observed, giving rise to less intense mass peaks adjacent to the molecular ion peak. The characteristic three iridium isotope pattern is again seen in both the measured and calculated patterns.

4.3.2 ^1H NMR analysis of heterometallic iridium species

Analysis of the resultant ^1H NMR spectra of the heterometallic complexes is convoluted, as expected. The differences between the spectra observed for the two pairs of complexes, for example **C1.4** and **C1.5**, are almost negligible. That is to say both complexes formed from **L1** have the $[\text{Ir}(\text{ppy})_2]^+$ metallotecton and the $[\text{Ir}(\text{dfppy})_2]^+$ metallotecton, it is just the relative ratios present that induces any observable change. The positions of the proton resonances in the spectrum of **C1.4** are almost identical to **C1.5**, as the protons are experiencing the same environment in each complex. The relative integrations of the peaks however, do change.

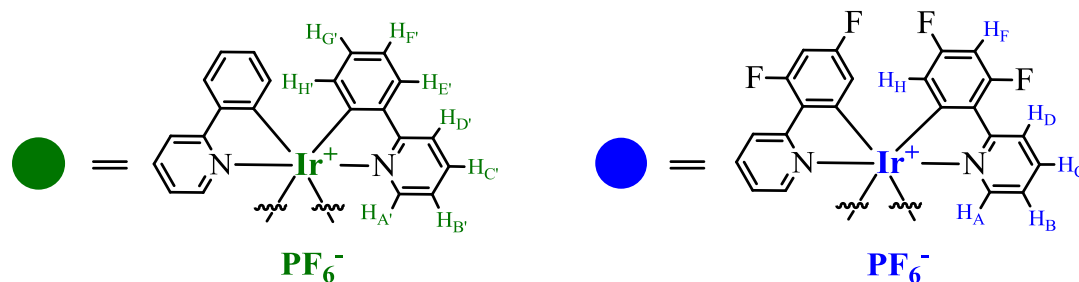


Figure 4.8: Chemical structure and nomenclature of both iridium metallotectons employed in the formation of **C1.4**, **C2.4**, **C1.5** and **C2.5**.

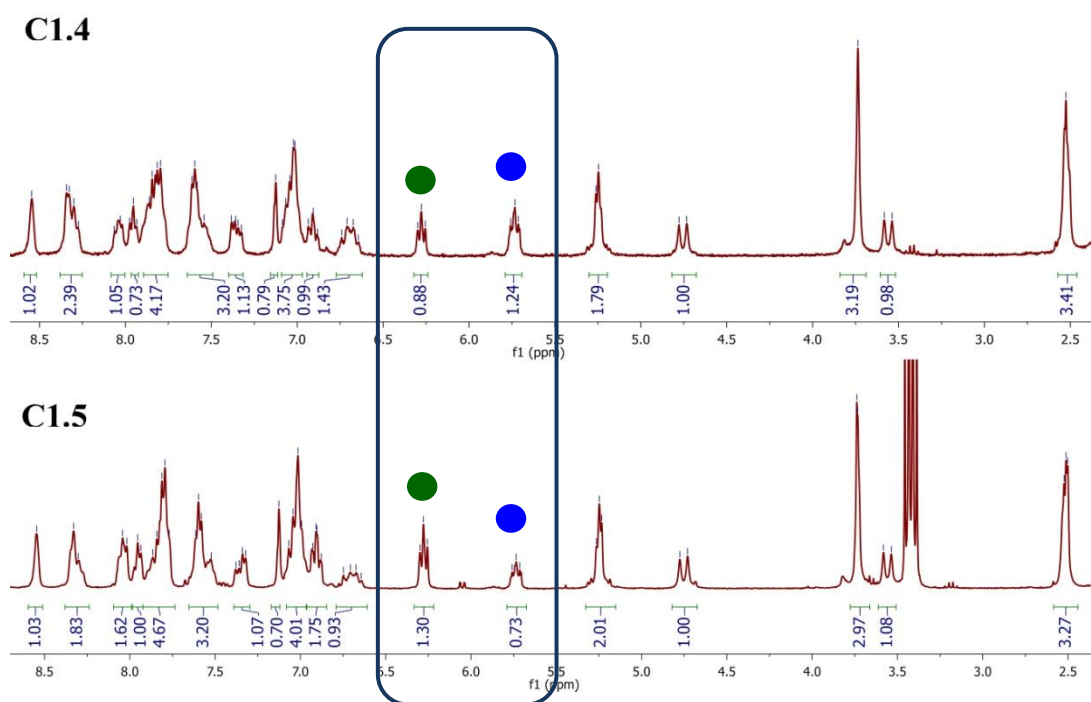


Figure 4.9: Stacked ^1H NMR spectra of **C1.4** and **C1.5** in CD_3CN , displaying almost identical peak positions, but differing peak integrals.

The heterometallic systems contain 28 distinct aromatic proton environments, leading to many overlapping and co-incident peaks in the ^1H NMR spectra. This made definitive assignments particularly problematic. However, some of the ligand protons could be assigned and through comparison with the spectra of both metallotectons individually, some of the diagnostic tecton protons could also be assigned. The protons closest to the cyclometallated carbon on both tectons, H_H and H_H' , appear most up-field, both in the ^1H spectra of the tectons themselves and in the spectra of the complexes.

The total aromatic integrations are 68 and 71 protons for **C1.4** and **C1.5** respectively compared to the theoretical values of 64 and 68 when compared to the integration of

the single diagnostic *endo* proton of the CTG core (multiplied by three to get an integral value for the whole system, not just a symmetric third of a molecule). These values are slightly higher than the theoretical values due to the difficulty in measuring each overlapping integral accurately. However, the relative ratios support the presence of an additional 4 protons per [Ir(ppy)₂] centre compared to an [Ir(dfppy)₂] centre.

The most obvious demonstration of the difference in integrals is highlighted in the navy box in Figure 4.9. The resonance at 6.2 ppm is assigned to H_{H'} on the unsubstituted metallotecton, described by the green circle, whilst the peak at 5.7 ppm is assigned to H_H on the fluorinated tecton, described by the blue circle. In **C1.4** (●●●), which contains one 'green' tecton and two 'blue' tectons, the relative integration between the two peaks is approximately 1:2. In the spectrum of **C1.5** (●●●) however, the ratio of the two tectons is reversed, the resonance at 6.2 ppm possesses a larger integral than the peak at 5.7 ppm, corresponding to two 'green' and one 'blue' tectons.

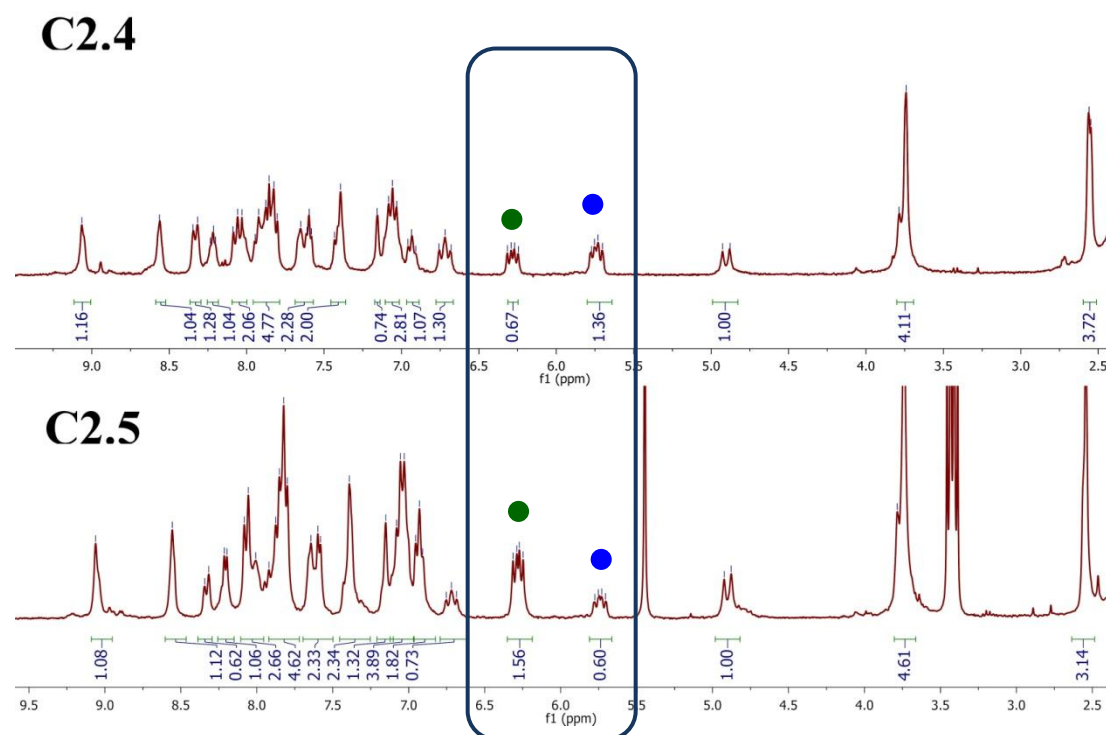


Figure 4.10: Stacked ¹H NMR spectra of **C2.4** and **C2.5** in CD₃CN, displaying almost identical peak positions, but differing peak integrals.

As with the heterometallic complexes resulting from **L1**, **C2.4** and **C2.5** show analogous switching of the integral ratios. In **C2.4** (●●●) the proton resonance at

6.2 ppm, again assigned to $H_{H'}$, equates to approximately half the integration of the peak at 5.7 ppm, assigned to H_H , whereas conversely in **C2.5** (●●●) the integration of the 6.2 ppm peak is roughly twice that of the 5.7 ppm peak. The relative ratio of these two peaks consequently corroborates the clean formation of desired complexes. Therefore, whilst the proton NMR data is suitably complex, the peak positions and integrals all support the assignments proposed. An added complexity that was briefly discussed in Chapter Three was the presence of both Δ and Λ isomers of all iridium tris-chelated centres, once again the chirality of each iridium centre is independent of the other isomers in the system.

4.4 Photophysical analysis of heterometallic fluorinated systems

Photophysical studies were undertaken at the University of St Andrews by PhD student Diego Rota Martir of the Zysman-Colman group.

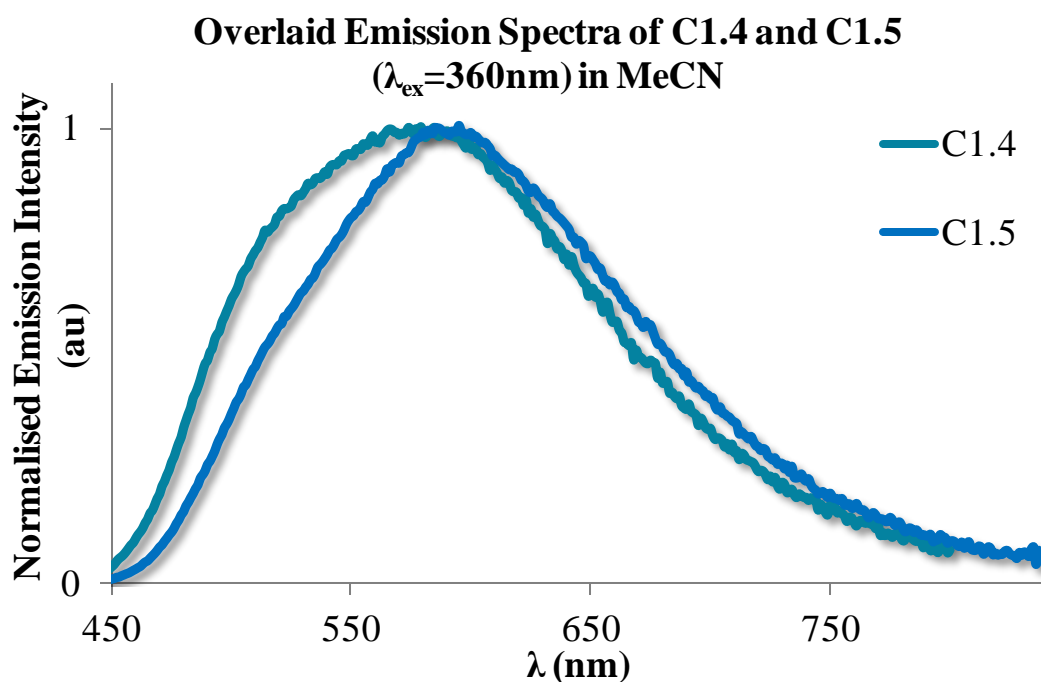


Figure 4.11: Overlaid emission spectra of C1.4 (●●●) and C1.5 (●●●) recorded in deaerated acetonitrile solution.

The emission profiles of **C1.4** and **C1.5** are remarkably similar; this is to be expected as only the ratio of the two metallotectons is changing, inverting from 1:2 to 2:1. **C1.4** is slightly blue-shifted with respect to **C1.5** due to the incorporation of more fluorinated ancillary ligands, which in turn stabilise the LUMO leading to a

larger HOMO-LUMO gap and thus bluer emission. Whilst the λ_{max} for **C1.4** is 574 nm, the corresponding λ_{max} for **C1.5** is 596 nm; therefore the effect of additional electron-withdrawing fluorine atoms on the ancillary ligand can be visualised, if only subtly.

The PLQY of both complexes are similar, 5.5 versus 4.3 %, with the more heavily fluorinated **C1.4** showing a slight improvement on **C1.5**. The lifetimes of the two complexes both show bi-exponential, two-component lifetimes comprised of a shorter (~270 ns) and a longer (>1000 ns) component. However, the relative weighting of the two components is inverted; in **C1.4** the longer component dominates whilst in **C1.5** the shorter component is more heavily weighted. **C1.4** consists of a 267 ns and a 1252 ns element in a 32:68 percentage ratio, therefore the 1252 ns component strongly dominates the lifetime. Whilst in **C1.5**, which consists of a 285 ns and a 1090 ns component, the shorter lifetime dominates in a 70:30 percentage ratio. The inversion of the lifetime weighting could suggest that the longer lifetime component is due in some part to the fluorinated metallotecton; as the ratio of tectons inverts from 1:2 to 2:1 the ratio of lifetime weighting inverts from 1:2.1 to 2.3:1, almost exactly mirroring the tecton ratio.

The lifetimes of the mono- and tri-nuclear homometallic iridium complexes discussed in Chapter Three, **C1.2** and **C1.3**, both possessed lifetimes around 550 ns, thus the shorter lifetime component (~270 ns) is not directly attributable to the non-fluorinated metallotecton unit. However, the two distinct metallotecton units incorporated into a single complex do not give rise to dual emission; therefore some form of energy transfer (ET) must be occurring within the complexes.

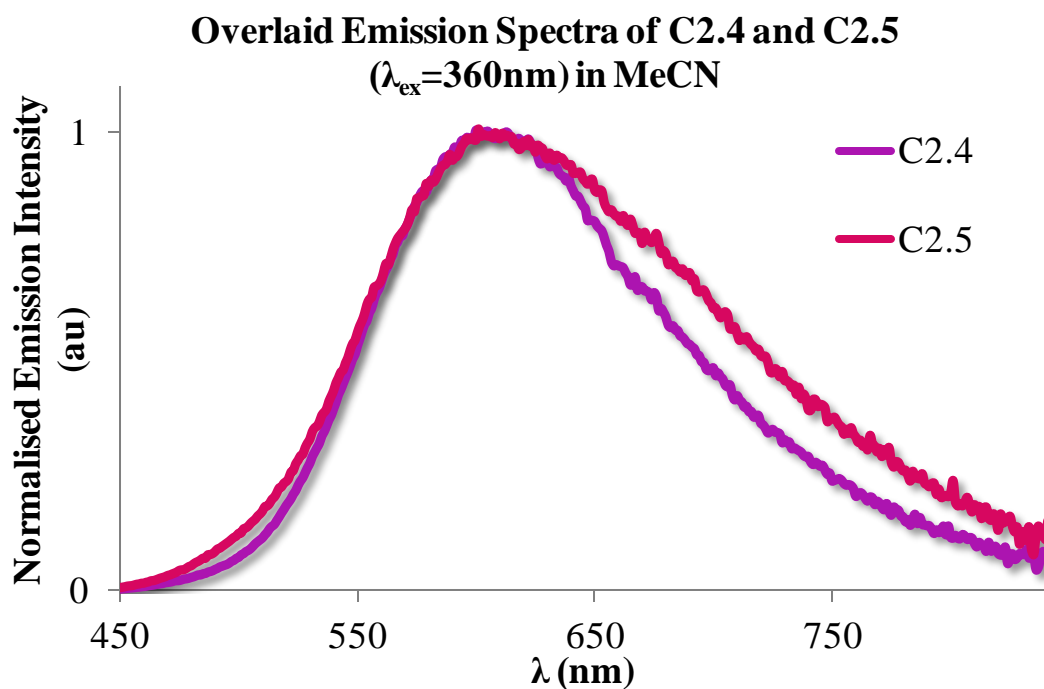


Figure 4.12: Overlaid emission spectra of C2.4 (●●●) and C2.5 (●●●) recorded in deaerated acetonitrile solution.

The heterometallic complexes resulting from **L2** are even more similar to each other than **C1.4** and **C1.5**. The λ_{max} of **C2.4** is 608 nm compared to a λ_{max} of 611 nm for **C2.5**. The main difference between **C2.4** and **C2.5** is the tail-off of emission above 650 nm; **C2.4**, containing two fluorinated metallotectons, tails-off quicker whilst **C2.5**, containing one fluorinated tecton, tails-off much slower leading to a higher relative proportion of emission above 650 nm. However, the fluorinated species are dramatically blue-shifted compared to both the mono- and tri-nuclear homometallic systems, which displayed λ_{max} of 686 nm. The fluorinated **C2.4** and **C2.5** also show a single, broad emission peak, compared to the dual-emission observed for the homometallic analogues. The lack of dual emission suggests that the transition responsible for the short-lived ligand-centric peak observed around 560 nm in the homometallic species is not present, or non-radiative in the heterometallic congeners. The single emission peak observed for **C2.4** and **C2.5** is indicative of some form of energy transfer; as if no energy transfer was occurring, two distinct emission peaks should be identifiable, one assignable to the un-substituted metallotecton and one assignable to the fluorinated tecton.

The PLQYs measured for **C2.4** (●●●) and **C2.5** (●●●) are both approximately doubled compared to the homometallic **C2.2** and **C2.3**, with QYs of 2.6 and 2.0 % respectively versus 1.4 and 1.0 % for the homometallic species.

The lifetimes of the fluorinated species are also bi-exponential, comprised of two components; though they are more evenly weighted than the complexes derived from **L1**, with relative weightings of 55:45 for **C2.4** and 48:52 for **C2.5**. The percentage weightings of the lifetime components are however, inverted upon inversion of the tecton ratio.

Complex	λ_{em} (nm) ^b	Φ_{PL} (%) ^c	t_e (ns) ^d
1.4	574	5.5	267 (32), 1252 (68)
1.5	596	4.3	285 (70), 1090 (30)
2.4	608	2.6	178 (55), 417 (45)
2.5	611	2.0	60 (48), 233 (52)

Table 4.1: Emission maxima, quantum yield and lifetime analysis of C1.4-5 and C2.4-5 in deaerated acetonitrile solution.

Table 4.1 summarises the photophysical data of all the fluorinated heterometallic complexes, highlighting the bi-exponential lifetimes of all complexes and the relatively similar emission maxima across the board.

When compared to the model complex of $[\text{Ir}(\text{dFppy})_2(\text{dmb})]^+$, where dmb=dimethylbipyridine, all of the fluorinated complexes discussed in this chapter are red-shifted. The λ_{max} of the model complex is 522 nm in acetonitrile solution,¹⁴ suggesting that the presence of both the ether- and ester-linked ligands stabilise the LUMO compared to simple dimethylbipyridine.

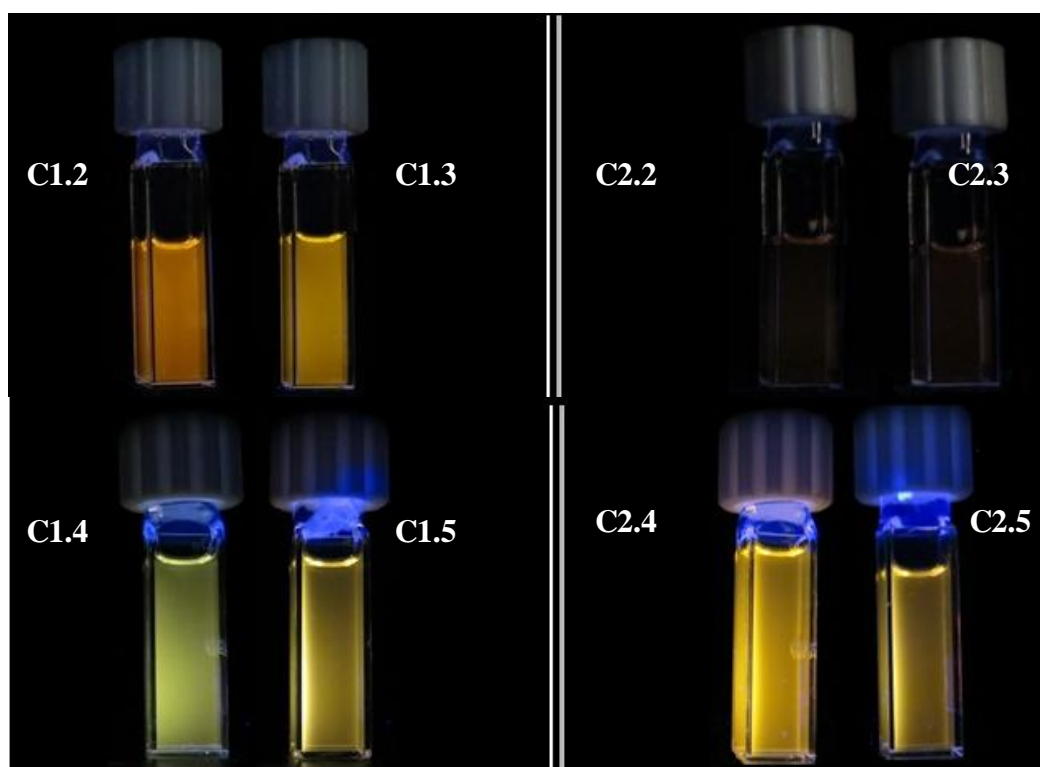


Figure 4.13: Dark-room images of fluorinated C1.4-5 and C2.4-5 in acetonitrile solution, with the homometallic C1.2-3 and C2.2-3 shown for comparison.

The dark-room images in Figure 4.13 most clearly demonstrate both the difference in emission wavelength, and also the relative PLQY. **C1.4** and **C1.5** are noticeably blue-shifted compared to **C1.2** and **C1.3** above, with the most fluorinated complex, **C1.4**, emitting light of a visibly greener colour than the homometallic systems.

The complexes derived from **L2** show a marked difference upon the incorporation of the fluorinated tecton, with a visible increase in PLQY.

Once again the photophysical properties of the fluorinated complexes were also investigated when incorporated into doped thin-films of PMMA.

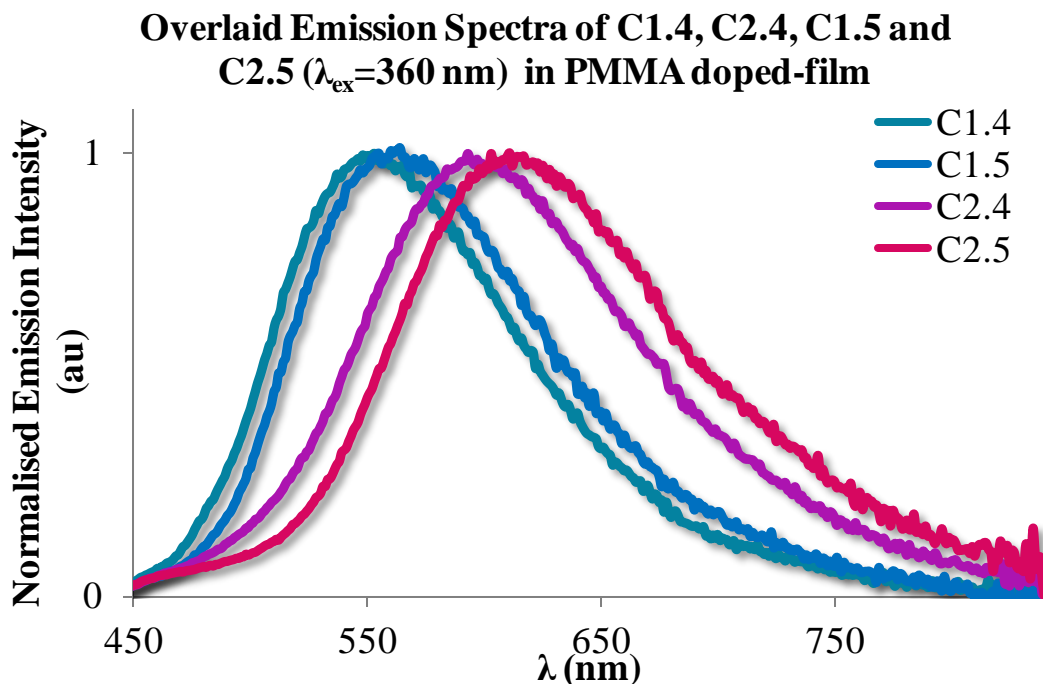


Figure 4.14: Overlaid emission spectra of C1.4, 1.5, 2.4 and 2.5 incorporated into a PMMA doped thin-film.

The emission of the heterometallic complexes is blue-shifted through incorporation into the inert matrix of the PMMA doped film, except for **C2.5** (●●●) which shows a minute red-shift of 4 nm compared to the acetonitrile solution-state measurements.

C1.4 and **C1.5** demonstrate blue-shifts of 21 and 33 nm respectively versus the solution-state measurements, whilst **C2.4** is shifted by just 14 nm. However, the PMMA thin-film emission maxima are much closer to those of the homometallic complexes than the solution-state data; λ_{em} of 565 and 566 nm were recorded for the homo tri- and mono-nuclear **C1.2** and **C1.3** respectively, therefore **C1.5** (●●●) shows just a 2 nm blue-shift through the incorporation of one fluorinated metallotecton. **C1.4** (●●●) shows a blue-shift of just ~10 nm through incorporation of two fluorinated metallotectons, thus suggesting that the fine-tuning of ancillary ligands has less effect on emission when the complex is confined to a thin-film.

The PLQYs though are much improved through use of the PMMA thin-film approach, with QYs of the complexes of **L1** improved by a factor of 4 whilst the complexes derived from **L2** showed QYs improved by a factor of 8 versus the acetonitrile solution data.

Complex	λ_{em} (nm) ^b	Φ_{PL} (%) ^c	t_e (ns) ^d
1.4	554	23.2	400 (30), 1254 (70)
1.5	563	17.6	381 (29), 1143 (71)
2.4	594	21.6	305 (44), 958 (66)
2.5	615	15.7	252 (46), 989 (62)

Table 4.2: Emission maxima, quantum yield and lifetime analysis of C1.4-5 and C2.4-5 in PMMA doped thin-films.

The lifetimes are again bi-exponential, **L1** derived complexes show lifetimes around 400 ns and 1100 ns, whilst **L2** derived complexes display lifetimes of around 270 ns and 960 ns. The percentage weighting of each component in these examples is exclusively dominated by the longer lifetime component.



Figure 4.15: Dark-room images of C1.4, 1.5, 2.4 and 2.5 incorporated in PMMA doped thin-films.

Figure 4.15 demonstrates the visual difference that 60 nm makes to the emission colour, as **C1.4** (●●●) is noticeably greener than **C2.5** (●●●) in the PMMA film.

4.5 Conclusions and further direction

Four heterometallic iridium complexes have been synthesised in good yields, and the photophysical properties of these systems investigated. The carefully modulated phosphorescent emission belies the remarkable structural similarities.

The photophysical emission of the most heavily fluorinated species, **C1.4** and **C2.4**, show the highest degree of hypsochromic shift, within their ligand sub-set. This discovery shows that electronic trends relevant to the $[\text{Ir}(\text{ppy})_2(\text{N}^{\wedge}\text{N})]^+$ model complex are applicable to this ligand scaffold. The increased degree of fluorination

on the ancillary ligand gives rise to a stronger electron-withdrawing effect, thus a more stabilised HOMO, thereby increasing the HOMO-LUMO energy gap and blue-shifting the emission wavelength. The single, broad, unstructured emission peak observed for the heterometallic species suggests some form of ET is occurring within the complexes. Further investigation into the precise nature of this is underway, including comparisons of the emission properties of statistical mixtures of homometallic complexes analogous to the ratio of each tecton in the mixed-tecton systems. For example, a 1:2 ratio of **C1.2** and a tri-nuclear homo-fluorinated analogue should have the same ratio of each of the previously discussed metallotectons as **C1.4**, therefore the emission profiles could be compared in the absence of any intra-complex ET.

The incorporation of a fluorinated tecton has improved the lifetimes compared to the homometallic species discussed in Chapter Three, with the heterometallic complexes formed from **L1** displaying lifetimes in the μs regime in both solution and solid-state, whilst complexes derived from **L2** possess lifetimes approaching the μs timescale in the solid-state.

This chapter therefore demonstrates that heterometallic species of the form **ABB**, where **A** is the primary metallotecton and **B** is the secondary metallotecton, can be reliably synthesised in a modular fashion. This approach gives a high degree of control over the resultant emission, allowing for fine-tuning and directed, rational synthesis towards a particular emission wavelength.

Through this two-tecton approach, if only five metallotectons were synthesised, with individual emission wavelengths covering the majority of the spectrum, twenty five resultant complexes could be formed, all with slightly different resultant emission properties, as shown in Figure 4.16.

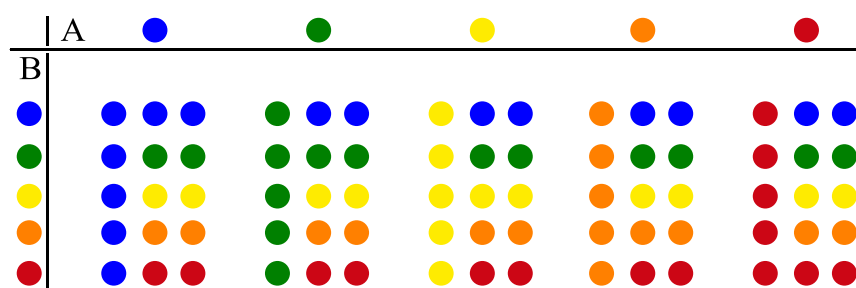


Figure 4.16: Generic scheme for the synthesis of ABB type emissive systems.

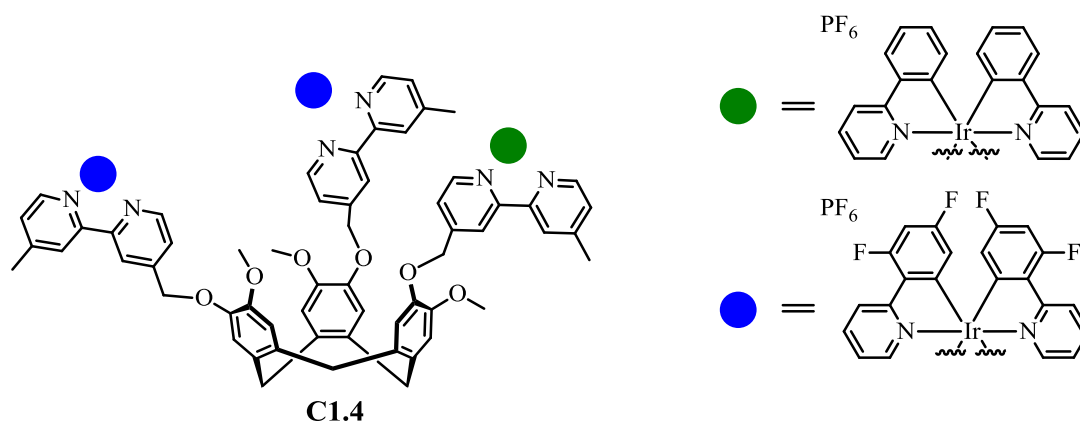
Thus, small-scale screening with an effort towards a specific emission wavelength becomes a possibility, particularly due to the diagnostic HR-MS peaks and isotope patterns of the resultant heterometallic complexes. Therefore, small-scale reactions combining different ratios of metallotectons could be performed, formation of the desired complex confirmed and the resultant reaction solution subjected to *in situ* photophysical excitation. Any favourable combinations of tecton could then be synthesised on a larger scale and fully characterised, in the knowledge that the resultant photophysics would be of the desired form.

The use of two structurally distinct iridium centres also opens the door to emission colours previously inaccessible, through complementary combinations of emission wavelengths. Although the complexes discussed in this chapter display ET, if the transfer mechanisms can be understood then the degree of ET could potentially be modulated through structural modification. Thus, if targeting the challenging goal of white-light emission, complementary combinations of metallotectons could be chosen that together appear white to the human eye.

4.6 Experimental

4.6.1 Synthesis

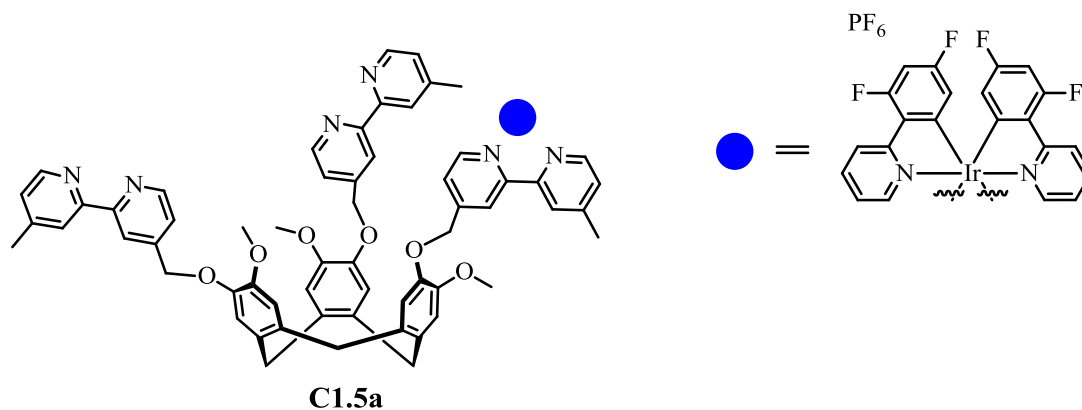
Preparation of complex [(Ir(III)(2-(2,4-difluorophenyl)pyridine)₂(Ir(III)(2-phenylpyridine)₂)(tris(4-[4'-methyl-2, 2'-bipyridyl]methyl)CTG)].(PF₆) (C1.4):



[Ir(dfppy)₂(MeCN)₂].PF₆ (0.020 g, 0.025 mmol) was dissolved in DCM (10 mL) and added to a stirred solution of **C1.3** (0.020 g, 0.0125 mmol) in DCM (10 mL) in the absence of light. The mixture was stirred at room temperature for 12 hrs until HR-MS analysis showed full conversion to the {[Ir(ppy)₂][Ir(dfppy)₂]₂(**L1**)}³⁺ species, **C1.4**. The DCM was removed *in vacuo*, and the residue re-dissolved in minimal DCM then diethyl ether was added to the solution to give the title product as a bright yellow powder (0.032 g, 86.4%) ¹H NMR (300 MHz, CD₂Cl₂) δ 8.68 (d, *J* = 11.2 Hz, 1H), 8.36 (dd, *J* = 27.8, 9.5 Hz, 1H), 7.94 (d, *J* = 7.1 Hz, 1H), 7.90 – 7.69 (m, 1H), 7.66 (d, *J* = 5.3 Hz, 1H), 7.62 – 7.37 (m, 1H), 7.27 (dd, *J* = 18.7, 4.9 Hz, 1H), 7.01 (ddd, *J* = 29.5, 13.9, 6.0 Hz, 2H), 6.60 (t, *J* = 10.5 Hz, 1H), 6.32 (d, *J* = 7.3 Hz, 1H), 5.76 (d, *J* = 8.2 Hz, 1H), 5.33 (s, 1H), 4.73 (d, *J* = 13.8 Hz, 1H), 3.83 (s, 1H), 3.60 (d, *J* = 13.4 Hz, 1H), 2.60 (d, *J* = 7.6 Hz, 1H); ¹³C{¹H} NMR (126 MHz, CD₃CN) δ 191.60, 168.62, 164.89, 163.60, 161.44, 153.82, 153.11, 151.93, 151.55, 151.36, 150.53, 150.14, 147.31, 145.12, 140.74, 140.58, 139.57, 132.70, 132.63, 131.46, 130.88, 130.52, 130.27, 129.04, 128.26, 127.25, 127.05, 126.73, 126.46, 125.99, 124.96, 124.72, 124.50, 124.04, 123.58, 123.23, 120.94, 119.05, 115.17, 114.90, 114.82, 100.00, 99.78, 99.56, 70.24, 56.98, 36.42, 21.60; TOF-MS ESI: *m/z* = 866.8737 (M³⁺); Analysis for C₁₂₆H₉₄F₂₆Ir₃N₁₂O₆P₃ (% calculated,

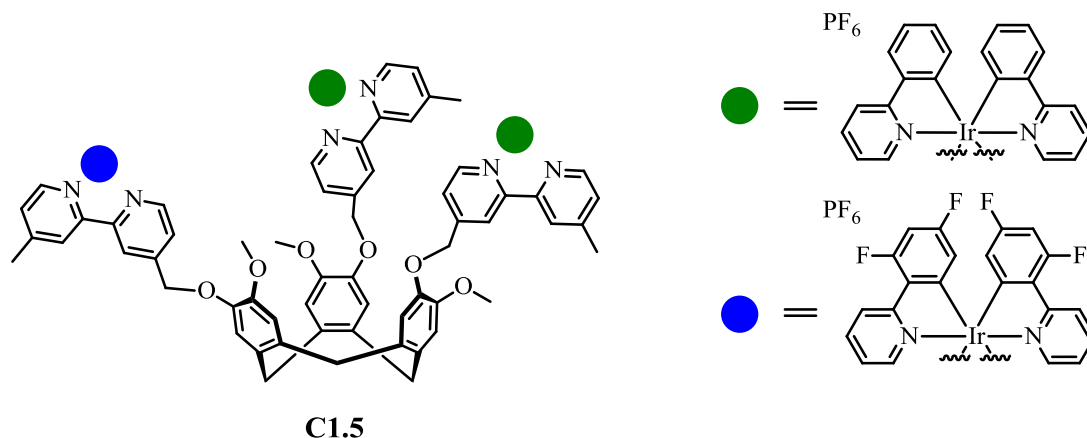
found) C (49.85, 48.35) H (3.12, 3.10) N (5.54, 5.30); Infrared Analysis (FT-IR, cm^{-1}) 556, 737, 756, 837, 1030, 1145, 1267, 1405, 1426, 1478, 1509, 1603 (s), 3066 (b)

Preparation of complex $[\text{Ir}(\text{III})(2-(2,4\text{-difluorophenyl})\text{pyridine})_2](\text{tris}(4-[4'\text{-methyl-2, 2'}\text{-bipyridyl]methyl)\text{CTG})].(\text{PF}_6)$ (C1.5a):



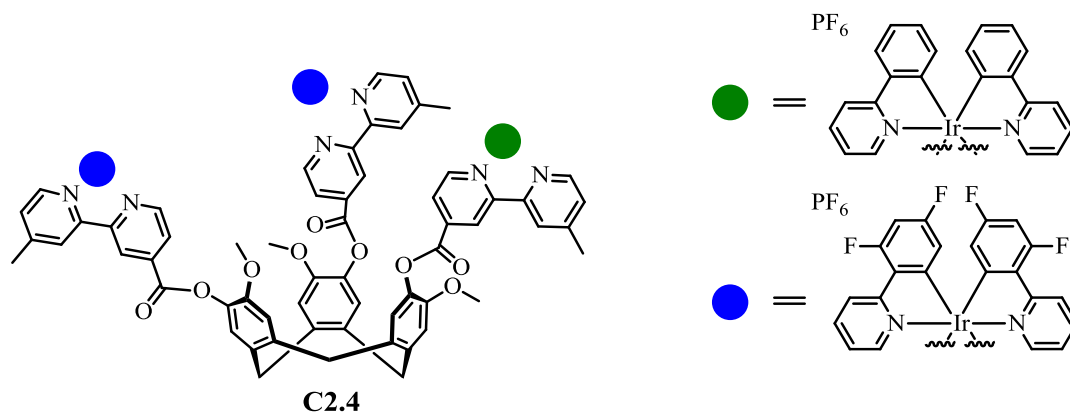
$[\text{Ir}(\text{dFppy})_2(\text{MeCN})_2].\text{PF}_6$ (0.036 g, 0.045 mmol) in DCM (100 mL) was added dropwise over a period of 3 hours to a stirring solution of (\pm)-**L1** (0.050 g, 0.052 mmol) in a mixture of DCM/MeOH (10:1) (150 mL total) at room temperature. Over time, after addition of the pale yellow-green iridium precursor solution to the colourless ligand solution, the reaction mixture became bright yellow and was analysed by HR-MS, stirring was continued until the main peak seen was the $\{[\text{Ir}(\text{dFppy})_2](\text{L1})\}^+$ cationic complex, **C1.5a**. The reaction mixture was taken to dryness *in vacuo*, re-dissolved in MeCN then filtered through celite to remove any un-reacted **L1**. The MeCN solution was removed *in vacuo* and the resultant residue re-dissolved in DCM and employed in the next step TOF-MS ESI: $m/z = 1527.4680$ (M^+)

Preparation of complex $[\text{Ir(III)}(2\text{-}(2,4\text{-difluorophenyl)pyridine})_2](\text{Ir(III)}(2\text{-phenylpyridine})_2)(\text{tris}(4\text{-}[4'\text{-methyl-2, 2'}\text{-bipyridyl]methyl)CTG})].(\text{PF}_6)$ (C1.5):



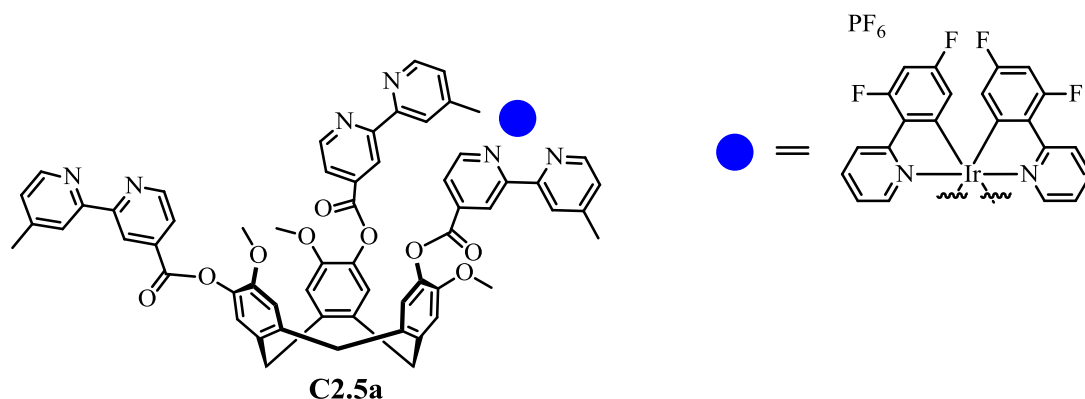
$[\text{Ir}(\text{ppy})_2(\text{MeCN})_2].\text{PF}_6$ (0.026 g, 0.035 mmol) was dissolved in DCM (5 mL) and added to a stirred solution of **C1.5a** (0.030 g, 0.017 mmol) in DCM (10 mL) in the absence of light. The mixture was stirred at room temperature for 12 hrs until HR-MS analysis showed full conversion to the $\{[\text{Ir}(\text{ppy})_2]_2[\text{Ir}(\text{dfppy})_2](\text{L1})\}^{3+}$ species, **C1.5**. The DCM was removed *in vacuo*, and the residue re-dissolved in minimal DCM then diethyl ether was added to the solution to give the title product as a bright yellow powder (0.038 g, 71%) ^1H NMR (300 MHz, CD_3CN) δ 8.55 (s, 1H), 8.32 (d, $J = 8.0$ Hz, 2H), 8.03 (d, $J = 7.6$ Hz, 1H), 7.94 (d, $J = 5.8$ Hz, 1H), 7.91 – 7.71 (m, 4H), 7.58 (dd, $J = 16.2, 11.3$ Hz, 3H), 7.35 (dd, $J = 11.4, 5.8$ Hz, 1H), 7.13 (s, 1H), 7.03 (dd, $J = 15.6, 7.1$ Hz, 4H), 6.90 (dd, $J = 8.2, 6.5$ Hz, 1H), 6.69 (dd, $J = 20.5, 10.7$ Hz, 1H), 6.28 (t, $J = 6.4$ Hz, 1H), 5.74 (t, $J = 6.8$ Hz, 1H), 5.25 (t, $J = 4.6$ Hz, 2H), 4.75 (d, $J = 13.7$ Hz, 1H), 3.74 (d, $J = 1.4$ Hz, 3H), 3.56 (d, $J = 14.0$ Hz, 1H), 2.57 – 2.42 (m, 3H); $^{13}\text{C}\{^1\text{H}\}$ NMR (126 MHz, CD_3CN) δ 168.45, 157.01, 156.17, 153.69, 152.98, 151.48, 151.42, 151.31, 151.22, 150.90, 150.42, 150.39, 150.04, 150.00, 149.50, 147.11, 145.04, 140.44, 139.43, 132.56, 132.48, 131.32, 130.12, 126.91, 126.32, 125.85, 124.82, 124.37, 123.44, 120.80, 114.99, 99.63, 70.16, 56.82, 36.27, 21.44; TOF-MS ESI: $m/z = 842. 8821$ (M^+); Analysis for $\text{C}_{126}\text{H}_{98}\text{F}_{22}\text{Ir}_3\text{N}_{12}\text{O}_6\text{P}_3$ (% calculated, found) C (51.06, 50.89) H (3.33, 3.46) N (5.67, 5.59); Infrared Analysis (FT-IR, cm^{-1}) 556, 737, 756, 835, 1031, 1145, 1267, 1405, 1424, 1478, 1509, 1605 (s), 3044 (b)

Preparation of complex $[\text{Ir}(\text{III})(2\text{-}(2,4\text{-difluorophenyl)pyridine})_2]_2[\text{Ir}(\text{III})(2\text{-phenylpyridine})_2](\text{tris}(4\text{-}[4'\text{-methyl-2, 2'}\text{-bipyridyl]carboxy)CTG)].(\text{PF}_6)$ (C2.4):



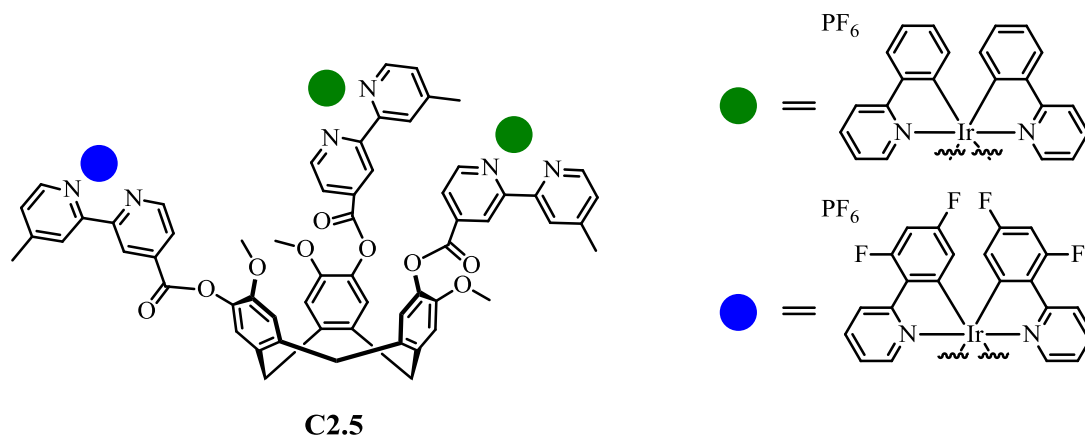
$[\text{Ir}(\text{dFppy})_2(\text{MeCN})_2].\text{PF}_6$ (0.019 g, 0.023 mmol) was dissolved in DCM (10 mL) and added to a stirred solution of **C2.3** (0.02 g, 0.012 mmol) in DCM (10 mL) in the absence of light. The mixture was stirred at room temperature for 12 hrs until HR-MS analysis showed full conversion to the $\{[\text{Ir}(\text{ppy})_2][\text{Ir}(\text{dFppy})_2]_2(\text{L2})\}^{3+}$ species, **C2.4**. The DCM solution was concentrated *in vacuo*, and diethyl ether was added to the solution to give the title product as a pale orange powder (0.035 g, 94.5%) ^1H NMR (300 MHz, CD_2Cl_2) δ 9.04 (d, $J = 11.2$ Hz, 1H), 8.40 (d, $J = 11.2$ Hz, 1H), 8.32 (d, $J = 9.7$ Hz, 1H), 8.20 (t, $J = 5.9$ Hz, 1H), 8.07 (dd, $J = 18.4, 6.8$ Hz, 1H), 7.95 (d, $J = 9.0$ Hz, 1H), 7.90 – 7.63 (m, 1H), 7.63 – 7.44 (m, 1H), 7.42 – 7.18 (m, 1H), 7.19 – 6.85 (m, 2H), 6.72 – 6.46 (m, 1H), 6.32 (t, $J = 7.7$ Hz, 1H), 5.75 (td, $J = 8.3, 2.2$ Hz, 1H), 4.87 (d, $J = 13.7$ Hz, 1H), 3.76 (d, $J = 12.0$ Hz, 1H), 2.61 (d, $J = 7.1$ Hz, 1H); $^{13}\text{C}\{^1\text{H}\}$ NMR (126 MHz, CD_3CN) δ 168.26, 164.83, 163.43, 162.91, 162.77, 161.39, 155.49, 153.96, 153.31, 151.23, 150.53, 150.19, 145.11, 144.87, 140.62, 140.56, 140.35, 139.62, 138.89, 132.58, 132.40, 131.38, 130.79, 130.65, 130.55, 128.70, 127.39, 127.24, 127.09, 125.88, 125.01, 124.87, 124.79, 124.52, 123.66, 120.91, 115.28, 114.71, 114.56, 105.95, 100.06, 99.83, 56.95, 36.22, 21.31; TOF-MS ESI: $m/z = 880.8553$ (M^{3+}); Analysis for $\text{C}_{126}\text{H}_{89}\text{F}_{25}\text{Ir}_3\text{N}_{12}\text{O}_9\text{P}_3$ (% calculated, found) C (49.46, 49.09) H (2.93, 3.06) N (5.48, 5.39); Infrared Analysis (FT-IR, cm^{-1}) 556, 755, 836, 1031, 1139, 1166, 1248, 1407, 1478, 1603, 1751 (s), 3084 (b)

Preparation of complex [(Ir(III)(2-(2,4-difluorophenyl)pyridine)₂)(tris(4-[4'-methyl-2, 2'-bipyridyl]carboxy)CTG)].(PF₆) (C2.5a):



[Ir(dfppy)₂(MeCN)₂].PF₆ (0.036 g, 0.045 mmol) in DCM (100 mL) was added dropwise over a period of 3 hours to a stirring solution of (±)-**L2** (0.050 g, 0.050 mmol) in a mixture of DCM/MeOH (10:1) (150 mL total) at room temperature. Over time, after addition of the pale yellow-green iridium precursor solution to the colourless ligand solution, the reaction mixture became pale orange and was analysed by HR-MS, stirring was continued until the main peak seen was the {[Ir(dfppy)₂](**L2**)}⁺ cationic complex, **C2.5a**. The reaction mixture was taken to dryness *in vacuo*, re-dissolved in MeCN then filtered through celite to remove any un-reacted **L2**. The MeCN solution was removed *in vacuo* and the resultant residue re-dissolved in DCM and employed in the next step TOF-MS ESI: *m/z* = 1569.4034 (M⁺)

Preparation of complex [(Ir(III)(2-(2,4-difluorophenyl)pyridine)₂)(Ir(III)(2-phenylpyridine)₂)(tris(4-[4'-methyl-2, 2'-bipyridyl]carboxy)CTG)].(PF₆) (C2.5):



[Ir(ppy)₂(MeCN)₂].PF₆ (0.0129 g, 0.017 mmol) was dissolved in DCM (5 mL) and added to a stirred solution of **C2.5a** (0.015 g, 0.008 mmol) in DCM (10 mL) in the absence of light. The mixture was stirred at room temperature for 12 hrs until HR-MS analysis showed full conversion to the {[Ir(ppy)₂]₂[Ir(dfppy)₂](**L2**)}³⁺ species, **C2.5**. The DCM was removed *in vacuo*, and the residue re-dissolved in minimal DCM, then diethyl ether was added to the solution to give the title product as a pale orange powder (0.020 g, 76%) ¹H NMR (300 MHz, CD₃CN) δ 9.06 (s, 1H), 8.56 (s, 1H), 8.33 (d, *J* = 7.7 Hz, 1H), 8.21 (d, *J* = 5.0 Hz, 1H), 8.05 (t, *J* = 11.8 Hz, 2H), 7.84 (dd, *J* = 15.8, 7.1 Hz, 3H), 7.72 – 7.52 (m, 1H), 7.39 (s, 1H), 7.15 (s, 1H), 7.12 – 6.97 (m, 2H), 6.93 (t, *J* = 7.3 Hz, 1H), 6.83 – 6.57 (m, 1H), 6.28 (dd, *J* = 13.0, 7.7 Hz, 1H), 5.74 (dd, *J* = 13.9, 8.6 Hz, 1H), 4.90 (d, *J* = 13.8 Hz, 1H), 3.76 (d, *J* = 13.4 Hz, 3H), 2.54 (s, 2H); ¹³C{¹H} NMR (126 MHz, CD₃CN) δ 168.39, 168.26, 164.64, 162.91, 158.54, 155.50, 153.98, 153.30, 152.91, 150.91, 150.50, 150.18, 145.09, 144.85, 140.61, 140.32, 139.61, 138.89, 132.57, 132.39, 131.39, 130.54, 128.55, 127.09, 125.88, 124.88, 124.51, 123.66, 120.91, 118.26, 115.27, 113.92, 56.95, 36.22, 21.30; TOF-MS ESI: *m/z* = 856.8657 (M³⁺); Analysis for C₁₂₆H₉₂F₂₂Ir₃N₁₂O₉P₃ (% calculated, found) C (50.35, 47.99) H (3.09, 3.26) N (5.59, 5.45); Infrared Analysis (FT-IR, cm⁻¹) 557, 755, 839, 1031, 1139, 1176, 1248, 1410, 1478, 1606, 1751 (s), 3040 (b)

4.6.2 Photophysical studies

All samples were prepared at the University of St Andrews by Diego Rota Martir, in HPLC grade acetonitrile with varying concentrations in the order of 10⁻⁴ - 10⁻⁶ M. Absorption spectra were recorded at room temperature using a Shimadzu UV-1800 double beam spectrophotometer. Molar absorptivity determination was verified by linear least-squares fit of values obtained from at least four independent solutions at varying concentrations with absorbance ranging from 6.05 × 10⁻⁵ to 2.07 × 10⁻⁵ M. The sample solutions for the emission spectra were prepared in HPLC-grade MeCN and degassed via freeze-pump-thaw cycles using a quartz cuvette designed in-house. Steady-state emission and excitation spectra and time-resolved emission spectra were recorded at 298 K using an Edinburgh Instruments F980. All samples for steady-state measurements were excited at 360 nm, while samples for time-resolved

measurements were excited at 378 nm using a PDL 800-D pulsed diode laser. Emission quantum yields were determined using the optically dilute method.³² A stock solution with absorbance of *ca.* 0.5 was prepared and then four dilutions were prepared with dilution factors between 2 and 20 to obtain solutions with absorbances of *ca.* 0.095, 0.065, 0.05 and 0.018, respectively. The Beer-Lambert law was found to be linear at the concentrations of these solutions. The emission spectra were then measured after the solutions were rigorously degassed via three freeze-pump-thaw cycles prior to spectrum acquisition. For each sample, linearity between absorption and emission intensity was verified through linear regression analysis and additional measurements were acquired until the Pearson regression factor (R^2) for the linear fit of the data set surpassed 0.9. Individual relative quantum yield values were calculated for each solution and the values reported represent the slope value. The equation $\Phi_s = \Phi_r (A_r/A_s)(I_s/I_r)(n_s/n_r)^2$ was used to calculate the relative quantum yield of each of the sample, where Φ_r is the absolute quantum yield of the reference, n is the refractive index of the solvent, A is the absorbance at the excitation wavelength, and I is the integrated area under the corrected emission curve. The subscripts s and r refer to the sample and reference, respectively. A solution of quinine sulfate in 0.5 M H₂SO₄ ($\Phi_r = 54.6\%$) was used as external references.³³

PMMA doped films were prepared by spin coating the samples from a solution of 2-methoxyethanol (HPLC grade) containing 5 % w/w of the desired sample. Steady-state emission and excitation spectra and time-resolved emission spectra of both powders and doped films were recorded at 298 K using an Edinburgh Instruments F980. Solid-state PLQY measurements of thin films were performed in an integrating sphere under a nitrogen purge in a Hamamatsu C9920-02 luminescence measurement system.³⁴

4.7 Bibliography

- 1 S. Fantacci and F. De Angelis, *Coord. Chem. Rev.*, 2011, **255**, 2704–2726.
- 2 E. Baranoff, J.-H. Yum, M. Graetzel and M. K. Nazeeruddin, *J. Organomet. Chem.*, 2009, **694**, 2661–2670.
- 3 J. Jayabharathi, V. Thanikachalam and R. Sathishkumar, *New J. Chem.*, 2014, **39**, 235–245.

-
- 4 R. D. Costa, E. Ortí, H. J. Bolink, F. Monti, G. Accorsi and N. Armaroli, *Angew. Chem. Int. Ed.*, 2012, **51**, 8178–8211.
 - 5 C.-C. Wang, Y.-M. Jing, T.-Y. Li, Q.-L. Xu, S. Zhang, W.-N. Li, Y.-X. Zheng, J.-L. Zuo, X.-Z. You and X.-Q. Wang, *Eur. J. Inorg. Chem.*, 2013, **2013**, 5683–5693.
 - 6 B. Tong, Q. Mei, D. Chen and M. Lu, *Synth. Met.*, 2012, **162**, 1701–1706.
 - 7 J. Jayabharathi, K. Jayamoorthy and V. Thanikachalam, *J. Organomet. Chem.*, 2014, **761**, 74–83.
 - 8 D. Ma, L. Duan, Y. Wei and Y. Qiu, *Chem. – Eur. J.*, 2014, **20**, 15903–15912.
 - 9 S. Ladouceur and E. Zysman-Colman, *Eur. J. Inorg. Chem.*, 2013, **2013**, 2985–3007.
 - 10 M. Tavasli, T. N. Moore, Y. Zheng, M. R. Bryce, M. A. Fox, G. C. Griffiths, V. Jankus, H. A. Al-Attar and A. P. Monkman, *J. Mater. Chem.*, 2012, **22**, 6419–6428.
 - 11 A. B. Tamayo, S. Garon, T. Sajoto, P. I. Djurovich, I. M. Tsyba, R. Bau and M. E. Thompson, *Inorg. Chem.*, 2005, **44**, 8723–8732.
 - 12 L. He, J. Qiao, L. Duan, G. Dong, D. Zhang, L. Wang and Y. Qiu, *Adv. Funct. Mater.*, 2009, **19**, 2950–2960.
 - 13 E. C. Constable, C. E. Housecroft, G. E. Schneider, J. A. Zampese, H. J. Bolink, A. Pertegás and C. Roldan-Carmona, *Dalton Trans.*, 2014, **43**, 4653–4667.
 - 14 K. P. S. Zaroni, B. K. Kariyazaki, A. Ito, M. K. Brennaman, T. J. Meyer and N. Y. Murakami Iha, *Inorg. Chem.*, 2014, **53**, 4089–4099.
 - 15 T. Kim, J. Lee, S. U. Lee and M. H. Lee, *Organometallics*, 2015, **34**, 3455–3458.
 - 16 P.-H. Lanoë, J. Chan, G. Gontard, F. Monti, N. Armaroli, A. Barbieri and H. Amouri, *Eur. J. Inorg. Chem.*, 2016, n/a–n/a.

-
- 17 BenRG, *English: CIE 1931 xy color space diagram. Drawn (or rather programmatically generated) from scratch, but the visual design is based on File:CIExy1931.png by w:User:PAR. Major differences:*, 2009.
- 18 A. M. Prokhorov, A. Santoro, J. A. G. Williams and D. W. Bruce, *Angew. Chem. Int. Ed.*, 2012, **51**, 95–98.
- 19 M. Y. Wong, G. Xie, C. Tourbillon, M. Sandroni, D. B. Cordes, A. M. Z. Slawin, I. D. W. Samuel and E. Zysman-Colman, *Dalton Trans.*, 2015, **44**, 8419–8432.
- 20 J. Fernández-Cestau, N. Giménez, E. Lalinde, P. Montaña, M. T. Moreno and S. Sánchez, *Organometallics*, 2015, **34**, 1766–1778.
- 21 R. D. Costa, G. Fernández, L. Sánchez, N. Martín, E. Ortí and H. J. Bolink, *Chem. – Eur. J.*, 2010, **16**, 9855–9863.
- 22 A. Auffrant, A. Barbieri, F. Barigelletti, J. Lacour, P. Mobian, J.-P. Collin, J.-P. Sauvage and B. Ventura, *Inorg. Chem.*, 2007, **46**, 6911–6919.
- 23 V. Ramu, M. R. Gill, P. J. Jarman, D. Turton, J. A. Thomas, A. Das and C. Smythe, *Chem. – Eur. J.*, 2015, **21**, 9185–9197.
- 24 M. C. Gimeno, V. Fernández-Moreira and I. Marzo, *Chem. Sci.*, 2014, **5**, 4443–4446.
- 25 P. M. Griffiths, F. Loiseau, F. Puntoriero, S. Serroni and S. Campagna, *Chem. Commun.*, 2000, **23**, 2297–2298.
- 26 G. Sahara, R. Abe, M. Higashi, T. Morikawa, K. Maeda, K. Ueda and O. Ishitani, *Chem. Commun.*, 2015, **51**, 10722–10725.
- 27 Y. Tamaki, K. Koike, T. Morimoto, Y. Yamazaki and O. Ishitani, *Inorg. Chem.*, 2013, **52**, 11902–11909.
- 28 V. W.-W. Yam, S. H.-F. Chong, K. M.-C. Wong and K.-K. Cheung, *Chem. Commun.*, 1999, 1013–1014.
- 29 V. L. Whittle and J. A. G. Williams, *Dalton Trans.*, 2009, 3929–3940.
- 30 F. Neve, A. Crispini, S. Serroni, F. Loiseau and S. Campagna, *Inorg. Chem.*, 2001, **40**, 1093–1101.

- 31 X. Shang, D. Han, Q. Zhan, G. Zhang and D. Li, *Organometallics*, 2014, **33**, 3300–3308.
- 32 G. A. Crosby and J. N. Demas, *J. Phys. Chem.*, 1971, **75**, 991–1024.
- 33 A. M. Brouwer, *Pure Appl. Chem.*, 2011, **83**, 2213–2228.
- 34 N. C. Greenham, I. D. W. Samuel, G. R. Hayes, R. T. Phillips, Y. A. R. R. Kessener, S. C. Moratti, A. B. Holmes and R. H. Friend, *Chem. Phys. Lett.*, 1995, **241**, 89–96.

5 Chapter 5

Heteronuclear ruthenium-iridium complexes and ruthenium containing supramolecular assemblies

5.1 Introduction

Ruthenium(II) polypyridine complexes, or indeed ruthenium systems of the form $\{[\text{Ru}(\text{N}^{\wedge}\text{N})_3]2\text{X}\}$, possess interesting photophysical properties. A wealth of research into many facets of their emission has been undertaken. These types of system have found applications in not only luminescent biomedical imaging, but combinatorial theranostic approaches too, due to their oxygen sensitive emission response.^{1,2} The oxygen-induced quenching of emission has been used to directly image hypoxic cells, a common signifier of cell death. Ruthenium polypyridyl complexes have also found application in anti-cancer and anti-microbial settings.³⁻⁵ In addition to the polypyridyl-type complexes, ruthenium-arene systems have also found applications as anti-cancer agents.⁶⁻⁹ The face-capped ruthenium systems have also been incorporated into metallo-supramolecular assemblies to combine the anti-cancer activity of the ruthenium unit with potential drug delivery applications as well.^{6,10} Aside from the biomedical application of ruthenium emission properties, the fabrication of light emitting electrochemical cells has also been a considerable area of research.¹¹⁻¹³ There are examples of ruthenium polypyridyls as the emissive layer in electroluminescent devices as far back as 1996, and the same modulation of emission that has previously been discussed in relation to the $[\text{Ir}(\text{C}^{\wedge}\text{N})_2(\text{N}^{\wedge}\text{N})]^+$ systems can be achieved within a ruthenium polypyridyl motif.¹⁴

There are examples of multi-metallic heteronuclear systems, notably a ruthenium-iridium system where the separate and successive emission of each component can be cycled through.¹⁵ There are also examples of Ir(III)-Ru(II) heteronuclear species with varying Ir:Ru ratios that display emission dominated by the ruthenium centre.¹⁶

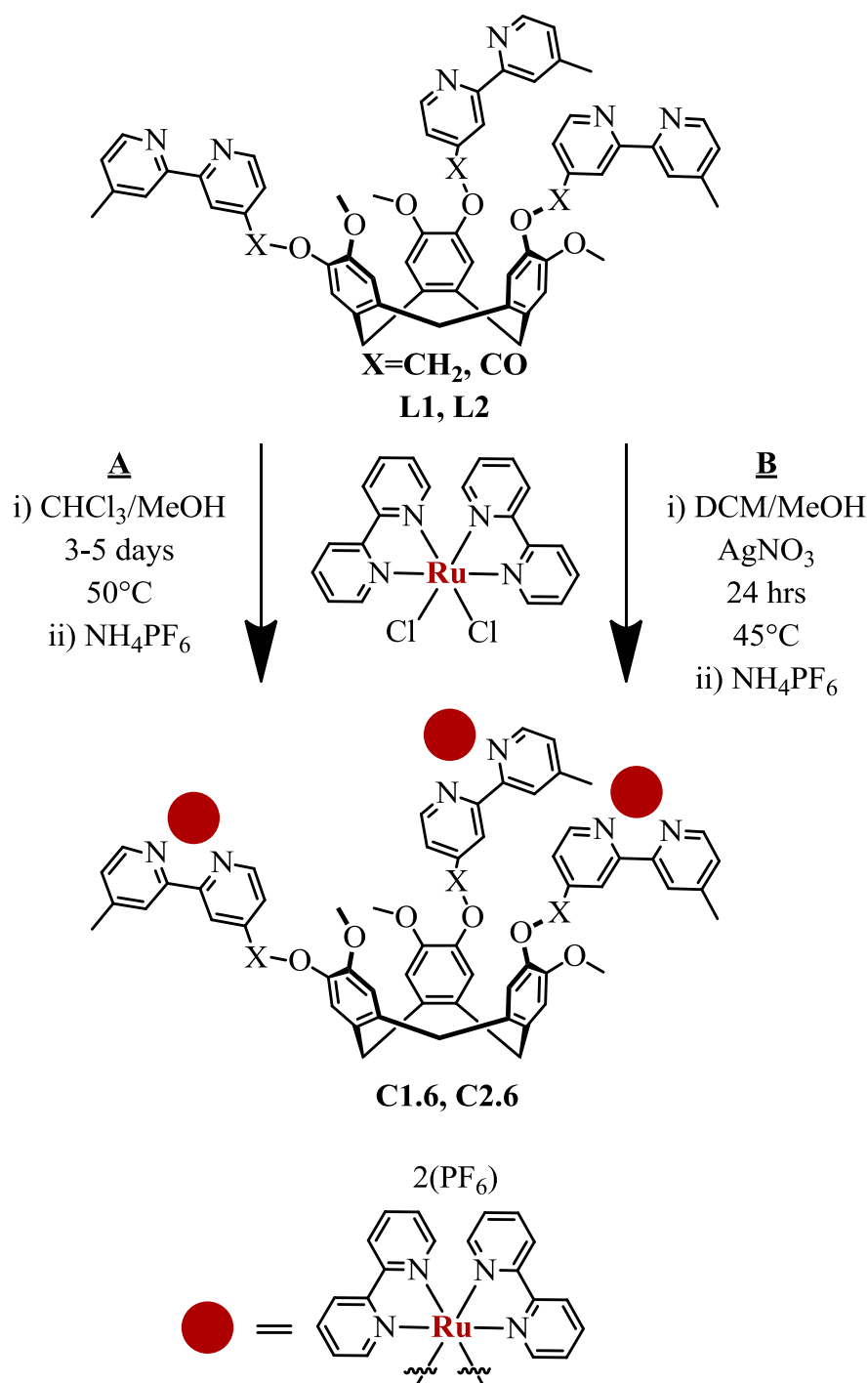
5.2 Preparation of tri-metallic ruthenium complexes

The synthesis of both homo- and hetero- tri-metallic iridium complexes were previously discussed in Chapters Three and Four. This chapter will concern the

analogous tri-ruthenium species, and subsequently moving on towards heteronuclear systems.

The ubiquitous ruthenium metallotecton, *cis*-bis(2,2'-bipyridine)dichlororuthenium, was employed as the ruthenium source in combination with **L1** and **L2** to furnish tri-metallic, tris-chelated ruthenium complexes **C1.6** and **C2.6**, as shown in Scheme 5.1. An almost identical synthetic procedure was employed as in Chapter two, whereby the ruthenium starting material was combined with **L1** or **L2** in a 9:1 mixture of chlorinated solvent to methanol. The temperature was elevated slightly compared to the iridium analogues, due to the more tightly bound terminally coordinated chloride anions, as opposed to the bridging chlorides in the iridium dimer, therefore chloroform was substituted for the lower boiling DCM solvent.

Generally, *tris*-chelate complexes of the form $[\text{Ru}(\text{bpy})_2(\text{N}^{\wedge}\text{N})]$ have been prepared through reaction of the previously mentioned *cis*-bis(2,2'-bpy)dichlororuthenium with an $\text{N}^{\wedge}\text{N}$ ligand in alcohol/water solvent mixtures.^{17–21} The aqueous alcoholic solvents employed help solubilise the metal precursor, however in this case **L1** and **L2** are particularly insoluble in alcoholic solvents; in fact the ligands are purified through precipitation with methanol solvent, accordingly, a modified procedure was implemented.²² The ruthenium metal precursor was dissolved in a minimum amount of methanol, whilst the ligands were dissolved in an excess of chlorinated solvent. The two solutions were combined slowly with vigorous stirring and the resultant dark purple solution was heated to just below reflux. Over time the dark purple solution lightened to a blood-red colour, indicative of $\text{Ru}(\text{bpy})_3$, during this time the reaction was followed and analysed through HR ESI-MS.



Scheme 5.1: General synthetic route towards tri-metallic C1.6 and C2.6.

The complete formation of **C1.6** and **C2.6** took between 3-5 days at $\sim 40^\circ\text{C}$, after which time the latent chloride anions were exchanged for hexafluorophosphate through addition of excess saturated ammonium hexafluorophosphate solution. The tri-metallic, hexa-cationic complexes are remarkably soluble; as such only partial precipitation of the hexafluorophosphate salts was observed. Therefore, the remaining solvent was removed *in vacuo* to leave a bright orange residue that was

dissolved in dichloromethane and washed with water to removed any excess inorganic salts. The resultant dark orange dichloromethane solution was dried through use of magnesium sulphate and concentrated, before addition of excess diethyl ether to furnish the desired products as bright orange powders. The isolatable yields were between 70-85%, showing no evidence of the mono- or di-metallic species.

Alternatively, **C1.6** and **C2.6** can be formed in 24 hours with the addition of a halide abstracting agent, in this case silver nitrate.²³ An analogous procedure was employed; dissolution of the ligand in dichloromethane solvent and the metal precursor in methanol solvent, however a third solution of two equivalents of silver nitrate in methanol was also prepared. Two separate dropping funnels were charged with the two methanolic solutions and added drop-wise over the course of one hour to a vigorously stirred solution of ligand. Once addition of the methanolic solutions was complete, the resultant solution was heated to reflux for 24 hours in the absence of light. After which time the solution was filtered, whilst still hot, through a pad of Celite and the anions once again exchanged for hexafluorophosphate.

Whilst the second method is advantageous in terms of the time required for the reaction to go to completion, the reaction is not as easily followed through HR-MS. Employing the first method, the reaction can be monitored regularly until the only product observed is the desired tri-metallic species, whereas use of a halide abstracting agent can lead to by-products consisting of un-reacted metallic starting material, leading to the necessity of column chromatography.

5.2.1 Spectroscopic analysis of ruthenium complexes

Whilst the previously discussed iridium complexes **C1.1-4** and **C2.1-4** all gave remarkably clean mass spectra, with the only notable peaks belonging to the 3+ tri-cationic complexes, the ruthenium analogues are markedly different in their behaviour.

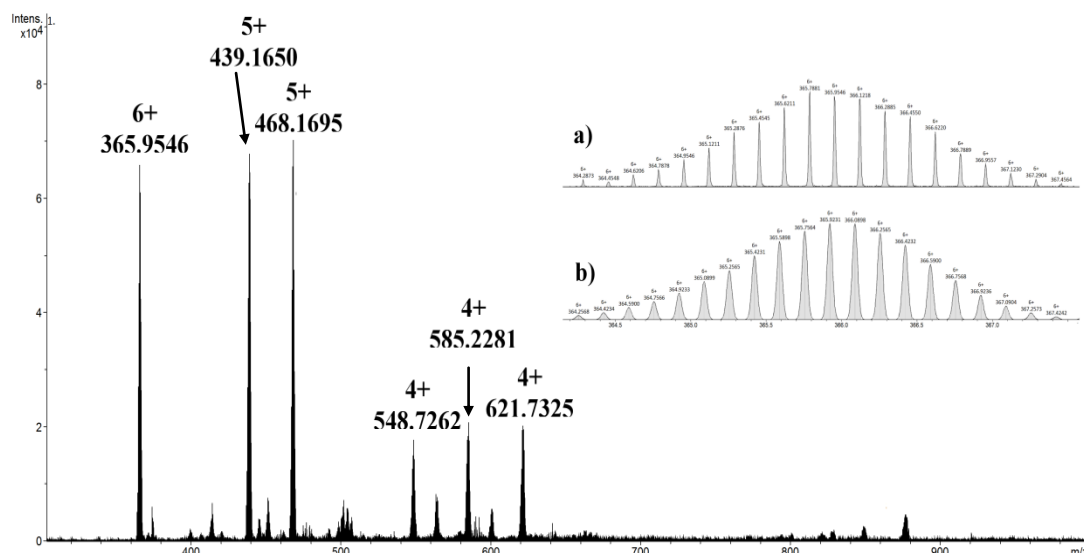


Figure 5.1 : HR ESI-MS of C1.6 showing not only the 6+ molecular ion peak, but also other notable charge states, with a) the measured isotope pattern of the 6+ peak and b) the calculated pattern for the 6+ peak of C1.6 shown inset.

At first glance the HR ESI-MS of C1.6 looks rather complicated, as evidenced in Figure 5.1, suggesting a complex mixture of products, partially substituted metal complexes and by-products. However once full analysis of the available counterions was considered, all of the observed charge states and charge state envelopes can be attributed to the desired tri-metallic C1.6. The expected molecular ion peak observed at 365.9546 m/z is attributable to the naked 6+ complex $\{[\text{Ru}(\text{bpy})_2]_3\text{L1}\}^{6+}$, observed without any non-coordinated hexafluorophosphate anions, calculated for 365.9233 m/z . The pair of 5+ peaks can be assigned to the mono-deprotonated complex $\{([\text{Ru}(\text{bpy})_2]_3\text{L1})\cdot(-\text{H}^+)\}^{5+}$ at 439.1650 m/z , and the mono-hexafluorophosphate associated complex $\{([\text{Ru}(\text{bpy})_2]_3\text{L1})\cdot(\text{PF}_6^-)\}^{5+}$ at 468.1695 m/z . Correspondingly the 4+ peaks belong to the doubly-deprotonated species $\{([\text{Ru}(\text{bpy})_2]_3\text{L1})\cdot(-2\text{H}^+)\}^{4+}$ at 548.7262, the mono-deprotonated mono-hexafluorophosphate associated species $\{([\text{Ru}(\text{bpy})_2]_3\text{L1})\cdot(-\text{H}^+)\cdot(\text{PF}_6^-)\}^{4+}$ at 585.2281 and the doubly-hexafluorophosphate associated species $\{([\text{Ru}(\text{bpy})_2]_3\text{L1})\cdot(2\text{PF}_6^-)\}^{4+}$ at 621.7325. The calculated theoretical isotope pattern of the 6+ charge state matches exactly with the observed pattern, displaying a diagnostic three-ruthenium roofed pyramid.

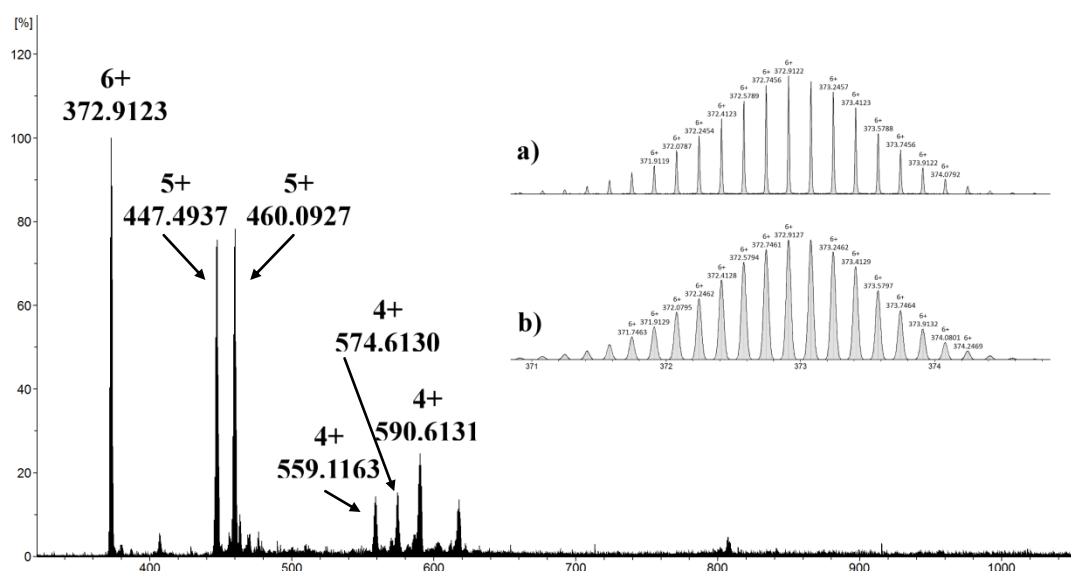


Figure 5.2 : HR ESI-MS of C2.6 showing not only the 6+ molecular ion peak, but also other notable charge states, with a) the measured isotope pattern of the 6+ peak and b) the claulated pattern for the 6+ peak of C2.6 shown inset.

A comparable mass spectrum was observed for **C2.6**, displaying charge state envelopes for both the 5+ and 4+ species, as shown in Figure 5.2. However, as a point of note, the above HR ESI-MS was recorded from a sample of **C2.6** formed through the silver nitrate method mentioned in Section 5.2 before the anion exchange step, and therefore contains an excess of nitrate anions.

The 6+ peak at 372.9123 m/z can be attributed to the naked 6+ cation $\{([Ru(bpy)_2]_3L2)\}^{6+}$ without the associated nitrate anions, calculated for 372.9127 m/z . Once again, the pair of 5+ peaks at 447.4937 and 460.0927 m/z are assigned to $\{([Ru(bpy)_2]_3L2)\cdot(-H^+)\}^{5+}$ and $\{([Ru(bpy)_2]_3L2)\cdot(NO_3^-)\}^{5+}$ respectively. The 4+ charge envelope is assigned to $\{([Ru(bpy)_2]_3L2)\cdot(-2H^+)\}^{4+}$ at 559.1163, $\{([Ru(bpy)_2]_3L2)\cdot(-H^+)\cdot(NO_3^-)\}^{4+}$ at 574.6130 and $\{([Ru(bpy)_2]_3L2)\cdot(2NO_3^-)\}^{4+}$ at 590.6131 m/z . The expected distinctive three-ruthenium isotope pattern can again be seen in the expanded view of the 6+ peak, matching the predicted pattern exactly.

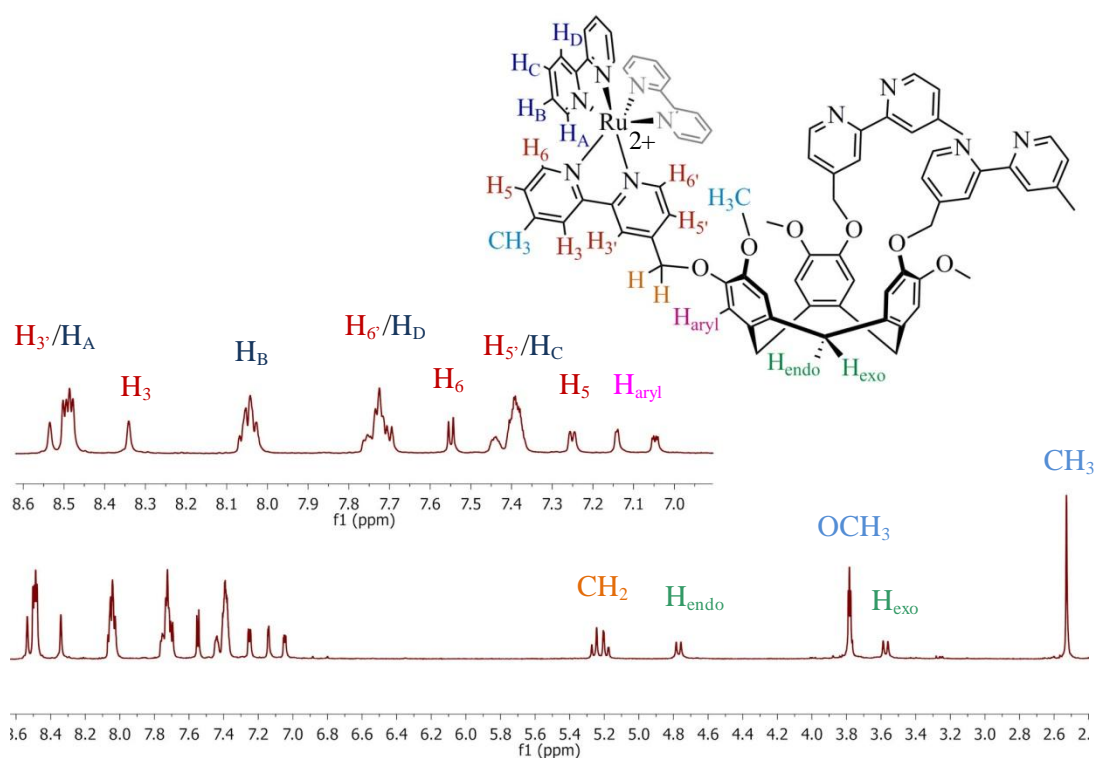


Figure 5.3: Assigned ^1H NMR spectrum of **C1.6** in CD_3CN , with an expanded view of the aromatic region and molecular structure shown inset (only one metallated arm is shown for clarity).

C1.6 exhibits C_3 symmetry in the solution state, hence the ^1H NMR spectrum is assigned to only one third of the complex. Whilst displaying complexity similar to the previously discussed iridium complexes, the proton NMR is simplified somewhat due to the symmetry of the 2,2'-bipyridine ancillary ligands; each pyridyl ring is magnetically equivalent on an NMR timescale, leading to just four distinct environments for all sixteen ancillary bipyridine protons. As shown in Figure 5.3, the protons of the methyl group of the bipyridine arm are observed as a sharp singlet at 2.5 ppm, as expected. The characteristic *endo/exo* doublets of the methylene bridge can be seen at 4.8 and 3.6 ppm respectively. Interestingly, the CH_2 of the bridging ethyl linkage is split into a roofed double-doublet at 5.2 ppm, becoming pseudo-diastereotopic due to the restricted rotation around the ether linking group. The aromatic region is noticeably complex; with eight one-proton aromatic resonances assigned to the bipyridine and aryl protons of the ligand, and four four-proton resonances assigned to the ancillary bipyridine ligand. Many of the peaks overlap with each other, but the precise assignments were once again ascertained from ^1H - ^1H COSY NMR spectrum.

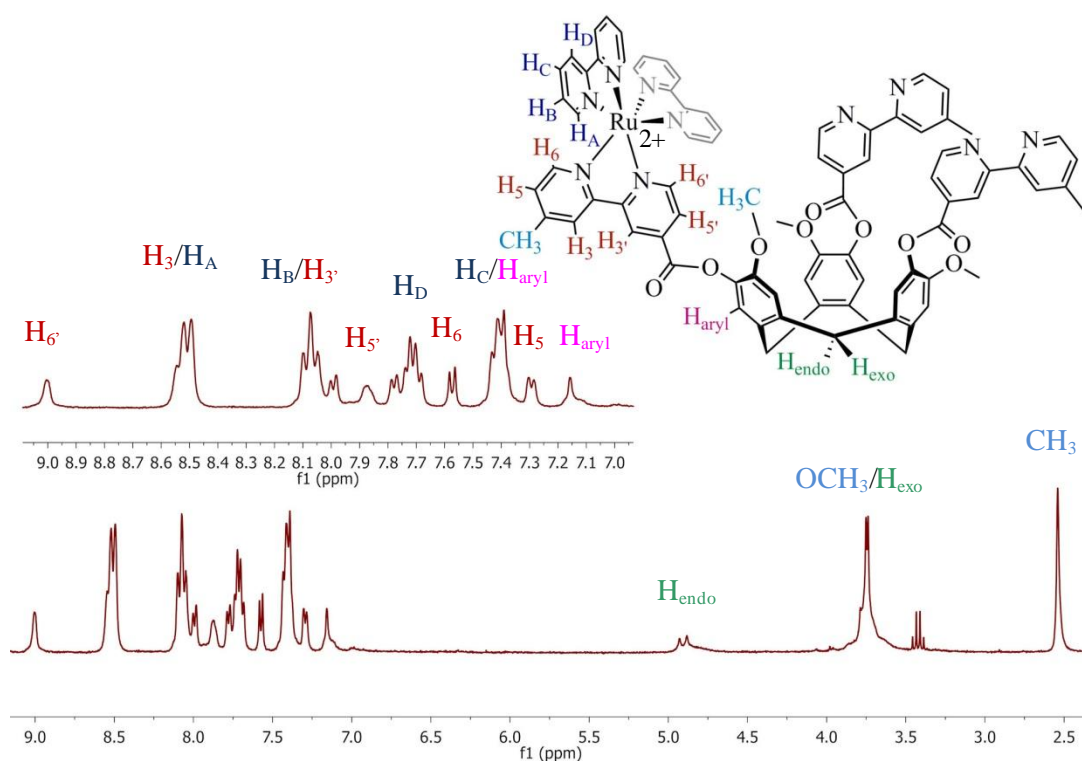


Figure 5.4: ^1H NMR spectrum of **C2.6** in CD_3CN , with an expanded view of the aromatic region and molecular structure shown inset (only one metallated arm is shown for clarity).

C2.6 displays a sharp singlet at 2.5 ppm belonging to the methyl protons on the bipyridine arm, whilst also showing a peak at 3.7 ppm assigned to both the *exo* proton and the methoxy protons overlapping, as seen in Figure 5.4. As is the case with **C1.6**, **C2.6** displays a complex aromatic region comprised of eight one-proton resonances assigned to the ligand scaffold and four four-proton resonances belonging to the ancillary bipyridine ligand.

5.2.2 Photophysical analysis of ruthenium complexes

The initial photophysical studies, presented herein, were undertaken at the University of Leeds, performed by the author in acetonitrile solution at 293 K. Further, more extensive photophysical investigations are projected to be performed at the University of St Andrews in collaboration with the Zysman-Colman Group.

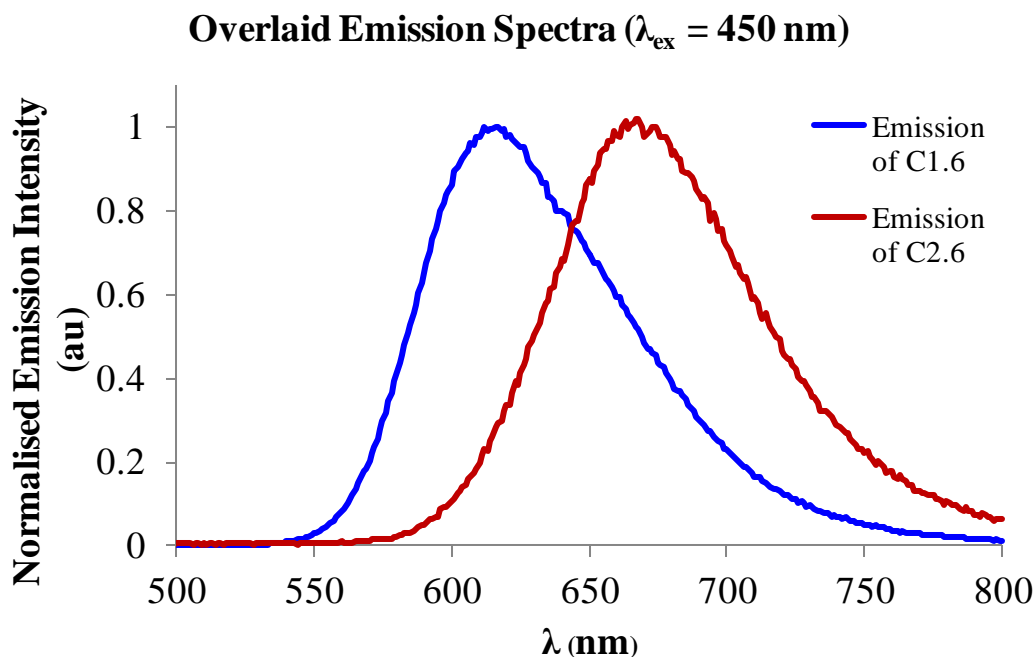


Figure 5.5 : Overlaid emission spectra for C1.6 and C2.6 recorded in acetonitrile solution.

Figure 5.5 contains the emission spectra of both the ether-linked **C1.6** and ester-linked **C2.6**, both spectra resulting from an excitation wavelength of 450 nm. The blue trace represents **C1.6** and displays a λ_{max} of 616 nm, whilst the red trace represents **C2.6** and shows a λ_{max} of 667 nm. Therefore, as in all the previous directly analogous complexes, the ester-linked congener displays a bathochromic shift with respect to the ether-linked complex. In this case, **C2.6** is red-shifted by over 50 nm towards the infra red region of the spectrum.

One point of note that differentiates the ruthenium complexes from the previously discussed rhenium and iridium congeners is the lack of dual-emission seen in the ester-linked species. In the rhenium complex discussed in Chapter 2, **C2.1**, and the iridium complexes discussed in Chapter 3, **C2.2** and **C2.3**, a higher-energy emission band was observed between 530-600 nm, as well as the lower energy, longer lifetime emission assigned to the desired $^3\text{MLCT}$. The conversely shorter lifetimes of the higher-energy peak suggest more ligand, organic-based character to the transition. Thus, it could be that excitation at 450 nm does not promote the ligand-based transition that previously gave rise to the dual-emission observed. However, further photophysical studies, including lifetime analysis and more in depth probing

of the resultant emission would be required to conclude with any degree of certainty the exact transitions occurring within the ruthenium complexes discussed here.

The archetypal $[\text{Ru}(\text{bpy})_3]^{2+}$ system displays a λ_{max} of between 608 and 620 nm in deaerated acetonitrile solution,^{23,24} thus **C1.6** is almost exactly analogous whereas **C2.6** is red-shifted compared to the mono-nuclear analogue. This work goes to show the validity and scope of the bipyridyl-CTG ligand scaffold, as **L1** and **L2** can be combined with rhenium, iridium and ruthenium to furnish a library of emissive complexes that with further ligand engineering could provide emission wavelengths covering a wide range of the colour spectrum.

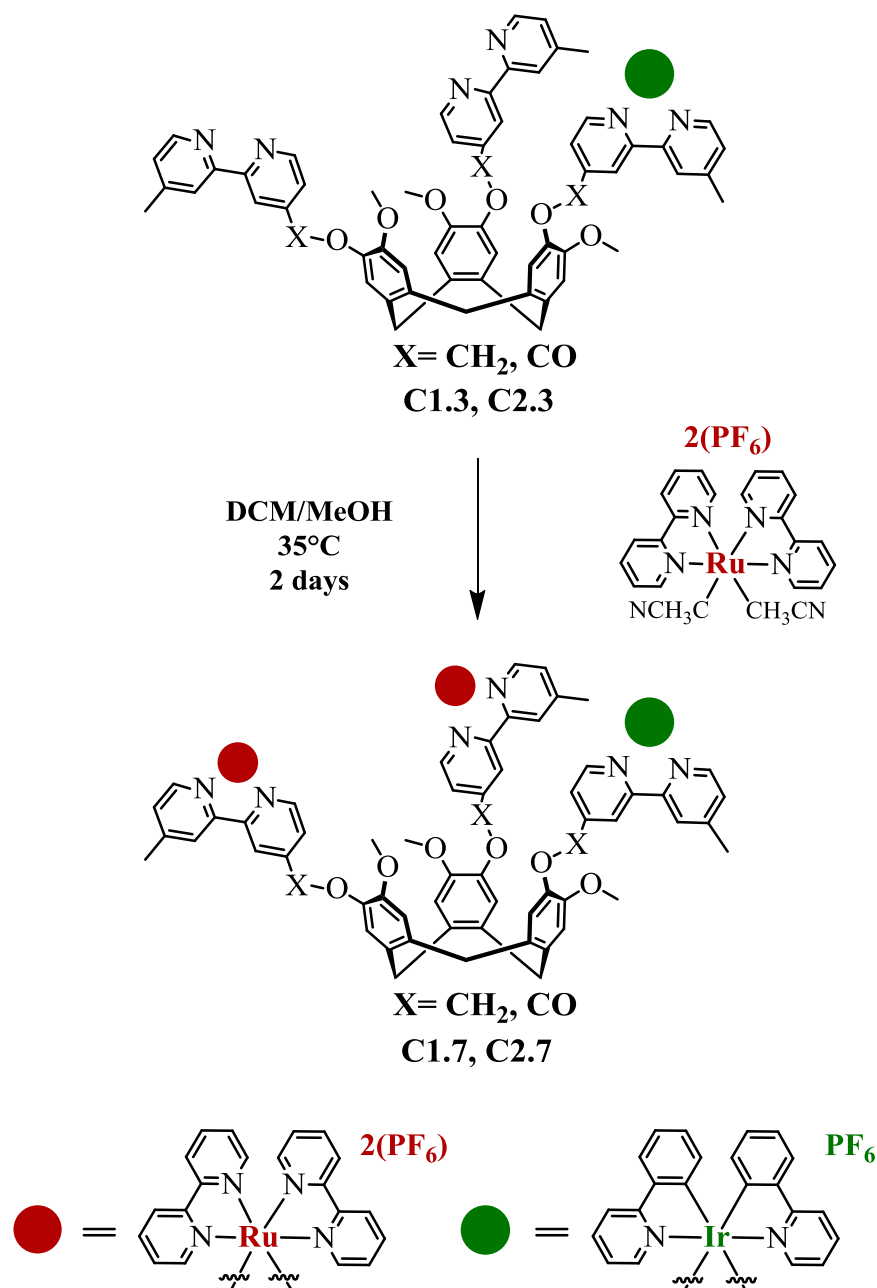
5.3 Preparation of heteronuclear ruthenium-iridium complexes

As was the case with the tri-metallic iridium complexes **C1.2** and **C2.2**, the rational design behind the synthesis of **C1.6** and **C2.6** was to prove the viability of appending bulky luminescent ruthenium centres to this particular ligand scaffold. Once again, the cyclononatriene core does not impede the photophysical properties of tri-metallic complexes, which display strong phosphorescence with emission red-shifted towards the lower energy end of the spectrum. The success of this partnership has been demonstrated in section 5.2.2. However, after establishing the favourable emission properties of **C1.6** and **C2.6**, the consequent objective was to incorporate ruthenium centres into a mixed-metal heteronuclear system. This approach was envisaged to yield a higher degree of discriminatory control over the resultant emission. A modular synthesis was employed, similar to the synthesis of **C1.4-5** and **C2.4-5**, whereby each ligand was mono-substituted and the residual binding sites substituted in a secondary reaction.

The initial combination was of the previously discussed mono-iridium **C1.3** and **C2.3**, further bound to secondary ruthenium centres. As noted in the synthesis of both tri-metallic iridium and ruthenium species, the iridium reaction proceeds at room temperature in an almost self-assembling fashion, whereas the ruthenium reaction requires slightly more forcing conditions, with temperatures of $\sim 50^\circ\text{C}$ required, thus the mono-iridium **C1.3** and **C2.3** were chosen as the initial building blocks. As a secondary consideration, the previously employed *cis*-bis-(2,2'-bipyridine)dichlororuthenium metal precursor was transformed to the bis-acetonitrile adduct in the presence of silver hexafluorophosphate, to removed any

potential need for a halide abstracting agent in the second step of the heteronuclear reaction.

Combination of a 2:1 stoichiometric ratio of mono-iridium complex and ruthenium acetonitrile adduct in dichloromethane solvent furnished both **C1.7** and **C2.7** in good yields, as shown in Scheme 5.2. A few drops of methanol solvent were added to the reaction mixture to ensure complete dissolution of both components. Once again, the progress of the reaction towards the desired product was followed through HR ESI-MS, eventually leading to a complex yet assignable mass spectrometry pattern.



Scheme 5.2 : Modular synthesis of heteronuclear C1.7 and C2.7 from mono-iridium precursors C1.3 and C2.3, key shown at the bottom; red circles representing ruthenium centres and green circles representing iridium centres.

Both constituents already bore hexafluorophosphate anions, negating the need for any anion exchange step. The crude reaction mixture was simply taken to dryness *in vacuo* and re-dissolved in the minimal amount of acetonitrile solvent before the desired product was precipitated as an orange powder through addition of excess diethyl ether.

5.3.1 Spectroscopic analysis of heteronuclear complexes

As with the majority of metal complexes contained herein, mass spectrometry was an invaluable tool for not only following and ascertaining the progress of reactions, but also as an indication of final purity and/or the presence of any un-desired by-products owing to the generally complex ^1H NMR spectra recorded.

C1.7 presents a HR ESI-MS similar to those previously discussed ruthenium-containing mass spectra, in that de-protonation occurs, as well as association with various anions that are present in the ionisation matrix.

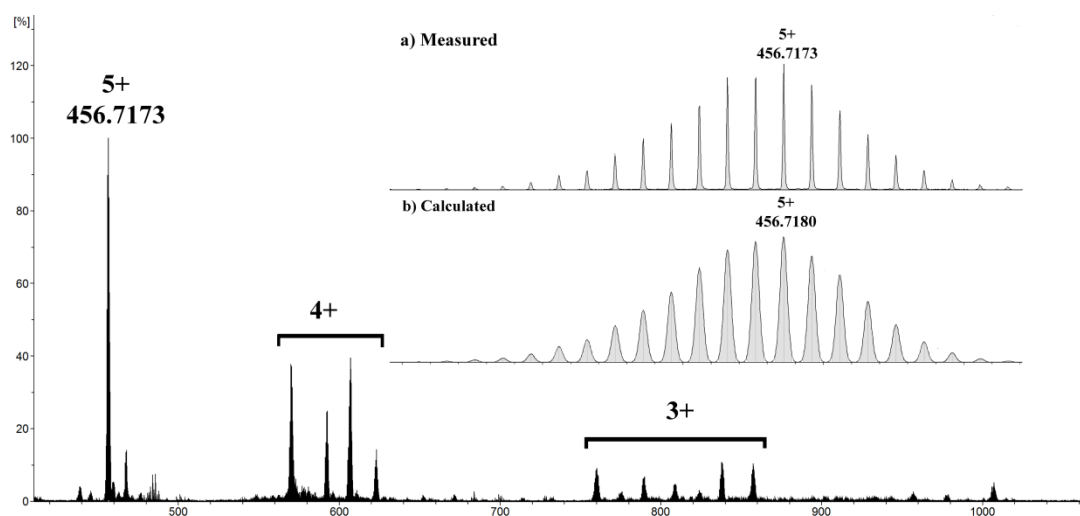


Figure 5.6: HR ESI-MS of C1.7 showing not only the 5+ molecular ion peak, but also the 4+ and 3+ charge state envelopes, the measured and calculated isotope patterns of C1.7 are shown inset.

The naked 5+ complex can be seen at 456.7173 m/z , assigned to $\{([\text{Ru}(\text{bpy})_2]_2[\text{Ir}(\text{ppy})_2]\mathbf{L1})\}^{5+}$ observed without any associated anions, the theoretical m/z being 456.7180. The 4+ charge envelope contains peaks at 570.1450, 592.6591 and 607.1380 m/z , assigned to $\{([\text{Ru}(\text{bpy})_2]_2[\text{Ir}(\text{ppy})_2]\mathbf{L1})\cdot(-\text{H}^+)\}^{4+}$, $\{([\text{Ru}(\text{bpy})_2]_2[\text{Ir}(\text{ppy})_2]\mathbf{L1})\cdot(\text{BF}_4^-)\}^{4+}$ and $\{([\text{Ru}(\text{bpy})_2]_2[\text{Ir}(\text{ppy})_2]\mathbf{L1})\cdot(\text{PF}_6^-)\}^{4+}$. The presence of tetrafluoroborate anions in the mass spectrum is simply due to residual anions present in the spectrometer, and is therefore an artefact of the technique. The 3+ charge state envelope displays peaks at 760.5242, 789.8766, 809.1829, 838.2016 and 857.8466 m/z , all assignable to various combinations of anions and de-protonated species. The 760 peak is assigned to the doubly-deprotonated $\{([\text{Ru}(\text{bpy})_2]_2[\text{Ir}(\text{ppy})_2]\mathbf{L1})\cdot(-2\text{H}^+)\}^{3+}$, with the subsequent peaks assigned to $\{([\text{Ru}(\text{bpy})_2]_2[\text{Ir}(\text{ppy})_2]\mathbf{L1})\cdot(-\text{H}^+)\cdot(\text{BF}_4^-)\}^{3+}$,

$\{([\text{Ru}(\text{bpy})_2]_2[\text{Ir}(\text{ppy})_2]\text{L1})\cdot(-\text{H}^+)\cdot(\text{PF}_6^-)\}^{3+}$,
 $\{([\text{Ru}(\text{bpy})_2]_2[\text{Ir}(\text{ppy})_2]\text{L1})\cdot(\text{BF}_4^-)\cdot(\text{PF}_6^-)\}^{3+}$ and
 $\{([\text{Ru}(\text{bpy})_2]_2[\text{Ir}(\text{ppy})_2]\text{L1})\cdot(2\text{PF}_6^-)\}^{3+}$ in varying degrees of intensity. Therefore all the peaks of notable intensity observable in the HR ESI-MS can be assigned to the desired **C1.7**.

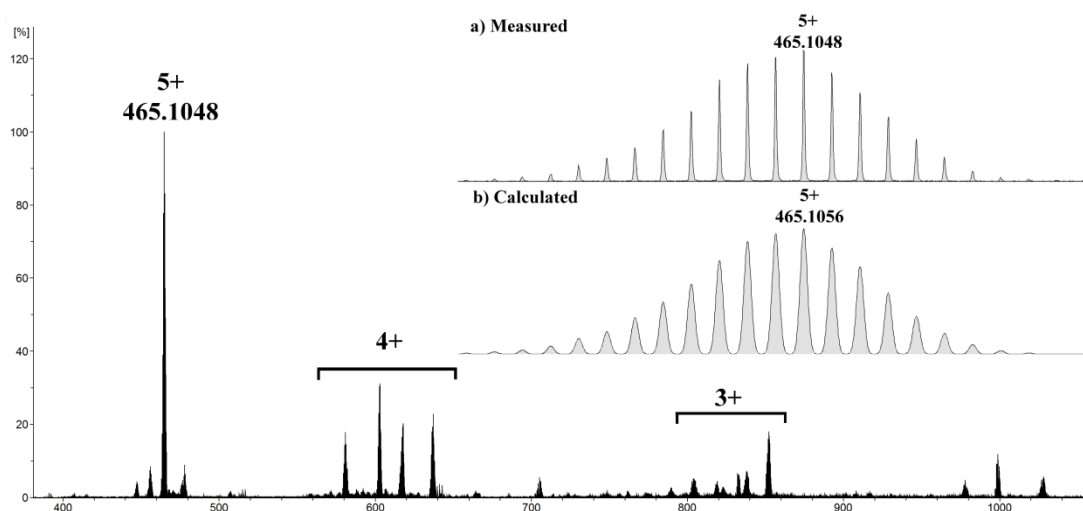


Figure 5.7: HR ESI-MS of C2.7 showing not only the 5+ molecular ion peak, but also the 4+ and 3+ charge state envelopes, the measured and calculated isotope patterns of C2.7 are shown inset.

Again, an analogous mass spectrum was obtained for **C2.7**, displaying the 5+ molecular ion peak and charge state envelopes for the 4+ and 3+ peaks. The molecular ion peak at 465.1048 m/z is assigned as $\{([\text{Ru}(\text{bpy})_2]_2[\text{Ir}(\text{ppy})_2]\text{L2})\}^{5+}$, calculated for 456.1056. The measured and calculated isotope patterns for the 5+ peaks can be seen in Figure 5.7, where the distinctive weighted-pyramid shape can be seen in both. The 4+ charge envelope displays peaks at 581.1295, 603.1437 and 617.8715 m/z , corresponding to $\{([\text{Ru}(\text{bpy})_2]_2[\text{Ir}(\text{ppy})_2]\text{L2})\cdot(-\text{H}^+)\}^{4+}$, $\{([\text{Ru}(\text{bpy})_2]_2[\text{Ir}(\text{ppy})_2]\text{L2})\cdot(\text{BF}_4^-)\}^{4+}$ and $\{([\text{Ru}(\text{bpy})_2]_2[\text{Ir}(\text{ppy})_2]\text{L2})\cdot(\text{PF}_6^-)\}^{4+}$ species. The 3+ charge envelope contains a multitude of peaks at 774.1687, 790.1703, 803.8511, 819.1938, 838.1644 and 852.5138 m/z , assigned to; $\{([\text{Ru}(\text{bpy})_2]_2[\text{Ir}(\text{ppy})_2]\text{L2})\cdot(-2\text{H}^+)\}^{3+}$, $\{([\text{Ru}(\text{bpy})_2]_2[\text{Ir}(\text{ppy})_2]\text{L2})\cdot(-\text{H}^+)\cdot(\text{COO}^-)\}^{3+}$, $\{([\text{Ru}(\text{bpy})_2]_2[\text{Ir}(\text{ppy})_2]\text{L2})\cdot(-\text{H}^+)\cdot(\text{BF}_4^-)\}^{3+}$, $\{([\text{Ru}(\text{bpy})_2]_2[\text{Ir}(\text{ppy})_2]\text{L2})\cdot(\text{BF}_4^-)\cdot(\text{COO}^-)\}^{3+}$, and $\{([\text{Ru}(\text{bpy})_2]_2[\text{Ir}(\text{ppy})_2]\text{L2})\cdot(\text{PF}_6^-)\cdot(\text{COO}^-)\}^{3+}$

$\{([\text{Ru}(\text{bpy})_2]_2[\text{Ir}(\text{ppy})_2]\text{L2})\cdot(\text{BF}_4^-)\cdot(\text{PF}_6^-)\}^{3+}$ respectively. Both the formate and tetrafluoroborate anions are artefacts of the spectrometer and are included in the resultant spectrum due to the ionisation matrix employed. Despite the surfeit of anions present, all notable peaks can be assigned to variants of **C2.7**, suggesting full substitution of all three bipyridine arms in the expected 2:1 ratio of Ru:Ir.

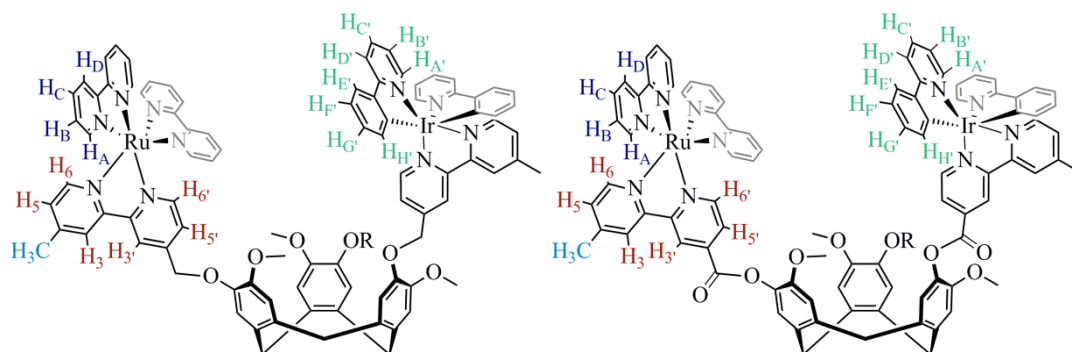


Figure 5.8: Chemical structure of heteronuclear **C1.7** and **C2.7**, with proton assignments referred to throughout the NMR discussion. The third bipyridine arm on each ligand, bound to a second ruthenium centre, is removed for clarity, as are the five counter ions.

The nomenclature used in discussion of the ^1H NMR spectra of **C1.7** and **C2.7** is shown in Figure 5.8. The second ruthenium-bound bipyridine arm is removed for clarity. Therefore, through consideration of relative integrals, the protons on the bipyridine ancillary ligand should integrate to 8, versus an integration of 2 for protons on the phenylpyridine ancillary, all referenced back to integrals of 3 for equivalent protons on the ligand scaffold, however, some of the protons assigned to the bipyridine arms are split due to the effect of binding to different metals.

As expected, the ^1H NMR spectra of both heteronuclear complexes are convoluted, however when compared to both tri-metallic homonuclear analogues, strong similarities appear.

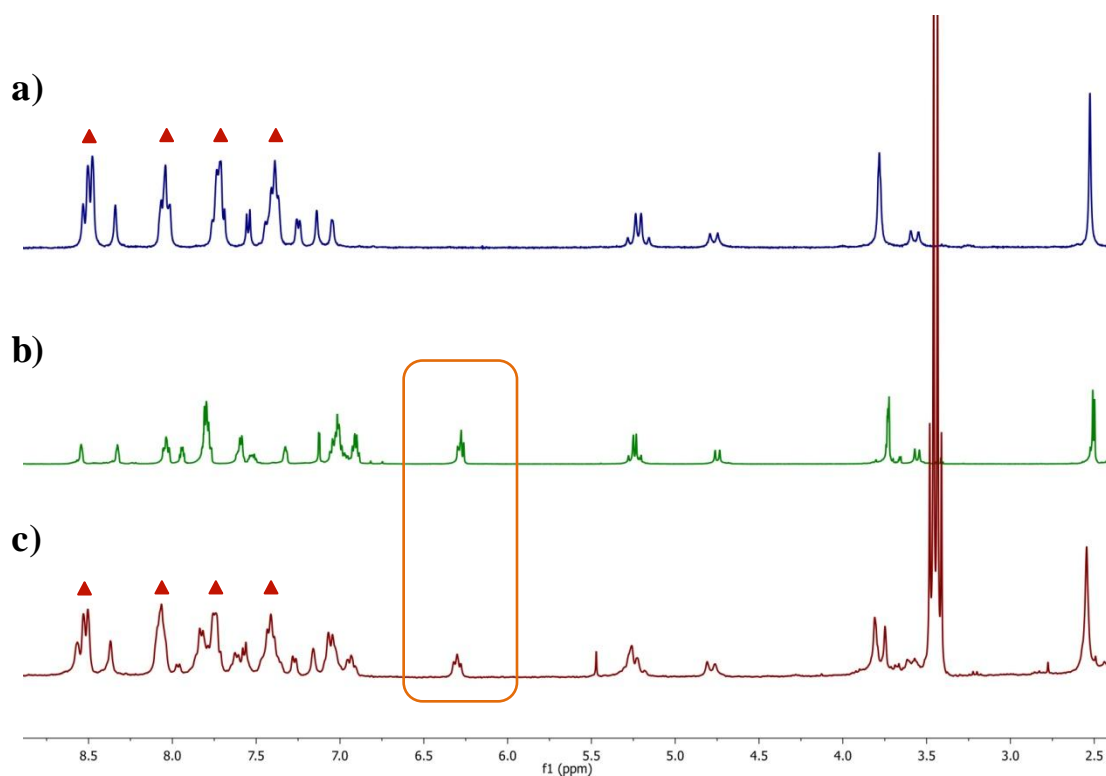


Figure 5.9: Overlay of ^1H NMR spectra in CD_3CN of (a) tris-ruthenium **C1.6**, (b) tris-iridium **C1.2** and (c) heteronuclear **C1.7**, showing the similarity between the homonuclear and heteronuclear analogues.

In Figure 5.9 the topmost blue trace (a) shows the ^1H NMR spectrum of the tri-metallic ruthenium **C1.6**, the middle green trace (b) shows the spectrum of the homo tri-metallic iridium **C1.2** and the bottom red trace (c) shows the spectrum of the resultant heteronuclear **C1.7**. As evidenced, the spectrum of the heteronuclear **C1.7** is almost a perfect superposition of the two previously mentioned homonuclear complexes, displaying both the triplet at ~ 6.2 ppm assigned to $\text{H}_{\text{H}'}$ on the iridium phenylpyridine ancillary ligand (highlighted in orange) and the four four-proton peaks assigned to the four protons $\text{H}_{\text{A}}\text{-H}_{\text{D}}$ on the ruthenium bipyridine ancillary (highlighted with red triangles).

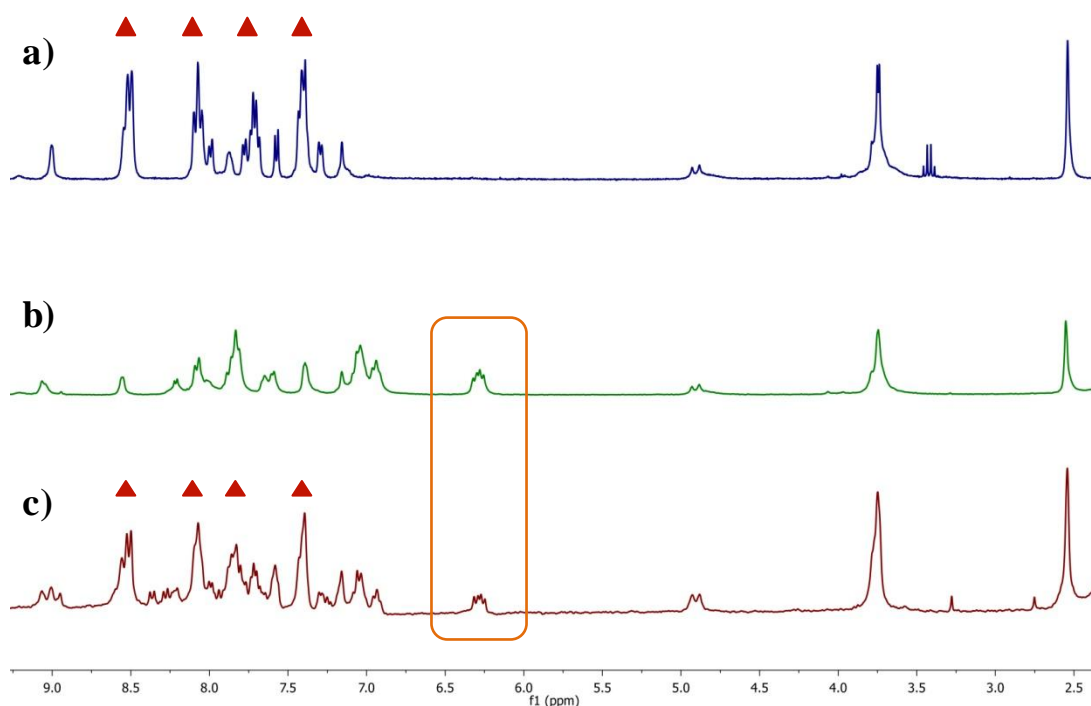


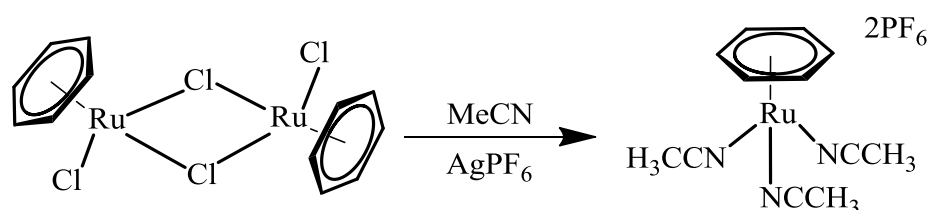
Figure 5.10: Overlay of ^1H NMR spectra in CD_3CN of (a) tris-ruthenium **C2.6**, (b) tris-iridium **C2.2** and (c) heteronuclear **C2.7**, showing the similarity between the homonuclear and heteronuclear analogues.

The spectrum of **C2.7** also shows strong similarities to both homonuclear analogues. The resonance assigned to H_H on the ancillary phenylpyridine ligand is again highlighted in orange, present in both **C2.2** and **C2.7**. All four H_A - H_D resonances belonging to the bipyridine ancillary ligand are highlighted with red triangles. The methyl and methoxy resonances at 2.5 and 3.7 ppm broaden slightly with respect to the homonuclear analogues, most likely due to slight differences in the precise peak position depending on the metal centre that each ligand arm is bound to.

5.4 Towards the preparation of ruthenium containing supramolecular assemblies

In supramolecular chemistry there are numerous examples of ruthenium containing assemblies, particularly self-assembled squares and cubic structures.^{6,7,25-27} Many of these systems employ face-capping ligands to give the ubiquitous ‘piano-stool’ arrangement around the octahedral ruthenium centre, leaving three vacant coordination sites at well defined angles. One approach commonly seen is a two-

component 'metallo-clip' method, whereby the geometrically locked metal centre is first bound to a linear bridging ligand, then subsequently bound to a second linking ligand, either linear or a planar multi-topic ligand.^{9,25,28–31} Two of the most common face-capping ligands are aromatic arene and *p*-cymene fragments, formed from the familiar chloro-bridged dimeric species. In this work in an effort towards supramolecular assemblies, the latent chloride ions were removed and replaced with acetonitrile solvent molecules in the presence of silver hexafluorophosphate, as shown in Scheme 5.3.



Scheme 5.3: Synthesis of 'piano stool' acetonitrile ruthenium precursor.

The aim of this work was to target a supramolecular cube; where four of the eight corners were described by the tripodal ligand **L4** and the remaining four corners by the tripodal ruthenium metallocene.

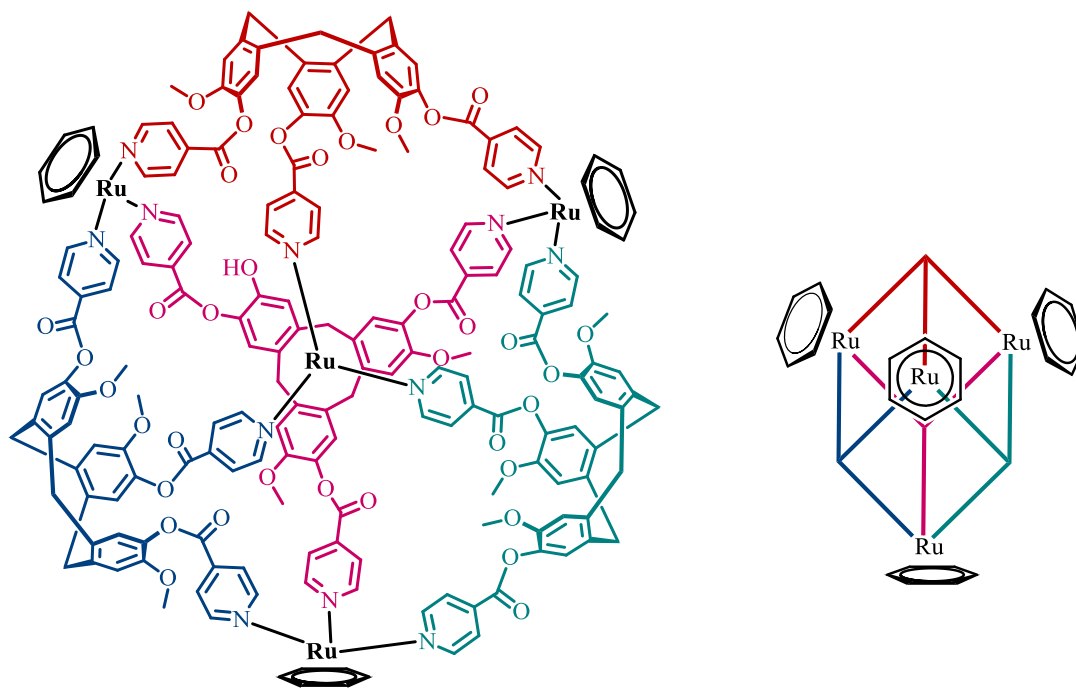


Figure 5.11: Targeted cubic supramolecular structure **CC4.1**, topmost arene ring removed for clarity, and a colour coded schematic showing which ligands and metal centres describe which vertices of the cube.

The tripodal nature of the ligand and the half-sandwich binding motif of the metal are complementary in geometry, describing the eight vertices of a compact cube. A stoichiometric ratio of **L4** and acetonitrile-activated ruthenium precursor, $[\text{Ru}(\text{arene})(\text{MeCN})_3] \cdot 2\text{PF}_6$, were dissolved in deuterated nitromethane solvent and the self-assembly of **CC4.1** followed over time by ^1H NMR spectroscopy with gentle heating.

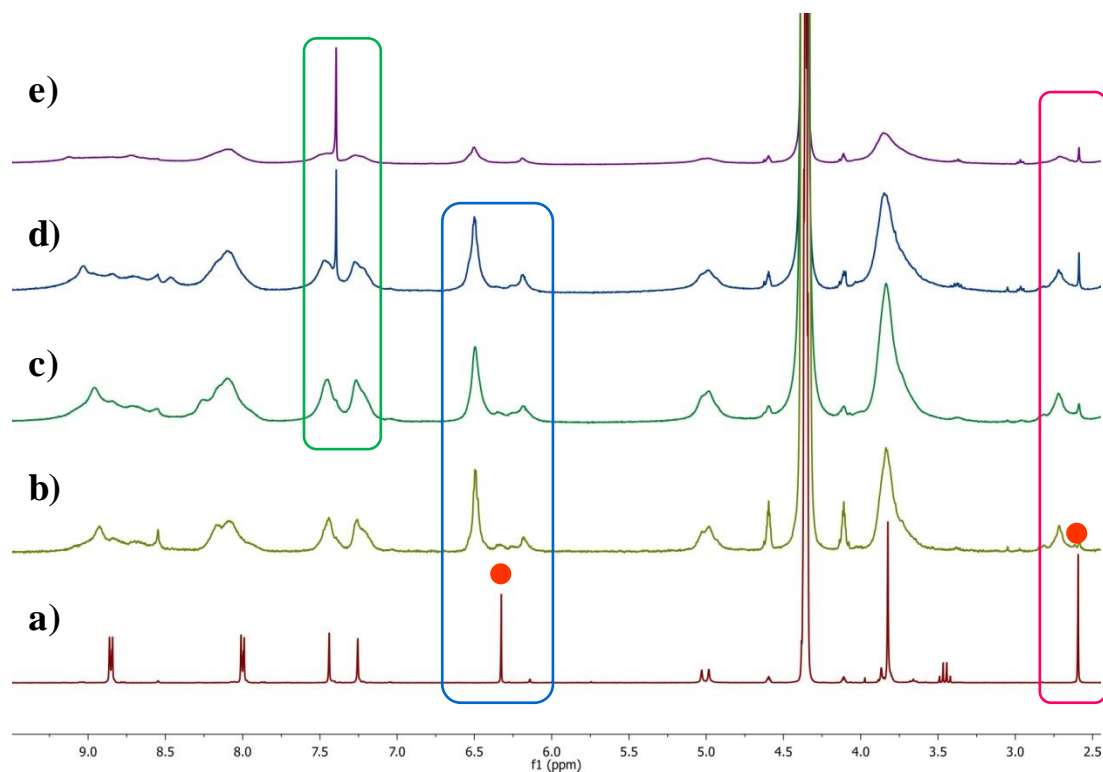


Figure 5.12: Timecourse ^1H NMR study of the formation of **CC4.1 and subsequent decomposition over time a) initial mixture of **L4** and metallocene b) after 4 hrs c) 12 hrs d) 1 week e) 3 weeks in solution.**

As Figure 5.12 shows, the ^1H NMR spectrum resulting from the initial mixture of components is extremely sharp; the resonances marked with an orange circle are due to the protons on the arene ring on the ruthenium metallocene (~ 6.3 ppm) and the coordinated acetonitrile ligands (~ 2.5 ppm). All other peaks in spectrum **a)** are assignable to **L4**. After 4 hours heating at 45°C spectrum **b)** was obtained, this shows the formation of a larger species, evident from the broadening of all the ligand based peaks, suggesting a more rigid, larger species that cannot rotate as freely on an NMR timescale. The almost total loss of the coordinated acetonitrile peak, highlighted in pink, also supports the formation of a supramolecular species whereby the pyridyl moiety of **L4** has displaced the coordinated acetonitrile ligands

on the metallotecton. The broadening out of the resonance assigned to the arene protons, highlighted in blue, also suggests formation of a larger species, as even though the η^6 -[arene-ruthenium] bond would not be restricted, the rotation of the assembly as a whole would be.

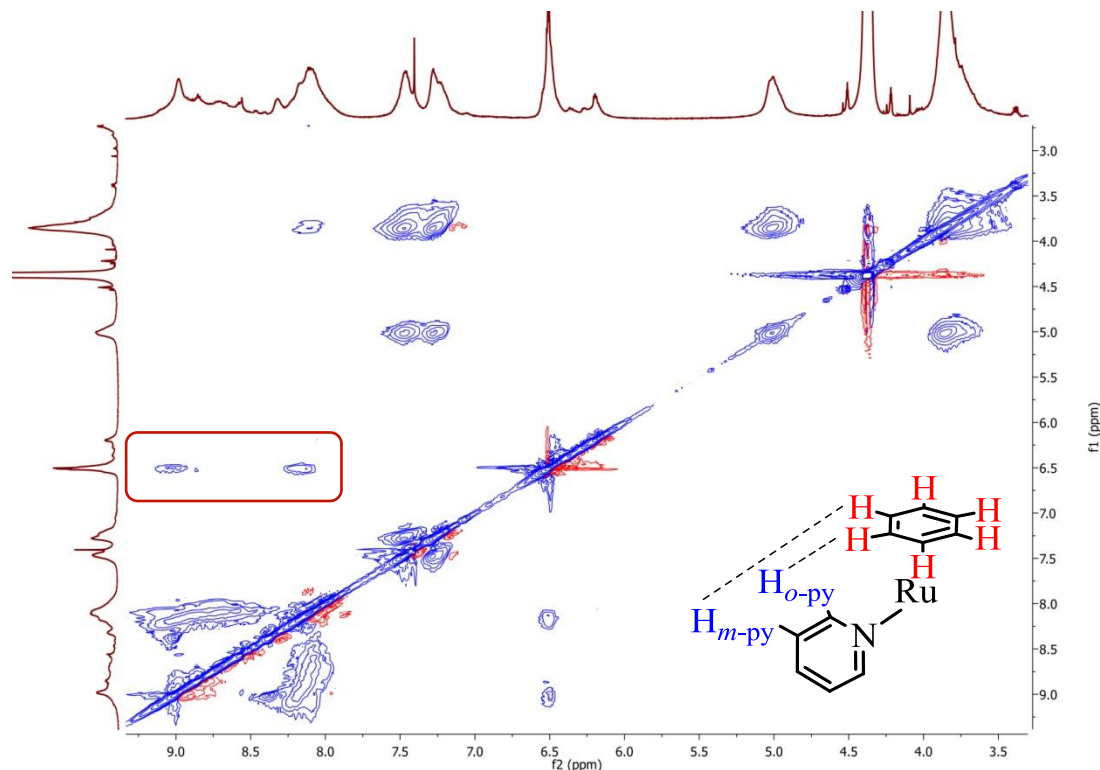


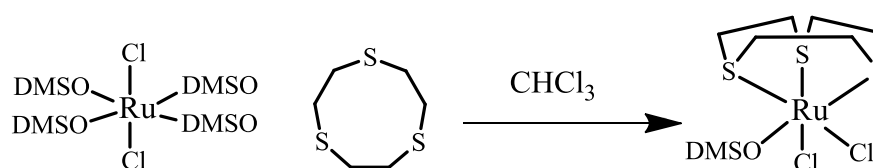
Figure 5.13: Interpreted partial 2D NOESY NMR spectrum of CC4.1 in d_3 - MeNO_2 solvent, $n\text{Oe}$ couplings between arene protons and ortho/meta-pyridyl protons highlighted, chemical structure and $n\text{Oe}$ couplings of CC4.1 shown inset.

The observed $n\text{Oe}$ coupling between protons on the arene ring at 6.4 ppm and the *ortho/meta*-pyridyl protons at 9.0 and 8.2 ppm, as highlighted in Figure 5.13, suggest close through-space association of the metallotecton and **L4**, providing supporting evidence for the formation of **CC4.1**.

After 12 hours heating at 45°C, as seen in Figure 5.12, there is no remaining metallo-starting material, as evidenced through the lack of proton resonances at 6.3 and 2.5 ppm, however a further investigation into the stability and potential self-sorting behaviour of the cage was also undertaken. Supramolecular assemblies of CTV-type ligands have been seen to display a degree of self-sorting in solution over time, usually with respect to the enantiomers contained within the assembly or the chirality of the assembly as a whole, leading to re-sharpening of the previously

broad peaks as a major isomer is formed.^{32–35} However, upon investigation of any self-sorting processes occurring within **CC4.1**, decomposition was seen to occur. This is most acutely highlighted through the appearance of a peak at ~7.3 ppm, assigned to free benzene in nitromethane solvent, emphasized in the green box in Figure 5.12. With the loss of the main geometrically directing ligand, there is no driving force towards retention of the cubic structure.

As **CC4.1** was seen to decompose in solution over time, an alternative approach towards an analogous cubic structure was undertaken. The second approach employed a different face-capping ligand, one that has previously showed no evidence of displacement over time, 1,4,7-trithiacyclononane.



Scheme 5.4: Formation of the second ruthenium ‘piano-stool’ complex employed as a geometrically directing metallotecton.

There are many previous examples of mono-nuclear complexes containing this ruthenium tecton, formed from pyridine-containing moieties.^{36–38} The first and seminal example of a supramolecular cube containing the $[[([9]\text{aneS}_3)\text{Ru}(\text{DMSO})\text{Cl}_2]$ came from Thomas *et al*, whereby the aforementioned metallotecton was reacted with 4,4'-bipyridine in nitromethane solvent to furnish the self-sorted, self-assembled cube after one month.³⁹ In addition to the mono-nuclear systems, Fujita has prepared analogues of his *cis*-protected Pd assemblies cornered by a comparable ruthenium tecton, simply the 12-membered thia-ring analogue.²⁶ This Ru_6L_4 assembly displayed a guest-induced chromic shift from yellow to orange upon encapsulation of the guest molecule.

In this case, the resultant metallotecton $[[([9]\text{aneS}_3)\text{Ru}(\text{DMSO})\text{Cl}_2]$ was combined with **L4** in deuterated nitromethane solvent; however a pale yellow precipitate was formed immediately upon mixing. It was surmised that the bound chloride anions would be slower to displace than the coordinated DMSO solvent, and therefore a polymeric structure was probably formed upon mixing, rather than the metallotecton providing the desired facial arrangement of binding sites. Consequently, the bound halide anions were removed through use of silver tetrafluoroborate in the presence

of non-coordinating nitromethane solvent to furnish the activated *bis*-tetrafluoroborate salt. The activated adduct was subsequently combined *in situ* with **L4** and the formation of **CC4.2** followed by ^1H NMR spectroscopy.

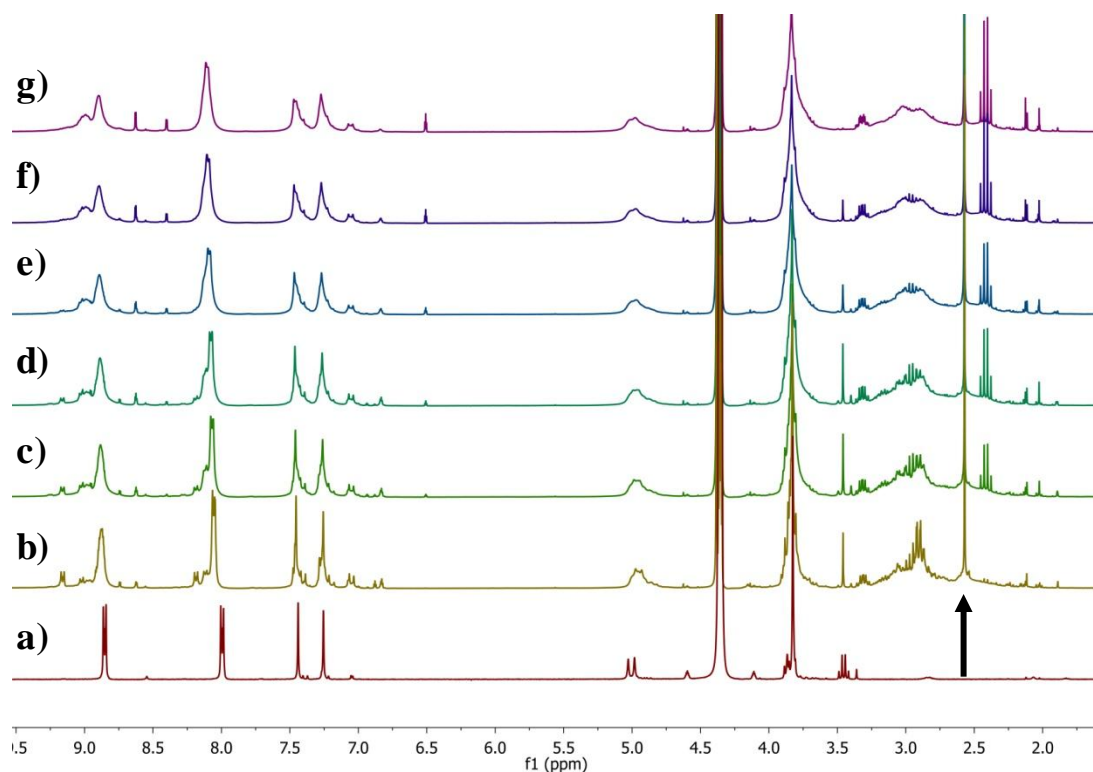


Figure 5.14: Timecourse ^1H NMR study of the formation of **CC4.2** from a) **L4** b) immediately after mixing c) 4 hrs at 65°C d) 8 hrs e) 24 hrs f) 48 hrs g) 5 days heating.

The initial combination of activated ruthenium tecton and **L4**, spectrum **b** in Figure 5.14, gives rise to a slight shift in peak position, and the formation of a smaller set of peaks adjacent to the previous aromatic peaks. Another point of note is the appearance of a peak at 2.5 ppm, highlighted by the arrow in Figure 5.14, characteristic of free dimethyl sulphoxide, suggesting that the bound DMSO ligand on the metallotecton has been displaced by the pyridyl *N*-donor on **L4**. As previously seen by Thomas *et al.*,³⁹ the ^1H NMR spectrum observed is initially sharp but complex, and over time, with further heating, simplifies. The same effect can be seen in Figure 5.14 whereby the sharp spectrum of **a**) gradually broadens into spectrum **e**) over 24 hours at 65°C . The proton resonance assigned to the *ortho*-pyridyl protons of **L4**, seen at ~ 8.7 ppm in spectrum **a**), split into two peaks at 8.8 and 9.0 ppm, whilst the *meta*-pyridyl proton peak, previously at 7.9 ppm, splits into a broad overlapping peak centred at 8.1 and 8.15 ppm. The integrals of all peaks in

spectrum **g**) are congruent with an **L4**:metallotecton ratio of 1:1, supporting the formation of a cubic assembly. Both split-peaks assigned to the *ortho*- and *meta*-pyridyl protons equate to two, whilst the broad aryl-CTG protons resonances at 7.46 and 7.26 ppm both integrate to one. The *endo* methylene-bridge resonance equates to one proton, whilst the broad multiplet between 2.5-3.2 ppm, assigned to the protons on the thia-crown tecton, integrates to 4 protons. Whilst the spectrum does simplify over time, it is still more complex than the final ^1H NMR spectrum observed by Thomas *et al*, this could be due to incomplete assembly of the cubic structure, or a chirality effect; as **L4** is present as both *M* and *P* isomers and thus the resultant supramolecular assembly may undergo further self-sorting towards a single enantiomeric product.

Strong evidence supporting the formation of a cubic structure is also found in the ^1H - ^1H NOESY NMR spectrum, see Figure 5.15.

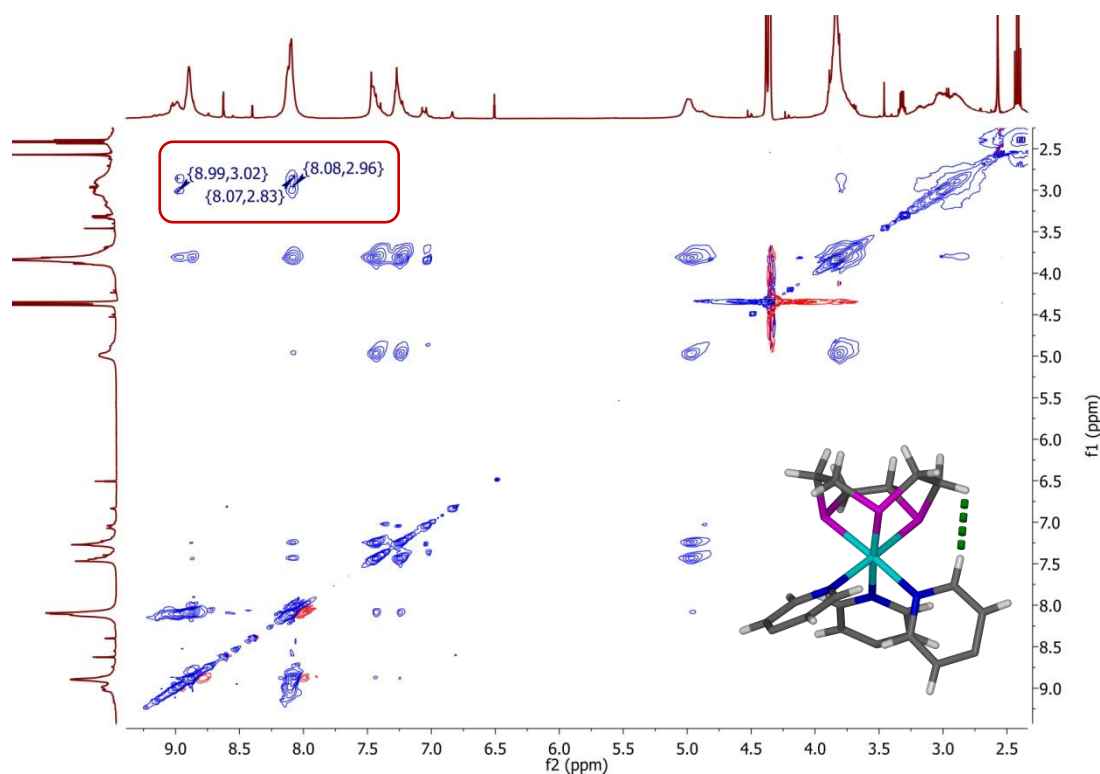


Figure 5.15: Interpreted 2D ^1H - ^1H NOESY spectrum of CC4.2 in d_3 -MeNO₂ solvent, nOe couplings between thia-crown protons and *ortho*/*meta*-pyridyl protons highlighted, partial crystal structure of the mono-nuclear analogue shown inset,³⁹ highlighting the nOe couplings in green seen in CC4.2.

The proton resonance between 2.5-3.5 ppm, belonging to the thia-crown moiety of the ruthenium metallotecton, can be seen to couple to both the *ortho*- and *meta*-

pyridyl protons on **L4**, highlighted in the red box in Figure 5.15. Strong through-space coupling can also be seen between the methoxy proton resonance at 3.8 ppm and the aromatic aryl-CTG protons at 7.4 and 7.2 ppm, as well as the *ortho*- and *meta*-pyridyl protons at 8.9 and 8.0 ppm. The *endo* methylene bridge protons at 4.9 ppm can also be seen to couple to the aryl-CTG protons. Importantly, the peak at 2.5 ppm, assigned to free dimethyl sulphoxide, does not couple to the thia-crown moiety, supporting the assertion that it is no longer bound to the metallotecton.

The HR-MS however, is less clear. A number of high charge, high mass peaks were observed, but no peaks assignable to the intact $\text{Ru}_4(\mathbf{L4})_4$ structure could be identified through the MS techniques available to the author. This suggests that a larger assembly was formed, but fragments during the ionisation process.

5.5 Conclusions and further directions

In this chapter, tri-metallic ruthenium complexes **C1.6** and **C2.6** were formed in good yields, and through the use of silver hexafluorophosphate, in just 24 hours. The photophysics of these systems show strong phosphorescent emission towards the near IR region. Once again, the difference between the ether and ester linked complexes is significant, allowing access to emission wavelengths over 50 nm apart. Importantly, the incorporation of ruthenium centres onto the cyclononatriene scaffold in **L1** and **L2** does not impede the emission, and provides a platform for the synthesis of heteronuclear systems **C1.7** and **C2.7**. The analysis of which shows complex yet clean HR ESI-MS data and a reproducibly convoluted ^1H NMR spectra. The relatively facile synthesis of heteronuclear complexes opens the door towards a highly tuneable system with respect to the resultant emission properties. There is the potential to incorporate rational design into the combination of metal centres and the precise structural nature of the supporting ancillary ligands bound to them, allowing for a diverse range of emission wavelengths, with the possibility to design energy transfer systems through judicious choice of metallotectons.

Whilst further photophysical investigations will be performed, the initial results are encouraging and reiterate the trend previously observed in that the **L2** containing systems are always red-shifted compared to the **L1** based congeners. Therefore, future efforts to tune the emission wavelength towards specific, desired colours

could be based not only on a considered choice of metal or ancillary ligand, but also the cyclononatriene ligand scaffold itself.

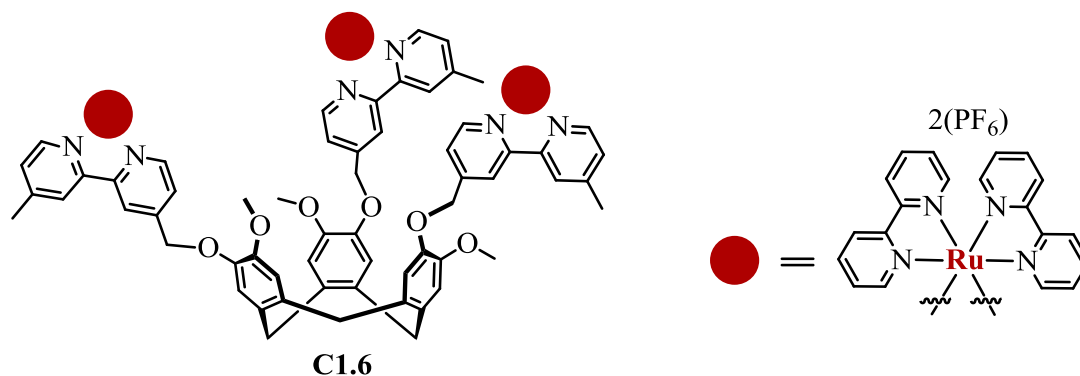
Although synthetically more challenging, there is also potential to target not just hetero bi-metallic systems, but also tri-metallic complexes, through careful stoichiometric control. This modular approach to complex colour tuning, could lead to a vast library of emissive complexes whereby the emission properties could be tuned to an end-users' specific needs.

An effort towards incorporating kinetically inert metal centres into supramolecular assemblies has also been trialled. Evidence for the synthesis of two distinct ruthenium containing M_4L_4 cubes has been obtained, although the SCXRD structures are yet to be obtained, the solution state data supports evidence of their formation. Whilst the ruthenium-arene cubic structure, **CC4.1**, displayed evidence of degradation over time, the tri-thiacyclononane analogue, **CC4.2**, showed a higher degree of stability. Further work on these systems could go towards obtaining their solid state structures and investigating their host-guest abilities.

5.6 Experimental

5.6.1 Synthesis

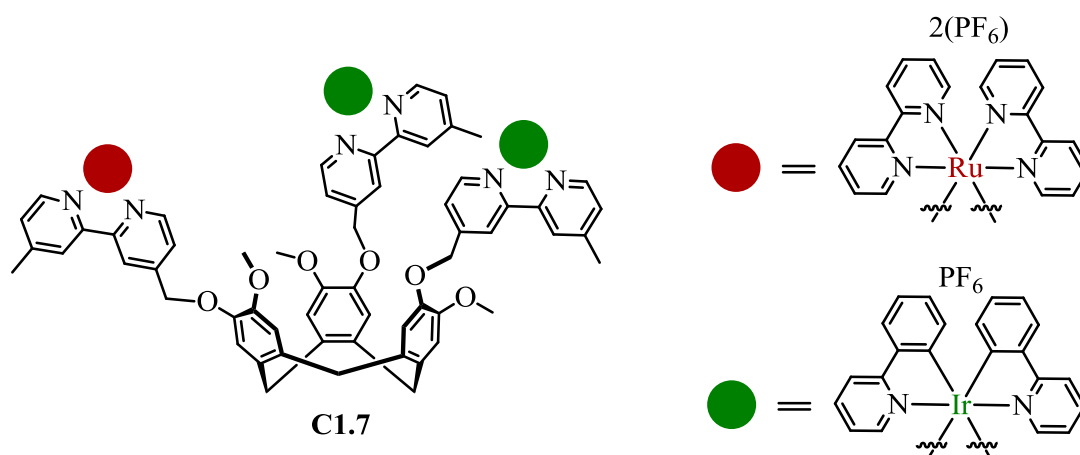
Preparation of complex $[\text{Ru}(\text{II})(2, 2'\text{-bipyridine})_2]_3(\text{tris}(4\text{-[4'-methyl-2, 2'\text{-bipyridyl]methyl})\text{CTG})]_6(\text{PF}_6)_6$ (**C1.6**):



$[\text{Ru}(\text{bipy})_2(\text{Cl})_2]$ (0.081 g, 0.156 mmol) and (\pm)-**L1** (0.050 g, 0.052 mmol) were combined in a mixture of $\text{CHCl}_3/\text{MeOH}$ (10:1) (25 mL total) and heated to 55°C . The reaction was followed by MS, and heating was continued until the main peak seen was the $[\text{Ru}(\text{bipy})_2]_3(\text{L1})^{6+}$ cationic complex, **C1.6**. The reaction mixture was taken to dryness *in vacuo* and re-dissolved in MeCN (10 mL), halide exchange was accomplished by addition of an aqueous solution of NH_4PF_6 . The soluble PF_6 salt did not precipitate and the MeCN was removed *in vacuo*, leaving an aqueous residue that was extracted with DCM, dried over MgSO_4 and concentrated to ~ 1 mL *in vacuo*. Diethyl ether was added to the solution to give the title product as a bright orange powder (0.136 g, 85%) TOF-MS ESI: $m/z = 366.0923$ (M^{6+}) ^1H NMR (500 MHz, CD_3CN) δ 8.53 (s, 1H, $\text{H}^{\text{3'}}$), 8.49 (dd, $J = 8.3, 4.2$ Hz, 4H, H^{a}), 8.34 (s, 1H, H^{3}), 8.05 (q, $J = 7.7$ Hz, 4H, H^{b}), 7.73 (tt, $J = 11.0, 5.3$ Hz, 5H, $\text{H}^{\text{5'}}$ / H^{d}), 7.55 (d, $J = 5.7$ Hz, 1H, $\text{H}^{\text{6'}}$), 7.44 (d, $J = 1.8$ Hz, 1H, H^{6}), 7.43 – 7.33 (m, 4H, H^{c}), 7.25 (d, $J = 5.4$ Hz, 1H, H^{5}), 7.14 (d, $J = 2.4$ Hz, 1H, H_{aryl}), 7.05 (dd, $J = 5.0, 2.0$ Hz, 1H, H_{aryl}), 5.32 – 5.13 (m, 2H, CH_2), 4.77 (d, $J = 13.7$ Hz, 1H, H_{endo}), 3.78 (t, $J = 3.7$ Hz, 3H, OMe), 3.57 (d, $J = 13.8$ Hz, 1H, H_{exo}), 2.53 (s, 3H, CH_3); $^{13}\text{C}\{^1\text{H}\}$ NMR (126 MHz, CD_3CN) δ 158.03, 157.96, 157.19, 152.66, 152.53, 151.85, 151.55, 149.49, 147.15, 138.68, 134.78, 133.00, 129.50, 128.53, 128.47, 126.29, 126.08, 125.22, 122.87, 117.79, 115.00, 70.00, 56.83, 36.34, 21.28., Analysis for $\text{C}_{120}\text{H}_{102}\text{F}_{36}\text{N}_{18}\text{O}_6\text{P}_6\text{Ru}_3$ (%)

calculated, found) C (47.02, 45.47) H (3.35, 3.32) N (8.23, 7.94), Infrared Analysis (FT-IR, cm^{-1}) 556, 729, 833, 1027, 1089, 1145, 1160, 1242, 1446, 1603 (s), 3084 (b)

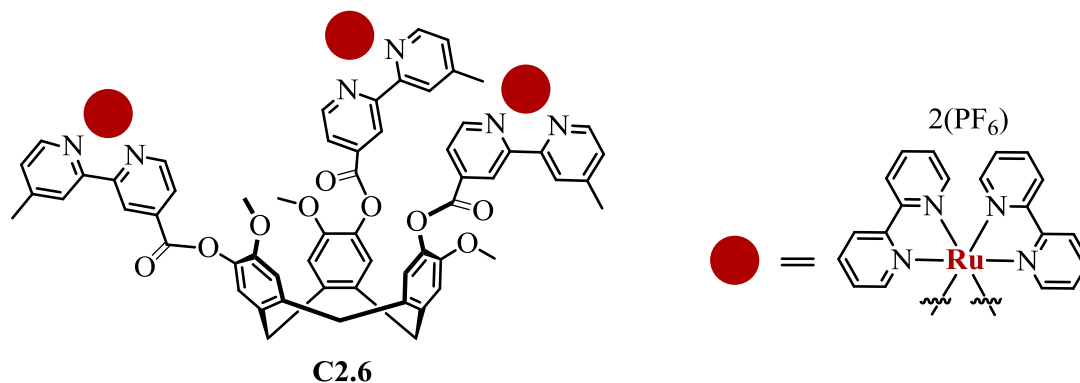
Preparation of complex [(Ru(II)(2, 2'-bipyridine)₂)(Ir(III)(2-phenylpyridine)₂)(tris(4-[4'-methyl-2, 2'-bipyridyl]methyl)CTG)]₅(PF₆) (C1.7):



[Ru(bipy)₂(MeCN)₂](PF₆) (0.029 g, 0.036 mmol) and **C1.3** (0.030 g, 0.018 mmol) were combined in a mixture of CHCl₃ (10 mL) and a few drops of MeOH and heated to 55°C. The reaction was followed by MS, and heating was continued until the main peak seen was the [Ru(bipy)₂]₃[Ir(ppy)₂](**L1**)⁵⁺ cationic complex, approximately 3 days. The reaction mixture was taken to dryness *in vacuo* and re-dissolved in MeCN (10 mL), diethyl ether was added to the solution to give the title product as a bright orange powder (0.042 g, 75%) TOF-MS ESI: $m/z = 456.7173$ (M^{5+}) ¹H NMR (300 MHz, CD₃CN) δ 8.64 – 8.44 (m, 3.4H, H_A/H_{3'}), 8.37 (s, 1H, H₃), 8.06 (s, 3.5H, H_B/H_{A'}), 7.97 (d, $J = 8.7$ Hz, 0.5H, H_{6'(Ir)}), 7.89 – 7.69 (m, 5.5H, H_D/H_{B'}/H_{D'}/H_{6(Ir)}/H_{6'(Ru)}), 7.59 (dd, $J = 13.8, 5.8$ Hz, 2H, H_{F'}/H_{6(Ru)}), 7.42 (d, $J = 6.3$ Hz, 3.6H, H_C/H_{5'(Ru)}), 7.27 (d, $J = 5.5$ Hz, 0.6H, H₅), 7.16 (s, 1H, H_{aryl}), 7.06 (d, $J = 7.2$ Hz, 2.4H, H_{C'}/H_{E'}/H_{aryl}), 6.94 (d, $J = 5.8$ Hz, 1H, H_{G'}), 6.30 (t, $J = 6.2$ Hz, 0.8H, H_{H'}), 5.24 (d, $J = 9.8$ Hz, 2H, CH₂), 4.79 (d, $J = 14.4$ Hz, 1H, H_{endo}), 3.78 (d, $J = 18.5$ Hz, 3H, OMe), 3.59 (d, $J = 13.2$ Hz, 1H, H_{exo}), 2.55 (s, 3H, Me). ¹³C{¹H} NMR (126 MHz, CD₃CN) δ 168.43, 158.00, 157.93, 157.17, 154.24, 153.08, 152.67, 152.62, 152.49, 151.83, 151.52, 151.46, 150.03, 139.43, 139.29, 138.91, 138.66, 134.74, 132.99, 132.54, 132.46, 131.30, 130.11, 129.47, 128.50, 128.44, 127.66, 126.33, 126.06, 125.83, 125.20, 124.83, 124.50, 124.36, 123.42, 123.09,

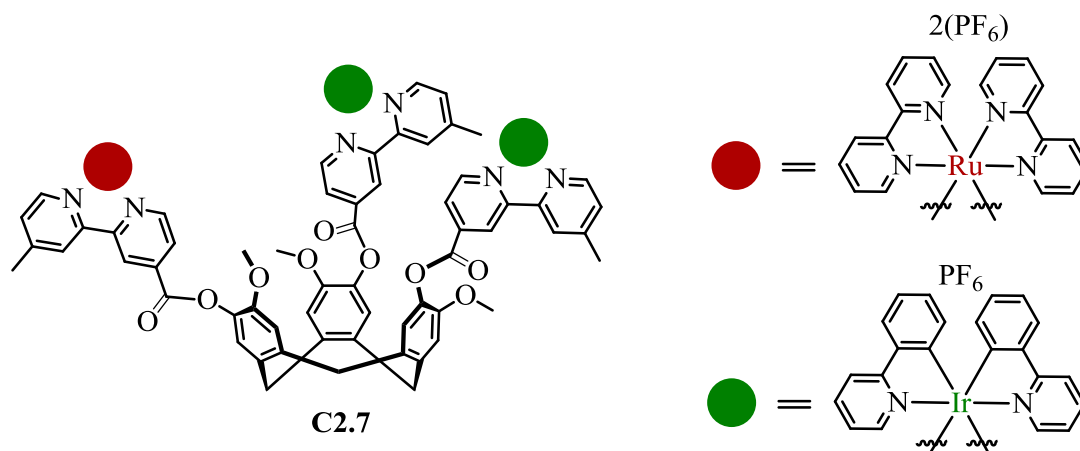
122.85, 120.79, 117.39, 66.23, 56.79, 36.30, 21.45, 21.25. Infrared Analysis (FT-IR, cm^{-1}) 556, 729, 833, 1027, 1089, 1145, 1160, 1242, 1446, 1603 (s), 3084 (b)

Preparation of complex [(Ru(II)(2, 2'-bipyridine)₂]₃(tris(4-[4'-methyl-2, 2'-bipyridyl]carboxy)CTG)].6(PF₆) (C2.6):



[Ru(bipy)₂(Cl)₂] (0.144 g, 0.297 mmol) and (±)-**L2** (0.100 g, 0.100 mmol) were combined in a mixture of CHCl₃/MeOH (10:1) (50 mL total) and heated to 55°C. The reaction was followed by MS, and heating was continued until the main peak seen was the [Ru(bipy)₂]₃(**L2**)⁶⁺ cationic complex, **C2.6**. The reaction mixture was taken to dryness *in vacuo* and re-dissolved in MeCN (10 mL), halide exchange was accomplished by addition of an aqueous solution of NH₄PF₆. The soluble PF₆ salt did not precipitate and the MeCN was removed *in vacuo*, leaving an aqueous residue that was extracted with DCM, dried over MgSO₄ and concentrated to ~1 mL *in vacuo*. Diethyl ether was added to the solution to give the title product as a dark orange powder (0.222 g, 71.1%) TOF-MS ESI: $m/z = 372.9122$ (M⁶⁺) ¹H NMR (300 MHz, CD₃CN) δ 9.01 (s, 1H, H^{6'}), 8.51 (d, $J = 7.5$ Hz, 5H, H³/H^a), 8.20 – 7.95 (m, 5H, H^b/H^{3'}), 7.88 (s, 1H, H^{5'}), 7.85 – 7.64 (m, 4H, H^d), 7.57 (d, $J = 5.4$ Hz, 1H, H⁶), 7.49 – 7.33 (m, 5H, H^c/H_{aryl}), 7.29 (d, $J = 5.1$ Hz, 1H, H⁵), 7.16 (s, 1H, H_{aryl}), 4.91 (d, $J = 13.4$ Hz, 1H, H_{endo}), 3.75 (s, 4H, H_{exo}/OMe), 2.54 (s, 3H, CH₃). ¹³C{¹H} NMR (126 MHz, CD₃CN) δ 163.02, 159.76, 157.94, 157.83, 157.63, 156.62, 154.12, 152.75, 152.51, 151.83, 150.54, 140.26, 138.98, 129.91, 128.66, 128.54, 127.08, 126.84, 125.33, 124.12, 117.60, 115.27, 56.94, 36.27, 21.14., Analysis for C₁₂₀H₉₆F₃₆N₁₈O₉P₆Ru₃. (% calculated, found) C (46.39, 46.22) H (3.11, 3.23) N (8.11, 7.85) Infrared Analysis (FT-IR, cm^{-1}) 556, 730, 761, 834, 1023, 1104, 1140, 1246, 1446, 1604, 1747 (s), 3082 (b)

Preparation of complex [(Ru(II)(2, 2'-bipyridine)₂)(Ir(III)(2-phenylpyridine)₂)(tris(4-[4'-methyl-2, 2'-bipyridyl]carboxy)CTG)].5(PF₆) (C2.7):



[Ru(bipy)₂(MeCN)₂](PF₆)⁺ (0.0124 g, 0.015 mmol) and **C2.3** (0.013 g, 0.008 mmol) were combined in a mixture of CHCl₃ (10 mL) and a few drops of MeOH and heated to 55°C. The reaction was followed by MS, and heating was continued until the main peak seen was the [Ru(bipy)₂]₃[Ir(ppy)₂](L2)⁵⁺ cationic complex, approximately 3 days. The reaction mixture was taken to dryness *in vacuo* and re-dissolved in MeCN (10 mL), diethyl ether was added to the solution to give the title product as a bright orange powder (0.017 g, 70%) TOF-MS ESI: *m/z* = 465.1048 (M⁵⁺) ¹H NMR (300 MHz, CD₃CN) δ 9.17 – 8.83 (m, 1H, H_{3'(Ir)}/H_{6'(Ru)}), 8.67 – 8.43 (m, 4H, H_A/H_{3(Ru)}), 8.43 – 8.17 (m, 1H, H_{3'(Ir)}/H_{6'(Ir)}), 8.04 (d, *J* = 20.8 Hz, 4H, H_A/H_B/H_{3'(Ru)}), 7.83 (dt, *J* = 18.0, 8.4 Hz, 4H, H_E/H_B/H_{5'(Ru)}), 7.76 – 7.64 (m, 3H, H_D/H_{D'}), 7.64 – 7.54 (m, 2H, H_C/H_{6(Ru)}), 7.41 (d, *J* = 10.9 Hz, 4H, H_C/H_{5'(Ir)}), 7.35 – 7.23 (m, 1H, H₅), 7.16 (s, 1H, H_{aryl}), 7.05 (d, *J* = 7.4 Hz, 1.8H, H_F/H_{aryl}), 7.00 – 6.82 (m, 0.6H, H_G), 6.28 (dd, *J* = 13.3, 7.5 Hz, 0.6H, H_H), 4.90 (d, *J* = 13.7 Hz, 1H, H_{endo}), 3.75 (s, 4H, H_{exo}/OMe), 2.54 (s, 3H, Me). ¹³C{¹H} NMR (75 MHz, DMSO) δ 166.81, 166.58, 161.57, 158.45, 157.53, 157.20, 156.63, 154.19, 153.16, 151.95, 151.71, 151.34, 150.21, 149.09, 143.86, 143.68, 139.18, 138.87, 138.58, 138.16, 137.42, 132.03, 130.97, 130.33, 127.96, 127.85, 127.19, 126.38, 125.12, 124.51, 124.25, 123.93, 122.44, 120.07, 114.56, 56.19, 35.05, 20.72. Infrared Analysis (FT-IR, cm⁻¹) 556, 730, 761, 834, 1023, 1104, 1140, 1246, 1446, 1604, 1747 (s), 3082 (b)

Preparation of complex [(Ru(II)(arene)₄](L4)].8(PF₆⁻) (CC4.1):

[Ru(arene)(MeCN)₃]•2PF₆⁻ (0.0026 g, 0.005 mmol) and **L4** (0.0040 g, 0.005 mmol) were dissolved in *d*₃-MeNO₂ (0.5 mL) and heated to 45°C. The formation of **CC4.1** was followed by ¹H NMR spectroscopy, with continued heating.

Preparation of assembly [(Ru(II)([9]aneS₃)₄)(L4)].8(BF₄⁻) (CC4.2):

[[[9]aneS₃)Ru(DMSO)Cl₂] (0.020 g, 0.046 mmol) was dissolved in *d*₃-MeNO₂ (2 mL) and AgBF₄ (0.019 g, 0.097 mmol) added in the absence of light. The solution was heated to 45°C for 12 hours before filtration through celite, to which **L4** (0.033 g, 0.046 mmol) was added. The solution was heated to 65°C and ¹H NMR spectra taken at various time intervals.

5.6.2 Photophysical studies

The photophysical studies on the tri-metallic homonuclear ruthenium complexes **C1.6** and **C2.6** were performed at the University of Leeds on a Jobin-Yvon Spex Fluorolog-3 Fluorimeter at 293 K. The samples were dissolved in acetonitrile to make up a 0.2 mM solution and run immediately.

5.7 Bibliography

- 1 C. Mari, V. Pierroz, S. Ferrari and G. Gasser, *Chem. Sci.*, 2015, **6**, 2660–2686.
- 2 H. Komatsu, K. Yoshihara, H. Yamada, Y. Kimura, A. Son, S. Nishimoto and K. Tanabe, *Chem. – Eur. J.*, 2013, **19**, 1971–1977.
- 3 V. Ramu, M. R. Gill, P. J. Jarman, D. Turton, J. A. Thomas, A. Das and C. Smythe, *Chem. – Eur. J.*, 2015, **21**, 9185–9197.
- 4 A. K. Gorle, M. Feterl, J. M. Warner, L. Wallace, F. R. Keene and J. G. Collins, *Dalton Trans.*, 2014, **43**, 16713–16725.
- 5 F. P. Dwyer, E. C. Gyarfas, W. P. Rogers and J. H. Koch, *Nature*, 1952, **170**, 190–191.
- 6 N. P. E. Barry, O. Zava, J. Furrer, P. J. Dyson and B. Therrien, *Dalton Trans.*, 2010, **39**, 5272–5277.
- 7 B. Therrien, *CrystEngComm*, 2014, **17**, 484–491.

- 8 A. K. Singh, D. S. Pandey, Q. Xu and P. Braunstein, *Coord. Chem. Rev.*, 2014, **270–271**, 31–56.
- 9 A. Dubey, J. W. Min, H. J. Koo, H. Kim, T. R. Cook, S. C. Kang, P. J. Stang and K.-W. Chi, *Chem. – Eur. J.*, 2013, **19**, 11622–11628.
- 10 B. Therrien, G. Süss-Fink, P. Govindaswamy, A. K. Renfrew and P. J. Dyson, *Angew. Chem.*, 2008, **120**, 3833–3836.
- 11 S. Fantacci and F. De Angelis, *Coord. Chem. Rev.*, 2011, **255**, 2704–2726.
- 12 R. D. Costa, E. Ortí, H. J. Bolink, F. Monti, G. Accorsi and N. Armaroli, *Angew. Chem. Int. Ed.*, 2012, **51**, 8178–8211.
- 13 H. Shahroosvand, L. Najafi, A. Sousaraei, E. Mohajerani and M. Janghouri, *J. Mater. Chem. C*, 2013, **1**, 6970–6980.
- 14 Y. Chuai, D. N. Lee, C. Zhen, J. H. Min, B. H. Kim and D. Zou, *Synth. Met.*, 2004, **145**, 259–264.
- 15 W. Sun, S. Sun, N. Jiang, H. Wang and X. Peng, *Organometallics*, 2015, **34**, 3385–3389.
- 16 M. Cavazzini, S. Quici, C. Scalera, F. Puntoriero, G. La Ganga and S. Campagna, *Inorg. Chem.*, 2009, **48**, 8578–8592.
- 17 N. Zabarska, D. Sorsche, F. W. Heinemann, S. Glump and S. Rau, *Eur. J. Inorg. Chem.*, 2015, **2015**, 4869–4877.
- 18 D. L. Ashford, D. J. Stewart, C. R. Glasson, R. A. Binstead, D. P. Harrison, M. R. Norris, J. J. Concepcion, Z. Fang, J. L. Templeton and T. J. Meyer, *Inorg. Chem.*, 2012, **51**, 6428–6430.
- 19 N. Kaveevivitchai, R. Chitta, R. Zong, M. El Ojaimi and R. P. Thummel, *J. Am. Chem. Soc.*, 2012, **134**, 10721–10724.
- 20 M. Abrahamsson, H.-C. Becker, L. Hammarström, C. Bonnefous, C. Chamchoumis and R. P. Thummel, *Inorg. Chem.*, 2007, **46**, 10354–10364.
- 21 W. R. Browne, P. Passaniti, M. T. Gandolfi, R. Ballardini, W. Henry, A. Guckian, N. O’Boyle, J. J. McGarvey and J. G. Vos, *Inorganica Chim. Acta*, 2007, **360**, 1183–1190.

- 22 M. Kuss-Petermann and O. S. Wenger, *Angew. Chem. Int. Ed.*, 2016, **55**, 815–819.
- 23 B. Laramee-Milette, F. Lussier, I. Ciofini and G. Hanan, *Dalton Trans.*, 2015, **44**, 11551–11561.
- 24 C. Kreitner and K. Heinze, *Dalton Trans.*, 2016, **45**, 5640–5658.
- 25 A. Mishra, S. C. Kang and K.-W. Chi, *Eur. J. Inorg. Chem.*, 2013, **2013**, 5222–5232.
- 26 K. Yamashita, M. Kawano and M. Fujita, *Chem. Commun.*, 2007, 4102–4103.
- 27 R. Pettinari, F. Marchetti, C. Pettinari, F. Condello, B. W. Skelton, A. H. White, M. R. Chierotti and R. Gobetto, *Dalton Trans.*, 2016, **45**, 3974–3982.
- 28 P. Thanasekaran, C.-C. Lee and K.-L. Lu, *Acc. Chem. Res.*, 2012, **45**, 1403–1418.
- 29 S.-L. Huang, Y.-J. Lin, T. S. A. Hor and G.-X. Jin, *J. Am. Chem. Soc.*, 2013, **135**, 8125–8128.
- 30 S.-L. Huang, Y.-J. Lin, Z.-H. Li and G.-X. Jin, *Angew. Chem. Int. Ed.*, 2014, **53**, 11218–11222.
- 31 W.-Y. Zhang, Y.-F. Han, L.-H. Weng and G.-X. Jin, *Organometallics*, 2014, **33**, 3091–3095.
- 32 Z. Zhong, A. Ikeda, S. Shinkai, S. Sakamoto and K. Yamaguchi, *Org. Lett.*, 2001, **3**, 1085–1087.
- 33 J. J. Henkelis, J. Fisher, S. L. Warriner and M. J. Hardie, *Chem. – Eur. J.*, 2014, **20**, 4117–4125.
- 34 A. Schaly, Y. Rousselin, J.-C. Chambron, E. Aubert and E. Espinosa, *Eur. J. Inorg. Chem.*, 2016, **2016**, 832–843.
- 35 J. J. Henkelis, C. J. Carruthers, S. E. Chambers, R. Clowes, A. I. Cooper, J. Fisher and M. J. Hardie, *J. Am. Chem. Soc.*, 2014, **136**, 14393–14396.
- 36 A. M. Todd, A. N. Swinburne, A. E. Goeta and J. W. Steed, *New J. Chem.*, 2012, **37**, 89–96.

- 37 E. Iengo, E. Zangrando, E. Baiutti, F. Munini and E. Alessio, *Eur. J. Inorg. Chem.*, 2005, **2005**, 1019–1031.
- 38 S. Roche, H. Adams, S. E. Spey and J. A. Thomas, *Inorg. Chem.*, 2000, **39**, 2385–2390.
- 39 S. Roche, C. Haslam, S. L. Heath and J. A. Thomas, *Chem. Commun.*, 1998, 1681–1682.

6 Chapter 6

Luminescent metallocryptophanes

6.1 Introduction

The idea of employing geometrically directing metallotectons is by no means a new one, with numerous examples of large supramolecular cages and polyhedral assemblies formed through combination of a geometrically restricted metal centre and corresponding ligands.¹⁻¹² Prime examples are the tetrahedral cages of the Nitschke group, formed through the concomitant self-assembly of aldehyde and amine appended units to form an imine containing ligand *in situ*, and octahedral iron(II) sources.¹³⁻¹⁶ The resultant tetrahedral cages have been employed in guest uptake, to stabilise white phosphorus and in pH dependant guest release. Another frequently used family of metallotectons employed in the self-assembly of supramolecular architectures are the ubiquitous *cis*-protected palladium sources; palladium ethylenediamine and *bis*-diphenylphosphine being some of the most common. These types of Pd sources provide a reliable and robust 90° angle due to the *cis*-protection of two of the square planar binding sites.^{6,7,17-20}

Whilst use of a geometrically restricted metallotecton goes some way to direct the formation of preferred architecture, combination with a rigid ligand is also advisable. Some of the seminal work in this respect comes out of the Fujita group, particularly a series of large supramolecular spheres, formed from rigid 4-pyridyl containing ligands that can be elongated through the incorporation of additional benzene rings, thus increasing the internal void space of the resultant spheres accordingly.^{21,22}

A ‘panelling’ approach has also been employed by various groups, utilising appended porphyrin^{23,24} and tripyridyltriazine ligands as 2D square or triangular panels, thus ‘sealing off’ the internal void space of resultant structures to move away from the more open framework type assemblies to truly encapsulated interior spaces. However, the work presented herein relates to the cyclotriguaiacylene ligand scaffold, and therefore the subset of metallocages called metallocryptophanes; a ‘head-to-head’ assembly of two CTG ligands bound through three linking metal centres. Whilst organically linked cryptophanes and their host-guest properties have

been extensively investigated,^{25–28} their metallo- analogues are much rarer.^{29–34} The first example of which was Shinkai's initial palladium-based metallocryptophane,³² employing the *cis*-protecting diphenylphosphino ligand. However, when less geometrically restricted metal centres are employed the formation of metallocryptophanes is often concomitant with the formation of a [2]-catenane system,^{30,31} whereby two distinct metallocryptophanes are mechanically interlinked. Whilst this occurrence is interesting from a topological standpoint, in order to fully exploit any internal void-space for applications such as catalysis and gas separations, the formation of interpenetrated structures is undesirable. In order to direct the formation of a single, independent metallocryptophane, strongly *cis*-protecting, bulky bis-NHC containing palladium metallotectons have been employed by Henkelis *et al*, and the resulting metallocryptophanes show evidence of gas sorption and iodine uptake.³³

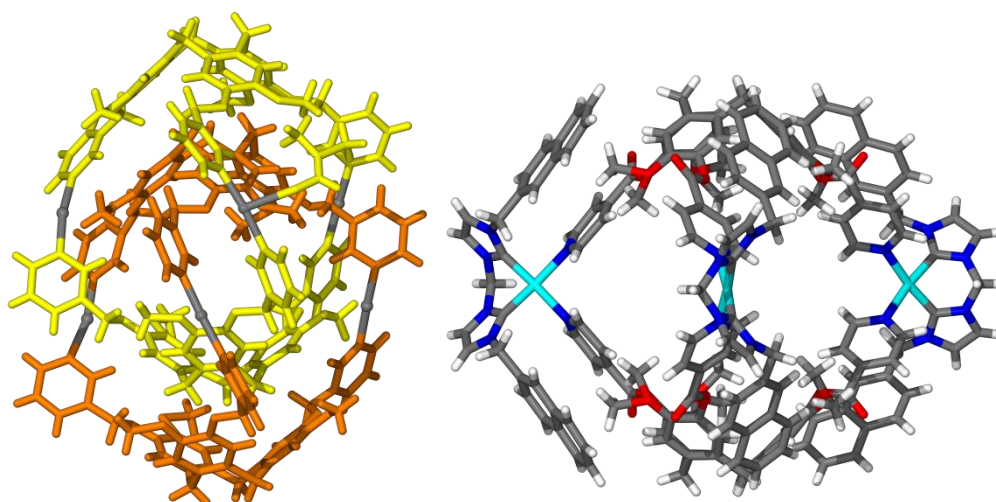


Figure 6.1: SCXRD structure of Ag_3L_2 [2]-catenane³⁰ and Pd_3L_2 NHC-containing metallocryptophane.³³

The metallocages discussed in this chapter all contain iridium(III) as the metal centre, unusually bearing phenylpyridine ancillary ligands, the same metallotecton as discussed in Chapters 2 and 3.

Most iridium supramolecular assemblies employ face-capping cyclopentadienyl-type ligands to direct the formation of metallarectangles or open framework assemblies from two or more ligand subsets.^{35,36} This method generally relies on a two-component approach, whereby bidentate ligands are pre-bound to the iridium-Cp* centre to form a ‘metallo-clip’, the pre-metallated scaffolds are then further

reacted with N-donor bridging ligands to form the supramolecular assembly. The synthesis of metallarectangles can therefore be expanded through use of trigonal N-donor ligands, such as tris-pyridyltriazine, in the place of linear N-donors to form more complex architectures.

In fact, there are only a handful of examples that make use of the luminescent iridium(III) *bis*-phenylpyridine metallotecton in the formation of metallocages and capsules,^{37,38} and none in combination with two pyridyl-containing ligands. Previous examples from Lusby³⁸ and Baranoff³⁷ both employ flexible nitrile ligands or ambidentate cyano/nitrile ligand motifs, as shown in Figure 6.2.

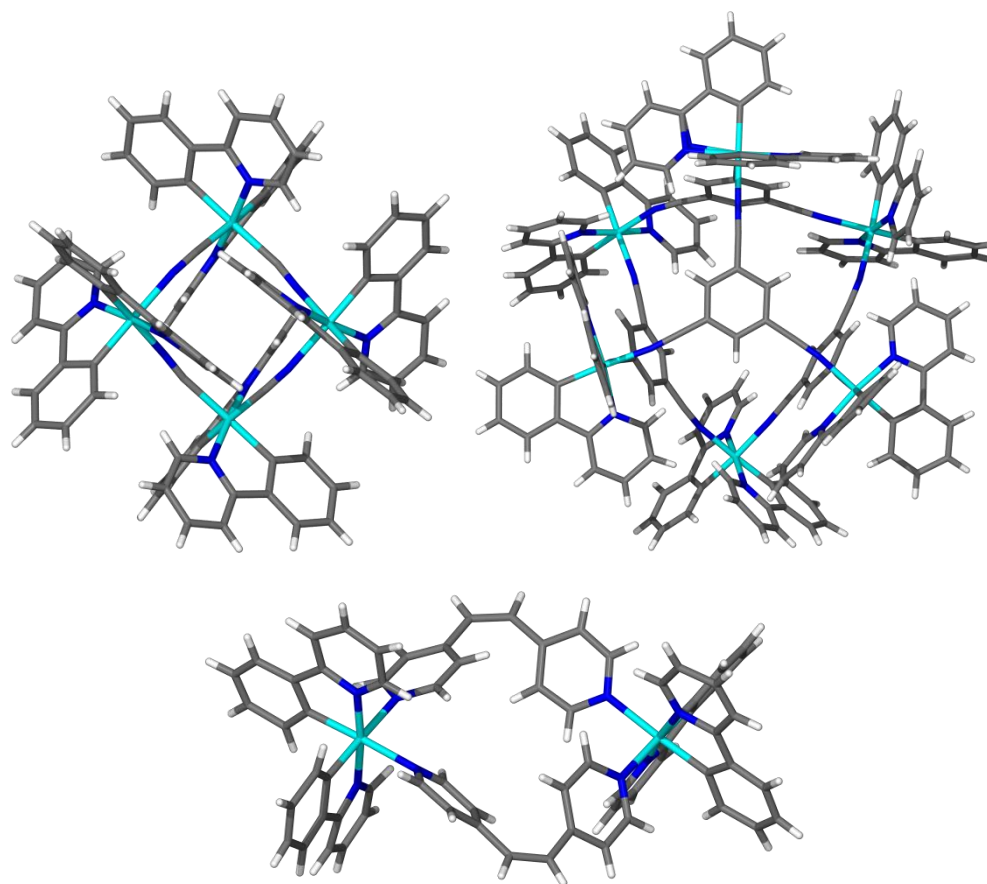


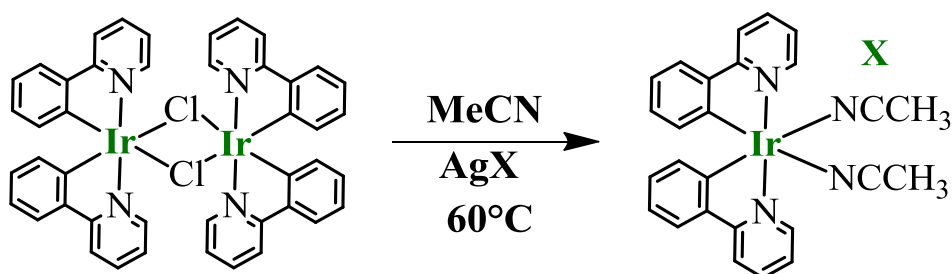
Figure 6.2: SCXRD structures of Baranoff's tetramer³⁷ and Lusby's M_6L_4 capsule³⁸ and Chandrasekhar's M_2L_2 dimer³⁹, all containing the $Ir(ppy)_2$ metallotecton.

Previously, only smaller M_2L_2 dimeric species have been formed with bridging pyridyl ligands,³⁹ Figure 6.2, with the caveat that the multi-topic ligand system must be flexible enough to allow torsion angles between the two pyridyl ligands of around 40° . Therefore it follows that successful attempts to form supramolecular assemblies

employing rigid, planar ligand systems, such as tris-pyridyltriazine that cannot accommodate such a distortion, have yet to be demonstrated.³⁸

6.2 Preparation of homocage metallocryptophanes

There are many examples of *cis*-protected square planar metals, particularly Pd(II), being employed in supramolecular self-assembly, therefore a bis-phenylpyridine iridium metallotecton should act in a comparable manner. To ensure the desired *cis*-coordination sites and promote the formation of a discrete metallocryptophane, the ubiquitous $[\text{Ir}(\text{ppy})_2\text{Cl}]_2$ dimer was transformed to the analogous bis-acetonitrile monomeric species, $[\text{Ir}(\text{ppy})_2(\text{MeCN})_2]\cdot(\text{X})$, where X is either the hexafluorophosphate or tetrafluoroborate anion, Scheme 6.1.



Scheme 6.1: Formation of the iridium metallotecton employed throughout this chapter, where X is either BF_4 or PF_6 .

The reaction of three equivalents of metallotecton, either the tetrafluoroborate or hexafluorophosphate analogue, along with two equivalents of **L3** or **L4** in nitromethane solvent, gives rise to rapid formation of the homocage M_3L_2 metallocryptophanes $\{\text{CC3.1}(3\text{X})\}$ and $\{\text{CC4.3}(3\text{X})\}$.

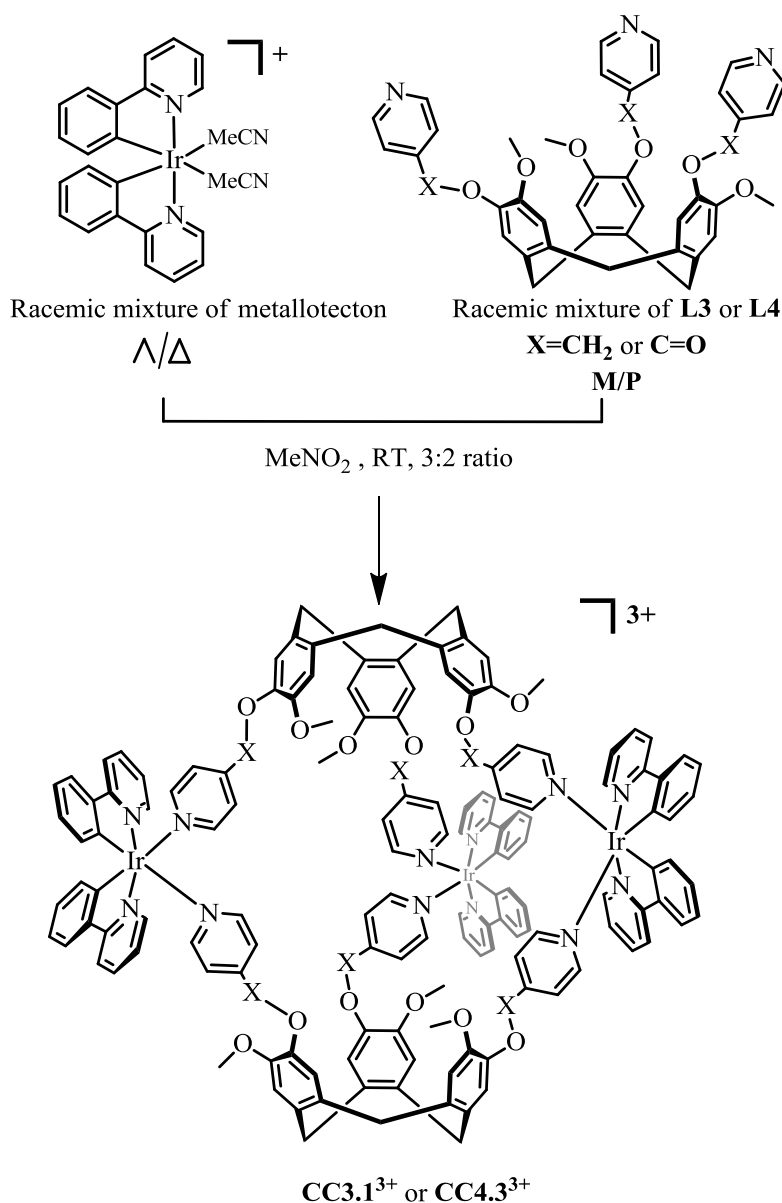


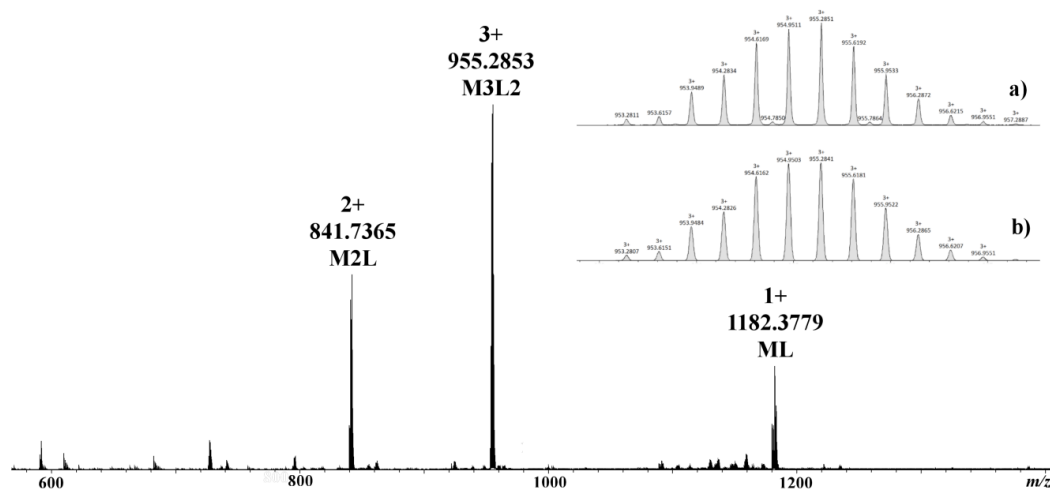
Figure 6.3: General scheme for the formation of M_3L_2 cryptophanes, where $M = [\text{Ir}(\text{ppy})_2]^+$.

As evidenced in Figure 6.3, there are a number of potential stereoisomers possible due to the Λ and Δ isomers of the octahedral iridium metallotecton and the helically chiral M and P isomers of the tripodal ligands **L3** and **L4**. When two of the tripodal ligands come together in a ‘head-to-head’ fashion, the resultant cage could either be chiral or of the *meso* form. The non-chiral *meso* cage would thus be composed of one ligand of each isomer, and is termed *syn-(MP)*. The chiral cage could be either *anti-(MM)* or *anti-(PP)*, whereby two ligands of the same enantiomer come together. This supramolecular chirality, in combination with the octahedral chirality of the tecton, gives rise to twelve potential stereoisomers; *syn-(MP)*, *anti-(MM)* or *anti-*

(*PP*) all in combination with $\Lambda\Lambda\Lambda$, $\Lambda\Lambda\Delta$, $\Lambda\Delta\Delta$ or $\Delta\Delta\Delta$ octahedral isomers of the metallocubane.

6.2.1 Spectroscopic analysis of metallocryptophanes

HR ESI-MS of the crude reaction mixture, Figure 6.4 and Figure 6.5, after 12 hours stirring at room temperature shows remarkably clear evidence of cryptophane formation, with the main peak at 955 or 983 m/z assigned to $\{\text{CC3.1}\}^{3+}$ or $\{\text{CC4.3}\}^{3+}$ respectively. Some fragmentation in the gas phase is observed, with peaks assigned to ML and M_2L seen in varying intensities.



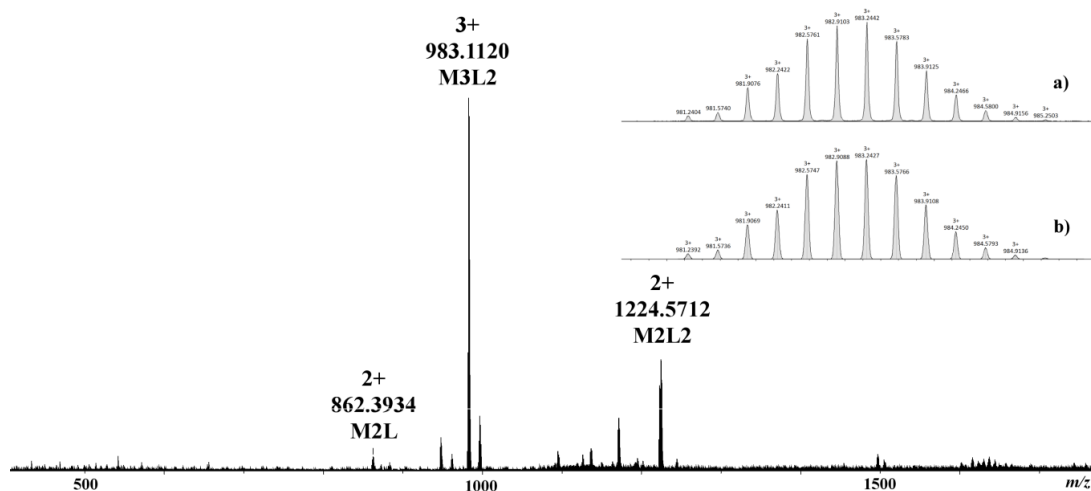


Figure 6.5: HR ESI-MS of M_3L_2 assembly CC4.3, along with fragmentation products, M_3L_2 peaks shown inset a) measured b) calculated isotope pattern, where $M=[Ir(ppy)_2]^+$. [PF_6^- salt employed].

The rapid and facile formation of the metallocage suggests an almost self-assembly like process, despite the relative inertness of the low-spin d^6 iridium metallotecton. The lability of the bound acetonitrile ligands on the iridium tecton, due in part to the *trans*-labilising effect of the *C,C-cis-N,N-trans* arrangement of the two phenylpyridine ligands, promotes the formation of a supramolecular architecture. The robust nature of the resultant cage is also evidenced through bulk precipitation of the intact assembly by addition of excess diethyl ether anti-solvent, to give a bright yellow powder that can subsequently be re-dissolved to give identical NMR and MS data as the reaction mixture.

1H NMR studies following the formation of both metallocage complexes **CC3.1** $^{3+}$ and **CC4.3** $^{3+}$ were performed in d_3 -MeNO $_2$, and show considerable broadening of the peaks immediately after addition of the metallotecton, suggesting dynamic formation of a much larger species in solution, as shown in Figure 6.7.

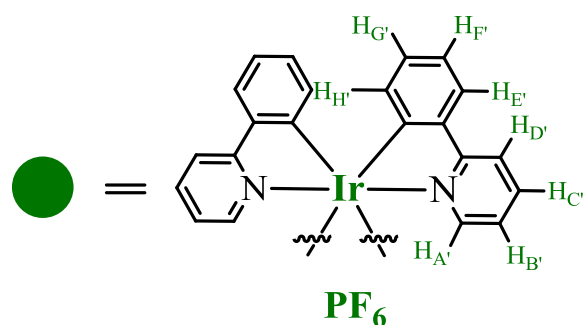


Figure 6.6: Structure of the iridium metallotecton (*M*) employed in formation of M_3L_2 metallocryptophanes, with ^1H NMR proton assignments shown.

The broad spectrum does sharpen to a degree over time, as self-assembly towards an M_3L_2 species occurs; there will also be some degree of self-sorting towards homochiral cages. As already commented, the bulk precipitated assembly can subsequently be re-dissolved to give a broad ^1H NMR spectrum that is almost indistinguishable from spectrum **d**), samples utilising this pre-formed approach also sharpen slightly over time.

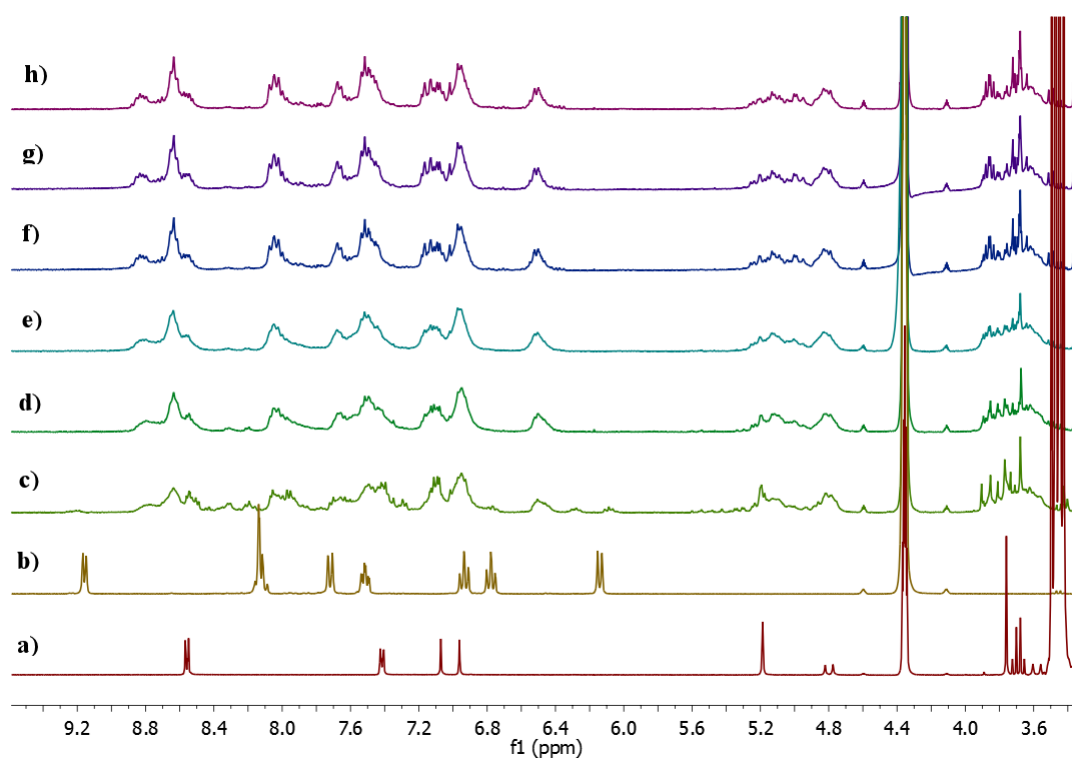


Figure 6.7: ^1H NMR timecourse experiment following the formation of $[\text{CC3.1}\cdot 3(\text{PF}_6)]$ a) *L3* b) metallotecton c) immediately after mixing d) 2hrs RT e) 12hrs RT f) 24hrs RT g) 48hrs RT h) 1 week RT.

Salient points of note are the significant broadening of the previously sharp CH₂ ether bridge singlet at 5.2 ppm in spectrum **a**) towards a complex multiplet as the free rotation around that bond becomes sterically hindered due to binding the iridium centre. The two protons closest to the iridium centre on the phenylpyridine, H_A' (~9.2 ppm) and H_H' (~6.2 ppm) are also dramatically shifted, with H_A' shifting upfield and conversely H_H' shifting downfield, to both become contained within the aromatic envelope of peaks. Both of these shifts are strongly indicative of complexation between the two units.

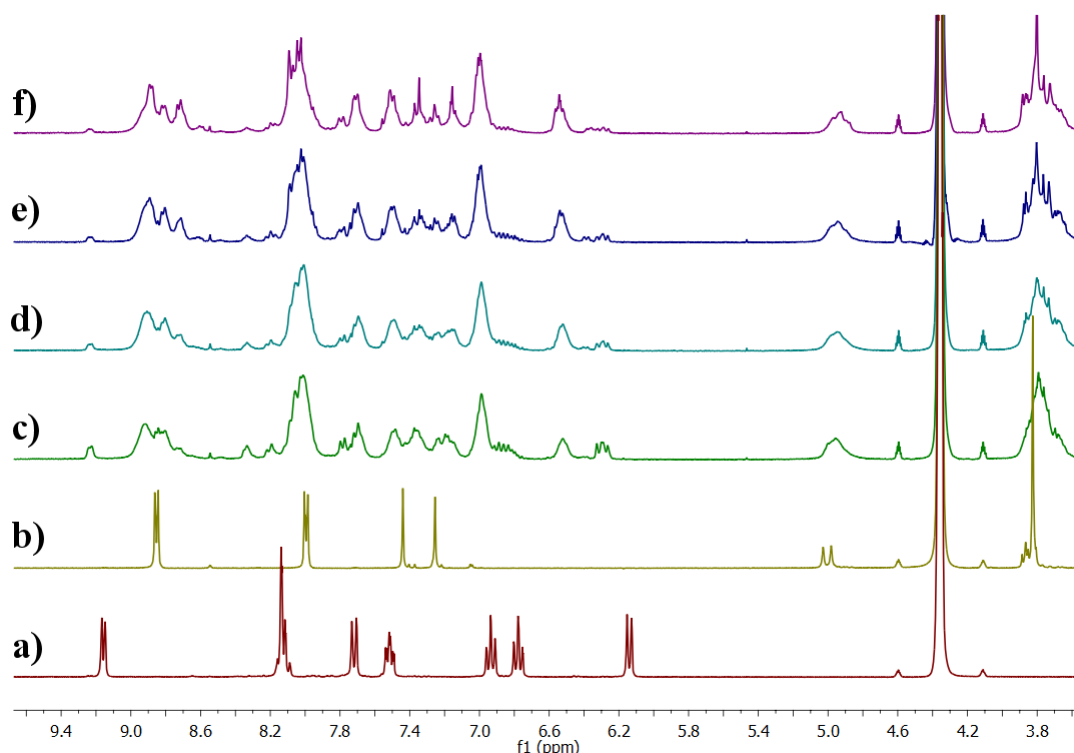


Figure 6.8: ¹H NMR timecourse experiment following the formation of [CC4.3•3(PF₆)] **a**) metallotecton **b**) L4 **c**) immediately after mixing **d**) 2hrs RT **e**) 12hrs RT **f**) 1 week RT.

Analogous to **CC3.1**, **CC4.3** shows shifting of H_A' and H_H' towards the centre of the aromatic envelope once again showing no evidence of uncomplexed starting material.

Diffusion-Ordered (DOSY) NMR spectroscopy of **CC4.3** also supports the formation of one larger species in solution, as demonstrated in Figure 6.9. All peaks present in the spectrum, barring those assigned to residual solvent and water contaminant, diffuse with one diffusion coefficient, highlighted in the red box below. The diffusion coefficient of **CC4.3** recorded in deuterated nitromethane was

$3.56 \times 10^{-10} \text{ m}^2 \text{ s}^{-1}$. Diffusion coefficients can be rationalised with respect to hydrodynamic radii through implementation of the Stokes-Einstein equation.

$$r = \frac{k_b T}{6\pi\eta D}$$

Equation 1.1: Stokes-Einstein equation, where r = hydrodynamic radius (m), k_b = Boltzmann's constant (J K^{-1}), T = Temperature (K), η = viscosity (Pa s^{-1}) D = diffusion coefficient ($\text{m}^2 \text{ s}^{-1}$).

However, a serious caveat to this equation is the required spherical nature of the compound being studied; the more a compound deviates from perfectly spherical; the less valid the Stokes-Einstein equation becomes. In relation to the metallocryptophanes under discussion, whilst symmetrical in nature, they are not spherical, thus the hydrodynamic radii obtained through the equation cannot be considered wholly accurate.

Implementing Equation 1.1 on the diffusion coefficient of **CC4.3**, a hydrodynamic radius of 9.73 \AA is obtained. Whilst this may seem smaller than expected, this value falls between the $7\text{-}12 \text{ \AA}$ range measured from the centre of the cage to the periphery, determined from the SCXRD data.

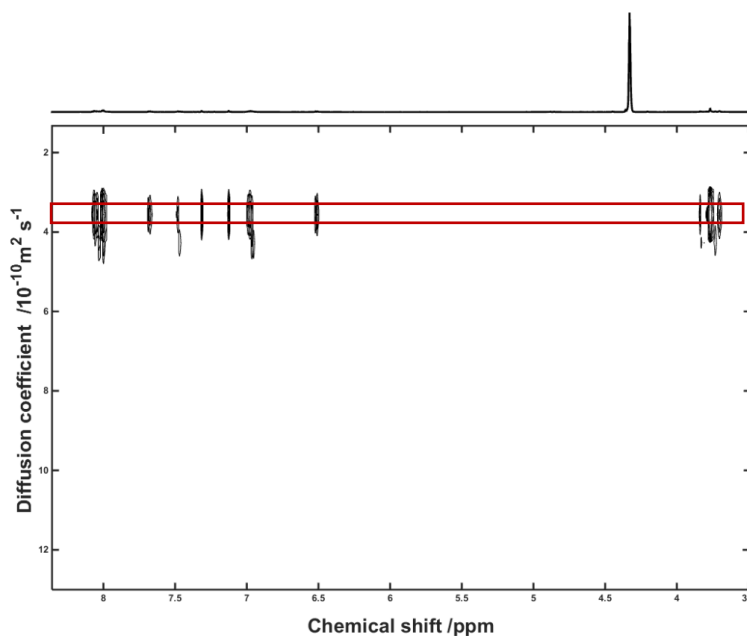


Figure 6.9: DOSY NMR spectrum of $[\text{CC4.3} \cdot 3(\text{PF}_6)]$ in $d_3\text{-MeNO}_2$, showing a D_c of $3.56 \times 10^{-10} \text{ m}^2 \text{ s}^{-1}$.

A comparative **L4** ligand spectrum was also recorded, under the same conditions, and gave a diffusion coefficient of $5.2 \times 10^{-10} \text{ m}^2 \text{ s}^{-1}$.

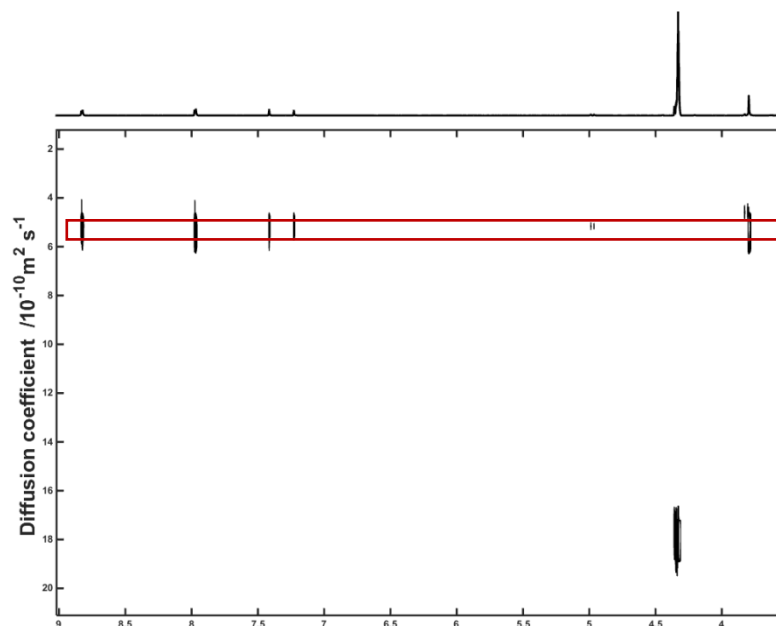


Figure 6.10: DOSY NMR spectrum of *L4* in d_3 -MeNO₂, showing a D_L of $5.2 \times 10^{-10} \text{ m}^2 \text{ s}^{-1}$.

Therefore, the relative ratio of complex to ligand, $D_C:D_L$, is 0.68. Previous work, both within the Hardie group and externally, has examined the range of $D_C:D_L$ ratios obtained from supramolecular assemblies of various sizes in DOSY NMR.^{40–42} This has led to a more accurate description of non-spherical diffusion coefficients of supramolecular assemblies, when related back to the ligand precursor, with a ratio of 0.72–0.75 generally accepted for a dimeric structure.

However, a previously reported M_3L_2 metallocryptophane assembly containing extended palladium *bis*-NHC metallotectons gave a diffusion ratio of 0.54.³³ This however, can be rationalised through consideration of their use of a large metallotecton ‘unit’ as the metal source, rather than the naked metal (Ag) ions previously examined in M_3L_2 DOSY analysis, thereby adding proportionally more ‘bulk’ to the assembly.⁴⁰ Therefore, the ratio obtained for **CC4.3** of 0.68 is within a reasonable range for a dimeric M_3L_2 species, as the metallotecton employed is smaller than the previous palladium *bis*-NHC, but larger than a simple silver ion.

6.2.2 Crystallographic analysis of metallocryptophane **CC4.3**

The more rigid metallocryptophane $\{(\mathbf{CC4.3}) \cdot 3(\text{BF}_4)\}$ crystallised as yellow hexagonal plates through the diffusion of diethyl ether vapours into a nitromethane

solution of pre-formed cage and their structure was determined through x-ray diffraction techniques.

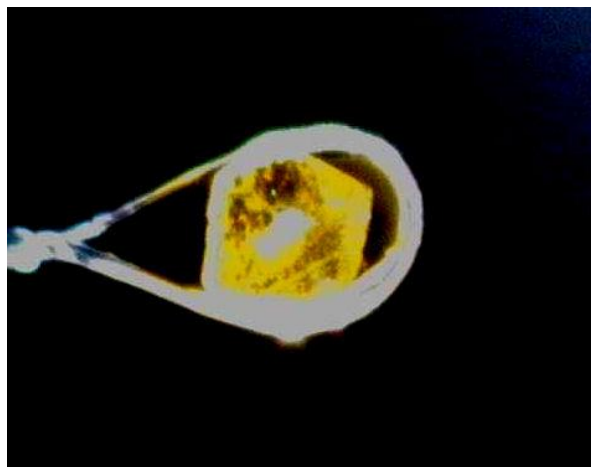


Figure 6.11: Visible appearance of crystals of $CC4.3 \cdot 3(BF_4^-)$.

The crystals were weakly diffracting and their structure was solved in the space group $P2_1/n$ to give the asymmetric unit as two whole metallocryptophanes. The weakly diffracting nature of the crystals is likely due to the presence of disordered tetrafluoroborate anions, none of which could be located in the difference map during structure refinement, as well as more disordered nitromethane solvent molecules. As previously mentioned, no precaution was taken to favour a particular enantiomer with respect to the octahedral iridium centre or the tripodal ligands, thus it was possible to form a complex mixture of isomeric cages. In reality however, as in many complex supramolecular systems,^{20,43,44} self-sorting of isomers occurs, in both modes of isomerisation upon crystallisation

Enantiomeric self-sorting, or an induced seeding effect, upon crystallisation gives rise to both of the possible *anti*-cryptophanes, with each chiral metallocryptophane containing only one iridium enantiomer, thus out of the twelve possible products only the $MM-\Lambda\Lambda\Lambda$ and $PP-\Delta\Delta\Delta$ configurations are seen. These assignments are deduced from the SCXRD data, whereby the unit cell consists of two metallocryptophanes, one of each enantiomer described above. Self-sorting processes are usually split into either *narcissistic* or *social* categories, whereby ligands of one type will associate solely with themselves, or with other ligand components in the assembly library, respectively.⁴⁴⁻⁴⁷ However, the root of the phrase *narcissistic self-sorting* is in the Greek god Narcissus, who fell in love with his own reflection, which by the very definition would be his mirror image and

consequently the opposite enantiomer.⁴⁸ Therefore, with respect to the self-sorting of [CC4.3•3(BF₄)], the term enantiomeric, or chiral, self-sorting is used.

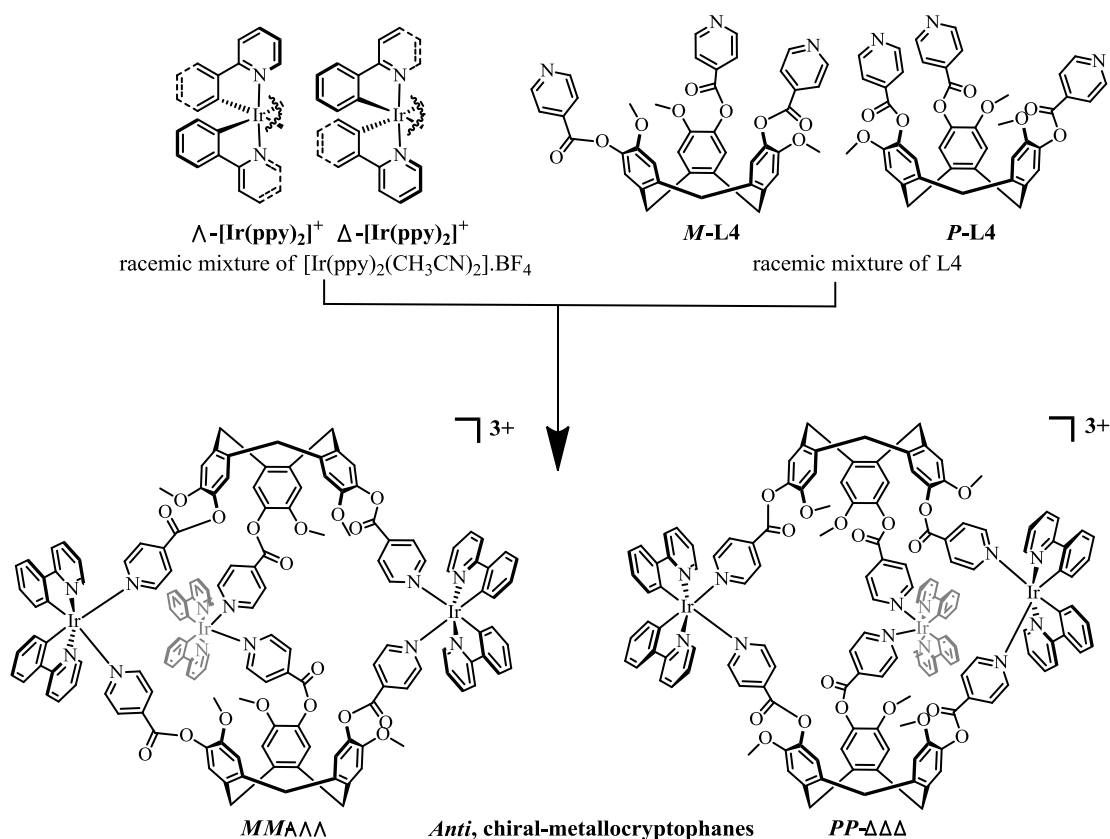


Figure 6.12: Racemic route to chiral metallocryptophanes *MM-AAA* and *PP-AAA*, both isomers are determined from the SCXRD data.

The two metallocryptophane enantiomers in the unit cell are crystallographically inequivalent, with the *MM*-cage exhibiting a bowl-centroid to bowl-centroid distance of 15.341 Å whereas the *PP*-cage shows a slightly longer distance of 15.673 Å. However, the *P*₂/*n* space group is centrosymmetric, thus the two crystallographically distinct cages appear as both homochiral enantiomers throughout the crystal lattice. Thus the compressed cage, which appears in the unit cell as the *MM* enantiomer is Cage Type I, whilst the slightly elongated cage represented in the unit cell by the *PP* enantiomer is Cage Type II.

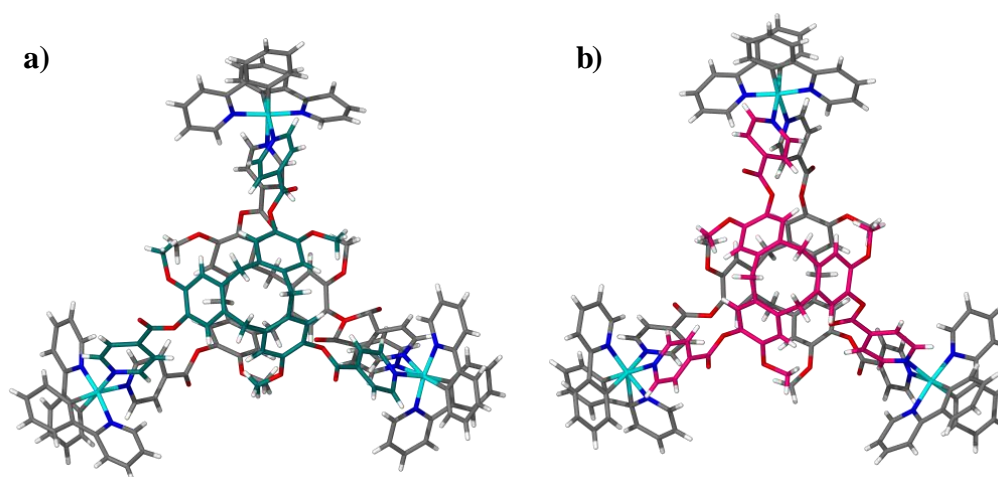


Figure 6.13: *The view down the centre of the cavitaand for the two Cage Types in the unit cell, a) Cage Type I as the MM-AAA enantiomer and b) cage Type II as the PP-AAA enantiomer, the topmost ligand is highlighted in teal (M) and pink (P) respectively.*

Chiral, *anti*-cryptophanes were formed from two ligands of the same enantiomer in a head-to-head fashion. As shown in Figure 6.13, when two ligands of the same chirality are combined in a head-up-head-down fashion, the resultant cryptophane displays a staggered arrangement of the central ligand scaffold when viewed down the centre of the capsule. The off-set between the two ligands is 60° , leading to the staggered arrangement seen above. The chirality around the iridium centre is also displayed in this view; whereby the *MM* cage is comprised of the Λ enantiomer and the *PP* cage the Δ enantiomer. This view also helps to illustrate the torsion angles of the pyridyl binding moieties with respect to idealised octahedral geometry around the iridium metal centre. The ability of the N-donor ligand to twist to accommodate this distortion is thought to be vital, as shown in Figure 6.14.

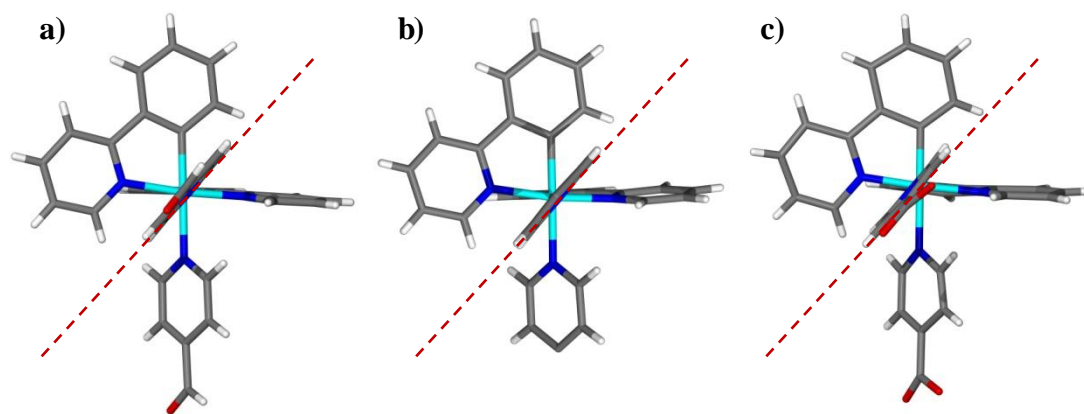
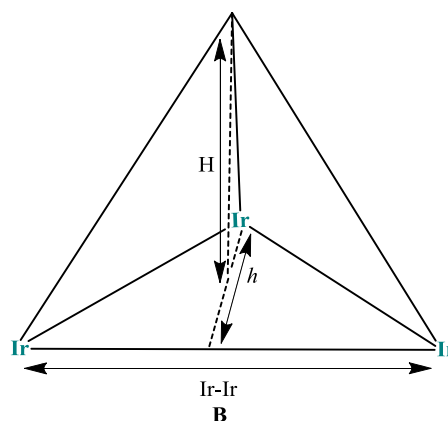


Figure 6.14: Torsion angle of the pyridyl ligands in a mono-nuclear $[\text{Ir}(\text{ppy})_2(\text{py})_2]$ complex,⁴⁹ in Chandrasekhar's dimer³⁹ and from the SCXRD data of CC4.3, all showing the torsion of the pyridyl ligand with respect to idealised octahedral geometry.

The capacity of the pyridyl ligand to twist from idealised octahedral geometry is a fundamental factor in the formation of any complex of the form $[\text{Ir}(\text{ppy})_2(\text{py})_2]^+$, but even more so if the structure is supramolecular in nature, requiring self-assembly conditions. If the formation relies on self-assembly then any ligand that cannot accommodate the above distortion is unlikely to result in a stable, isolatable assembly.

The 4-formyl pyridine containing mono-nuclear structure,⁴⁹ displayed in Figure 6.14 as complex **a**), possesses an average torsion angle of 36.9° , whilst complex **b**), a partial representation of Chandrasekhar's dimeric structure,³⁹ shows an average torsion angle of 38.0° . Complex **c**) is a partial view of $[\text{CC4.3}\cdot\mathbf{3}(\text{BF}_4)]$, displaying two pyridyl arms and one iridium metallotecton for clarity. The average torsion angle, calculated from an average of all pyridyl-iridium bonds within the SCXRD data of $[\text{CC4.3}\cdot\mathbf{3}(\text{BF}_4)]$, was 38.04° . This is congruent with the values measured from both mono- and di-nuclear iridium-pyridyl species. The required torsion of the pyridyl moiety is thought to be due to sterics between the two pyridyl ligands; if there was no distortion the *ortho*-protons on the pyridyl moieties would clash, either leading to no reaction or an unstable product.

$$1/6(BHh)$$



Distance	Cage Type I (Å)	Cage Type II (Å)
Ir-Ir	17.856	17.383
Ir-Ir	17.872	17.836
Ir-Ir	16.691	16.677
Average Ir-Ir	17.473	17.299
H	7.696	7.852
<i>h</i>	14.794	14.919
<i>h</i>	15.795	14.512
<i>h</i>	14.808	15.512
Average <i>h</i>	15.132	14.981
Volume of Cage (Å ³)	678.27	678.29

Table 6.1: Schematic of triangular based pyramid and the distances used to calculate the cage volume, along with relevant inter-atomic bond distances from the SCXRD data of [CC4.3•3(BF₄)].

Table 6.1 clearly demonstrates the differences in inter-atomic distances exhibited by each crystallographically distinct type of cage, however these differences are the result of compression or elongation in various directions, hence the almost identical overall volume calculated.

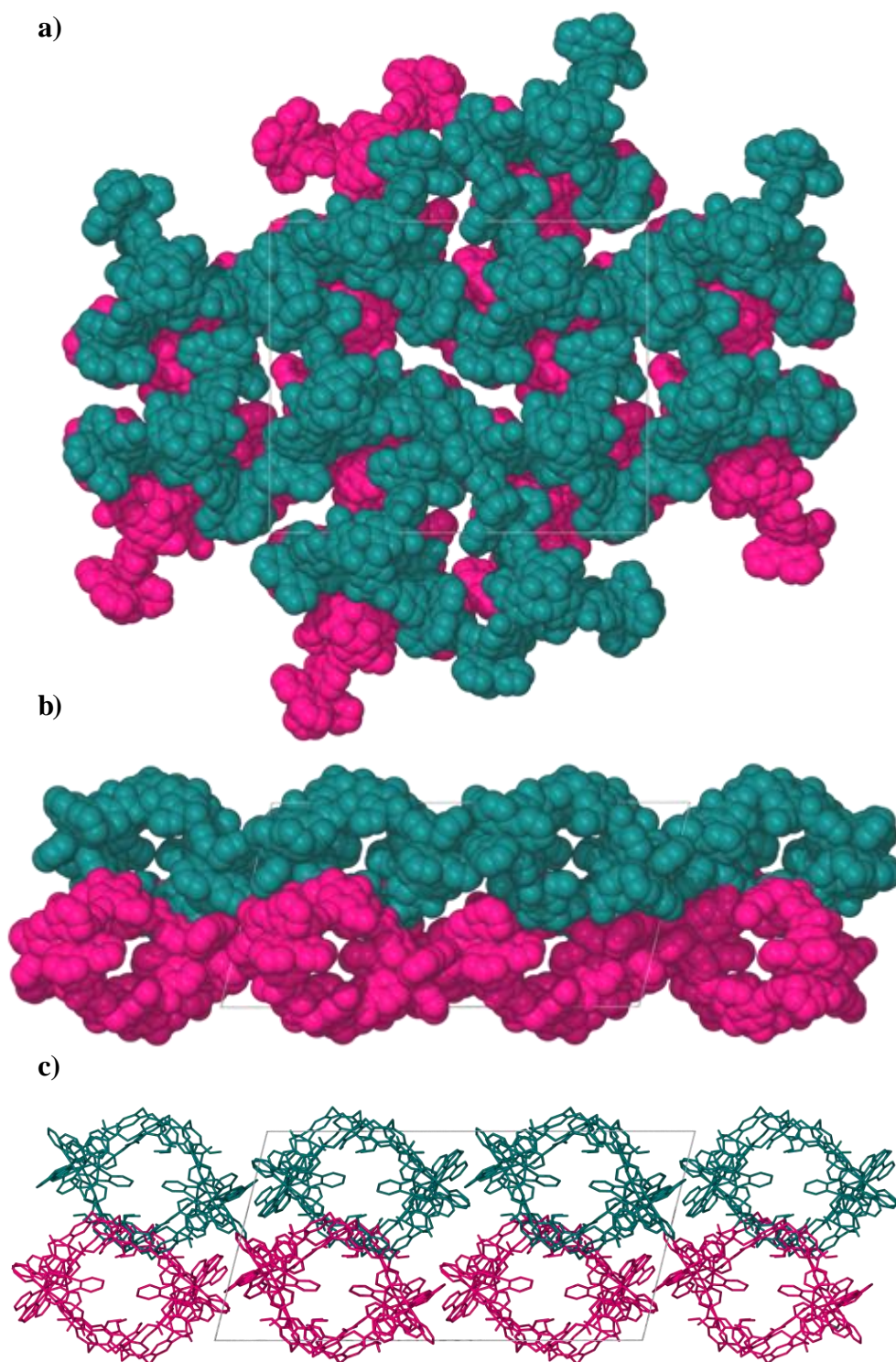


Figure 6.15: Packing diagram looking down the crystallographic *a* axis (a) *b* axis, shown in space-filling mode (b) and the *b* axis in wire-frame mode (c), to show the tessellation of cryptophane units and the enclosed void space within the cryptophane assemblies.

The *PP*- enantiomer is shown in pink and the *MM*- enantiomer shown in teal. The packing structures, as shown in Figure 6.15, show 2D sheets of each enantiomer of metallocryptophane, clearly seen looking down the crystallographic *a* axis, where the enantiomerically pure sheets are off-set slightly with respect to each other. With regards to the Cage types, each enantiomeric layer displays alternating 1D chains of Cage Type I and II. The cryptophane units in the individual layers are relatively tightly packed, as seen in the space-filling model, with only small channels visible through the crystal lattice. The alternating 2D sheets of each single enantiomer form an *ABAB* arrangement, whereby the sheets of the same enantiomer overlay perfectly. The tessellation between the two sheets is shown in the crystallographic *b* axis, whereby the off-set seen in the *a* axis allows the pyramidal shape of the assemblies to slot together. Through consideration of the wire-frame view of the *b* axis, the enclosed void space within the cryptophane units can be more clearly seen. Whilst the cryptophane units may fit together tightly, leading to low extrinsic void space, there are significant cavities within each individual capsule, leading to high levels of intrinsic void space. However, as none of the counter-ions could be located, the apparent ‘void space’ will contain both BF_4^- anions and further disordered solvent molecules.

The extensive internal void space can be quantified through the SQUEEZE⁵⁰ routine of PLATON, whereby the total void space was established to be 22017 \AA^3 . The total cell volume is 43182 \AA^3 , thus the void space accounts for over 50% of the total cell volume, going some way to explain the weakly diffracting nature of the crystals.

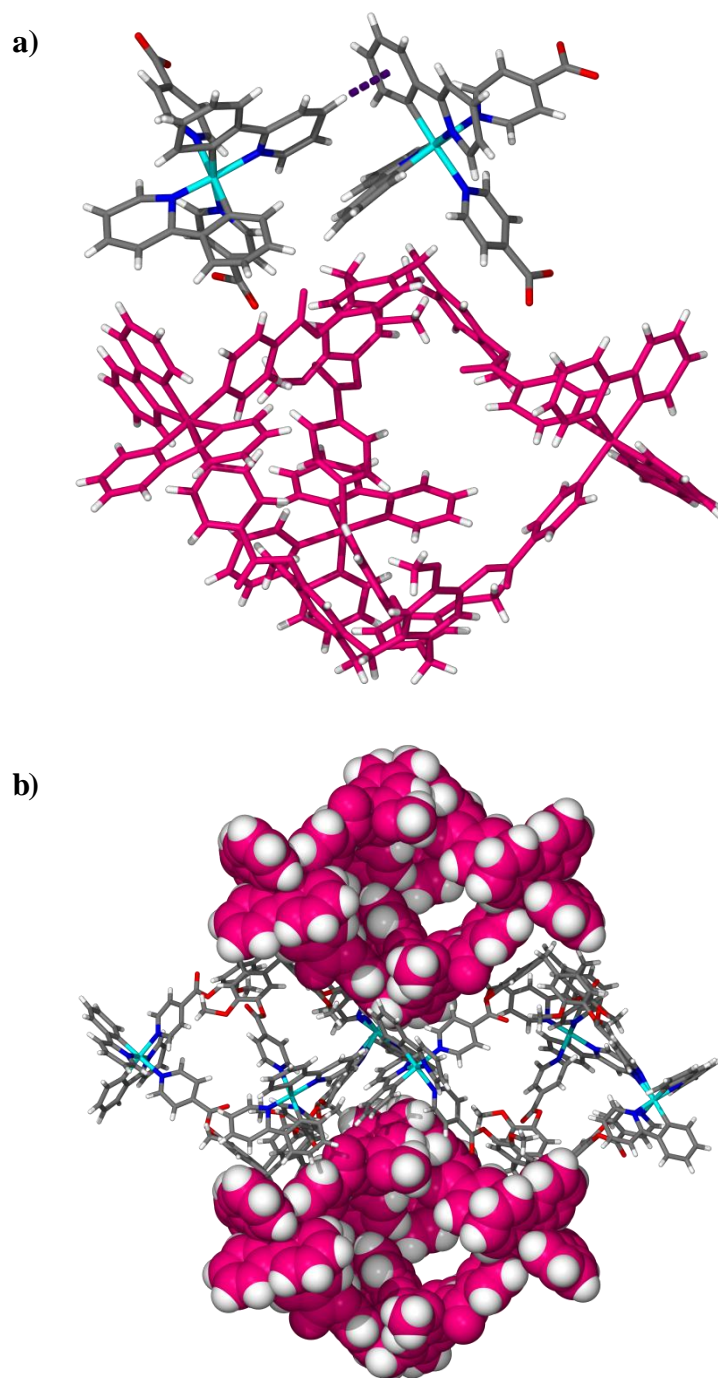


Figure 6.16: Complementary nature of the phenylpyridine and ligand cavity angles of CC4.3, along with the inter-molecular H- π bonding seen between phenylpyridine moieties (a), extended view along the crystallographic c axis showing the packing of alternating enantiopure sheets.

The angle created by the central cyclononatriene core fits into the space described by the phenylpyridine-iridium-pyridyl angle, as demonstrated through **a)** in Figure 6.16. The two closest units of the same enantiomer experience H- π bonding, highlighted in Figure 6.16 by the dashed purple bond. The π -cloud of a

phenylpyridine ligand on one cage is 2.5 Å away from H_C on the adjacent cryptophane unit, with H_C pointing directly into the centre of the phenyl ring. The H-bonding effect can be seen proliferated throughout the crystal lattice in Figure 6.16, image **b**), whereby the interlocking nature of the 2D sheets is obvious, as well as the alternating arrangement of enantiopure sheets. The combination of H-bonding and complementary angles provided by both the ligand scaffold and the metallotecton give rise to the tightly packed sheets of metallocryptophane units.

6.3 Speciation studies of homo- and hetero-cage metallocryptophanes

The chiral self-sorting of **CC4.3** upon crystallisation demonstrates a high level of discrimination; forming homochiral cryptophanes with regards to both the ligand component as well as the metallotecton, that the ability of the system to self-sort in solution was thus investigated. Both the enantiomeric, chiral self-sorting of the homocage metallocryptophanes and the ligand self-sorting of the hetero/homocage mixture were investigated.

A speciation study was undertaken to ascertain the discriminatory self-sorting behaviour of the ligands whilst the cages self-assemble in solution. Three equivalents of the tetrafluoroborate metallotecton and one equivalent each of **L3** and **L4** were combined in nitromethane solvent and stirred at RT. HR ESI-MS was employed to follow not only the self-assembly of the previously discussed homocage cryptophanes, but also the ligand speciation contained within the **M₃L₂** cages.

As shown in Figure 6.17, taken 8 hours after mixing, both *homo*- and *hetero*cage cryptophane assemblies form in solution; the resultant mass spectrum shows a statistical mixture of all three possible metallocryptophanes. The homo/hetero cage solution was left stirring for a period of weeks, with no evidence of self-sorting of the reaction mixture over time or indeed any preferential combination of ligands, suggesting that the two possible metallocryptophanes, homo- and hetero-, must be of similar energies.

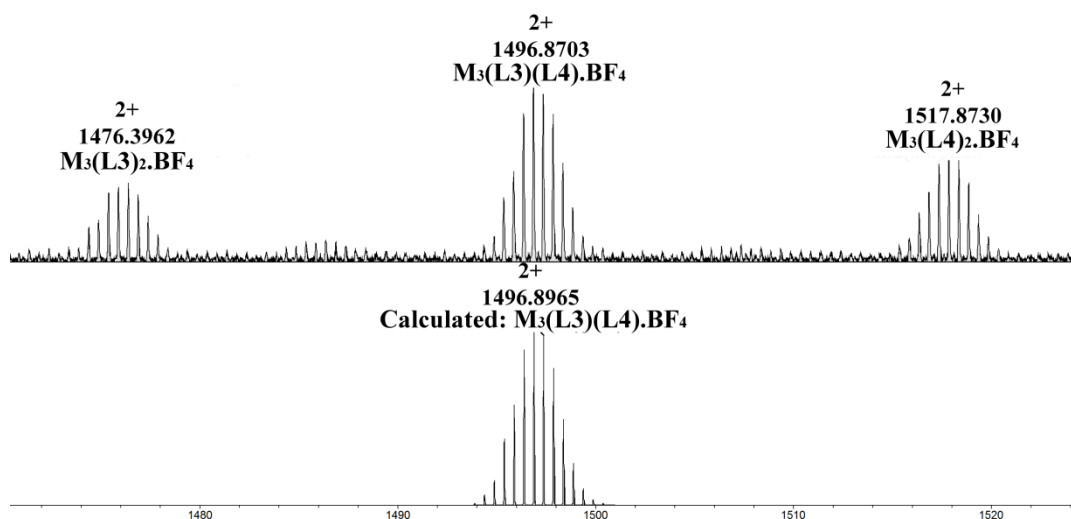


Figure 6.17: HR ESI-MS of heterocage formation from L3, L4 and the Ir metallotecton, where $M=[Ir(ppy)_2]^+$. [BF_4^- salt employed].

The behaviour seen in Figure 6.17 suggests that the initial formation of the cage species is non-discriminatory, as evidenced through the statistical formation of homo cages **CC3.1** and **CC4.3**, as well as the hetero cage **CC3.2** containing three iridium centres and one equivalent each of **L3** and **L4**.

However, if one equivalent of each bulk precipitated cage **CC3.1** and **CC4.3** are combined in $MeNO_2$ solvent, the homo cages stay mostly intact. Initially, barely any ligand scrambling to form heterocage **CC3.2** can be seen through HR ESI-MS, suggesting that the initial formation of the cages is non-discriminatory, but once formed the stability and robustness of the M_3L_2 assembly in solution, in non-coordinating solvents, strongly disfavours the dissociation-association mechanism required to form hetero **CC3.2** in solution.

The cage mixtures were followed by HR ESI-MS over a period of weeks, and only after ~4 weeks did any appreciable peak assignable to the heterocage metallocryptophane begin to appear. The time-course HR ESI-MS is shown below in Figure 6.18.

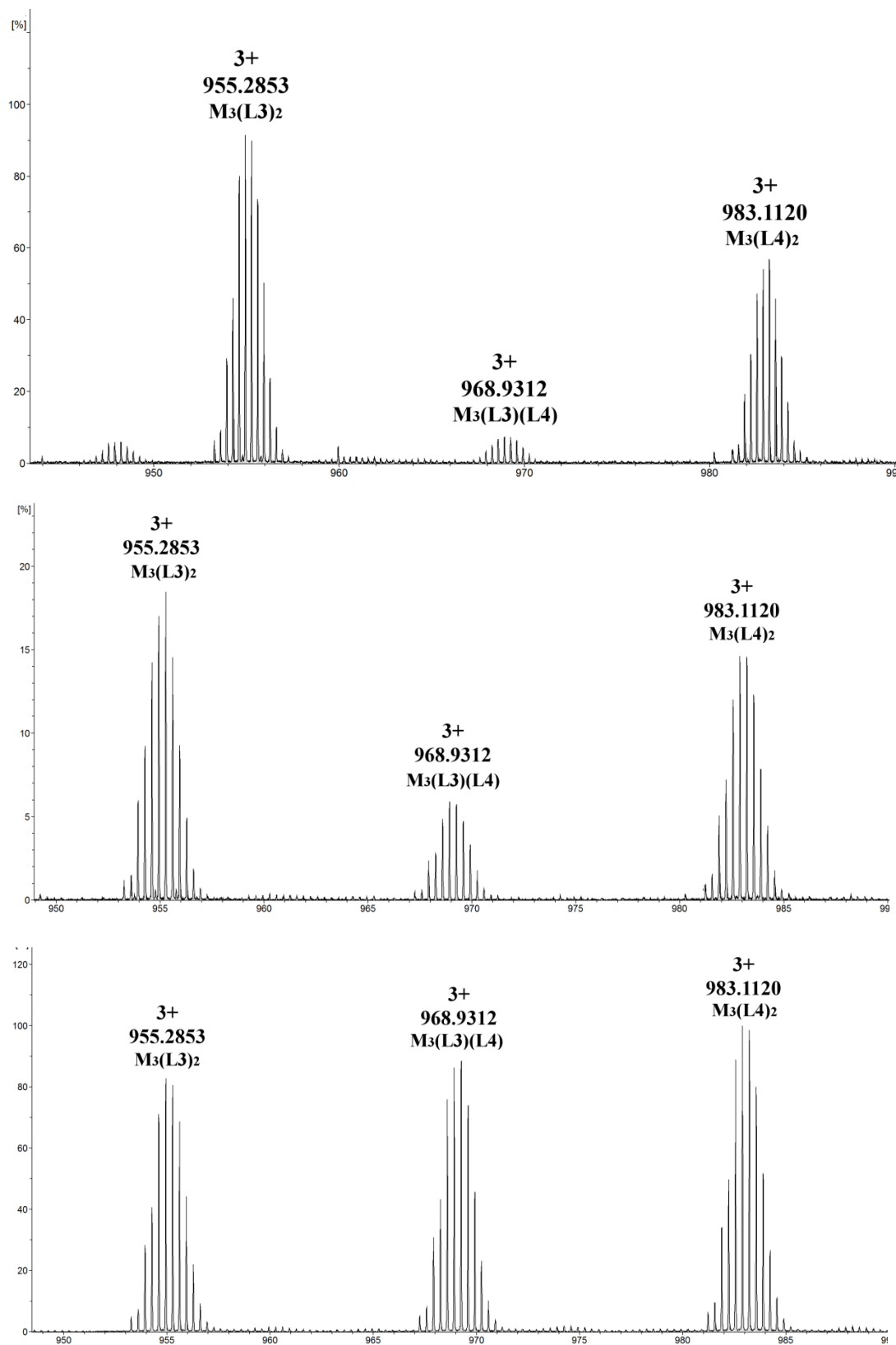


Figure 6.18: HR ESI-MS of CC3.1 and CC4.3 combined in MeNO₂ after 24hrs (top) 4 weeks (middle) and 6 weeks (bottom). [BF_4^- salt employed].

Continuing to follow the speciation by HR-MS, further self-sorting was observed, however only over a period of months. The solution eventually formed a statistical mixture of both the homo and hetero cages, similar to that seen in the previous speciation study of the formation of the cages in Figure 6.17.

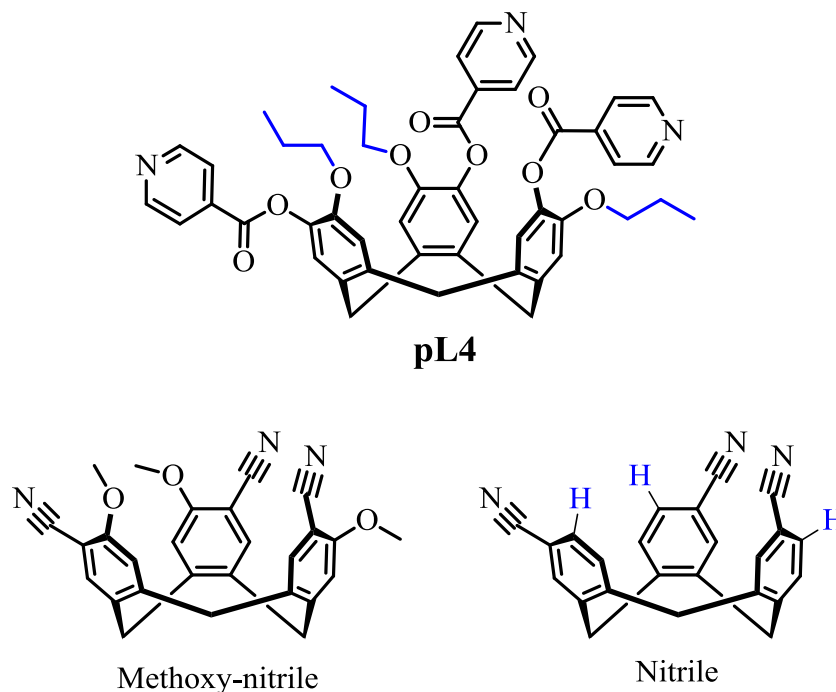


Figure 6.19: Chemical structures of the structurally analogous ligands employed in palladium containing supramolecular assemblies, **pL4**⁵¹ (top) and the two nitrile-containing ligands employed in the formation of *pd*-metallocryptophanes.³⁴

This eventual self-sorting is in contrast to previously reported palladium supramolecular assemblies formed in combination with this ligand type.⁵¹ The combination of eight equivalents of **L4** or the direct propyloxy analogue, **pL4** shown in Figure 6.19, with six equivalents of palladium(II) tetrafluoroborate gave rise to a stella octangula^{52–54} type structure of the form Pd₆L₈, where L = **L4** or **pL4**. In this case a heteroleptic assembly could be formed through combination of starting palladium metal salt and ligand components to form [Pd₆(**L4**)_{8-n}(**pL4**)_n]¹²⁺, in an analogous fashion to the non-discriminatory behaviour seen in the formation of heterocage **CC3.2** in Figure 6.17. However, when pre-formed homoleptic Pd₆L₈ assemblies were combined in DMSO solvent no evidence of ligand scrambling or inter-conversion to the heteroleptic assembly was seen, even over a period of six months. The co-existing mixture of homo cages was therefore heated to 60°C for over 12 hours, and still no evidence of ligand scrambling was observed.

More recently Schaly *et al.* described the formation of a palladium metallocryptophane,³⁴ along with the platinum congener, formed from a nitrile functionalised CTG ligand and a *cis*-protected palladium source of the form $[M(\text{dppp})][\text{OTf}]_2$, where $M = \text{Pt}, \text{Pd}$, $\text{dppp} = 1,3\text{-bis(diphenylphosphino)propane}$. The tripodal nitrile ligand was formed both bearing a methoxy group adjacent to the nitrile and just a proton, shown in Figure 6.19. When three equivalents of $[M(\text{dppp})][\text{OTf}]_2$ and one equivalent of each ligand were combined in deuterated tetrachloroethane the two homoleptic metallocryptophanes were exclusively formed, with no evidence observed for the heterocage in the ^1H NMR spectra.

In the wider context, Stang has repeatedly shown the formation of exclusively homoleptic assemblies through considered use of deuterated ligand precursors, as well as the subsequent formation of heteroleptic assemblies through ligand scrambling over time, or in the presence of aqueous solvent.^{55,56} Whilst work from Schmittel shows that the formation of a heteroleptic assembly is preferred over the two homoleptic congeners.⁵⁷ It was shown that the combination of two metals, Cu(I) and Zn(II) , with four distinct ligands lead overwhelmingly to the formation of two heteroleptic species, despite the possibility to form over 20 homo- and heteroleptic assemblies. Schmittel has also demonstrated formation of homoleptic Cu(I) complexes that do not undergo ligand scrambling, however this was through the use of sterically demanding substrates.⁵⁸

Nitschke has also shown the formation of an exclusively heteroleptic iron(II) assembly, formed from two similar but distinct N^2N chelating ligands and subsequently locked into place to form a [3]-catenane.⁵⁹

Therefore, despite the relative inertness of the low-spin iridium(III) metal centre employed in the formation of metallocryptophanes **CC3.1** and **CC4.3**, the resultant cages are more dynamic in solution than the previously reported palladium systems. However, the slow exchange seen in the ligand scrambling experiments and the non-discriminatory formation of the metallocryptophane units has been previously observed.

To further examine the solution-state speciation and enantiomeric self-sorting processes a number of single crystals of **CC4.3** were re-dissolved in deuterated nitromethane solvent, thus looking at the chirality of the resultant species rather than the type of ligand. The single crystals of **CC4.3**, as discussed in section 6.2.2, have

already been seen to self-sort into enantiomerically pure cage complexes, meaning that upon dissolution the resultant ^1H NMR spectrum should display sharper, more well-defined proton resonances due to the presence of only homochiral cages. The resultant spectrum is relatively weak, with the presence of a significant amount of diethyl ether due to the inherent presence of the anti-solvent throughout the crystal lattice.

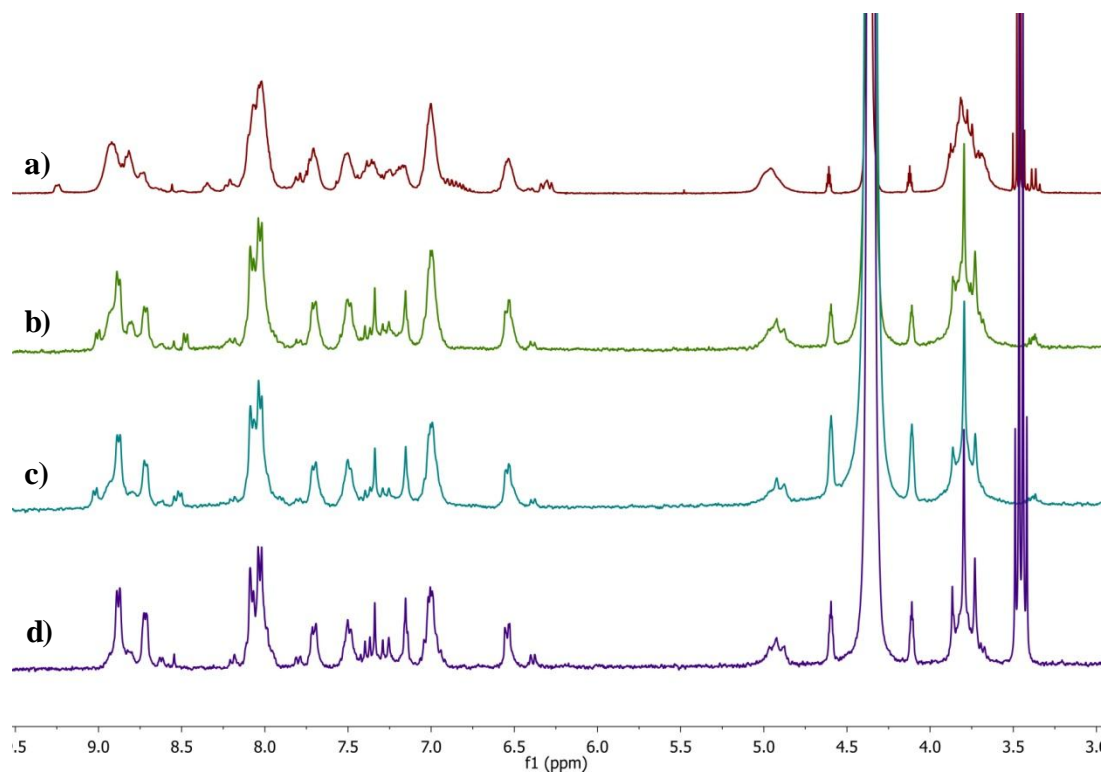


Figure 6.20: Stacked ^1H NMR spectra of a) CC4.3 6 hours after the separate components were mixed b) CC4.3 2 months after the components were mixed, showing a significant degree of self-sorting c) CC4.3 6 months after the components were mixed, showing a slightly further degree of self-sorting d) single crystals of CC4.3 re-dissolved in deuterated nitromethane.

In Figure 6.20, the topmost ^1H NMR spectrum (a) shows the formation of CC4.3 six hours after the two components (M & L, where M=[Ir(ppy) $_2$](PF $_6$) and L=L4) were combined together in deuterated nitromethane, the resultant spectrum has broadened with respect to the two starting components, but shows no evidence of self-sorting, displayed through broad, unstructured peaks. The broadness of the observed peaks is likely due to a dynamic library of species and isomers present in solution at the time the spectrum was recorded.

The green trace (b) represents an NMR sample of CC4.3•3(PF $_6$) formed in deuterated nitromethane and left to equilibrate for 2 months; some of the broadness

is still apparent, however most of the aromatic peaks have sharpened up significantly, up to the point that the multiplet nature of some peaks is now evident. Further self-sorting of the cages towards homochiral products occur over a 6 month period, shown in trace (c), although to a lesser degree than over the initial 2 month period.

The bottom trace (d) is the result of re-dissolving the isolated single crystals of **CC4.3•3(BF₄)**, displaying much sharper peaks than spectrum (a). Spectrum (d) is known to be of an enantiomerically self-sorted assortment of cages, and thus the proton resonances observed are much sharper and well-defined than both other spectra. However, when comparing spectra (b/c) and (d) there are similarities; many of the sharpest peaks are coincident, with spectrum (b) displaying additional broader peaks as well. This suggests that after a period of approximately 2 months, there has been significant enantiomeric self-sorting of **CC4.3**, with the remaining broader peaks not visible in spectrum (d) due to incomplete self-sorting or self-assembly. After 6 months the recorded ¹H NMR spectrum is essentially super-imposable with the re-dissolved crystals, as evidenced in Figure 6.21. The two remaining peaks not visible in the spectrum of the re-dissolved crystals could be due to a slight stoichiometric miss-match or the presence of a minute amount of the *syn*-isomer in solution.

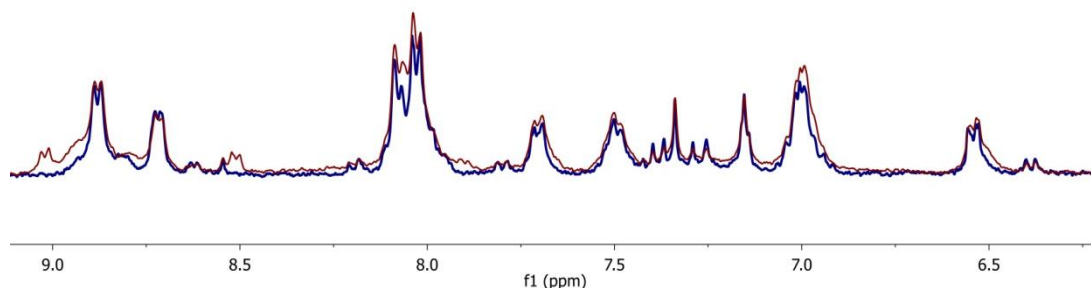


Figure 6.21: Overlaid ¹H NMR spectra of CC4.3 after 6 months self-sorting, shown in red, and the re-dissolved enantiomerically self-sorted crystals of CC4.3, shown in navy.

The previously reported palladium metallocryptophanes all show immediate self-sorting, under certain conditions. The example from Hardie *et al*, immediately forms the *syn meso*-cryptophane when a naphthylated Pd(NHC) metallotecton is employed.³³ This is in accordance with the example from Shinkai *et al*; where a slight excess of ligand furnishes exclusively the *syn meso*-cage once again.³²

Conversely the recent example from Schaly forms the chiral *anti*-cryptophane, however the self-sorted cage still forms immediately upon mixing.³⁴

Consequently, it follows that the discriminatory self-sorting observed in the SCXRD data is a phenomenon of crystallisation, and by no means precludes the existence of other stereoisomers in solution. However, over a significant time period, up to 6 months, the preference of the system towards a homochiral arrangement can be observed, tending towards completeness.

Previous work by Cooper *et al*, on a library of imine-linked covalent organic cages employed DFT calculations in an effort to explain experimental trends seen in the SCXRD data of a series of tetrahedral imine cages.⁶⁰⁻⁶² They found that seemingly small structural alterations could lead to the opposite effect in cage packing, with some systems forming exclusively homochiral packing structures, whilst slightly altered analogues form exclusively heterochiral arrays. This work shows how complex the crystallisation process for supramolecular assemblies is, with a myriad of inter- and intra-molecular forces acting upon the molecules along with effects of templating, seeding and self-sorting.

6.4 Photophysical properties of metallocryptophanes

The photophysical studies were performed at the University of St Andrews by Diego Rota Martir of the Zysman-Colman research group.

The photophysical properties of both cages were studied in non-coordinating DCM solvent, to prevent any breakdown of the cages back to their constituent parts during investigation. Solution state photoluminescence spectra were obtained, as well as solid state powder emission and doped film spectra, to give a more comprehensive overview of the photophysics and to relate any spectral changes to changes in vibrational quenching due to solution/solid state interactions.

6.4.1 Photophysical properties of CC3.1

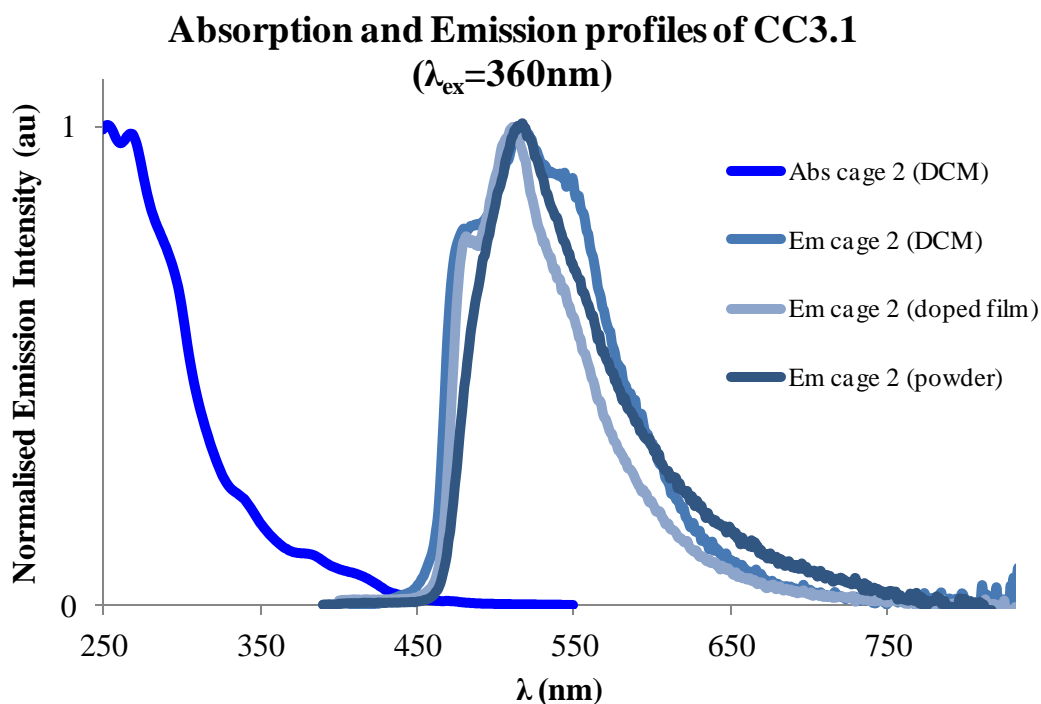


Figure 6.22: Absorption and Emission profiles of CC3.1 in DCM solution, doped thin-film and powder form.

The emission of **CC3.1** is remarkably similar, independent of the method used to analyse it; that is the solution state emission in DCM, the solid state powder emission and the emission when incorporated into a doped thin-film, are all almost coincidental. The λ_{max} in all cases is between 510-520 nm. The rationale behind exploring the solid state emission is to ascribe any alterations in emission to potential vibrational/collisional quenching experienced by the cage in solution. In the solid state, the individual molecules are in a more stationary environment, reducing vibrational quenching. However conversely, there is no additional stability imparted to the assembly due to any complementary interactions between solvent and cage components. The similarities of the solution, powder and thin-film emissions, suggests that the major contributor of **CC3.1** is ligand-based, as ligand-based emission would be less effected by vibrational quenching.

6.4.2 Photophysical properties of CC4.3

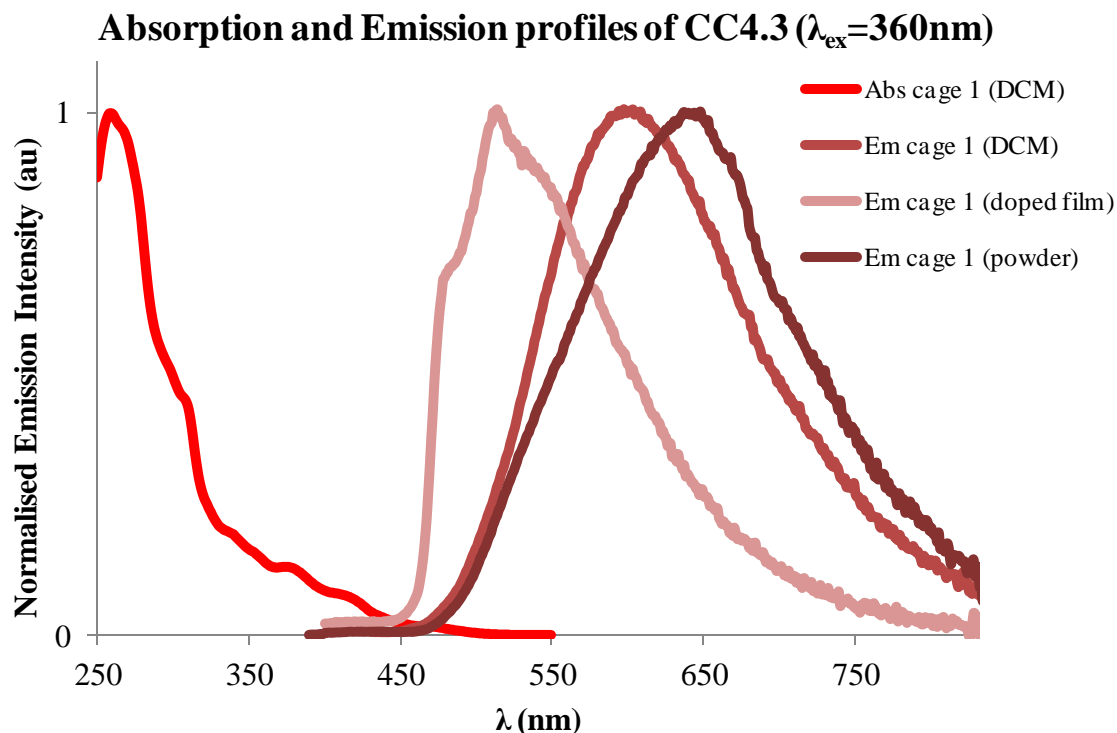


Figure 6.23: Absorption and Emission profiles of CC4.3 in DCM solution, doped thin-film and powder form.

In contrast to **CC3.1**, **CC4.3** shows markedly different emission depending on the method employed. In a doped thin-film, the emission is most similar to **CC3.1**, suggesting again that in this form the emission is mainly due to ligand-based transitions. In DCM solution, the emission of **CC4.3** experiences a bathochromic shift of over 100 nm with respect to the doped film; this shift in conjunction with the broad unstructured emission suggests that in solution the emission is more $^3\text{MLCT}$ in character. The excited state of **CC4.3** must therefore have been stabilised to an extent in order to induce the observed red-shift in emission.

6.4.3 Comparison of the photophysics of CC3.1 and CC4.3

The contrast between the emission properties of **CC3.1** and **CC4.3** is most clearly demonstrated through the dark-room images.

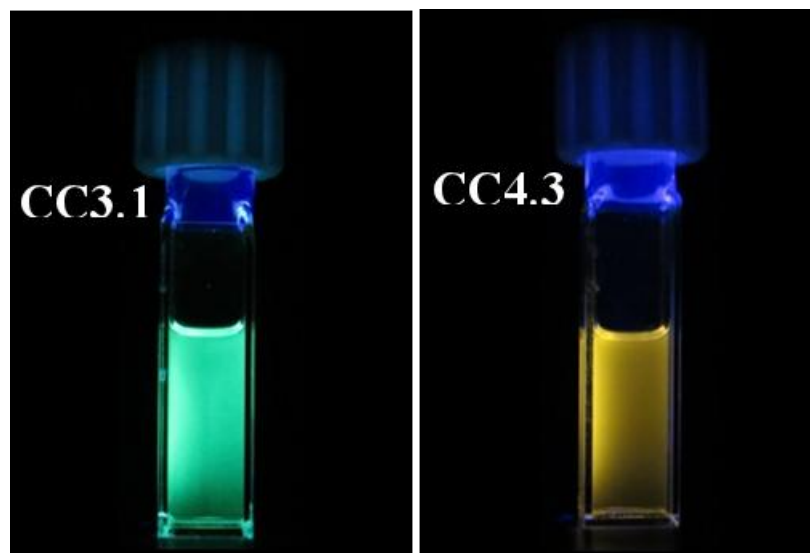


Figure 6.24: Dark-room images of CC3.1 and CC4.3 in DCM solution after irradiation with 360 nm light.

Solution state data shows the largest disparity between the two cages; the ether-linked **CC3.1** displays cyan emission, resulting from an emission maximum on the border between blue and green light at 505 nm, whilst **CC4.3** shows bright yellow emission resulting from an emission maximum at 587 nm. Figure 6.24 also gives an indication of the relative brightness of the two cages; the same intensity excitation wavelength was employed in both instances, and yet **CC3.1** exhibits much brighter emission than that of **CC4.3**.

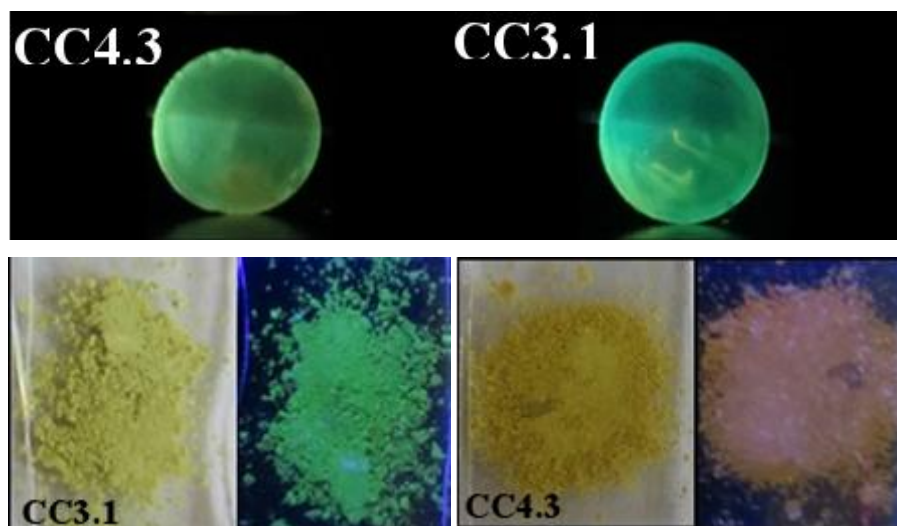
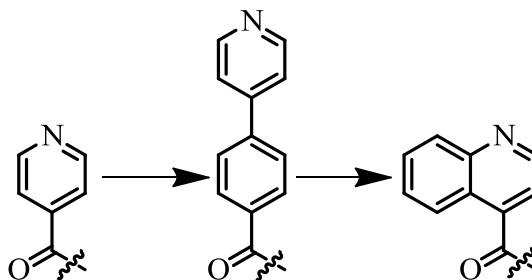


Figure 6.25: Solid-state emission of CC3.1 and CC4.3 in doped thin-film (top) and powder form (bottom).

The emission properties of the cages when doped into thin-films are remarkably similar, as evidenced above. The emission maximum of **CC3.1** and **CC4.3** are both approximately 510 nm, giving rise to the similar cyan colour seen in Figure 6.25. In powder form, however, the differences arise once again. **CC3.1** shows an emission maximum at 511 nm, displaying a hypsochromic shift of over 100 nm with respect to **CC4.3**, which has a maximum at 632 nm.

6.5 Expanding the complexity

The formation of a pair of novel, discrete and luminescent metallocryptophanes derived from what are the simplest cyclotriguaiacylene based ligands, opens the door to investigating the formation of metallocryptophanes with more complex ligand systems. A previous family of metallocryptophanes, those formed through coordination of a Pd(*bis*-NHC) source and **L4**,³³ were expanded upon through elongation of the ligand in both directions, vertical (4-phenylpyridine appended) and horizontal (4-quinolyl appended), but retaining the 4-pyridyl binding angle.



Scheme 6.2: Increasing complexity and/or steric bulk of 4-pyridyl ligands employed in metallocryptophane formation.

Currently within the group, there is a concerted effort towards structurally dynamic capsules and assemblies, particularly focussing on *cis/trans* isomerisation and the resultant geometric changes of the azobenzene group. Another PhD student in the group, Sam Oldknow, has produced a library of cyclotriguaiacylene ligands appended with pyridyl binding moieties whilst also incorporating the azobenzene functional group. The synthesis and characterisation of these ligands will not be discussed in this thesis, just the collaborative effort towards dynamic metallocryptophane cages.

The most remarkable point to come of this collaboration was the relative ease of formation of the M_3L_2 cryptophane cage with **L6**, as there are no previous examples

of the iridium *bis*-phenylpyridine tecton binding to any 3-pyridyl motif. Previous attempts to form a metallocryptophane motif through use of the 3-pyridyl analogue of **L4** were unsuccessful and no evidence of M_3L_2 assemblies or supramolecular assemblies of any size could be seen. It was, however, envisaged that the additional flexibility afforded through the azo group could circumvent any steric issues preventing the formation of the desired product.

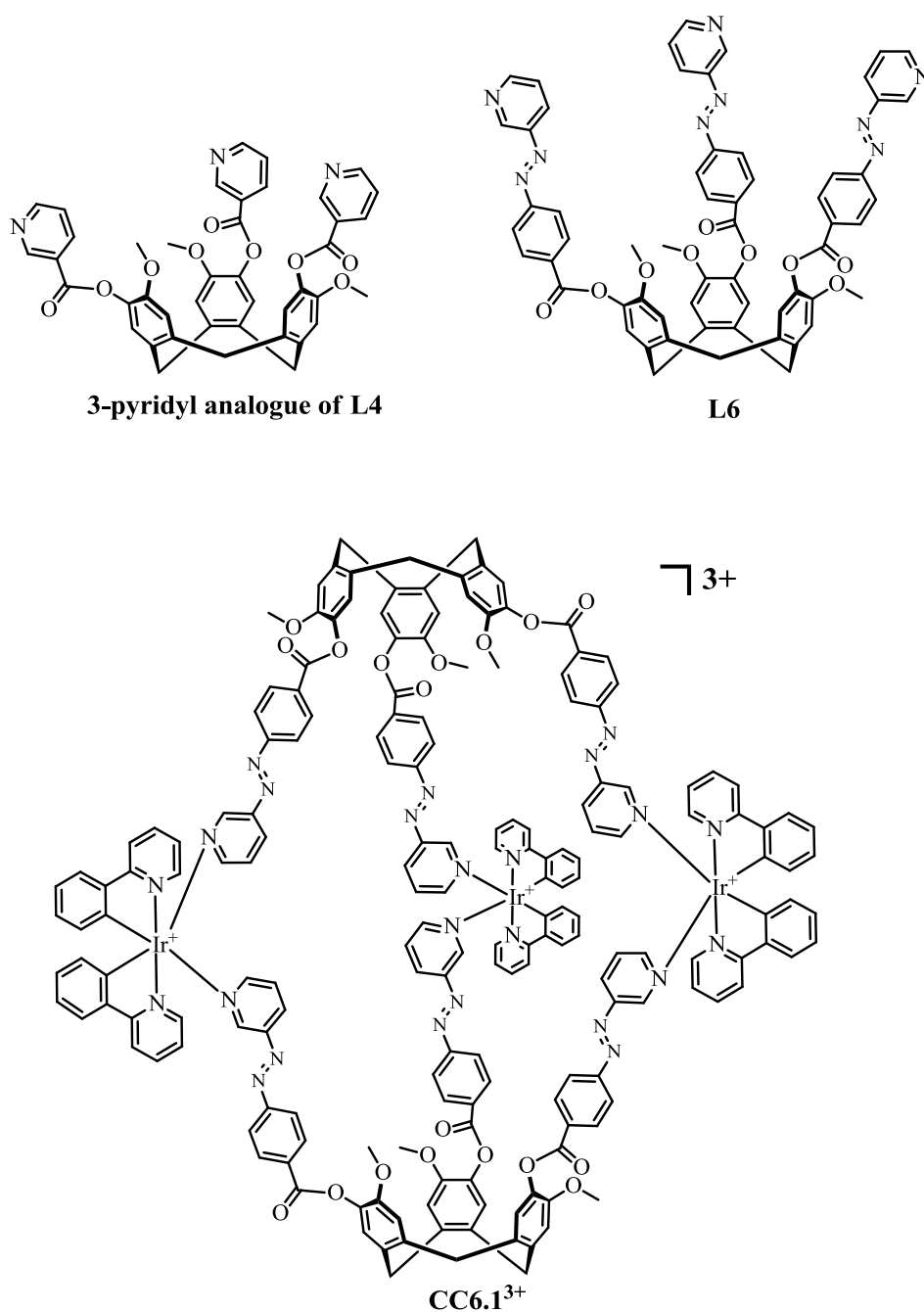


Figure 6.26: Structure of the ligand employed in unsuccessful M_3L_2 attempts, **L6** and the resultant M_3L_2 assembly **CC6.1**.

The synthesis of the dynamic, luminescent metallocryptophane **CC6.1** is analogous to the smaller, simpler cages **CC3.1** and **CC4.3**. Appropriate amounts of azobenzene containing **L6** and metallotecton were combined in nitromethane solvent at room temperature. After 12 hours stirring, the main peak visible through HR ESI-MS was assigned to the triply charged metallocryptophane, Figure 6.27. As with the previously discussed cages, there is some fragmentation into smaller species.

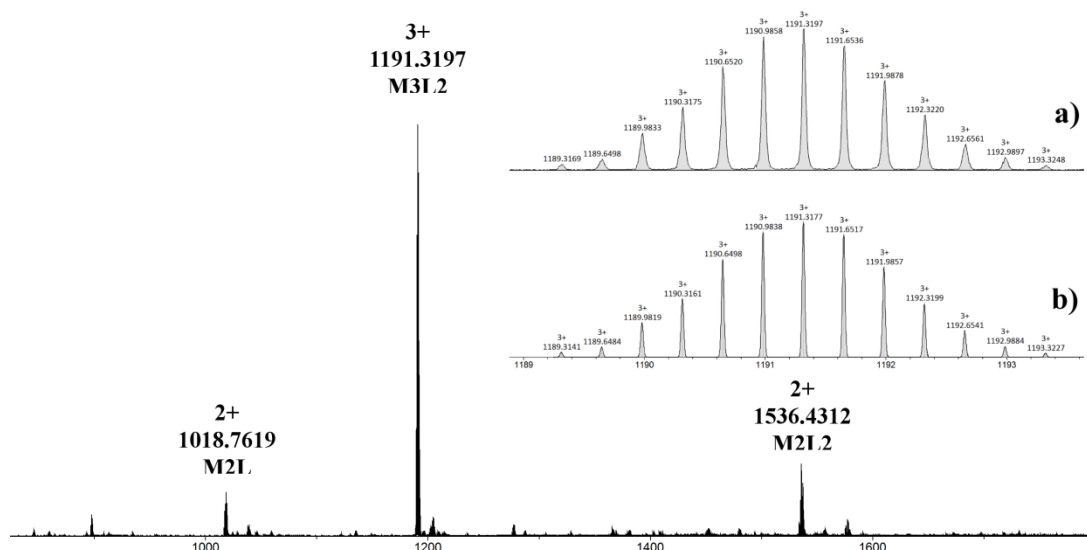


Figure 6.27: HR ESI-MS of M_3L_2 assembly **CC6.1, along with fragmentation products, M_3L_2 peak shown inset a) measured b) calculated isotope pattern for the 3+ peak of **CC6.1**, where $M=[Ir(ppy)_2]^+$ and $L=L6$.**

The formation of **CC6.1** was found to occur on an accelerated timescale when compared to the smaller, more rigid metallocryptophanes **CC3.1** and **CC4.3**. This is thought to be due to the additional flexibility imparted to the ligand scaffold through incorporation of the azobenzene units and extending the ligand arm, thus allowing more torsion and therefore greater ease of formation.

As for to the initial cages, the formation of **CC6.1** was followed by ^1H NMR in d_3 - MeNO_2 solvent. Both components were dissolved in the minimum amount of deuterated nitromethane and combined, as seen in Figure 6.28. The accelerated formation of the cryptophane cage can also be seen in the proton NMR spectrum recorded just 10 minutes after mixing the two components.

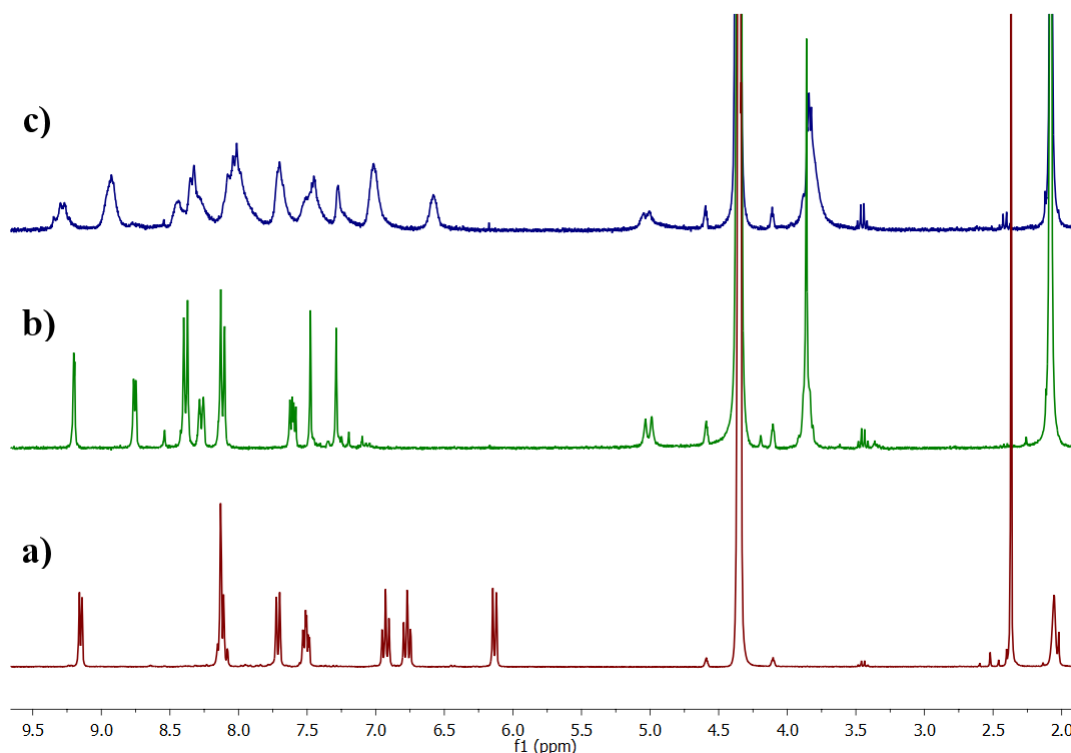


Figure 6.28: ¹H NMR spectra depicting a) metallotecton b) **L6** and c) 10 minutes after combining the two components.

As Figure 6.28 shows, similar to the formation of the previous metallocryptophanes, the most notable peak shift once again belongs to H_{H'}, the proton adjacent to the cyclometallated carbon on the phenylpyridine ancillary ligand. In the metallotecton H_{H'} is found at 6.2 ppm, upon binding to the azobenzene containing **L6** the peak is shifted to 6.5 ppm. The resultant spectrum, c), of the assembled metallocryptophane is noticeably sharper than those of the smaller cages, most likely due to the additional flexibility imparted through the more dynamic ligand, thus allowing more rotational freedom on a NMR timescale.

This reactivity is not restricted to just **L6**, a variety of pyridyl-containing azobenzene-linked ligands have been trialled in the formation of **M₃L₂** metallocryptophanes, all show analogous data with regards to ¹H NMR and HR ESI-MS supporting the formation of cryptophane cages. The ability of these luminescent, structurally-dynamic cages to undergo photo-isomerisation is currently under investigation.

6.6 Conclusions and future direction

A predictable and rational route towards luminescent metallocryptophanes was established, based upon known ligand and metallotecton binding geometries and a complementary design process. The facile room temperature synthesis furnished two novel metallocryptophane complexes, **CC3.1** and **CC4.3**, possessing interesting photophysical properties. The aforementioned supramolecular cages are, as far as the author is aware, the first examples of iridium metallocryptophanes and one of only a handful of examples of supramolecular assemblies incorporating the iridium phenylpyridine metallotecton.

The absolute structure of **CC4.3** was elucidated crystallographically to reveal a doubly enantiomerically self-sorted structure, giving rise to both chiral *anti*-cryptophanes *MM*- $\Lambda\Lambda\Lambda$ and *PP*- $\Delta\Delta\Delta$. The asymmetric unit contains both metallocryptophane enantiomers in full, with each cage possessing an internal void space of $\sim 675 \text{ \AA}^3$ denoting only the second example of rationally designed, chemically robust metallocryptophane cages that show no evidence of catenation or interpenetration.

High solubility of the resultant cages allowed for in depth solution-based investigations into not only the self-assembly of the homo cages, but also the heterocage analogue. The formation of the cages was found to be non-discriminatory, with both homo- and hetero- cages formed upon mixing of the two components. The high stability of the cages was demonstrated through ligand scrambling experiments, whereby the inter-conversion of both pre-formed homo cages to the heterocage analogue was seen to occur over a period of six weeks.

The enantiomeric self-sorting of the cages was exemplified through NMR comparison of the re-dissolved single crystals, known to be enantiomerically sorted, and the *in situ* formed cage, allowed to self sort over time. This study revealed that the self-sorting process takes up to 6 months to occur in solution, as ^1H NMR analysis shows almost complete self-sorting of isomers after this time.

A collaborative effort also resulted in the formation of the first structurally-dynamic azobenzene-containing metallocryptophane **CC6.1**. This work will be continued and expanded upon by current PhD student Sam Oldknow.

Further work could expand upon the potential host-guest chemistry of this metallocryptophane family, exploiting the inherent luminescent emission for sensing

purposes. The incorporation of a structurally dynamic unit in the azobenzene derivative also leads on to potential cargo delivery systems whereby guests could be selectively released through a change in geometry and therefore cage window size/orientation.

6.7 Experimental

6.7.1 Synthesis

Preparation of $\{[\text{Ir}(\text{ppy})_2]_3(\text{L3})_2\} \cdot 3(\text{BF}_4)$ (CC3.1)

$[\text{Ir}(\text{ppy})_2(\text{MeCN})_2] \cdot \text{BF}_4$ (0.036 g, 0.054 mmol) and $(\pm)\text{-L3}$ (0.025 g, 0.037 mmol) were combined in nitromethane solvent (5 mL) and stirred for 12 hours at room temperature. Following HRMS analysis, the main peak visible was the $\{\text{M}_3(\text{L3})_2\}^{3+}$ cation, with smaller peaks assignable as both $\{\text{M}_2(\text{L3})\}^{2+}$ and $\{\text{M}(\text{L3})\}^{1+}$, presumed to be fragmentation products of the M_3L_2 metallocryptophane. The remaining solution was concentrated *in vacuo* and diethyl ether was added to the solution to give the title product, **CC3.1** as a bright yellow powder (0.056 g, 97%) TOF-MS ESI: $m/z = 955.2853$ $[\text{M}_3(\text{L3})_2]^{3+}$ (where $\text{M}=[\text{Ir}(\text{ppy})_2]$), 841.7365 $[\text{M}_2(\text{L3})]^{2+}$, 1182.3779 $[\text{M}(\text{L3})]^+$.

^1H NMR studies were carried out in $d_3\text{-MeNO}_2$, $[\text{Ir}(\text{ppy})_2(\text{MeCN})_2] \cdot \text{BF}_4$ and **L3** were dissolved in deuterated nitromethane, and the individual spectra recorded for comparison. The two solutions were mixed together and an immediate colour change was observed, from the green of the iridium metallocryptophane solution to bright yellow. Immediate broadening of the resultant spectra was observed, indicating coordination and formation of a larger species. ^1H NMR (300 MHz, CD_3NO_2) δ 8.58 (bm, $J = 27.4$ Hz, 3H, $\text{H}_A/\text{H}_{ortho}$), 8.04 (bm, 2H, H_C/H_D), 7.59 (bm, $J = 48.9$ Hz, 4H, $\text{H}_E/\text{H}_B/\text{H}_{meta}$), 7.05 (bm, $J = 48.4$ Hz, 4H, $\text{H}_F/\text{H}_G/2x\text{H}_{aryl}$), 6.50 (bs, 1H, H_H), 5.39 – 4.89 (m, 2H, CH_2), 4.81 (bs, 1H, H_{endo}), 3.99 – 3.36 (bm, 4H, $\text{H}_{exo}/\text{OMe}$).

Preparation of $\{[\text{Ir}(\text{ppy})_2]_3(\text{L4})_2\} \cdot 3(\text{BF}_4)$ (CC4.3)

$[\text{Ir}(\text{ppy})_2(\text{MeCN})_2] \cdot \text{BF}_4$ (0.036 g, 0.054 mmol) and $(\pm)\text{-L4}$ (0.025 g, 0.035 mmol) were combined in nitromethane solvent (5 mL) and stirred for 12 hours at room temperature. Following HRMS analysis, the main peak visible was the $\{\text{M}_3(\text{L4})_2\}^{3+}$ cation, with smaller peaks assignable as both $\{\text{M}_2(\text{L4})\}^{2+}$ and $\{\text{M}(\text{L4})\}^{1+}$, presumed to be fragmentation products of the M_3L_2 metallocryptophane. The remaining solution was concentrated *in vacuo* and diethyl ether was added to the solution to give the title product, **CC4.3** as a bright yellow powder (0.050 g, 90%) TOF-MS ESI: $m/z = 983.1120$ $[\text{M}_3(\text{L4})_2]^{3+}$ (where $\text{M}=[\text{Ir}(\text{ppy})_2]$), 862.3934 $[\text{M}_2(\text{L4})]^{2+}$, 1224.5712 $[\text{M}(\text{L4})]^+$.

^1H NMR studies were carried out in d_3 -MeNO₂, [Ir(ppy)₂(MeCN)₂] \cdot BF₄ and **L4** were dissolved in deuterated nitromethane, and the individual spectrum recorded for comparison. The two solutions were mixed together and an immediate colour change was observed, from the green of the iridium metallotecton solution to bright yellow. Immediate broadening of the resultant spectra was observed, indicating coordination and formation of a larger species. ^1H NMR (300 MHz, CD₃NO₂) δ 9.12 – 8.54 (bm, 3H, H_A/H_{ortho}), 8.05 (bd, $J = 15.5$ Hz, 4H, H_C/H_D/H_{meta}), 7.88 – 7.67 (bm, 1H, H_E), 7.62 – 7.10 (bm, 3H, H_B/2xH_{aryl}), 7.09 – 6.72 (bm, 2H, H_F/H_G), 6.54 (bs, 1H, H_H), 4.97 (d, $J = 15.3$ Hz, 1H, H_{endo}), 3.80 (bd, $J = 14.4, 10.2$ Hz, 4H, H_{exo}/OMe).

Preparation of {[Ir(ppy)₂]₃(L6)₂}\cdot3(PF₆) (CC6.1)

[Ir(ppy)₂(MeCN)₂] \cdot PF₆ (0.025 g, 0.034 mmol) and (\pm)-**L6** (0.024 g, 0.023 mmol) were combined in nitromethane solvent (5 mL) and stirred for 12 hours at room temperature. Following HRMS analysis, the main peak visible was the {**M₃(L6)₂**}³⁺ cation, with smaller peaks assignable as both {**M₂(L6)**}²⁺ and {**M₂(L6)₂**}²⁺, presumed to be fragmentation products of the **M₃L₂** metallocryptophane. The remaining solution was concentrated *in vacuo* and diethyl ether was added to the solution to give the title product, **CC6.1** as a bright orange powder (0.034 g, 73%) TOF-MS ESI: $m/z = 1191.3197$ [**M₃(L6)₂**]³⁺ (where M=[Ir(ppy)₂]), 1018.7619 [**M₂(L3)**]²⁺, 1536.4312 [**M₂(L3)₂**]²⁺.

^1H NMR studies were carried out in d_3 -MeNO₂, [Ir(ppy)₂(MeCN)₂] \cdot PF₆ and **L6** were dissolved in deuterated nitromethane, and the individual spectrum recorded for comparison. The two solutions were mixed together and a slight colour change was observed, from the green of the iridium metallotecton and the dark orange of the ligand solution to bright orange. Immediate broadening of the resultant spectra was observed, indicating coordination and formation of a larger species. ^1H NMR (300 MHz, CD₃NO₂) δ 9.48 – 9.12 (bm, 1H, H_A), 9.04 – 8.81 (bm, 2H, H₂/H₄), 8.51 – 8.16 (bm, 3H, H_{ortho}/H₆), 8.18 – 7.86 (bm, 4H, H_{meta}/H_C/H_D), 7.70 (bs, 2H, H_E/H₅), 7.48 (bd, $J = 22.2$ Hz, 2H, H_{aryl}, H_B), 7.27 (bs, 1H, H_{aryl}), 7.01 (bd, $J = 9.1$ Hz, 2H, H_F/H_G), 6.59 (bs, 1H, H_H), 5.03 (bd, $J = 9.1$ Hz, 1H, H_{endo}), 3.83 (bd, $J = 5.2$ Hz, 4H, H_{exo}/OMe).

6.7.2 X-ray crystallography

Crystals were mounted under inert oil on a MiTeGen tip and flash frozen to 100(1) K using an OxfordCryosystems low temperature device. X-ray diffraction data were collected using Cu- K_{α} radiation ($\lambda = 1.54184 \text{ \AA}$) using an Agilent Supernova dual-source diffractometer with Atlas S2 CCD detector and fine-focus sealed tube generator. Data were corrected for Lorentzian and polarization effects and absorption corrections were applied using multi-scan methods. The structures were solved by direct methods using SHELXS-97 and refined by full-matrix on F^2 using SHELXL-97.⁶³

Crystals were very poorly diffracting due to high levels of solvation and disordered counter-anions. Most high angle data was unobserved. While the cage framework and some solvent nitromethane positions were located in the difference map and included in the refinement, the BF_4^- counter-anions were not located and the true degree of solvation is likely to be significantly higher than was determined crystallographically. Counter-anions were included in the molecular formula, but not missing solvent. The large void spaces and diffuse nature of residual electron density meant that the SQUEEZE⁵⁰ routine of PLATON was employed. Fifteen of the phenyl or pyridyl groups were refined with rigid body constraints. Only the Ir and ordered parts of the CTG-type ligands were refined anisotropically and global restraints were employed on anisotropic displacing parameters. One isonicotinoyl group was refined as being disordered across two positions, each at 0.5 occupancy. Two phenyl-pyridyl groups and one isonicotinoyl groups were each refined with a group isotropic displacement parameter. Nine inter-atomic distances (for Ir-C/N or C-C bonds of phenyl-pyridines) were restrained to be chemically reasonable.

Compound	CC4.3•n(BF₄)
Empirical formula	C₃₀₅H₂₄₃N₂₉O₄₆F₂₄B₆Ir₆
Formula weight	6724.34
Temperature/K	100.15
Crystal system	monoclinic
Space group	<i>P</i> 2 ₁ / <i>n</i>
a (Å)	24.1556(6)
b (Å)	38.3982(8)
c (Å)	48.0129(11)
α (°)	90.00
β (°)	104.151(3)
γ (°)	90.00
Volume (Å ³)	43182.1(17)
Z	4
ρ _{calc} (gcm ⁻³)	1.034
M (mm ⁻¹)	4.013
F(000)	13408.0
Crystal size (mm ³)	0.2 × 0.2 × 0.2
Radiation	CuKα (λ = 1.54184)
2θ range for data collection/°	6.14 to 103.04
Index ranges	-21 ≤ h ≤ 24, -38 ≤ k ≤ 35, -48 ≤ l ≤ 41
Reflections collected	73142
Independent reflections	39064 [R _{int} = 0.0468, R _{sigma} = 0.0656]
Data/restraints/parameters	39064/599/1943
Goodness-of-fit on F ²	1.090
Final R indexes [I ≥ 2σ (I)]	R ₁ = 0.1191, wR ₂ = 0.3191
Final R indexes [all data]	R ₁ = 0.1407, wR ₂ = 0.3357
Largest diff. peak/hole / e Å ⁻³	6.48/-2.25

6.7.3 Photophysical Studies

All samples were prepared at the University of St Andrews by Diego Rota Martir, in HPLC grade DCM with varying concentrations in the order of 10⁻⁴ - 10⁻⁶ M. Absorption spectra were recorded at room temperature using a Shimadzu UV-1800 double beam spectrophotometer. Molar absorptivity determination was verified by linear least-squares fit of values obtained from at least four independent solutions at varying concentrations with absorbance ranging from 6.05 × 10⁻⁵ to 2.07 × 10⁻⁵ M.

The sample solutions for the emission spectra were prepared in HPLC-grade DCM and degassed via freeze-pump-thaw cycles using a quartz cuvette designed in-house.

Steady-state emission and excitation spectra and time-resolved emission spectra were recorded at 298 K using an Edinburgh Instruments F980. All samples for steady-state measurements were excited at 360 nm, while samples for time-resolved measurements were excited at 378 nm using a PDL 800-D pulsed diode laser. Emission quantum yields were determined using the optically dilute method.⁶⁴ A stock solution with absorbance of *ca.* 0.5 was prepared and then four dilutions were prepared with dilution factors between 2 and 20 to obtain solutions with absorbances of *ca.* 0.095, 0.065, 0.05 and 0.018, respectively. The Beer-Lambert law was found to be linear at the concentrations of these solutions. The emission spectra were then measured after the solutions were rigorously degassed via three freeze-pump-thaw cycles prior to spectrum acquisition. For each sample, linearity between absorption and emission intensity was verified through linear regression analysis and additional measurements were acquired until the Pearson regression factor (R^2) for the linear fit of the data set surpassed 0.9. Individual relative quantum yield values were calculated for each solution and the values reported represent the slope value. The equation $\Phi_s = \Phi_r (A_r/A_s)(I_s/I_r)(n_s/n_r)^2$ was used to calculate the relative quantum yield of each of the sample, where Φ_r is the absolute quantum yield of the reference, n is the refractive index of the solvent, A is the absorbance at the excitation wavelength, and I is the integrated area under the corrected emission curve. The subscripts s and r refer to the sample and reference, respectively. A solution of quinine sulfate in 0.5 M H_2SO_4 ($\Phi_r = 54.6\%$) was used as external references.⁶⁵

PMMA doped films were prepared by spin coating the samples from a solution of 2-methoxyethanol (HPLC grade) containing 5 % w/w of the desired sample. Steady-state emission and excitation spectra and time-resolved emission spectra of both powders and doped films were recorded at 298 K using an Edinburgh Instruments F980. Solid-state PLQY measurements of thin films were performed in an integrating sphere under a nitrogen purge in a Hamamatsu C9920-02 luminescence measurement system.⁶⁶

6.8 Bibliography

- 1 C. Wang, X.-Q. Hao, M. Wang, C. Guo, B. Xu, E. N. Tan, Y. Zhang, Y. Yu, Z.-Y. Li, H.-B. Yang, M.-P. Song and X. Li, *Chem. Sci.*, 2013, **5**, 1221–1226.

- 2 I. Elguraish, K. Zhu, L. A. Hernandez, H. Amarne, J. Luo, N. V. Vukotic and S. J. Loeb, *Dalton Trans.*, 2014, **44**, 898–902.
- 3 M. Wang, C. Wang, X.-Q. Hao, X. Li, T. J. Vaughn, Y.-Y. Zhang, Y. Yu, Z.-Y. Li, M.-P. Song, H.-B. Yang and X. Li, *J. Am. Chem. Soc.*, 2014, **136**, 10499–10507.
- 4 A. Metherell and M. D. Ward, *Chem. Commun.*, 2014, **50**, 10979–10982.
- 5 Y.-P. Liang, Y.-J. He, Y.-H. Lee and Y.-T. Chan, *Dalton Trans.*, 2015, **44**, 5139–5145.
- 6 D. K. Chand, M. Fujita, K. Biradha, S. Sakamoto and K. Yamaguchi, *Dalton Trans.*, 2003, 2750–2756.
- 7 M. Yoshizawa, M. Nagao, K. Kumazawa and M. Fujita, *J. Organomet. Chem.*, 2005, **690**, 5383–5388.
- 8 K. Yamashita, M. Kawano and M. Fujita, *Chem. Commun.*, 2007, 4102–4103.
- 9 E. C. Constable, C. E. Housecroft, S. Vujovic and J. A. Zampese, *CrystEngComm*, 2013, **16**, 328–338.
- 10 S.-L. Huang, Y.-J. Lin, T. S. A. Hor and G.-X. Jin, *J. Am. Chem. Soc.*, 2013, **135**, 8125–8128.
- 11 G. Meyer-Eppler, F. Topić, G. Schnakenburg, K. Rissanen and A. Lützen, *Eur. J. Inorg. Chem.*, 2014, **2014**, 2495–2501.
- 12 A. Peuronen, S. Forsblom and M. Lahtinen, *Chem. Commun.*, 2014, **50**, 5469–5472.
- 13 P. Mal, D. Schultz, K. Beyeh, K. Rissanen and J. R. Nitschke, *Angew. Chem. Int. Ed.*, 2008, **47**, 8297–8301.
- 14 A. Jiménez, R. A. Bilbeisi, T. K. Ronson, S. Zarra, C. Woodhead and J. R. Nitschke, *Angew. Chem. Int. Ed.*, 2014, **53**, 4556–4560.
- 15 J. L. Bolliger, T. K. Ronson, M. Ogawa and J. R. Nitschke, *J. Am. Chem. Soc.*, 2014, **136**, 14545–14553.

-
- 16 P. Mal, B. Breiner, K. Rissanen and J. R. Nitschke, *Science*, 2009, **324**, 1697–1699.
- 17 P. Bonakdarzadeh, F. Topić, E. Kalenius, S. Bhowmik, S. Sato, M. Groessel, R. Knochenmuss and K. Rissanen, *Inorg. Chem.*, 2015, **54**, 6055–6061.
- 18 C. Schouwey, J. J. Holstein, R. Scopelliti, K. O. Zhurov, K. O. Nagornov, Y. O. Tsybin, O. S. Smart, G. Bricogne and K. Severin, *Angew. Chem. Int. Ed.*, 2014, **53**, 11261–11265.
- 19 D. Samanta and P. S. Mukherjee, *J. Am. Chem. Soc.*, 2014, **136**, 17006–17009.
- 20 R. Hovorka, G. Meyer-Eppler, T. Piehler, S. Hytteballe, M. Engeser, F. Topić, K. Rissanen and A. Lützen, *Chem. – Eur. J.*, 2014, **20**, 13253–13528.
- 21 K. Harris, D. Fujita and M. Fujita, *Chem. Commun.*, 2013.
- 22 D. K. Chand, K. Biradha, M. Fujita, S. Sakamoto and K. Yamaguchi, *Chem. Commun.*, 2002, 2486–2487.
- 23 R. A. Bilbeisi, T. K. Ronson and J. R. Nitschke, *Angew. Chem. Int. Ed.*, 2013, **52**, 9027–9030.
- 24 D. M. Wood, W. Meng, T. K. Ronson, A. R. Stefankiewicz, J. K. M. Sanders and J. R. Nitschke, *Angew. Chem. Int. Ed.*, 2015, **54**, 3988–3992.
- 25 A. Collet, *Tetrahedron*, 1987, **43**, 5725–5759.
- 26 R. Tyagi, C. Witte, R. Haag and L. Schröder, *Org. Lett.*, 2014, **16**, 4436–4439.
- 27 J. Canceill and A. Collet, *J. Chem. Soc. Chem. Commun.*, 1988, 582–584.
- 28 T. Brotin and J.-P. Dutasta, *Chem. Rev.*, 2009, **109**, 88–130.
- 29 T. K. Ronson, H. Nowell, A. Westcott and M. J. Hardie, *Chem. Commun.*, 2011, **47**, 176.
- 30 J. J. Henkelis, T. K. Ronson, L. P. Harding and M. J. Hardie, *Chem. Commun.*, 2011, **47**, 6560–6562.
- 31 A. Westcott, J. Fisher, L. P. Harding, P. Rizkallah and M. J. Hardie, *J. Am. Chem. Soc.*, 2008, **130**, 2950–2951.
-

- 32 Z. Zhong, A. Ikeda, S. Shinkai, S. Sakamoto and K. Yamaguchi, *Org. Lett.*, 2001, **3**, 1085–1087.
- 33 J. J. Henkelis, C. J. Carruthers, S. E. Chambers, R. Clowes, A. I. Cooper, J. Fisher and M. J. Hardie, *J. Am. Chem. Soc.*, 2014, **136**, 14393–14396.
- 34 A. Schaly, Y. Rousselin, J.-C. Chambron, E. Aubert and E. Espinosa, *Eur. J. Inorg. Chem.*, 2016, **2016**, 832–843.
- 35 N. Singh, J.-H. Jo, Y. Song, H. Kim, D. Kim, M. S. Lah and K.-W. Chi, *Chem. Commun.*, 2015, **51**, 4492–4495.
- 36 W.-Y. Zhang, Y.-F. Han, L.-H. Weng and G.-X. Jin, *Organometallics*, 2014, **33**, 3091–3095.
- 37 E. Baranoff, E. Orselli, L. Allouche, D. D. Censo, R. Scopelliti, M. Grätzel and M. K. Nazeeruddin, *Chem. Commun.*, 2011, **47**, 2799–2801.
- 38 O. Chepelin, J. Ujma, X. Wu, A. M. Z. Slawin, M. B. Pitak, S. J. Coles, J. Michel, A. C. Jones, P. E. Barran and P. J. Lusby, *J. Am. Chem. Soc.*, 2012, **134**, 19334–19337.
- 39 V. Chandrasekhar, T. Hajra, J. K. Bera, S. M. W. Rahaman, N. Satumtira, O. Elbjeirami and M. A. Omary, *Inorg. Chem.*, 2012, **51**, 1319–1329.
- 40 C. J. Sumbly, J. Fisher, T. J. Prior and M. J. Hardie, *Chem. – Eur. J.*, 2006, **12**, 2945–2959.
- 41 T. Haino, M. Kobayashi, M. Chikaraishi and Y. Fukazawa, *Chem. Commun.*, 2005, 2321–2323.
- 42 V. V. Krishnan, *J. Magn. Reson.*, 1997, **124**, 468–473.
- 43 S. A. Boer and D. R. Turner, *Chem. Commun.*, 2015, **51**, 17375–17378.
- 44 L.-L. Yan, C.-H. Tan, G.-L. Zhang, L.-P. Zhou, J.-C. Bünzli and Q.-F. Sun, *J. Am. Chem. Soc.*, 2015, **137**, 8550–8555.
- 45 P. N. Taylor and H. L. Anderson, *J. Am. Chem. Soc.*, 1999, **121**, 11538–11545.
- 46 L. R. Holloway, M. C. Young, G. J. O. Beran and R. J. Hooley, *Chem. Sci.*, 2015, **6**, 4801–4806.

- 47 O. Gidron, M. Jirásek, N. Trapp, M.-O. Ebert, X. Zhang and F. Diederich, *J. Am. Chem. Soc.*, 2015, **137**, 12502–12505.
- 48 F. G. Terrade, M. Lutz and J. N. H. Reek, *Chem. – Eur. J.*, 2013, **19**, 10458–10462.
- 49 W.-S. Sie, G.-H. Lee, K. Y.-D. Tsai, I.-J. Chang and K.-B. Shiu, *J. Mol. Struct.*, 2008, **890**, 198–202.
- 50 A. Spek, *Acta Crystallogr. Sect. A*, 1990, **46**, c34.
- 51 J. J. Henkelis, J. Fisher, S. L. Warriner and M. J. Hardie, *Chem. – Eur. J.*, 2014, **20**, 4117–4125.
- 52 N. J. Cookson, J. J. Henkelis, R. J. Ansell, C. W. G. Fishwick, M. J. Hardie and J. Fisher, *Dalton Trans.*, 2014, **43**, 5657–5661.
- 53 T. K. Ronson, C. Carruthers, J. Fisher, T. Brotin, L. P. Harding, P. J. Rizkallah and M. J. Hardie, *Inorg. Chem.*, 2010, **49**, 675–685.
- 54 T. K. Ronson, J. Fisher, L. P. Harding and M. J. Hardie, *Angew. Chem. Int. Ed.*, 2007, **46**, 9086–9088.
- 55 B. H. Northrop, H.-B. Yang and P. J. Stang, *Chem. Commun.*, 2008, 5896–5908.
- 56 Y.-R. Zheng and P. J. Stang, *J. Am. Chem. Soc.*, 2009, **131**, 3487–3489.
- 57 M. Schmittel, *Chem. Commun.*, 2015, **51**, 14956–14968.
- 58 M. Schmittel and A. Ganz, *Chem. Commun.*, 1997, 999–1000.
- 59 C. S. Wood, T. K. Ronson, A. M. Belenguer, J. J. Holstein and J. R. Nitschke, *Nat. Chem.*, 2015, **7**, 354–358.
- 60 E. O. Pyzer-Knapp, H. P. G. Thompson, F. Schiffmann, K. E. Jelfs, S. Y. Chong, M. A. Little, A. I. Cooper and G. M. Day, *Chem. Sci.*, 2014, **5**, 2235–2245.
- 61 M. A. Little, S. Y. Chong, M. Schmidtman, T. Hasell and A. I. Cooper, *Chem. Commun.*, 2014, **50**, 9465–9468.
- 62 S. Jiang, K. E. Jelfs, D. Holden, T. Hasell, S. Y. Chong, M. Haranczyk, A. Trewin and A. I. Cooper, *J. Am. Chem. Soc.*, 2013, **135**, 17818–17830.

- 63 G. M. Sheldrick, *Acta Crystallogr. A*, 2008, **64**, 112–122.
- 64 G. A. Crosby and J. N. Demas, *J. Phys. Chem.*, 1971, **75**, 991–1024.
- 65 A. M. Brouwer, *Pure Appl. Chem.*, 2011, **83**, 2213–2228.
- 66 N. C. Greenham, I. D. W. Samuel, G. R. Hayes, R. T. Phillips, Y. A. R. R. Kessener, S. C. Moratti, A. B. Holmes and R. H. Friend, *Chem. Phys. Lett.*, 1995, **241**, 89–96.